7-6-2017

Structure and Function of Protein Kinase R

Christopher B. Mayo
University of Connecticut - Storrs, chrismayo826@gmail.com

Structure and Function of Protein Kinase R

Christopher B. Mayo, PhD
University of Connecticut, 2017

Protein Kinase R (PKR) is a central component of the innate immunity antiviral pathway and is activated by dsRNA. PKR contains two tandem dsRNA binding domains and a C-terminal kinase domain. In the canonical activation model, binding of multiple PKR monomers to dsRNA enhances dimerization of the kinase domain, leading to enzymatic activation. A minimal dsRNA length of 30 bp is required for activation. However, short (~15 bp) stem-loop RNAs containing flanking single stranded tails (ss-dsRNAs) are capable of activating PKR. Here, we characterize the structural features of ss-dsRNAs that contribute to activation. We have designed a model ss-dsRNA containing 15 nt single stranded tails and a 15 bp stem and made systematic truncations of the tail and stem regions. Activation potency and binding affinity decrease as the ssRNA tails are truncated and activation is abolished in cases where the binding affinity is strongly reduced. We demonstrate that isolated single-stranded RNAs bind to PKR with micromolar dissociation constants and can induce activation. Single-stranded RNAs also activate PKR constructs lacking the double-stranded RNA binding domain and bind to a basic region adjacent to the N-terminus of the kinase. The length of the duplex regions in several natural RNA activators of PKR is below the minimum of 30 bp required for activation and similar interactions with single stranded regions may contribute to PKR activation in these cases.

We have also solved the crystal structure of the PKR kinase domain. PKR forms a unique oligomeric assembly of alternating front-to-front and back-to-back interfaces. Within the front-to-front interface activation segments from each protomer are exchanged and oriented toward the active site of the reciprocal protomer. Similar complexes have been reported for other kinases and are interpreted to represent a *trans*-autophosphorylation complex. This structure has profound implications for PKR activation models.

Structure and Function of Protein Kinase R

Christopher B. Mayo

B.S., Worcester Polytechnic Institute, 2008

A Dissertation

Submitted in Partial Fulfillment of the

Requirements for the Degree of

Doctor of Philosophy

at the

University of Connecticut

2017

APPROVAL PAGE

Doctor of Philosophy Dissertation

Structure and Function of Protein Kinase R

Presented by

Christopher B. Mayo, B.S.

Major Advisor_____
James L. Cole

Associate Advisor _____
Carolyn M. Teschke

Associate Advisor _____
Victoria L. Robinson

University of Connecticut
2017

Table of Contents

List of Figures

Chapter 4: Interaction with single-stranded nucleic acids

Chapter 5: Structural analysis of the kinase domain

Chapter 6: Host and viral protein regulators of PKR

List of Tables

Chapter 1: Introduction

1.1 Introduction

Protein kinase R (PKR) is a key component of the interferon-induced viral response pathway (1). The protein is comprised of tandem N-terminal dsRNA binding domains (dsRBD1 and dsRBD2) and a C-terminal serine/threonine kinase domain connected by an ~80 residue flexible linker (Fig. 1.1). PKR is synthesized in a latent state and is activated by autophosphorylation upon binding to double-stranded regions present in RNAs (dsRNA) (2). Stimulatory RNAs typically originate from viral infection but several endogenous RNAs have also been identified as PKR activators (3-7). Activated PKR phosphorylates the alpha subunit of eukaryotic initiation factor 2 (eIF2α) leading to inhibition of protein synthesis and viral replication in infected cells (8). The myriad of virally-encoded PKR inhibitors highlights the importance of the PKR antiviral pathway (9). PKR also phosphorylates insulin receptor substrate (10) and participates in pathways regulating stress response, cellular growth and proliferation, nutrient signaling and metabolism (8, 11).

Figure 1.1 PKR domain organization. Each dsRBD is ~70 amino acids long and are separated by a 25 residue linker. An ~80 residue region separates dsRBD2 from the kinase domain which is composed of 300 amino acids.

1.2 Interaction with dsRNA

Nature has produced a variety of RNA-binding modules which are appended to RNA-binding proteins to bestow specificity toward certain RNA forms. Multiple copies are typically present to confer increased binding affinity (12). PKR contains two copies of a highly conserved domain, the dsRBD, which binds duplex RNA (13). The structure of the dsRBDs was solved by NMR (14) however a structure in complex with dsRNA is unavailable. Both dsRBDs adopt a canonical αβββα fold where the two helices pack against a three stranded anti-parallel beta sheet (Fig. 1.2A). The dsRBD selectively interacts with A-form RNA duplexes over other forms

of nucleic acid (15). Structures of homologous dsRBDs in complex with dsRNA provide insight into the recognition mechanism (16-22). The structure of Xlrbpa2 from *Xenopus laevis* in complex with a coaxially stacked RNA duplex (23) is presented in Figure 1.2B as a model for how PKR presumably engages dsRNA. Basic and polar residues along the RNA binding surface interact with the phosphates and 2′-hydroxyls which decorate the RNA backbone in a geometric pattern which is specific for the morphology of the A-form RNA duplex. The interface spans two minor grooves and the intervening major groove with a binding footprint of ~15 bp. Three regions mediate RNA recognition. Their amino acid composition is highly conserved within the dsRBD family (Fig. 1.2B) (13). Regions one and three also contact bases within the minor groove however the deep major groove precludes contact with bases at region three. These interactions are not sequence specific, which is attributed to minimal interactions with nucleotide bases and a lack of sufficient sequence-specific functional groups within the minor groove (13). RNA structural features can contribute to the interaction. In Rnt1p RNaseIII and ADAR2, an RNA tetraloop engages the dsRBD to orient the catalytic domain of the protein (24, 25). Affinity cleavage and NMR experiments indicate loops and bulges can modulate PKR binding although the functional relevance is unclear (26-28).

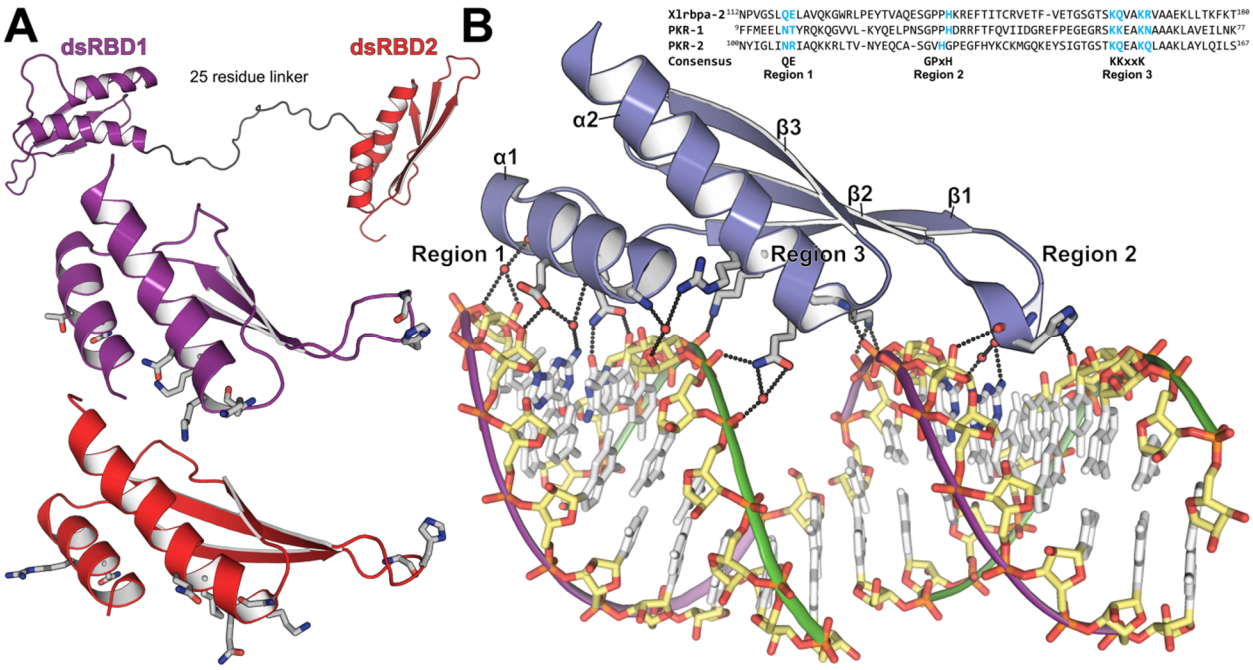

Figure 1.2 dsRBD interaction with dsRNA. (A) NMR structure of dsRBD1-dsRBD2 from PKR (1QU6). Enlarged images of the dsRBD1 (purple) and dsRBD2 (red) are shown below with the residues at conserved RNA interaction sites shown as sticks. **(B)** Crystal structure of the Xlrbpa dsRBD2 in complex with dsRNA (1DI2). 10 bp helices coaxially stack to form an extended duplex within the crystal. The path of the duplex is indicated by green and purple traces of the phosphates. Atoms are colored by the standard coloring scheme (red: oxygen, blue: nitrogen, phosphorous: orange). The ribose sugar is yellow. Nucleotide bases are white with exception to those involved in protein interaction. Oxygens from water molecules are shown is red spheres. Protein residues participating in the interaction are rendered as grey sticks and hydrogen bonds are depicted as black dashed lines. An alignment between the structures shown in the Figure is included. Side chains which are shown as sticks are indicated in the alignment. The consensus RNA-binding residues are included (13).

1.3 General mechanisms of kinase activation applied to PKR

Two structural analyses of the PKR kinase domain have yielded three structures all solved by X-ray crystallography. One study reports the kinase domain in its active form, as categorized by a phosphorylated activation loop, and in complex with its substrate, eIF2α (29). Two structures were obtained: one containing AMP-PNP and magnesium in the active site (PDB: 2A19) and the other without (PDB: 2A1A). The other study reports a structure containing an inactivating mutation, K296R, in the absence of ligands (30) (PDB: 3UIU). Both structures exhibit a similar domain architecture and back-to-back dimeric configuration of PKR molecules. The kinase domain has a bilobal structure typical of eukaryotic protein kinases (31) consisting of

a smaller N-terminal lobe and larger C-terminal lobe connected by a flexible hinge region (Fig. 1.3). The active site is formed in the cleft between the two lobes. The back-to-back dimer interface is formed between the N-lobes and orients the active sites toward opposite faces of the complex (Fig 1.3A). In the structure of K296R PKR a face-to-face dimer is also reported which is formed across a crystallographic symmetry axis (30). The biological relevance of the interface remains unclear. In PKR and many eukaryotic kinases the transition from an inactive to active state is controlled by activation loop phosphorylation (32). An upstream activating kinase has not been identified so PKR must phosphorylate its own activation loop indicating a basal level of activity in the latent state (33). Both intra (*cis*) (34) and intermolecular (*trans*) (35-38) autophosphorylation mechanisms have been proposed. An allosteric pathway is proposed to link the active site to the back-to-back dimer interface via a critical regulatory structural element, helix αC (29). The functional relevance of the back-to-back dimer is supported by mutagenesis of key interfacial residues which abrogates enzymatic activity (39). The conserved structural features of eukaryotic kinases are discussed below and described in the context of PKR.

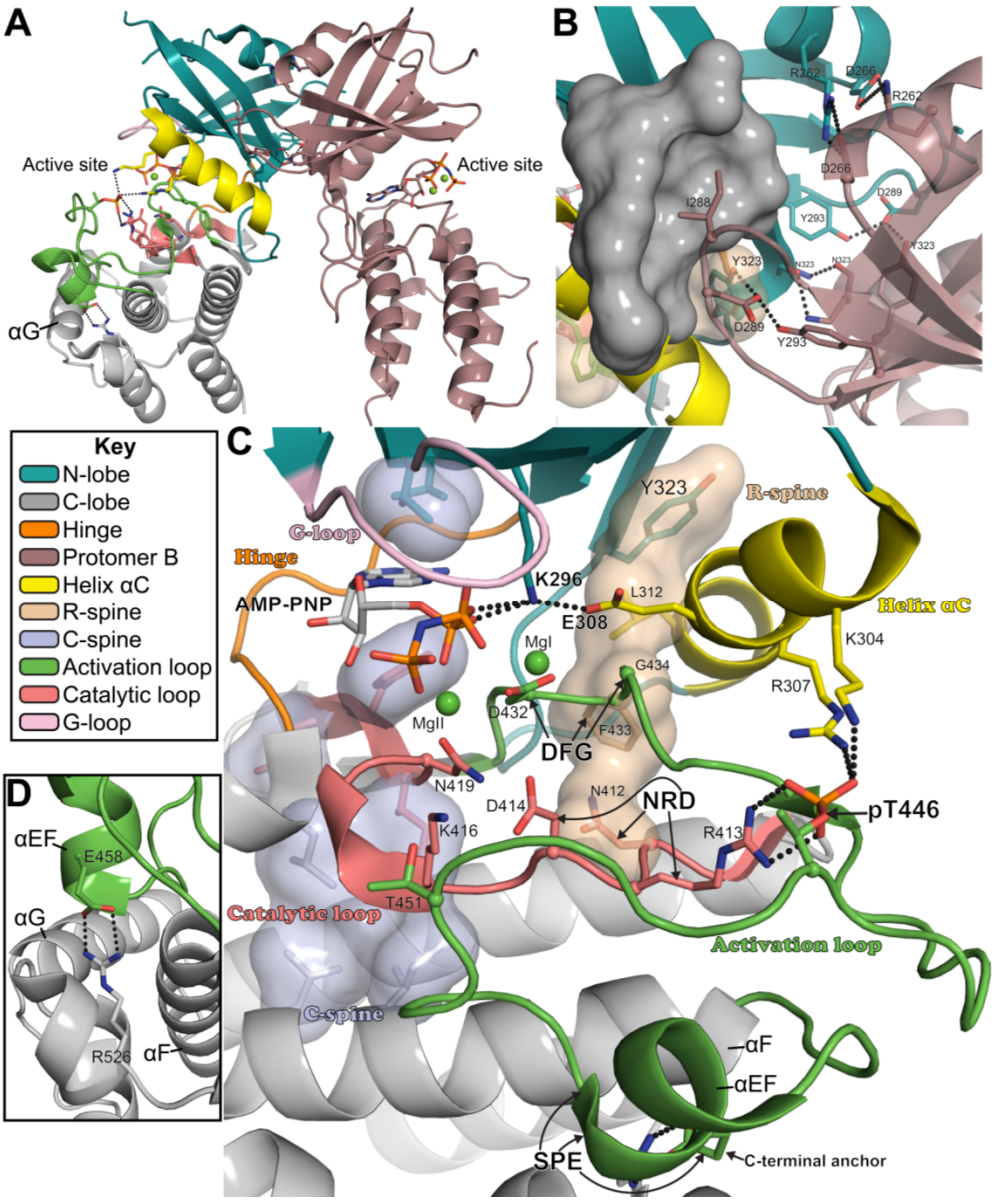

Figure 1.3 Structure of the PKR kinase domain (PDB: 2A19). Color coding in the key underneath panel A applies to the entire figure. **(A)** Back-to-back dimer interface. **(B)** Enlarged view of the dimer interface. Residues contributing to the interaction are shown as sticks with hydrogen bonds drawn as black dashed lines. I288 packs into a hydrophobic pocket on the back of helix αC shown as a surface representation. **(C)** View looking into the active site. Canonical structural motifs are annotated onto PKR. **(D)** Enlarged view of C-terminal anchor.

The inactive conformations of eukaryotic kinases are quite divergent however the active state is conserved and characterized by a group of canonical structural motifs and interactions (40). The prototypical Ser/Thr kinase PKA has served as a model to define the features of the active kinase core structure (41). The nomenclature which has been adopted to describe the

anatomy of the kinase is annotated onto PKR in Figure 1.3B. Two hydrophobic spines bridge the kinase domain connecting the N- and C-lobes (42). The catalytic spine (C-spine) provides a binding pocket for the adenosine purine ring and orients the catalytic loop and is typically assembled even in inactive kinases. The regulatory spine (R-spine) is more dynamic and is usually disassembled in inactive structures due to conformational changes to αC (43). In PKR, the R-spine is intimately linked to the dimer interface by Y323 which completes the spine at the back of the N-lobe. Y323 participates in dimerization by engaging in a hydrogen bond triad with Y293 and D289 from the reciprocal protomer (Fig. 1.3B).

The catalytic loop runs along the base of the active site and contains the canonical tripeptide motif HRD (NRD in PKR). The aspartate within NRD (D414) acts as a catalytic base during the phosphoryl transfer reaction. In kinases regulated by activation loop phosphorylation the catalytic aspartate is typically preceded by an arginine (R413) which interacts with the phosphorylated moiety in the activation loop (44). Also contained within the catalytic loop are N419 which chelates a magnesium ion (MgII) and K416 which typically interacts with the terminal phosphate.

The activation segment is commonly defined as the region lying between two conserved tripeptide motifs DFG and APE (SPE in PKR). The aspartate (D432) from DFG chelates a magnesium ion (MgI) and the phenylalanine (F433) is a component of the R-spine. When the regulatory spine is broken a destabilizing effect is imposed upon the aspartate which impairs magnesium binding and catalysis. The SPE motif forms part of a short helix, αEF, at the C-terminal end of the activation segment. A conserved salt bridge interaction between the glutamic acid and an arginine from the base of the C-lobe anchors the C-terminal portion of the activation segment (Fig. 1.3D). The activation segment is sometimes further delineated into the activation loop and the P+1 loop. The activation loop contains the primary phosphorylation site which corresponds to T446 in PKR and is phosphorylated in the structure presented in Figure 1.3. Activation loop phosphorylation significantly enhances activity (45) although the nuances of the

structural regulatory mechanism are still a subject of some debate (32, 46). Generally, the improved catalytic activity can be ascribed to a disordered to ordered transition of the activation loop mediated by coordination of the phosphorylated residue. Kinases regulated by activation loop phosphorylation typically contain the tripeptide motif HRD within the catalytic loop and are classified as 'RD' kinases (44). The histidine is less conserved (32). In PKA, this residue is a tyrosine and proposed to contributed to the hydrophobic R-spine (42) however in PKR an asparagine fills this position so the hydrophobic character is lost. The arginine from HRD promotes folding of the activation loop by an anchoring interaction with the phosphorylated side chain. In PKR, basic residues emanating from helix αC also contribute to phosphate coordination (Fig. 1.3C). The P+1 portion of the activation segment forms the docking site for the substrate peptide. However, PKR may not use this canonical substrate docking platform to achieve specificity. In the structure of PKR in complex with its protein substrate, eIF2α, the region containing the substrate serine (S51) is disordered (29). eIF2α binds at a site remote to the active site on helix αG. The interaction is postulated to induce a conformational change within eIF2α which increases flexibility of the S51 loop to promote a transient interaction within the active site (47). PKR possesses a noncanonical secondary phosphorylation site within the P+1 loop at residue T451 (48). A serine or threonine residue occupies this position in all Ser/Thr kinases however it is not typically phosphorylated (32). In PKA, a catalytic function has been proposed (49, 50) although it is unclear whether phosphorylation is compatible with the catalytic mechanism.

The final structural element which will be discussed here is the αC helix. By now, a few of its regulatory mechanisms have been addressed. L312 from helix αC interdigitates into the R-spine to stabilize the active site region. Basic residues (K304 and R307) protrude from the helix and interact with T446 to stabilize the activation loop. The final regulatory role is an invariant salt bridge formed between a glutamate from helix αC (E308) and a lysine from β3 (K296). This

interaction favorably orients the lysine to coordinate the α- and β- phosphates and position ATP for catalysis.

Conformational changes to the activation loop and helix αC are most commonly associated with the on/off regulatory switch (51). These dynamic elements form the periphery of the active site and the interactions they make with the catalytic machinery rationalizes their regulatory role (44). As previously stated, the conformations adopted by inactive kinases are quite diverse (40). However, the general molecular motions associated with the switch to the active state are characterized by a more closed and rigid conformation. The dynamic elements of the kinase which include the glycine rich loop (G-loop) above ATP, helix αC, and the activation segment clamp around the active site. These conformational changes protect the active site from solvent, provide necessary stabilizing interactions, and provide a docking site for the substrate. In PKR, the dimer interface regulates kinase activation by an allosteric pathway that involves helix αC (29).

1.4 Mechanism of PKR activation

Two models have been proposed to describe how RNA binding at the N-terminus activates the C-terminal kinase domain which is separated by an ~80 residue linker. In the autoinhibition model, an intramolecular interaction between the dsRBDs and the kinase domain maintains PKR in a closed conformation which prohibits access of ATP substrate to the active site (52, 53). Interaction with RNA relieves the inhibition activating the kinase. The most convincing evidence in support of this model are NMR experiments which demonstrate chemical shift perturbations within dsRBD2 and the kinase domain when the isolated components are mixed (54, 55). Additionally, affinity cleavage (56), analytical ultracentrifugation, and NMR experiments (57) indicate that only dsRBD1 interacts with nonactivating RNAs whereas both dsRBDs engage activating RNAs. ATP crosslinking experiments indicate that active site becomes more accessible following RNA binding or kinase phosphorylation (53).

The dimerization model emphasizes intermolecular interactions mediated by RNA binding (58). More recent investigations dispute the aforementioned intramolecular interaction or indicate it is insufficient to induce autoinhibition. A dsRBD1/2 construct interacts only very weakly with the isolated kinase domain (K_d ~ 250 μM) (59). This is consistent with SAXS analysis which indicates PKR samples multiple compact and extended conformations in solution with an intramolecular equilibria of ~1-10 (60). These affinities are too weak to maintain the closed conformation required for inhibition. Finally, the resonance assignments for the isolated dsRBDs and kinase domains superimpose with the NMR spectra of full length PKR indicating the two domains behave independently in solution (38).

Biochemical and biophysical data indicate that dimerization plays a critical role in the PKR activation mechanism (61). The structural relevance of the dimer interface was addressed in the previous section. PKR dimerizes weakly in solution and dimerization is sufficient to activate PKR in the absence of RNA (35). Consistent with the dimerization model, activation by dsRNAs requires a lattice length of 30 bp which correlates with the minimal length capable of binding at least two PKR monomers (62-64). FRET measurements indicate activating RNAs induce kinase domain dimerization (65). Activation of PKR by dsRNA shows a characteristic bell-shaped dependence on dsRNA concentration (Fig. 1.4) (64, 66). This behavior is rationalized in a model where high dsRNA concentration reduces the number of PKR monomers bound to the same dsRNA and thus inhibits dimerization (67). Binding affinity measurements can be used to simulate the fractional concentration of PKR contained within a complex containing one RNA and two PKR molecules, denoted as the RP_2 species. The RNA concentration dependence of the simulated RP_2 species distributions mirror the bell-shaped activation curves with maxima at approximately equal RNA concentrations (63). These observations have led to a simple model where the role of RNA is to serve as a scaffold to facilitate kinase domain dimerization. Because of the strong correlation between RP_2 and

activation we typically characterize PKR activators by their ability to mediate PKR oligomerization and will be a predominant theme in the studies presented here.

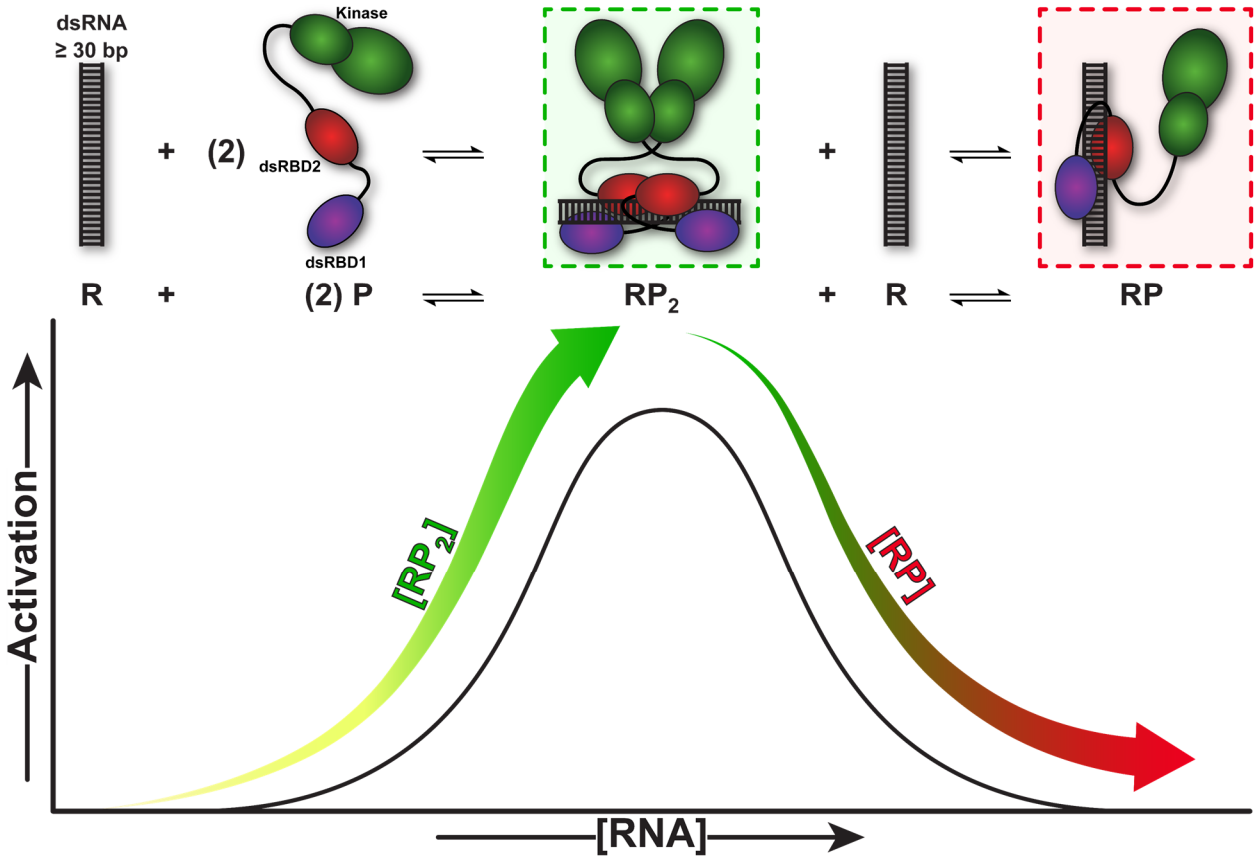

Figure 1.4 Dimerization model for activation. A theoretical bell-shaped activation curve is shown on the bottom generated by a titration of activating RNA against a fixed concentration of PKR. The width of the stylized arrows which follow the path of the curve are meant to represent the relative concentrations of RP_2 (green) and RP (red) species.

1.5 Interaction with complex RNAs

Perfect duplex RNAs have served as a model to establish the basic rules which govern RNA mediated activation of PKR. However, the RNAs which PKR interacts with *in vivo* rarely contain 30 bp of uninterrupted duplex RNA. Instead, their structures are punctuated by features such as stem-loops, bulges, internal loops, single-stranded regions, and more complex tertiary interactions (68) (Fig. 1.5). These structural elements can positively and negatively regulate PKR activity and, in some cases, do not adhere to the rubric for duplex lattice length. The structural features which differentiate activating RNAs from those which function as inhibitors

remain largely undefined. It has become apparent that a rigorous examination is required to characterize the effects of various RNA folded conformations on PKR activation. The effect of bent duplex structures introduced by mismatched base pairs has been extensively investigated. PKR is able to straighten the duplex (69) although activation is reduced and activation potency is determined by the geometry of the kinked structure (70). These types of investigations which analyze simple RNA features must be extended to develop a catalog which describes how combinations of basic RNA structural building blocks affect PKR activity.

Several mRNAs activate PKR for regulatory purposes and some utilize complex structures which function effectively as noncanonical stimulatory elements. PKR is involved in a negative feedback loop which regulates production of interferon-γ during the interferon-mediated antiviral response. Interferon-γ mRNA attenuates its own translation by PKR activation, providing a method to regulate both PKR levels and interferon production within the infected cell (71). Activation is dependent on a pseudoknot formed within the mRNA 5′ UTR which mimics an extended duplex by coaxial stacking interactions with the neighboring stems (4, 6). TNF-α induces PKR gene expression and a positive feedback loop has been proposed which upregulates PKR (71). Splicing of TNF-α mRNA is dependent on activation of PKR by a 17 bp stem-loop found within its 3′ UTR (72, 73). Duplex RNA has not been detected during infection from negative sense RNA viruses such as influenza yet cells lacking PKR are deficient in viral defense (74, 74, 75). The activating component during influenza infection is postulated to be a ~15 bp duplex panhandle formed by the complementary 5′ and 3′ termini of the segmented genomic RNA (74, 74, 76).

In vitro selection experiments have identified a unique class of RNA activators which contain a 16 bp duplex stem and flanking 5′ and 3′ single-stranded RNA tails (ss-dsRNAs, Fig. 1.5A) (77). Activation has been shown to require a 5′-triphosphate (5′-ppp) and minimal ssRNA regions of 9 nucleotides on the 5′ tail and 10 nucleotides on the 3′ end (77, 78). A shorter 5′-ppp dependent construct has also been described which contains two stems 5 and 4 bp in length

flanked by a 13 nt 5′ tail (ssRNA-47, Fig. 1.5A) (78). A 5′-triphosphate is a molecular pattern unique to viral transcripts and provides a mechanism to recognize foreign RNA within the cytoplasm (79). Thus, 5′-ppp dependence aligns with the role of PKR in antiviral defense (80). Short stem-loop regions flanked by ssRNA are common in many of RNAs previously discussed and this likely represents a physiologically relevant activation motif. Indeed, a class of small nucleolar RNAs have recently been identified which activate PKR in response to metabolic stress (7). Some exhibit 5′-ppp dependence and can loosely be categorized as ss-dsRNAs based on minimal regions of extended duplex (SNORD113, Fig. 1.5A). The duplex regions of the ss-dsRNAs are too short to mediate activation of PKR alone and the function of the single-stranded regions is unknown. There is evidence that ss-dsRNA- and dsRNA-mediated activation are mechanistically different. Duplex RNAs do not require a 5′-ppp to activate PKR (78). Incorporation of nucleoside modifications leads to nonequivalent effects in dsRNA versus ss-dsRNA activation (81, 82). These effects suggest single-stranded regions may engage a different region of PKR.

Viruses have evolved elaborate mechanisms to inhibit PKR during infection (83, 83). Adenovirus and Epstein-Barr viruses produce large quantities RNAs named VAI and EBER, respectively, which bind PKR tightly but do not activate thereby sequestering PKR during infection (83, 83). We have shown that magnesium modulates PKR-VAI binding stoichiometry and that at physiological magnesium concentrations only a single PKR binds (84). However, PKR is able to bind the isolated constituent domains of VAI (85). In the context of full length VAI, steric hindrance is believed to prevent binding of multiple PKR molecules which prevents activation (85). Both VAI and EBER are relatively large RNAs which contain many of the stimulatory structural features present in the smaller activating RNAs shown in Figure 1.5A. The mechanism by which VAI confers an inhibitory phenotype remains unclear.

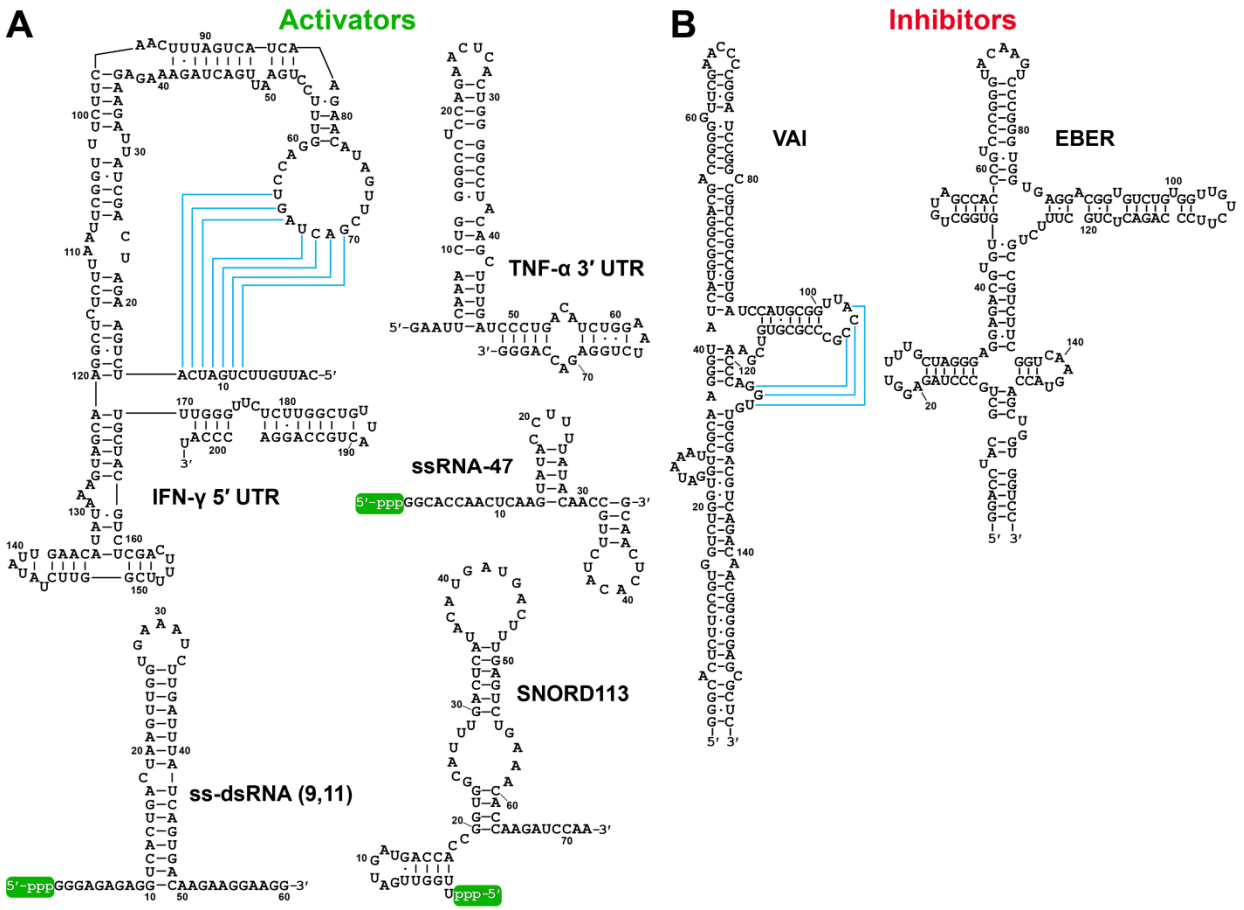

Figure 1.5 Activating and inhibiting RNA ligands. Blue lines represent tertiary interactions. **(A)** Activating RNAs. RNAs which exhibit 5′-ppp dependence are indicated by a green cap on their 5′ terminus. **(B)** PKR inhibitors. RNA folds are adapted from the following references: IFN-γ 5′ UTR: (4), TNF-α 3′ UTR: (72), ssRNA-47 (78), ss-dsRNA (9,11) (77), SNORD113 (7), VAI (86), EBER (87).

1.6 Alternative PKR activators

The canonical PKR activator contains long stretches of duplex RNA derived either from the viral genome itself or produced as a replicative intermediate during the viral life cycle (1, 88). Alternative activators have also been identified and pose intriguing questions regarding their mechanism of activation. PKR is activated by a variety of polyanionic molecules including heparin, chondroitin sulfate, dextran sulfate, and poly(L-glutamine) (89). Heparin is the best characterized polyanionic activator (90). The heparin binding pocket has been mapped to a basic cleft within the kinase domain located between helix αC and the C-lobe (91). Heparin polymers as short as hexasaccharides activate PKR to produce a bell-shape activation profile

implying heparin mediates activation by acting as a scaffold for the assembly of PKR molecules (90, 91). However, this mechanism is not compatible with analytical ultracentrifugation studies which indicate a sequential assembly of an activating complex which consists of two PKR and two heparin molecules (91). In this model heparin binds to PKR to form a 1:1 complex which allosterically enhances the intrinsic PKR dimerization affinity to promote formation of the activating 2:2 complex. Dilution of PKR monomers onto heparin molecules is not expected to produce the observed inhibitory effect. PKR activated by dsRNA can phosphorylate catalytically inactive PKR yet heparin-activated PKR cannot perform the same reaction (90). These results imply heparin and RNA mediated activation are fundamentally different and produce different forms of activated PKR.

A protein activator, PACT, has also been identified (92). Like PKR, PACT contains two tandem N-terminal dsRBDs at its N-terminus. A third domain at the C-terminus belongs to a class of dsRBDs which resemble the dsRBD in sequence yet lack key residues necessary for RNA interaction (93). This third domain constitutes the PKR activating component of PACT (94, 95). PACT activates PKR in response to a variety of stress stimuli including serum withdrawal, H_2O_2, arsenite, and peroxide (96). The stress response signal is mediated by phosphorylation of residues within domain 3 which increases PKR binding affinity and activation potency (97). The domain 3 interaction site has been mapped to an acidic loop within the N-lobe of the kinase domain (98). The same study detected an interaction between dsRBD2 from PKR and a peptide containing the loop sequence. A mechanism for PACT activation has been proposed where PACT-domain 3 and PKR-dsRBD2 both interact with the same site on the N-lobe. The PKR-dsRBD2 is autoinhibitory whereas the PACT-domain 3 interaction is stimulatory (98). Note, however, that another study mapped the PKR-dsRBD2 autoinhibitory interaction to a region within the C-terminal lobe (55).

1.7 Objectives

The work presented in this thesis includes several studies of the mechanism of activation of PKR. In *Chapter 3* an ss-dsRNA is designed using ss-dsRNA (9,11) (Fig. 1.4A) as a template. The parental ss-dsRNA contains 15 nt 5′- and 3′-tails and a 15 bp stem-loop capped with a tetraloop. What follows is a rigorous examination of the structural features required for activation. Each tail and the stem are systematically truncated in 5 nt or bp increments. The effects of truncation are characterized by PKR binding affinity measurements and activation assays. The analysis is guided by our previous investigation which characterized the length dependence of duplex regions by similar methodologies (63). In that study we found a strong correlation between RNA binding affinity and stoichiometry and activation potency where activation required formation of an RP_2 complex and activation potency was proportional to the relative amount of RP_2. Under the conditions we have examined, all of the ss-dsRNAs produce the RP_2 species yet not all activate. In cases where the tails are drastically reduced or eliminated we observe a reduction in the maximal population of RP_2 which correlates with the inability to activate. However, this correlation is lost with some RNAs with intermediate tail lengths. The results imply that PKR directly engages single-stranded regions and that this interaction can produce a stimulatory effect. The potency of activation may be dictated by specific conformational requirements which are only partially determined by tail length.

The results from *Chapter 3* are expanded in *Chapter 4* where we investigate the ability of PKR to interact with single-stranded nucleic acids. We find that two regions on PKR can independently interact with a variety of nucleic acids: the dsRBD and a basic region lying N-terminal to the kinase domain. An isolated kinase domain construct containing the basic region is weakly activated by single-stranded RNA. However, a kinase domain construct lacking the basic region is not activated. We propose a model in which a bivalent interaction between the dsRBD and the kinase domain gives rise to stronger affinity between PKR and RNAs containing single-stranded regions. In some cases this can produce a stimulatory effect.

Chapter 5 reports a new atomic resolution crystal structure of the kinase domain. The objective of the structural analysis was to gain insight into the nucleic acid binding mechanism of the basic region. Diffraction quality crystals were obtained of a kinase domain construct containing the basic region. Unfortunately, the basic region is unresolved in the structure. However, we observe a unique conformation of the activation segment which has profound implications for the PKR activation mechanism. PKR forms alternating back-to-back and front-to-front interfaces in the crystal. In the front-to-front interface activation segments are exchanged between reciprocal protomers suggestive of a *trans*-autophosphorylation complex.

Finally, *Chapter 6* investigates two proteins reported to interact with PKR and elicit opposite effects on enzymatic activity. Influenza viruses express the NS1 protein during infection (99) and it has been reported that NS1 interacts with PKR to prevent activation (100-102). PACT is an endogenous protein which activates PKR in response to stress (96). Both PACT and NS1 are proposed to modulate activity by controlling an autoinhibitory interaction in PKR between the dsRBD and kinase domain. PACT disrupts the interaction to promote activation (98) while NS1 stabilizes the autoinhibited state (101). However, the assays which have characterized these interactions are primarily co-immunoprecipitation or yeast two-hybrid assays performed in cell lysates which do not assess the oligomeric state of the complex or whether additional components are involved in the interaction (92, 95, 96, 100, 101). We have purified NS1 and PACT and analyzed their interaction with PKR by sedimentation velocity analytical ultracentrifugation.

Chapter 2: Materials and Methods

2.1 Buffers

All buffers were made from reagent grade chemicals with deionized, distilled water (Mili-Q, Millipore, MA). Buffers were filter sterilized (0.22 µm) and autoclaved prior to use. Table 2.1 reports the buffer names, components, and their experimental purpose.

Table 2.1 Buffers.

Name	Components	Purpose
AU75	75 mM HEPES (pH 7.5), 75 mM NaCl, 0.1 mM EDTA, 0.1 mM TCEP	General / Binding
AU200	75 mM HEPES (pH 7.5), 200 mM NaCl, 0.1 mM EDTA, 0.1 mM TCEP	General / Binding
AU75 / Mg^{2+}	75 mM HEPES (pH 7.5), 75 mM NaCl, 5 mM $MgCl_2$, 0.1 mM EDTA, 0.1 mM TCEP	Activation
AU200 / Mg^{2+}	75 mM HEPES (pH 7.5), 200 mM NaCl, 5 mM $MgCl_2$, 0.1 mM EDTA, 0.1 mM TCEP	Activation
P50	20 mM HEPES (pH 7.5), 50 mM KCl, 5 mM $MgCl_2$, 0.1 mM TCEP	Activation
AU75 / EDTA	75 mM HEPES (pH 7.5), 75 mM NaCl, 10 mM EDTA, 0.1 mM TCEP	Crosslinking
CD	50 mM NaH_2PO_4 (pH = 7.0)	Circular Dichroism
Melt 1	10 mM $NaPO_4$ (pH 7.0), 0.1 mM EDTA	Thermal denaturation
Melt 2	20 mM cacodylic acid (pH 7.5), 75 mM NaCl, 0.1 mM EDTA +/- 5 mM $MgCl_2$	Thermal denaturation
Hep-A	20 mM HEPES (pH 7.5), 50 mM NaCl, 0.1 mM EDTA, 10% glycerol, 10 mM BME	PKR purification
Hep-B	20 mM HEPES (pH 7.5), 1.2 M NaCl, 0.1 mM EDTA, 10% glycerol, 10 mM BME	PKR purification
HA1	40 mM KH_2PO_4 (pH 7.0), 10 mM BME	PKR purification
HA2	400 mM KH_2PO_4 (pH 7.0), 10 mM BME	PKR purification

Table 2.1 continued Buffers.

Name	Components	Purpose
p20-A_0	20 mM Bicine (pH 8.65), 5% glycerol, 1 mM EDTA, 10 mM BME	dsRBD purification
p20-A	20 mM Bicine (pH 8.65), 50 mM NaCl, 5% glycerol, 1 mM EDTA, 10 mM BME	dsRBD purification
p20-B	20 mM Bicine (pH 8.65), 1 M NaCl, 5% glycerol, 1 mM EDTA, 10 mM BME	dsRBD purification
PACT-Lysis	20 mM HEPES (pH 7.5), 50 mM NaCl, 0.1 mM EDTA, 10% glycerol, 10 mM BME	Full length PACT purification
PACT-Solubilization	20 mM MES (pH 6.0), 4 M Urea, 500 mM NaCl, 30 mM Imidazole, 10% glycerol, 10 mM BME	Full length PACT purification
PACT-Refolding	20 mM MES (pH 6.0), 500 mM NaCl, 30 mM Imidazole, 10% glycerol, 10 mM BME	Full length PACT purification
PACT-Elution	20 mM MES (pH 6.0), 500 mM NaCl, 500 mM Imidazole, 10% glycerol, 10 mM BME	Full length PACT purification
D3-Lysis	20 mM HEPES (pH=7.5), 200 mM NaCl, 20 mM imidazole, 10% glycerol	PACT domain 3 purification
D3-Elution	20mM HEPES (pH=7.5), 200mM NaCl, 500mM imidazole, 10% glycerol, 20 mM BME	PACT domain 3 purification
NS1-Lysis	50 mM Tris (pH=8.0), 75 mM NaCl, 30 mM imidazole, 10 mM BME	NS1 purification
NS1-Elution	50 mM Tris (pH=8.0), 75 mM NaCl, 500 mM imidazole, 10 mM BME	NS1 purification

2.2 Protein purification: PKR

Unphosphorylated PKR was expressed and purified using previously established protocols (35, 91). PKR was expressed in BL21 Rosetta 2 (pLysS) (Novagen) cells from a pET-11a vector (Novagen) under control of the lac operon. Cells were grown in lysogeny broth (LB) media in a shaking incubator at 37 °C at 250 rpm until optical density reached 0.7 OD. The culture was cold-shocked by incubation on ice for ~15 minutes and protein expression was

induced by addition of 1 mM IPTG. Protein expression was allowed to proceed for 5 hours at RT. Cell pellets were stored at -80 °C until use. Pellets were lysed in buffer Hep-A containing protease inhibitor cocktail (Sigma) by sonication and clarified by centrifugation. The supernatant was applied to a heparin Sepharose column (GE Healthcare) equilibrated in Hep-A and eluted by a salt gradient with Hep-B. Fractions containing PKR elute at ~500 mM NaCl and are combined and diluted 1:1 with HA1 buffer. The sample is then applied to a hydroxyapatite column (HA, CHT ceramic hydroxyapatite; Bio-Rad) equilibrated in 40% HA-2 buffer. PKR is eluted from the column by a 40-100% gradient of HA-2 and elutes at ~220 mM potassium phosphate. Fractions were concentrated and either stored at -80 °C or applied to size exclusion chromatography.

PKR kinase domain constructs were created by inserting a TEV protease cleavage site (ENLYFQ↓G/S) upstream of the desired N-terminus. The 185- and 229-Kinase domain constructs contain an extra glycine as the N-terminus. The 242-kinase utilizes the wild-type serine to complete the P1′ portion of the protease site. Proteins were treated with TEV protease following elution from the heparin Sepharose column overnight at 4 °C. TEV protease was either obtained from a commercial supplier (AcTEV protease; Thermo Fisher Scientific) or was produced in our laboratory (103). The cleavage reaction was purified on the hydroxyapatite column. Chromatography was slightly modified from protocol for full length PKR. The column was equilibrated in HA-1 buffer and protein was eluted by a gradient from 0-100% HA-2. The kinase domain typically eluted at ~200 mM potassium phosphate and was well separated from the N-terminal dsRBD portion of the cleaved protein which eluted at ~100 mM potassium phosphate. Fractions were concentrated and either stored at -80 °C or applied to size exclusion chromatography.

The dsRBD (residues 1-184) was expressed and purified as previously described (104). The dsRBD was expressed with the same expression system as full length PKR except that protein expression was allowed to proceed overnight at 37 °C. The cells were lysed in buffer

p20-A in the presence of 0.1 mg/ml lysozyme by sonication. 0.2% w/v polyethylenimine was added to eliminate contaminating nucleic acids from the preparation and the lysate was clarified by centrifugation. The supernatant was loaded onto a SP Sepharose Fast Flow column (GE Healthcare) equilibrated in buffer p20-A and eluted with salt by a 0-50% linear gradient with p20-B. Fractions containing the dsRBD were pooled and diluted with buffer p20-A_0 to lower the salt concentration and loaded onto a heparin Sepharose column equilibrated in buffer p20-A. Another linear salt gradient from 0-50% p20-B was used to elute the dsRBD. Fractions were concentrated and either stored at -80 °C or applied to size exclusion chromatography.

Immediately prior to use, all proteins were further purified by a final size exclusion chromatography step on Superdex 75 or 200 HiLoad 16/60 columns (GE Healthcare) into the experimentally appropriate buffer, typically AU75.

2.3 Protein Purification: PACT

PACT was expressed in BL21 Rosetta 2 (pLysS) (Novagen) cells from a pET-15b vector (Novagen) under control of the lac operon. Cells were grown in LB media in a shaking incubator at 37 °C and 250 rpm until optical density reached 0.7 OD. Protein expression was induced by addition of IPTG to 1 mM and allowed to proceed for 4 hours at 37 °C. Cells are pelleted by centrifugation at 5,000 x g for 10 min and stored at -80 °C until use. The protein is expressed into the insoluble fraction of the *E. coli* lysate. Modifications made to the expression and purification protocols including cold-shock, lower expression temperature and time, lysis by French press, and different lysis buffers failed to yield soluble protein. Cells were resuspended in PACT-lysis buffer, lysed by sonication, and pelleted by centrifugation at 22,000 x g for 20 min. The pellet was resuspended in PACT-lysis buffer and submitted to another round of sonication and centrifugation. The final pellet was solubilized in PACT-solubilization buffer which contains 4 M urea. PACT contains a hexahistidine (His) tag at its N-terminus and was purified by Ni^{2+}-NTA chromatography. The solubilized pellet was loaded onto a pre-packed column of Ni^{2+}-NTA agarose beads at a flow rate of 0.5 ml/min. PACT was refolded while bound to the column by

running a decreasing urea gradient into refolding buffer at a flow rate of 0.5 ml/min. Urea depletion was monitored by conductivity and confirmed by measuring the refractive index of the solution. PACT was eluted from the column with a 100 mL gradient into PACT-elution buffer (500 mM imidazole) at a flow rate of 0.5 ml/min. Figure 2.1 shows SDS-PAGE analyses of the purification steps for full length PACT and a construct of domain 3 (D3). A thrombin protease site separates the wild-type PACT sequence from the His-tag. The His-tag was cleaved overnight at 4 °C using thrombin-agarose beads (Thrombin CleanCleave Kit, Sigma) following the manufacturer's instructions. The sample was passed over the Ni^{2+}-NTA resin to collect uncleaved protein and the cleaved his-tag. The flow through was submitted to size exclusion chromatography on a Superdex 200 HiLoad 16/60 columns (GE Healthcare) into the experimentally appropriate buffer. Phosphomimetic mutations (S246D and S287D) were introduced by standard PCR techniques and the proteins were purified by the same protocol.

An isolated PACT domain 3 (D3) construct was created by deletion mutagenesis of the parental pET-15b-PACT plasmid. A PACT dsRBD1+2 was also created but the protein has only been characterized by a solubility test on a small scale induction. D3 also contains an N-terminal His-tag separated by a thrombin protease site. D3 was expressed in BL21 Rosetta 2 (pLysS) (Novagen) cells. Cells were grown at 37 °C at 250 rpm until OD reached 0.7 and induced by addition of IPTG to 1 mM. Expression was allowed to proceed for 5 hours. Cells were pelleted by centrifugation at 5,000 x g for 10 min and stored at -80 °C until use. The cells were resuspended in D3-lysis buffer and lysed by sonication. The lysate was clarified by centrifugation at 22,000 x g for 20 min and applied to prepacked Ni^{2+}-Sepharose column (HisTrap HP, GE Healthcare) at 1 ml/min. D3 was eluted from the column at 1 ml/min by a 100 ml gradient into D3 elution buffer (500 mM imidazole). D3 elutes with a peak at 250 mM imidazole. The His-tag was cleaved by the same protocol as used for full length PACT. The protein was purified by a final size exclusion chromatography step with a Superdex 75 10/300 GL column (GE Healthcare).

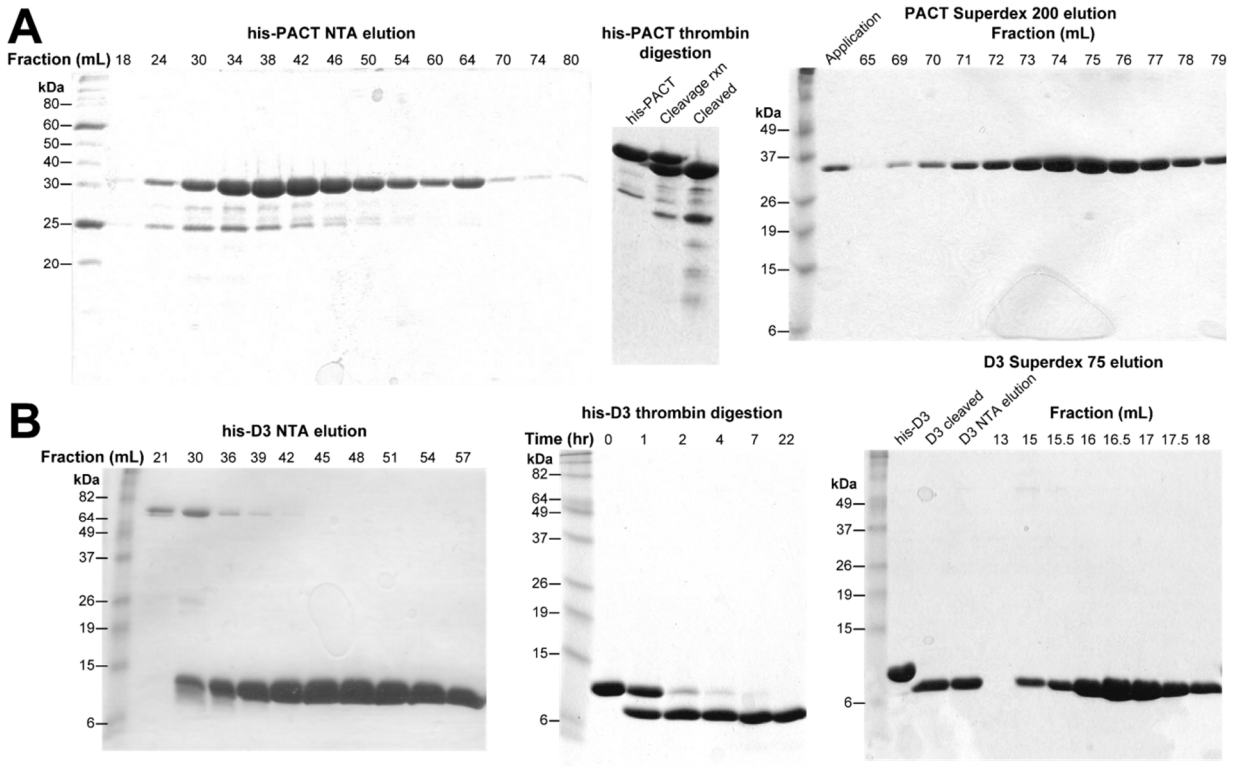

Figure 2.1 PACT purification. (A) Full length PACT. **(B)** Domain 3. Fractions collected from chromatography are indicated in mL. For fractions collected from the nickel column (NTA) the fractionation volume begins with the elution gradient. For size exclusion chromatography (Superdex 75 and 200) the fractionation volume begins with sample injection.

2.4 Protein Purification: NS1

The NS1 effector domain (NS1-ED) was derived from H1N1 influenza A/Puerto Rico/8/1934 and encodes residues 74-230 with an N-terminal His-tag. The protein was expressed in BL21 Rosetta 2 (pLysS) (Novagen) cells from a pET-15b vector (Novagen) under control of the lac operon. Cells were grown at 37 °C at 250 rpm until OD reached 0.7 and induced by addition of IPTG to 1 mM. Expression was allowed to proceed for overnight. Cells were pelleted by centrifugation at 5,000 x g for 10 min and stored at -80 °C until use. The cells were resuspended in NS1-lysis buffer and lysed by sonication. The lysate was clarified by centrifugation at 22,000 x g for 20 min and applied to prepacked Ni^{2+}-Sepharose column (HisTrap HP, GE Healthcare) at 1 ml/min. NS1 was eluted from the column at 1 ml/min by a 100

ml gradient into NS1-elution buffer (500 mM imidazole). The protein was purified by a final size exclusion chromatography step with a Superdex 75 10/300 GL column (GE Healthcare).

2.5 Nucleic acid synthesis and purification

ss-dsRNAs were typically produced by *in vitro* transcription off a plasmid template using conditions established by Gurevich and reported in Table 2.2 (105). Templates coding for the target RNA sequences were created by PCR and inserted into the plasmid between the T7 promoter site and a 3′-ribozyme. Plasmids carrying the desired RNA sequence were purified and linearized as previously described (106). T7 polymerase has a tendency to prematurely fall off the template or add non-coded nucleotides to the 3′-end of the transcript leading to 3′-end heterogeneity (107, 108). To produce RNAs with homogeneous 3′-ends the hepatitis delta virus (HDV) ribozyme was included at the 3′-end of the transcript. The ribozyme cleaves immediately 5′ to its own sequence to release the desired RNA transcript (106, 109). Efficient transcription using T7 polymerase requires that the transcript begins with two guanosine residues (107). Therefore, to create the 3′-strands used to make 15-15-15-ΔT which begin with either 5′-AAGU…-3′ (3′-blunt) or 5′-UCCG…-3′ (3′-UCCG), the hammerhead ribozyme was included at the 5′-end of the transcript. The hammerhead sequence was engineered so that cleavage would occur immediately 5′ to the desired RNA sequence (106). Synthetic oligoribonucleotides were obtained from GE Dharmacon (15-15-15, U30, Het30, 5′-blunt, 5′-UCCG, 3′-blunt, 3′-UCCG, ds30, ds40), TriLink Biotechnologies, Inc. (5-15-10, ppp-Het30), or IDT, Inc. (dT30, dHet30). RNA obtained from Dharmacon was deprotected according to the manufacturer′s protocol prior to use. All RNAs were purified by denaturing 8 M urea PAGE followed by electroelution using an Elutrap device (Schleicher and Schuell, NH). Samples were ethanol precipitated from the electroeluter and typically resuspended in AU75 for use. ss-dsRNAs were annealed by heating ~2 μM of RNA in AU75 at 90°C for 5 min followed by snap cooling. Figure 2.3 shows urea-PAGE analysis of several transcription reactions with the purified RNA shown in two of the gels.

Table 2.2 Transcription conditions.

Component	Concentration in reaction
HEPES-KOH, pH 7.5	200 mM
$MgCl_2$	28 mM
Spermidine	2 mM
Dithiothreitol (DTT)	40 mM
NTP mix (ATP, GTP, CTP, UTP)	6 mM (each)
DNA template	100 µg/ml
Murine RNase inhibitor (NEB M0314S)	40 units/ml
T7 RNA polymerase	~0.7 µM

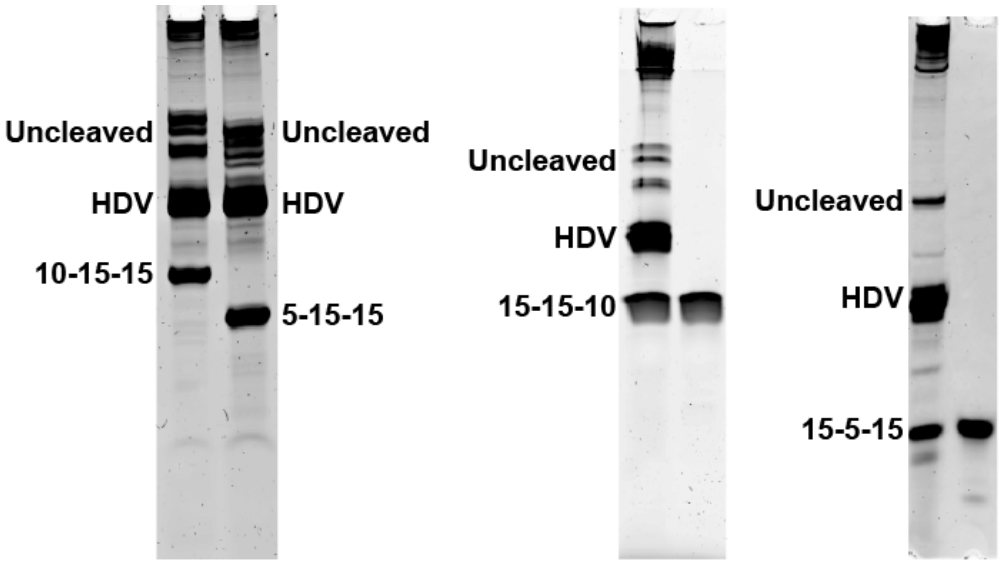

Figure 2.2 RNA transcription reactions. Predominant species are labeled. In the two gels on the right the final purified product is included in the second lane.

2.6 Determination of ε_{260}

Nucleic acid absorbance is largely dependent on structural conformation due to a hypochromic effect on nucleotide absorbance induced by base stacking and pairing interactions (110). Nearest neighbor calculations are accurate for predicting single-stranded extinction coefficients but fail to accurately predict extinction coefficients for nucleic acids with complex folds. In these cases, the extinction coefficient must be experimentally determined either by measuring the hyperchromicity induced by thermal denaturation, by tedious analysis of phosphorous content in a sample, or by hydrolysis of the nucleic acid into its component

nucleotides. We employed the latter method to determine the extinction coefficient of ss-dsRNAs at 260 nm (ε_{260}). The extinction coefficient was estimated by nucleotide composition and the sample was folded at 2 µM by the snap-cooling previously discussed. The absorbance of the sample was measured and the sample was enzymatically hydrolyzed with 1 U RiboShredder RNase Blend (Epicentre). Figure 2.4 shows a time course for the hydrolysis of 10-15-10. The hyperchromic effect from hydrolysis plateaus around 80 minutes. Reactions were left overnight to ensure complete hydrolysis. At a minimum, samples were prepared in triplicate. Values for ε_{260} of the folded RNA were back calculated from the hydrolyzed solution using the known extinction coefficients of the component nucleotides (111). Extinction coefficients are reported in Appendix 1.

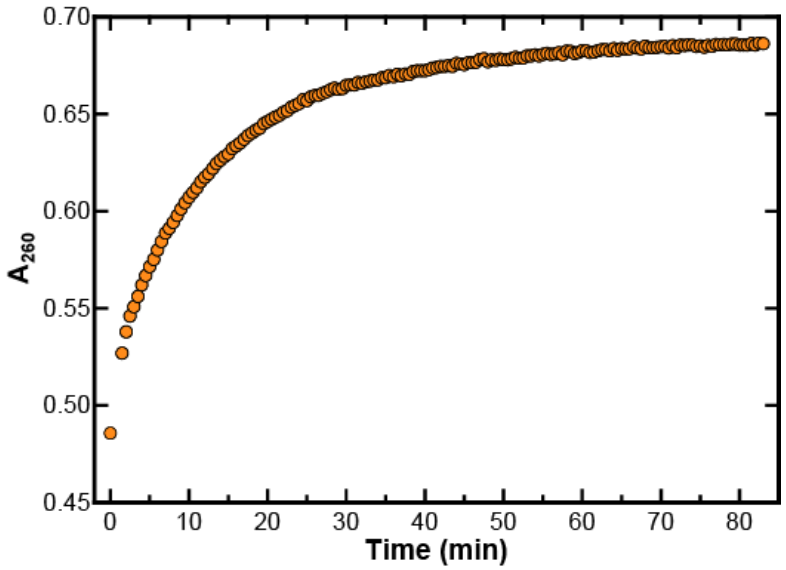

Figure 2.3 Time course for ε_{260} quantification by enzymatic hydrolysis.

2.7 Enzymatic treatment of RNAs

RNAs produced by *in vitro* transcription contain a 5′-ppp and ribozyme cleavage leaves a 2′,3′-cyclic phosphate (112). The dependence of the 5′-triphosphate on PKR activation was tested by dephosphorylation of the RNAs with calf intestinal alkaline phosphatase (CIP). RNAs containing a 5′-OH were generated by incubating 100 µL of 2 µM *in vitro* transcribed RNA with 10 U CIP (New England BioLabs, MA) in 50 mM Tris pH 7.9, 100 mM NaCl, 10 mM $MgCl_2$, 1

mM DTT at 37°C for 1 hour. The 2′,3′-cyclic phosphate was selectively removed with T4 polynucleotide kinase (T4 PNK, New England BioLabs, MA). T4 PNK is typically used to phosphorylate the 5′-end of nucleic acids yet the enzyme contains a phosphatase domain which is specific for phosphates on the 3′-terminus (113, 114). The phosphatase activity can be promoted by modifying the reaction conditions from those recommended for kinase activity (109). The cyclic phosphate was removed by incubating 2 µM RNA with 10 U T4 PNK in 100 mM MES (pH 5.85), 300 mM NaCl, 10 mM MgCl2, 10 mM BME at RT for 3 hours. A reduction in electrophoretic mobility in a denaturing polyacrylamide gel confirmed phosphate removal (Figure 3.8D).

RNAs were 5′-labeled with ^{32}P for enzymatic structure probing and crosslinking studies. Transcripts were first dephosphorylated with calf intestinal alkaline phosphatase (CIP, New England BioLabs) to remove the 5′-triphosphate and phosphorylated with [γ-^{32}P]ATP (Perkin Elmer) by T4 polynucleotide kinase (T4 PNK, New England BioLabs). The labeling reaction was performed by incubating 1 µM RNA with 50 U T4 PNK in 70 mM Tris-HCl pH 7.6, 10 mM $MgCl_2$, 5 mM DTT, and 4 µCi [γ-^{32}P]ATP (Perkin Elmer, MA) at 32 °C for 20 min.

RNAs were typically purified after any enzymatic treatment by phenol-chloroform extraction followed by ethanol precipitation and refolded prior to use.

2.8 Enzymatic structure probing

Enzymatic structure probing assays were conducted by incubating 2 µg 5′-^{32}P labeled RNA with varying concentrations of RNases T1, V1, or A (Ambion) and 4 µg yeast RNA in 10 mM Tris pH 7.0, 100 mM KCl, 10 mM $MgCl_2$ at room temperature for 15 min. An alkaline hydrolysis ladder was produced by incubating 5′-^{32}P labeled RNA and yeast RNA in 50 mM sodium carbonate pH 9.2, 1 mM EDTA at 95 °C for 2, 5, or 15 minutes. The RNase T1 sequencing ladder was produced by first incubating 5′-^{32}P labeled RNA and yeast RNA in 20 mM sodium citrate (pH 5.0), 1 mM EDTA, 7 M urea at 50 °C for 5 minutes. Either 1 or 0.1 U of RNase T1 was then added and incubated for 15 minutes at RT. The cleavage reactions were

stopped by ethanol precipitation and resolved by 12% TBE-Urea PAGE. The gel was dried and exposed to a phosphor screen then scanned with a Typhoon phosphorimager.

2.9 Activation assays

PKR autophosphorylation was monitored by incorporation of ^{32}P from [γ-^{32}P]ATP (Perkin-Elmer). Samples contained a fixed concentration of PKR and a variable concentration of activator. Reactions were typically performed with 100 nM PKR in AU75 / Mg^{2+} buffer at 32 °C. Activation assays with PACT were performed with 200 nM PKR in P50 buffer. Samples were equilibrated at the experimentally appropriate temperature for 10 minutes prior to initiating the reaction. Reactions containing ssRNA and PACT were prepared on ice. Phosphorylation reactions were initiated by addition of ATP to a final concentration of 0.4 mM containing 0.125 (ss-dsRNAs / PACT) or 0.25 (ssRNA) µCi/µL [γ-^{32}P]ATP. Reactions were quenched with sample loading buffer after 20 min and resolved on SDS-PAGE. The gel was then dried and exposed to a phosphor screen followed by quantification on a Typhoon phosphorimager (GE Healthcare, NJ). For ss-dsRNAs, each gel contained an autophosphorylation reaction performed with ppp-15-15-15 at 100 nM and a 40mer dsRNA (ds40) at 50 nM. Activation plots were normalized to the ppp-15-15-15 control and ds40 served as an internal standard. In assays with ssRNAs, low molecular weight heparin (4-6 kDa) (Sigma-Aldrich) is included as a positive control. In assays with PACT ds40 is the positive control.

2.10 Analytical ultracentrifugation

Sedimentation velocity analytical ultracentrifugation experiments were performed in a Beckman Coulter XL-I analytical ultracentrifuge. Table 2.3 lists the rotor speed, optical system, temperature, and buffer used for the experiments. Samples only containing protein were monitored by the interference optical system. RNA binding was monitored by the absorbance optical system set to 260 nm. Sapphire windows were used with the interference optical system and quartz windows were equipped for absorbance. Initial data analysis was performed using the time derivative method (115) as implemented in DCDT+, version 2.3.2 (116) to obtain g^(s*)

distributions. While not usually shown, the data were also analyzed by the c(s*) method to assess homogeneity and RNA degradation (117). Sample heterogeneity is sometimes more apparent by c(s*) analysis due to the higher resolution afforded by deconvolution of the diffusional broadening assuming a single frictional coefficient, f/f_0. Distributions were typically normalized by area for presentation. Binding affinities and stoichiometries were extracted by global fits of multiple data sets to the Lamm equation incorporating different association models using SEDANAL, version 6.01 (118). Confidence intervals were obtained using the F-statistic to define a statistically significant increase in the variance upon adjusting each parameter from its best-fit value. Correction of sedimentation coefficients to standard conditions was performed using Equation 1.

$$s_{20,w} = s_{T,b} \frac{\left(1-\bar{\upsilon}\rho\right)_{20,w}}{\left(1-\bar{\upsilon}\rho\right)_{T,b}} \frac{\eta_{T,b}}{\eta_{20,w}} \quad (1)$$

where the subscript 20,w refers to the parameter measured at 20ºC in pure water, the subscript T,b refers to the parameter measured at temperature T in buffer, s is the sedimentation coefficient, $\bar{\upsilon}$ is the partial specific volume, ρ is the buffer density and η is the buffer viscosity. Frictional ratios (f/f_0) for RNAs and RNA-PKR complexes were calculated using Equation 2.

$$\frac{f}{f_0} = \frac{M\left(1-\bar{\upsilon}\rho\right)_{20,w}}{N_A 6\pi\eta_{20,w} s_{20,w}} \left(\frac{4\pi N_A}{3\bar{\upsilon}M}\right)^{1/3} \quad (2)$$

where N_A is Avogadro′s number and M is the molecular weight. For ssRNA interactions, it was not possible to fit for the sedimentation coefficients of some of the RNA-protein complexes due to cross-correlation with the binding constants. These parameters were fixed at physically reasonably values based on our experience that RNA complexes with PKR have frictional ratios (f/f_0) near 1.5 (62, 63, 119). Buffer densities, viscosities, and protein partial specific volumes

were calculated using SEDNTERP, version 2011120 (120). RNA partial specific volumes were fixed at 0.55 mL g^{-1} (121).

Table 2.3 Experimental parameters for analytical ultracentrifugation.

Project	Buffer	Rotor Speed (rpm)	Optical System	Temperature (°C)
ss-dsRNAs	AU75 / AU200	40,000	Absorbance	20
ssRNAs	AU75	50,000	Absorbance	20
ssRNAs:PKR constructs	AU75	50,000	Interference	20
Full length PACT	AU200	50,000	Interference	4
PACT-D3	AU200 / P50	50,000	Interference	20
NS1	AU200	45,000 / 50,000	Interference	20

2.11 Thermal denaturation analysis of RNAs

Thermal denaturation experiments were performed on an Agilent Cary 300 UV-Vis spectrophotometer. Data were collected by monitoring the absorbance change at 260 nm at a heating rate of 0.5 °C/min. Absorbance readings were collected every 0.5 °C. ss-dsRNAs and ssRNAs were characterized in 10 mM $NaPO_4$ (pH 7.0) with 0.1 mM EDTA. Thermal denaturation experiments were also conducted to determine whether Mg^{2+} induces secondary structure in the single-stranded tails of ss-dsRNAs by comparing thermal denaturation of 15-15-15 and 0-15-0 in the presence and absence of Mg^{2+}. Those data were collected in 20 mM cacodylic acid (pH 7.5), 75 mM NaCl, 0.1 mM EDTA +/- 5 mM $MgCl_2$. The initial absorbance of each sample was ~0.5 OD. The first derivative of the melting curves was calculated in Kaleidagraph, version 4.5.0 (Synergy Software). The derivative curves were smoothed by boxcar averaging over a 5 °C window. Melting points (T_m values) were determined by a Gaussian fit to the derivative curves.

2.12 Small angle X-ray scattering

Small angle X-ray scattering (SAXS) data were collected in AU75 buffer at 20 °C on a Nanostar instrument (Bruker). RNA data were collected as 4, 1 hour frames and the buffer for

background subtraction was collected as 15, 1 hour frames. The sample to detector distance was 67.4 cm and the wavelength was 1.54 Å. Data were reduced with the Bruker SAXS software. All scans overlaid indicating the absence of radiation induced damage in the samples and were averaged for analysis. Data were analyzed with the ATSAS software package (122). Values for R_g and I_o were determined by Guinier analysis of the low q region of the data where $R_g \bullet q < 1.25$. Distance distributions functions (p(r)) were calculated in GNOM (123). The maximum scattering vector (D_{max}) was determined by increasing the maximum distance of the p(r) distribution until it asymptotically approached zero. For 0-15-0, simulated scattering data were generated from a modified NMR structure (PDB: 2L2K) computed with CRYSOL (124).

2.13 UV crosslinking

Crosslinking reactions were carried out using RNAs containing 4-thiouridine generated by replacing UTP with 4-Thio-UTP (TriLink Biotechnologies, Inc.) in the transcription reactions. RNAs were labeled at 5′-end with ^{32}P to monitor crosslinked complexes. Spurious autophosphorylation of PKR during the crosslinking reaction due to [γ-^{32}P]ATP contamination from the labeling reaction would complicate interpretation of the results. Therefore, we took extraordinary steps to eliminate free [γ-^{32}P]ATP. The RNA was purified by phenol-chloroform extraction followed by ethanol precipitation. The RNA pellet was resuspended in AU75 buffer containing 10 mM EDTA and submitted to a series of buffer exchange steps by iterative dilution and concentration in a 10,000 MWCO centrifugal filter (Millipore). Crosslinking was performed in AU75 buffer containing 10 mM EDTA. Samples contained 0.5 µM RNA and 1 µM protein in 15 µL. For the dsRBD construct, an additional sample was prepared containing 0.5 µM RNA and 10 µM protein. Samples were incubated on ice 15 minutes prior to UV exposure. An 8 watt ultraviolet lamp (UVP; model 3UV-38) was used to irradiate the samples at 365 nm at a distance of 5 cm for 10 minutes on ice. Samples containing a TEV cleavage site were treated with TEV AcTEV protease (Thermo Fisher Scientific) by combining 5 µL of the crosslinking reaction with 0.5 µL protease and incubating at 32 °C for one hour. Crosslinking reactions were resolved by

SDS-PAGE. Gels were fixed in 7.5% acetic acid and stained with SYPRO Orange (ThermoFisher) to visualize the location of protein within the gel. Gels were then dried and exposed to a phosphor screen followed by imaging and quantification on a Typhoon phosphorimager (GE Healthcare).

2.14 Chemical crosslinking

The interaction between PACT and PKR was probed by chemical crosslinking using disuccinimidyl suberate (DSS). Samples were prepared in P50 buffer with 10 mM PKR and a titration of PACT. Crosslinking reactions were initiated by addition of DSS to 10-fold molar excess of the protein concentration. The reaction was allowed to proceed for 30 minutes at RT and quenched by addition of 50 mM Tris-Cl. Crosslinked products were resolved by SDS-PAGE in a 4-12% acrylamide tris-glycine gel and visualized by Coomassie Blue staining.

2.15 Circular dichroism

CD spectra of RNA:PKR mixtures or of refolded full length PACT were measured with an Applied Photophysics Pi Star-180 spectrapolarimeter. The RNA:PKR mixtures were collected using 2 mm path length cuvettes in AU75 buffer at 20 °C. For each sample, 5 wavelength scans were collected and averaged. Scans were collected between 200 and 340 nm with a 1 nm step, 2 nm bandpass, and time-perpoint averaging of 2 s. Samples contained 5 μM RNA and the protein was manually added from a concentrated stock. Dilution effects were corrected for by concurrent addition of the appropriate RNA stock. Contribution from the protein to the spectra at wavelengths >240 nm was minimal. Both buffer only and protein only spectra were subtracted from the RNA:PKR mixtures.

Spectra of full length PACT were collected from 170 to 270 nm in 1 mm path length cuvettes in 50 mM NaH_2PO_4 (pH = 7.0) at 15 °C. The slits were set to 2 nm and the data were collected with a 1 nm step and time-perpoint averaging of 12.5 s. The spectrum presented in Figure 6.4A is the average of two measurements.

2.16 Limited proteolysis

Full length PACT(his) was incubated at 0.67 mg/ml with various ratios of PACT/trypsin for one hour at 4 °C in AU200 buffer. A 3 hour incubation was also performed and yielded the same digestion pattern. Reactions were quenched by addition of SDS loading buffer and heated for 5 min at 90 °C. Digestion products were resolved by SDS-PAGE in a 4-14% acrylamide tris-glycine gel. Peptides were visualized by Coomassie Blue staining.

Chapter 3: ss-dsRNAs

3.1 Introduction

A novel family of RNA activators of PKR has been described that contain a 16 bp imperfect duplex stem capped by a variable length loop with flanking ssRNA regions on the 5′- and 3′-ends (ss-dsRNAs) (77, 78). The presence of a 5′-triphosphate (5′-ppp) and minimal ssRNA tails of 9 nt on the 5′- and 10 nt on the 3′-side are crucial to PKR activation. Activation is also observed for longer (≥ 47 nt) ssRNAs containing short (5 bp) stems. The duplex regions in all of these RNAs are too short to mediate PKR activation alone and the mechanism by which the 5′-ppp and ssRNA regions elicit activation is not known. A 5′-ppp is an important structural feature for activation of RIG-I (125, 126), an intracellular sensor of foreign RNAs. The 5′-ppp binding site lies within a positively charged pocket at the C-terminus of RIG-I (127-130). However, sites for ssRNA or triphosphate binding have not been identified in PKR (131).

Here, we characterize the structural features of ss-dsRNAs that contribute to PKR binding and activation. We have designed a model ss-dsRNA PKR activator containing two single stranded tails of 15 nt and a 15 bp stem capped with a tetraloop (15-15-15) and made systematic truncations and modifications to the tail, stem, and loop regions. Our studies confirm that stem-loops containing flanking ssRNA regions function as PKR activators. However, we obtain disparate results regarding the dependence of the 5′-ppp for activation. Synthetic RNAs containing either a 5′-OH or 5′-ppp do not activate PKR. However, RNAs created by *in vitro* transcription (IVT) activate PKR in both 5′-OH and 5′-ppp forms. The chemical difference(s) between synthetic and IVT RNA which leads to opposing regulation of PKR activity is unclear. The investigation into the role of the tetraloop is marred by the use of synthetic oligonucleotides to create some constructs and a critical control experiment in which ligation of RNAs containing a broken tetraloop does not restore activation. Systematic truncation of the 5′- and 3′- ssRNA arms generally causes a decrease in binding affinity and activation potency. ss-dsRNAs lacking either 5′- or 3′- arm bind weakly and do not activate. However, activity and tail length is not

correlated with binding for ss-dsRNAs with intermediate affinities. These data support a model where ss-dsRNA induced PKR dimerization is required but not sufficient to activate the kinase.

Results

3.2 Characterization of ss-dsRNAs

We have designed a series of ss-dsRNAs to characterize the length dependence of ssRNA tails and stem-loop region and the contribution of the 5′-triphosphate to the binding energetics and activation of PKR. Truncations were made to a model ss-dsRNA with a 15 bp duplex stem capped by a stable UCCG tetraloop (132) flanked by 15 nt single stranded tails (Fig. 3.1A). The sequences of the ssRNA tails have been designed to prevent formation of unwanted secondary structure. Tail truncation constructs were designed by deletion of nucleotides immediately flanking the stem. Additional mutations within the single stranded regions were required in some cases to disrupt formation of alternative secondary structures. The sequences are deposited in Appendix 1. Analysis of the sequences using MFOLD (133) indicate the absence of alternative folded conformations (data not shown). Enzymatic structure probing experiments confirm the predicted secondary structure of the model 15-15-15 ss-dsRNA (Fig. 3.1A,B). Thermal denaturation measurements indicate a single cooperative transition associated with unfolding of the stem region (Fig. 3.1C). RNAs with 15 bp duplex regions exhibit a single cooperative melting transition between 72 – 75 °C. The T_m decreases to 66 °C when the duplex is reduced to 10 bp in 15-10-15. Importantly, we do not detect additional cooperative unfolding transitions indicating the absence of alternative folded conformations within the tail regions. The monotonically increasing baseline prior to the cooperative unfolding of the duplexes is due to decreased stacking interactions within the tails. Thus, the tails do no adopt unwanted secondary structure. Self-complementary RNA hairpins have the potential to dimerize, which can complicate analysis of their interactions with PKR (134, 135). Sedimentation velocity analysis indicates that all of the ss-dsRNAs are homogeneous and monomeric (Appendix 2). Small angle X-ray scattering (SAXS) provides further evidence for the

appropriately folded structures (Fig. 3.1D-G). SAXS analysis was performed on the parental model construct, 15-15-15, a construct lacking tails, 0-15-0, and a construct lacking the tetraloop capping the stem, 15-15-15-ΔT. All constructs contain a 5′-ppp and 15-15-15-ΔT was created by hybridizing synthetic oligonucleotides. Transformation of the data into real space, represented as a weighted distribution of interatomic distances, P(r), provides information on the general shape of the molecules in solution (Fig. 3.1G). As expected for an RNA duplex, the distributions exhibit characteristic features of rod shaped molecules (136). The curves have a maxima at ~20 Å which corresponds to the cross sectional diameter of an A-form helix. For 0-15-0, the maximum interatomic distance (D_{max}) is determined by the distance from the base of the stem to the top of the tetraloop (expected distance = ~55 Å). For a 15 bp duplex capped by a tetraloop the expected distance is ~55 Å and 0-15-0 has a fitted D_{max} of 60 Å. Scattering data for 0-15-0 are validated by theoretical scattering data calculated using Crysol (124) from the solution structure of a 15 bp stem-loop RNA (PDB: 2L2J). In 15-15-15 and 15-15-15-ΔT, the tails increase D_{max} to ~100 Å.

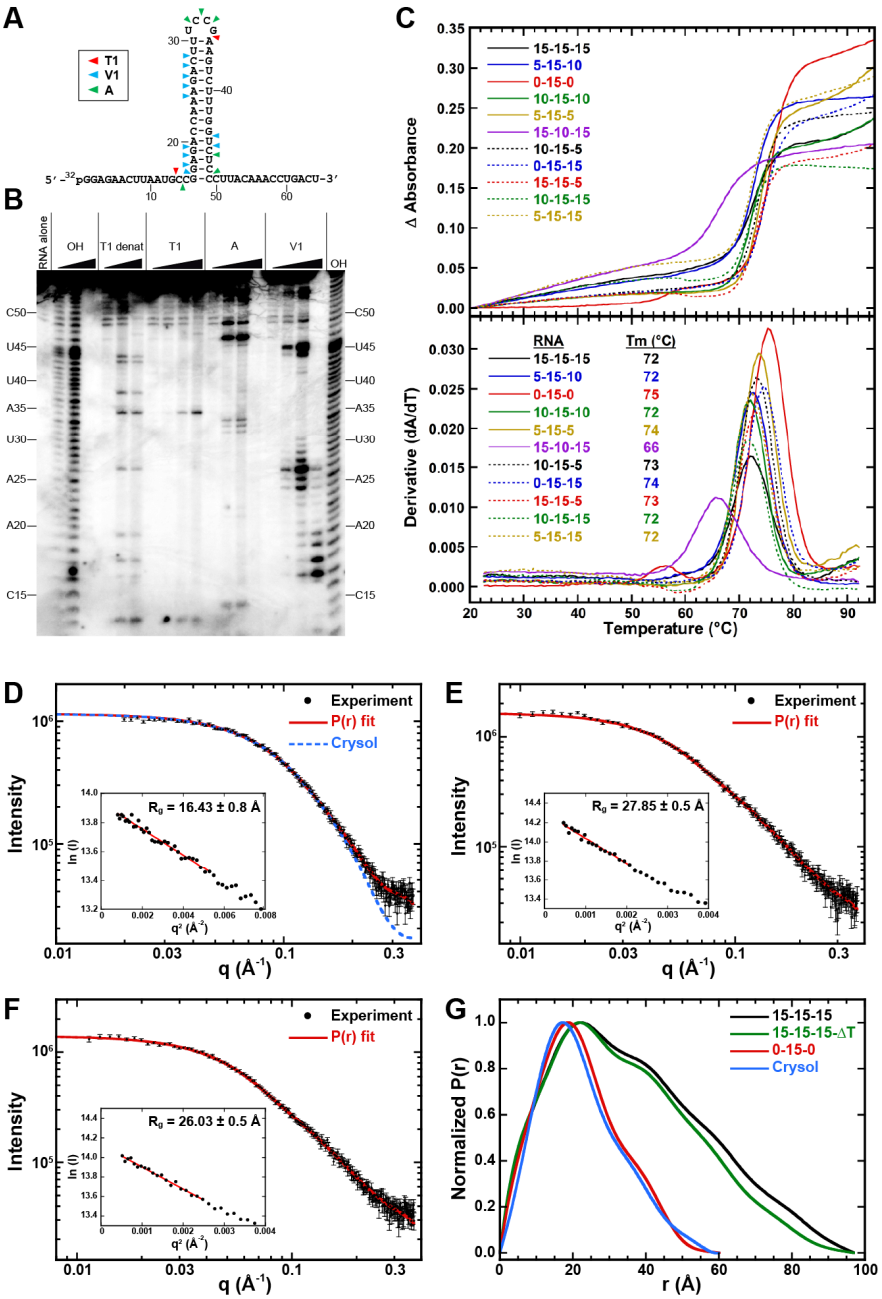

Figure 3.1 Structural analysis of ss-dsRNAs. (A) Predicted secondary structure of 15-15-15 and enzymatic cleavage sites for RNases T1 (red), V1 (cyan) and A (green). **(B)** Enzymatic cleavage products of 15-15-15 resolved by urea-PAGE. **(C)** Thermal denaturation analysis of ss-dsRNAs. The top panel shows the absorbance melting curves, vertically adjusted to 0 OD at 20 °C. The first derivative of the melting curves is shown in the bottom panel. T_m values were determined by a Gaussian fit to the derivative curves. **(D-G)** SAXS analysis of ss-dsRNAs. Scattering data (points) and the p(r) fit (solid red line) for 0-15-0 **(D)**, 15-15-15 **(E)**, and 15-15-15-ΔT **(F)**. Guinier analyses with calculated R_g are shown in the insets. The scattering profile for a 15 bp stem loop was calculated from PDB: 2L2J using Crysol (124) and is shown as a dashed teal curve in **(A)**. The predicted R_g from the Crysol simulation is 17.3 Å. **(G)** p(r) distributions calculated by an indirect Fourier transform of the data using GNOM (137).

3.3 Effect of tail deletions on binding

The PKR binding stoichiometries and affinities of the ss-dsRNAs were measured using a sedimentation velocity analytical ultracentrifugation method (138). Initial experiments were performed in a buffer containing 200 mM NaCl (AU200) to correlate with our previous PKR-RNA binding measurements (63, 84, 134). The data were first analyzed by the time derivative method (115, 116) to determine the qualitative behavior of the system and to define the correct association model to use for subsequent global analysis (138). As shown in Figure 3.2A, the peak of the g^(s*) distribution for ppp-15-15-15 shifts to the right from ~3 S to ~5 S when PKR binds due to formation of a protein-RNA complex with a higher sedimentation coefficient. The shift is saturated upon addition of six equivalents of PKR. Assuming a 1:1 binding stoichiometry, a sedimentation coefficient of ~5 S corresponds to a frictional ratio f/f_0 ~1.5 (Appendix 2), which is in the range that we typically observe for PKR-RNA complexes (138). Thus, the sedimentation data are consistent with binding of a single PKR to ppp-15-15-15 in AU200.

PKR dissociation constants were obtained by globally fitting the sedimentation velocity data using SEDANAL (118). We obtain an excellent fit of the ppp-15-15-15 data to a 1:1 binding model with K_d = 360 nM and a low RMS deviation of 0.00587, which is on the order of the noise level of the absorbance optics (Table 3.1). Hydrodynamic calculations indicate that each of tail deletion RNAs also binds a single PKR in AU200 (Appendix 2). Deletion of the 5′-tail has a negligible effect on K_d whereas deletion of the 3′-tail or both tails decreases binding affinity by about three-fold (Table 3.1).

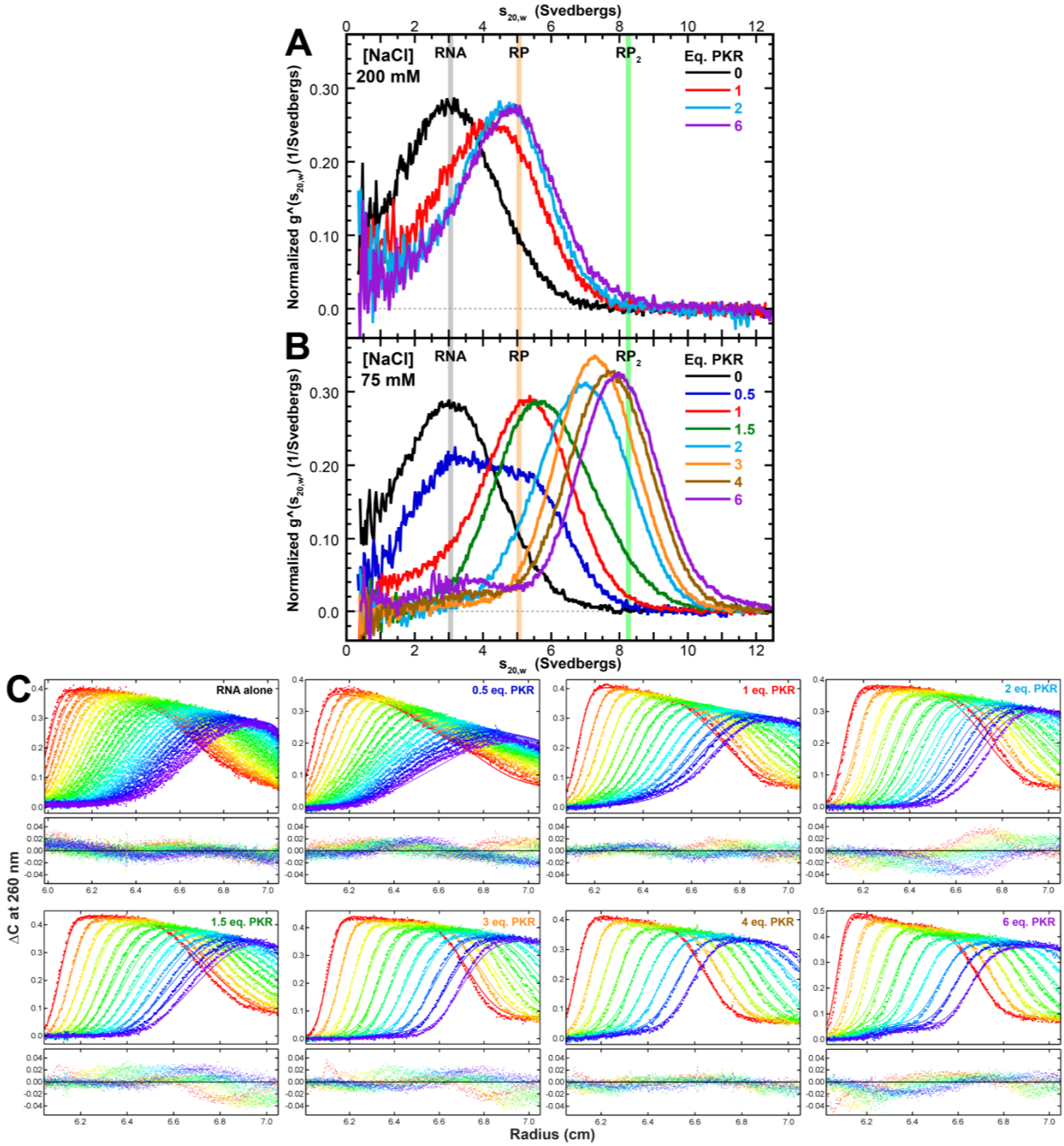

Figure 3.2 Sedimentation velocity analysis of PKR binding to ppp-15-15-15. Normalized g^(s*) distributions obtained in **(A)** 200 mM NaCl (AU200 buffer) or **(B)** 75 mM NaCl (AU75 buffer). Samples contain 0.7 µM 15-15-15 and the indicated equivalence ratio of PKR. Fitted sedimentation coefficients for the RNA, 1:1 species (RP), and 2:1 species (RP_2) obtained from the 75 mM NaCl dataset are indicated by vertical lines across both distributions. **(C)** Global analysis of the sedimentation difference curves. The fit corresponds to the 75 mM NaCl data shown in panel B. Scans were subtracted in pairs to remove time-invariant background and fit to a sequential 2:1 binding model using SEDANAL (118). The top panels show the data (points) and the fitting results (continuous lines) using the parameters presented in Table 3.2 and Appendix 2. The bottom panels show residuals. Only every other difference curve is shown for clarity. A similar analysis was used for the 200 mM NaCl data although the data were fit to a 1:1 binding model. Measurements were performed at 20 °C and 40,000 rpm using absorbance detection at 260 nm.

Table 3.1 PKR binding to tail deletion constructs measured in AU200.

RNA	K_d (nM)	RMSD[a]
ppp-15-15-15	360 (304, 420)	0.00587
ppp-15-15-0	1240 (1169,1319)	0.00483
ppp-0-15-15	449 (409, 491)	0.00652
ppp-0-15-0	935 (840, 1042)	0.00607

Parameters obtained by global nonlinear least square analysis of sedimentation velocity experiments. The values in parentheses represent the 95% joint confidence intervals obtained using the F-statistic.
[a] Root mean square deviation in absorbance units.

3.4 Enzymatic effect of tail deletion

Activation of PKR by ss-dsRNAs was assayed by measuring PKR autophosphorylation in AU200. Deletion of either of the flanking ssRNA tails abolishes the ability to activate (Fig. 3.3). At the PKR concentration used in the assay, the maximum level of activation occurs at 1 μM and PKR is inhibited at higher RNA concentrations, giving rise to a bell shaped curve similar to activation by simple dsRNAs (Fig. 3.3B). Our previous analysis of a truncation series of dsRNAs revealed a correlation between the ability to activate PKR autophosphorylation and the binding of two or more monomers in AU200 (62, 63). Thus, it is noteworthy that ppp-15-15-15 functions as a potent activator without detectable formation of a 2:1 species in 200 mM NaCl. The bell shape activation curve suggests that like duplex RNAs, ss-dsRNAs activate PKR by facilitating dimerization of PKR on the RNA. The amount of 2:1 species populated may be below the detection limits for the sedimentation velocity analysis.

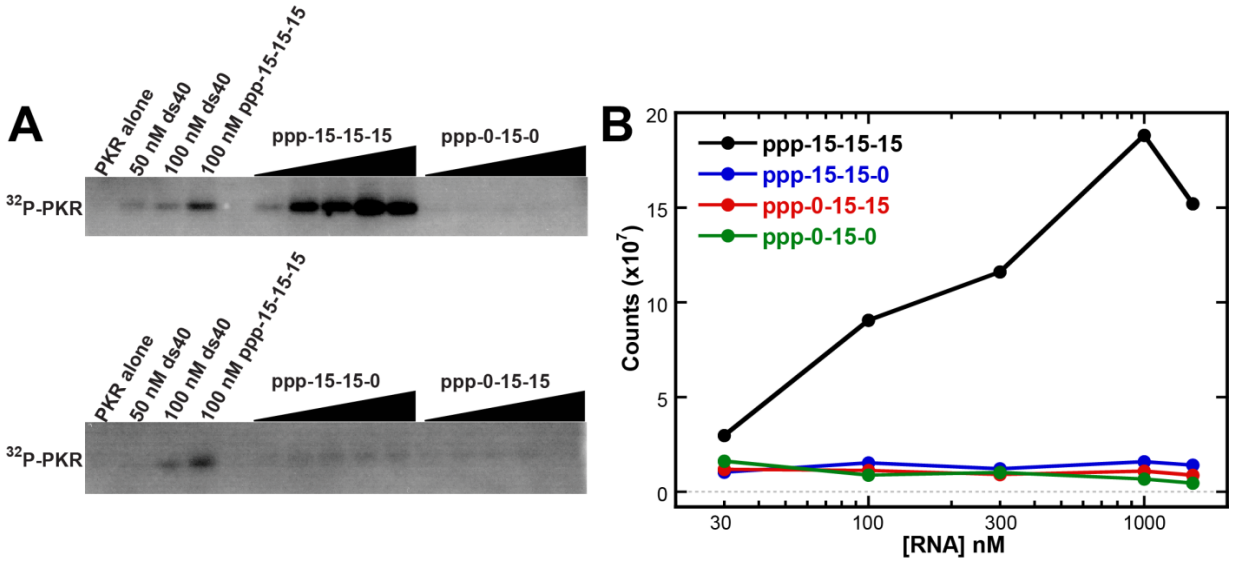

Figure 3.3 Activation of PKR by tail deletion constructs in 200 mM NaCl. Experiments were performed in AU200 buffer plus 5 mM $MgCl_2$ at 32 °C. Each reaction contains 200 nM PKR, 400 μM ATP, 2 μCi γ-^{32}P-ATP and the indicated amount of RNA. The reaction was allowed to proceed for 20 min before quenching with SDS loading buffer and products were resolved on 12% denaturing SDS-PAGE. The incorporation of ^{32}P into PKR was measured by phosphorimager analysis. **(A)** ppp-15-15-15 and ppp-0-15-0 (top), ppp-15-15-0 and ppp-0-15-15 (bottom). **(B)** Quantitation of gels shown in panel (A). PKR activation level is plotted as a function of RNA concentrations. ppp-15-15-15 (black), ppp-15-15-0 (blue), ppp-0-15-15 (red), ppp-0-15-0 (green).

3.5 Measurements in 75 mM NaCl

The affinity of PKR binding to dsRNA is strongly dependent on monovalent ion concentration (15, 139) and the stoichiometries can increase upon decreasing [NaCl] from 200 to 75 mM (62, 63). Figure 3.2B shows the normalized g^(s*) distributions of a PKR titration against ppp-15-15-15 in 75 mM NaCl (AU75 buffer) directly beneath the distributions obtained in 200 mM NaCl (AU200). Addition of a large molar excess of PKR increases the sedimentation coefficient to ~8 S whereas the maximal sedimentation coefficient in 200 mM NaCl is only ~5 S (Appendix 2). A sedimentation coefficient of 8 S is larger than expected for a 1:1 complex (RP) of PKR and ppp-15-15-15 but is consistent with formation of a 2:1 complex (RP_2). Reducing the NaCl concentration to 75 mM also induces a large increase in the maximum sedimentation coefficient for PKR binding to the nonactivating RNAs ppp-0-15-15, ppp-15-15-0, and ppp-0-15-0 (Appendix 2). Again, the limiting sedimentation coefficients of the protein-RNA complexes

indicate that two PKR monomers also bind to these RNAs under these conditions. Despite the ability to bind two PKR monomers, the tail deletion constructs are deficient in enzymatic activation measured at 75 mM NaCl (Figure 3.5). Thus, the binding stoichiometries alone cannot explain the difference in PKR activation among these ss-dsRNAs.

Global analysis reveals significant differences in the PKR binding affinities for the activating and non-activating ss-dsRNAs measured in AU75. PKR binds strongly to ppp-15-15-15 with K_{d1} and K_{d2} lying in the low and mid nanomolar region, respectively (Table 3.2). Deletion of the 3′-tail increases K_{d1} by about 6-fold and K_{d2} by about 3-fold. Deletion of the 5′-tail results in a 30-fold increase in K_{d1} and a 2.5-fold increase in K_{d2}. The largest penalty is observed when both tails are deleted.

For a panel of dsRNAs of increasing length, the rate of PKR autophosphorylation is proportional to the maximum population of PKR that is contained in RNA complexes containing two PKR monomers, denoted RP_2 (62, 63). Table 3.2 shows the maximum percentage of RP_2 for the ss-dsRNAs calculated using the experimentally determined dissociation constants. The activating ppp-15-15-15 RNA produces a maximum of about 13% RP_2 and the nonactivating tail deletion constructs induce about half as much.

Table 3.2 PKR binding to tail deletion constructs measured in AU75.

RNA	K_{d1} (nM)	K_{d2} (nM)	Maximum % RP_2[a]	RMSD[b]
ppp-15-15-15	4 (2, 6)	294 (252, 343)	12.9	0.00821
ppp-15-15-0	26 (20, 34)	928 (782, 1108)	4.9	0.00667
ppp-0-15-15	128 (96, 170)	746 (568, 1003)	5.9	0.00620
ppp-0-15-0	138 (105, 178)	1662 (1311, 2131)	2.8	0.00906

Parameters obtained by global nonlinear least square analysis of sedimentation velocity experiments. The values in parentheses represent the 95% joint confidence intervals obtained using the F-statistic.
[a] The maximum population of the RNA-PKR_2 species calculated from K_{d1} and K_{d2} at the concentration of PKR used in activation assays (100 nM).
[b] Root mean square deviation in absorbance units.

3.6 Magnesium effects

Further analysis of the ss-dsRNA structure-activity relationships was carried out in 75 mM NaCl so that correlations could be made between the population of the RP_2 species and activation potency. Magnesium is required for kinase activity and is present in autophosphorylation assays at 5 mM. However, addition of 5 mM $MgCl_2$ to the buffer containing 75 mM NaCl causes a significant decrease in binding affinity which complicates measurement of the second dissociation constant (Table 3.3). We performed experiments to examine the effect of magnesium on ss-dsRNA structure and PKR affinity. Divalent ions can diffusely interact with the phosphate backbone or site specifically bind to facilitate RNA folding (140). PKR affinity to dsRNAs is not regulated by divalent ion (15) but the interaction of PKR with a large, complex RNA, Adenovirus VAI, is modulated by Mg^{2+} (84). Shielding of the phosphate backbone by diffuse interaction is expected to cause a similar decrease in PKR binding affinity for both RNAs. We asked whether the interaction of PKR with ss-dsRNAs is affected by Mg^{2+} by comparing binding affinities in AU75 and AU60 / 5 Mg buffers, where the increase in ionic strength conferred by the addition of 5 mM Mg^{2+} to AU75 is compensated for by reducing the NaCl concentration to 60 mM. For both ppp-15-15-15 and ppp-0-15-0, which lacks single stranded tails, the binding affinities decrease strongly in AU60 / 5 Mg (Table 3.3). This observation is consistent with previous studies indicating that Mg^{2+} is ~100-fold more efficient at charge screening of RNAs compared to monovalent cations (141, 142). As indicated by a similar reduction in the maximum RP_2 for the two RNAs, there are no specific Mg^{2+} effects conferred by the single stranded tails. Furthermore, thermal denaturation measurements indicate that Mg^{2+} does not induce formation of additional secondary structure in ss-dsRNAs (Figure 3.4). In the absence of Mg^{2+}, 15-15-15 exhibits a monotonic increase in absorbance followed by cooperative unfolding of the duplex region at ~85 °C. The presence of Mg^{2+} does not induce additional unfolding transitions for 15-15-15 but simply shifts the duplex unfolding to higher temperature. Additionally, enzymatic structure probing experiments (Figure 3.1) were performed in the presence of 10 mM $MgCl_2$ and indicate the absence of folded regions within the ssRNA tails although the entire tail region is not resolved on the gel.

Table 3.3 Effect of Mg^{2+} on PKR binding.

RNA	Buffer	K_{d1} (nM)	K_{d2} (nM)	Maximum % RP_2	Relative RP_2[a]	RMSD[b]
ppp-15-15-15	AU75	4	294	12.9	-	0.0082
ppp-15-15-15	AU60 / 5 Mg[c]	21	2,104	2.3	18	0.0101
ppp-15-15-15	AU75 / 5 Mg[d]	42	3,704	1.3	10	0.0108
ppp-0-15-0	AU75	138	1,662	2.8	-	0.0090
ppp-0-15-0	AU60 / 5 Mg[c]	331	11,627	0.4	14	0.0110
ppp-0-15-0	AU75 / 5 Mg[d]	267	13,918	0.4	14	0.0880

Parameters obtained by global nonlinear least square analysis of sedimentation velocity experiments.
[a] Maximum % RP_2 relative to AU75 (in percent).
[b] Root mean square deviation in absorbance units
[c] 20 mM HEPES pH 7.5, 60 mM NaCl, 5 mM $MgCl_2$, 0.1 mM EDTA, 0.1 mM TCEP.
[d] 20 mM HEPES pH 7.5, 75 mM NaCl, 5 mM $MgCl_2$, 0.1 mM EDTA, 0.1 mM TCEP.

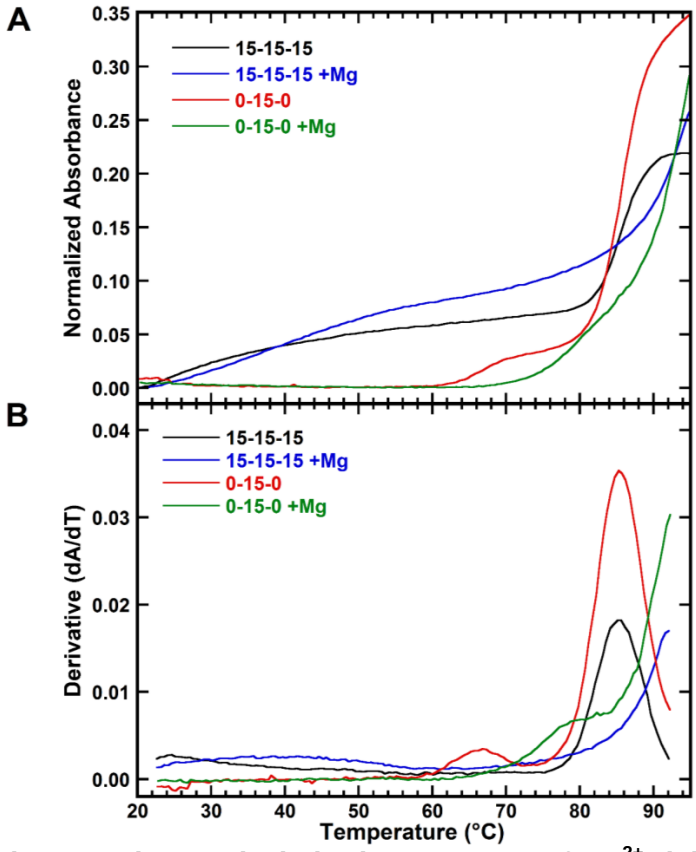

Figure 3.4 Thermal denaturation analysis in the presence of Mg^{2+}. (A) Absorbance melting curves. Thermal denaturation was analyzed by monitoring the absorbance change at 260 nm at a heating rate of 0.5 °C/min. Data were collected every 0.5 °C. The measurements were conducted in 20 mM cacodylic acid (pH 7.5), 75 mM NaCl, 0.1 mM EDTA +/- 5 mM $MgCl_2$. The absorbance of each sample was 0.5 OD. **(B)** First derivative of the melting curves. The derivative curves were smoothed by boxcar averaging over a 5°C window.

3.7 Effect of tail truncations.

We further examined the contribution of each single-stranded tail to binding affinity and activation by creating a series of ss-dsRNAs with 5 nt incremental symmetric and asymmetric truncations of the tails. The portfolio of ss-dsRNAs was designed to resolve the minimum length requirements for activation and test whether the 5′- and 3′-tails are equivalent in their contribution to affinity and activation. Measurements were obtained in AU75 to investigate whether ss-dsRNAs exhibit a similar correlation between $\%RP_2$ and activation potency as we have previously observed with duplex RNAs (62, 63). Figure 3.5 shows the RNA concentration dependence of activation for all of the tail truncation constructs. Panels C and D show the effects of a series of 5 nt incremental truncations made to either 5′ or 3′ tail while maintaining the 15 nt opposing tail length. Some RNAs exhibit a bell shape activation profile while other activation profiles show a monotonic increase with RNA. The absence of a maximum in the activation profile is correlated with weaker binding (*vide infra*). Activity measurements at ss-dsRNA concentrations greater than 1.5 μM are precluded by potential dimerization of the self-complementary sequences. Truncation of either tail leads to a gradual decrease in activation potency indicating a direct relationship between tail length and stimulation of enzymatic activity. Truncations made to the 5′ tail have a slightly greater effect on PKR activation than those made to the 3′ tail. In particular, ppp-15-15-5 retains its ability to activate PKR where little or no activation is detected for ppp-5-15-15.

Figure 3.5B shows the percentage of PKR molecules contained in the RP_2 species plotted as a function of RNA concentration for the 3′-tail truncation series. The distributions mirror the trend in the activation plot (Fig. 3.5C). Binding affinity, and maximum $\%RP_2$, decrease in parallel with activation potency as the 3′-tail is reduced in 5 nt increments (Table 3.4). However, the correlation does not hold for the 5′ tail truncation series (Fig. 3.5D). ppp-10-15-15 exhibits weaker PKR binding than the full-length ss-dsRNA, removal of an addition 5 nt from the 5′-tail results in enhanced affinity such that the ppp-5-15-15 has a maximal $\%RP_2$ close to ppp-

15-15-15. Despite the similar population of the RP_2 species, ppp-15-15-15 is a potent activator whereas ppp-5-15-15 fails to activate, indicating that these parameters are not well correlated for all ss-dsRNAs.

The next series of truncations were made to both tails. Activation plots are grouped according to the symmetry of the truncations. Asymmetric truncation (Fig. 3.5E) to produce ppp-5-15-10 shifts the maximum to slightly higher RNA concentration whereas ppp-10-15-5 shows weaker activation. The effects of symmetric truncation (Fig. 3.5F) of both tails are more dramatic: deletion to 10 nt or less essentially abolishes activation. Within the asymmetric truncation group the relative binding affinity and activation potency are somewhat correlated: ppp-5-15-10 populates a higher percentage of RP_2 and is a more potent activator than ppp-10-15-5 (Table 3.4). The correlation is less clear for the symmetric constructs. PKR binding to ppp-10-15-10 is only slightly reduced relative to the parent ppp-15-15-15 yet it does not activate. Curiously, addition of three nucleotides to create 13-15-10 restores stimulatory properties (Fig. 3.5G).

Table 3.4 PKR binding to tail truncation constructs measured in AU75.

RNA	K_{d1} (nM)	K_{d2} (nM)	Maximum % RP_2[a]	RMSD[b]
ppp-15-15-15	4 (2, 6)	294 (252, 343)	12.9	0.00821
ppp-10-15-15	30 (21, 41)	685 (581, 812)	6.4	0.00859
ppp-5-15-15	31 (22, 43)	272 (225, 329)	13.7	0.00870
ppp-15-15-10	4 (2, 6)	483 (418, 557)	8.6	0.00579
ppp-15-15-5	20 (13, 28)	647 (558, 752)	6.7	0.00782
ppp-13-15-10	93 (64, 133)	601 (475, 776)	7.2	0.00655
ppp-13-15-5	95 (67, 136)	358 (273, 472)	11.1	0.00697
ppp-5-15-10	49 (38, 62)	520 (440, 617)	8.1	0.00645
ppp-10-15-5	30 (21, 41)	1062 (885, 1280)	4.3	0.00679
ppp-10-15-10	22 (11, 37)	400 (323, 498)	10.1	0.00821
ppp-5-15-5	67 (43, 99)	838 (650, 1094)	5.3	0.00848

Parameters obtained by global nonlinear least square analysis of sedimentation velocity experiments. The values in parentheses represent the 95% joint confidence intervals obtained using the F-statistic.

[a] The maximum population of the RNA-PKR$_2$ species calculated from K_{d1} and K_{d2} at the concentration of PKR used in activation assays (100 nM).
[b] Root mean square deviation in absorbance units.

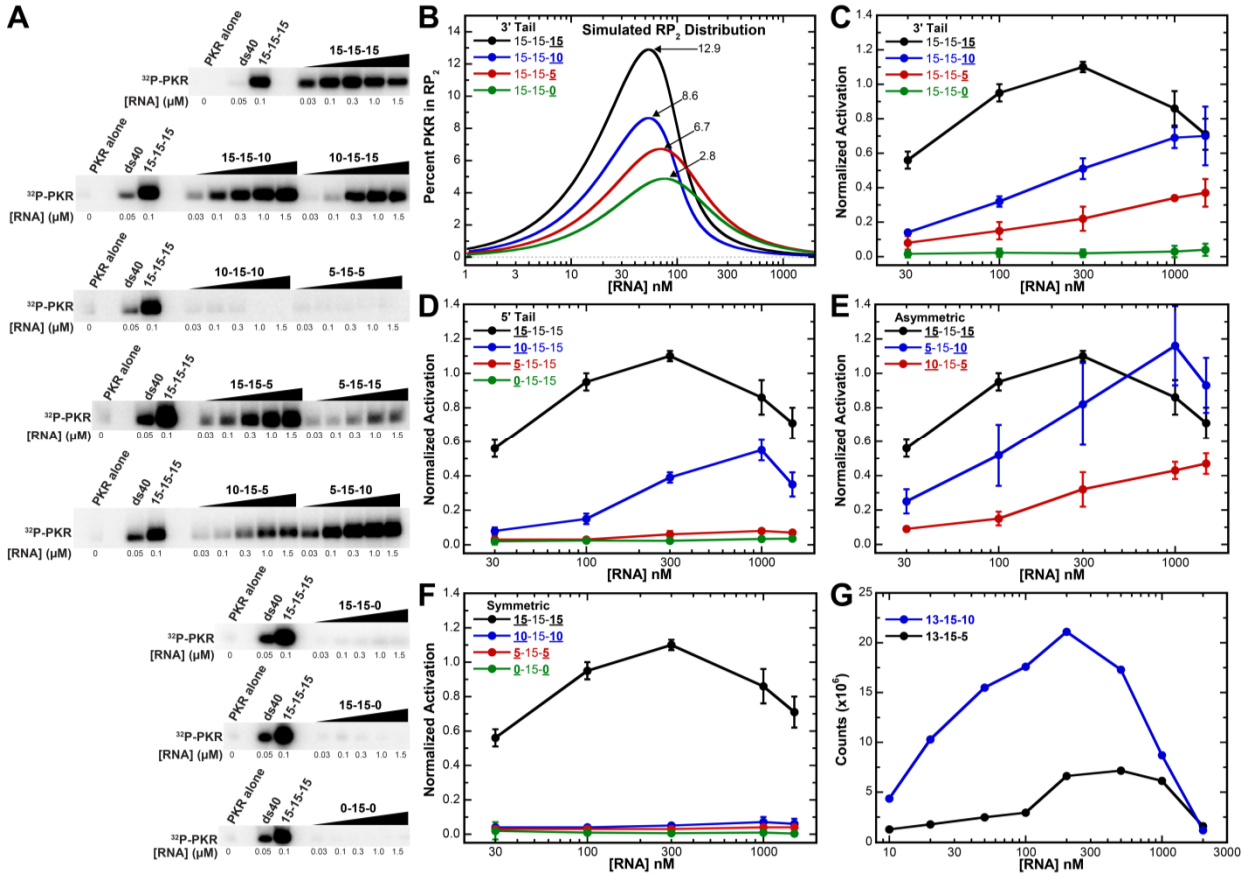

Figure 3.5 Activation of PKR by tail truncation constructs in 75 mM NaCl. (A) Phosphorimages for one of the three experiments quantified in panels C-F. Experiments were performed in AU75 buffer plus 5 mM $MgCl_2$ at 32 °C. Activation is monitored by incorporation of ^{32}P. Each reaction contains 100 nM PKR, 400 μM ATP, 2 μCi γ-^{32}P-ATP, and the indicated amount of RNA. **(B)** Simulated distribution of RP_2 species. K_d measurements presented in Tables 3.2 and 3.4 were used to solve for the percentage of PKR molecules contained in the RP_2 species as a function of RNA concentration. PKR concentration was held at 100 nM. The maximum %RP_2 for each distribution is indicated on the graph. Distributions produced in Igor Pro (Wavemetrics Inc.). **(C-F)** Quantification of ^{32}P incorporation. The signals quantified by phosphorimager analysis were normalized to the ^{32}P incorporation in control samples containing 100 nM 15-15-15 (lane 4 in panel A). Error bars represent the standard deviation of three experiments. **(C)** 3′ tail truncations. **(D)** 5′ tail truncations. **(E)** Asymmetric truncations to both tails. **(F)** Symmetric truncations to both tails. **(G)** Activation by 13-15-10 and 13-15-5. The standard for activation, 15-15-15, was not included in these assays. The data are plotted as raw counts.

3.8 Effect of stem truncations

The effects of decreasing the length of the duplex stem were investigated by creating ppp-15-10-15 and ppp-15-5-15. PKR is potently activated by ppp-15-10-15 with a maximum level about equal to the control ss-dsRNA (Fig. 3.6). Further reduction of the stem to 5 bp abolishes RNA-induced autophosphorylation. In the case of the stem deletions, the binding affinities correlate with activation. For the 10 bp stem construct, K_{d1} is increased somewhat but K_{d2} is essentially unchanged, resulting in a similar %RP_2. For the 5 bp construct, both K_d values are significantly increased, consistent with the loss of measureable activation.

Table 3.5 PKR binding to stem truncation constructs measured in AU75.

RNA	K_{d1} (nM)	K_{d2} (nM)	Maximum % RP_2	RMSD[a]
ppp-15-15-15	4 (2, 6)	294 (252, 343)	12.9	0.00821
ppp-15-10-15	72 (44, 115)	303 (201, 458)	12.6	0.0103
ppp-15-5-15	118 (93, 150)	853 (673, 1103)	5.3	0.00667
ppp-0-5-0	5402 (4929, 5896)	-	-	0.00460

Parameters obtained by global nonlinear least square analysis of sedimentation velocity experiments. The values in parentheses represent the 95% joint confidence intervals obtained using the F-statistic.
[a] Root mean square deviation in absorbance units.

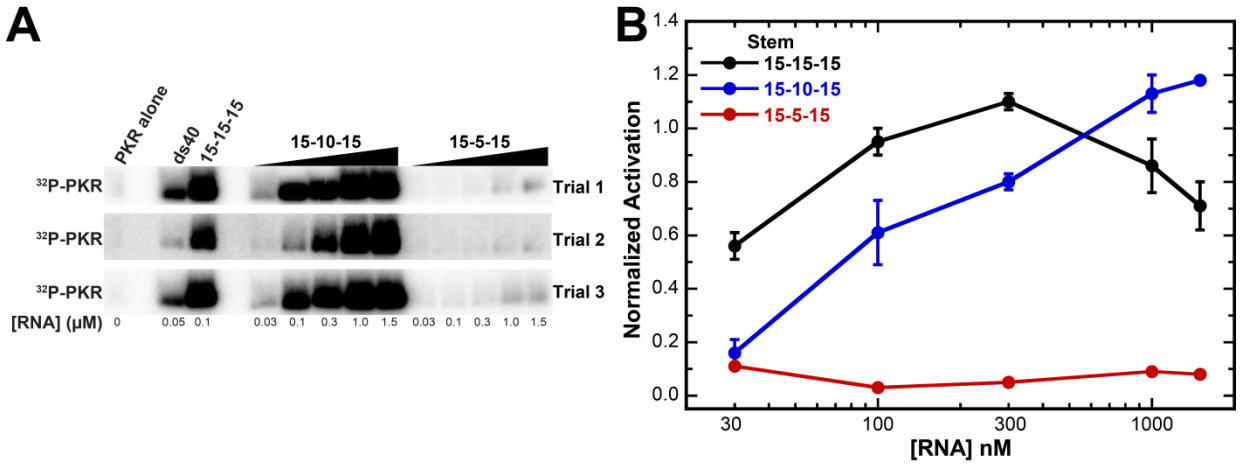

Figure 3.6 Activation of PKR by stem truncation constructs in 75 mM NaCl. (A) Phosphorimage for the data quantified in panel B. Experiments performed as described in Figure 3.5 **(B)** Quantification of ^{32}P incorporation. The signals quantified by phosphorimager analysis were normalized to the ^{32}P-incorporation in control samples containing 100 nM 15-15-15 (lane 4 in panel A). Error bars represent the standard deviation of three experiments.

3.9 0-5-0: A 5 bp stem loop

The dsRBD binding footprint is ~15 bp (143) so it is surprising that 15-5-15 accommodates multiple PKRs with relatively high affinity. To gain insight into the contribution of the single stranded regions to affinity and stoichiometry we prepared a 5 bp stem loop construct lacking the flanking tails (0-5-0). Analysis of PKR binding was complicated by the propensity of the construct to dimerize. Decreasing the RNA refolding and assay concentration minimized the relative population of the dimeric species. However, at the concentrations required for absorbance detected sedimentation velocity, a significant population of the dimeric species persisted (~10 %). The g^(s*) distributions for 0-5-0, PKR mixtures are shown in Figure 3.7A with 15-5-15 in 3.7B for comparison. The distributions are plotted on the same x-axis scale to highlight the difference in binding stoichiometries. Only one PKR binds 0-5-0 to shift the distribution to a maximal sedimentation coefficient of ~4 S whereas distributions containing 15-5-15 are shifted to a limiting sedimentation coefficient of ~6.5 S due to sequential binding of two PKR molecules. Depletion of the RNA peak upon PKR addition provides a qualitative assessment of the relative binding affinities. Freely sedimenting 15-5-15 is depleted by addition of 1.5 equivalents of PKR however 0-5-0 requires ~10 equivalents to achieve similar reduction. This behavior is reflected in the fitted dissociation constant reported in Table 3.5. Due to the contaminating dimer the 0-5-0 affinities should be interpreted with some trepidation. The fitting procedure cannot differentiate whether PKR binds the monomeric or dimeric form of the RNA and parameters for the monomeric form were used in the fit. Regardless of which form PKR interacts with the data provide further evidence for single stranded interactions. In the context of a 15 bp duplex the single stranded regions confer increased affinity (15-15-15 and 0-15-0, Table 3.2). Yet when appended to a 5 bp duplex the single-stranded regions provide additional binding sites resulting in both increased affinity and stoichiometry.

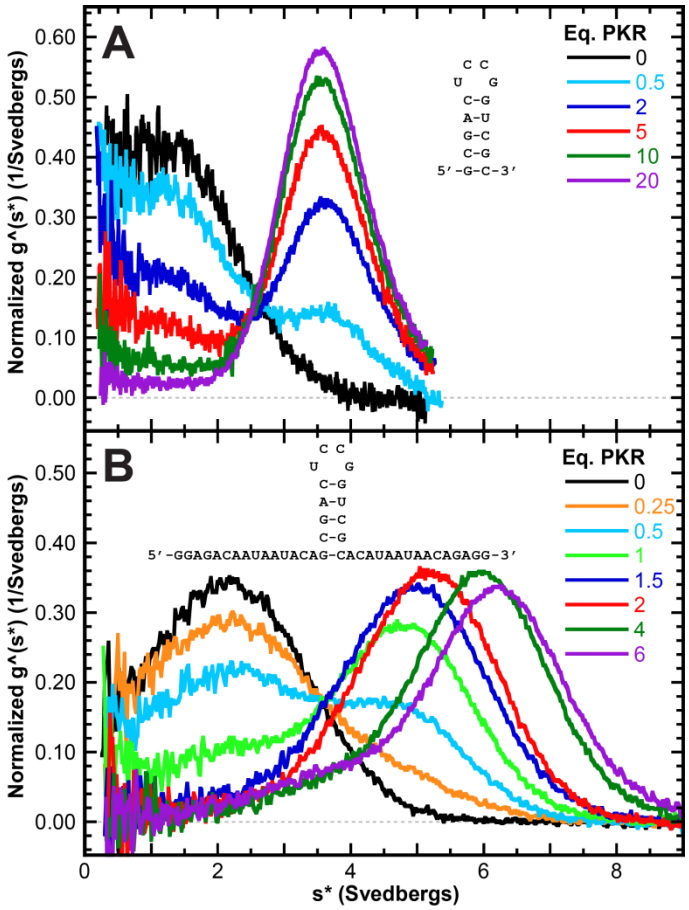

Figure 3.7 Contribution of single stranded regions to PKR binding a 5 bp duplex. g^(s*) distributions normalized by area are shown for **(A)** 0-5-0 and **(B)** 15-5-15. The sequence and predicted secondary structure of the RNA constructs are shown in each panel. The 0-5-0 data were obtained with a rotor speed of 50,000 rpm whereas the 15-5-15 data were obtained at 40,000 rpm. Higher rotor speed leads to decreased diffusional broadening making the 0-5-0 distributions narrower. The 0-5-0 data were fit to an association model in SEDANAL where a single PKR binds. The resulting parameters are reported in the Table 3.5 and in Appendix 2.

3.10 Interaction of dsRBD with ss-dsRNAs

Tail truncation leads to decreased binding affinity and reduced activation potency even though PKR lacks a defined ssRNA binding motif. We performed binding experiments with a domain construct of the dsRBD (residues 1-184) to investigate whether this is the region on PKR which interacts with ssRNA. Binding affinities were determined for 15-15-15 and 0-15-0 and reported with the corresponding measurements obtained for the full length protein in Table 3.6. Unlike the full length protein, our measurements detect a weak, third binding event in the mixture of the dsRBD and 15-15-15 resulting in the RP_3 species. Steric occlusion by the linker

and kinase domain may prevent the interactions which facilitate RP_3 formation in the context of the full length protein. Alternatively, the RNA may interact with regions outside the dsRBD so that the full length protein occupies a larger footprint than the isolated dsRBD construct preventing formation of the RP_3 species.

Similar to the full length protein, the dsRBD binds to 15-15-15 with higher affinity than 0-15-0 indicating that the dsRBD interacts with single stranded regions. However, the increase in affinity for 15-15-15 is not nearly as dramatic as is seen in the full length protein. The relative affinities of the first binding event provide evidence that the single stranded regions also engage PKR outside of the dsRBD. The values of K_{d1} for full length PKR binding 0-15-0 and dsRBD binding to both 15-15-15 and 0-15-0 are all similar. However, K_{d1} for interaction of full length PKR with 15-15-15 interaction is ~28-fold tighter indicated a significant contribution of the single-stranded regions. These observations are corroborated in Chapter 4 where an RNA binding region is identified near the N-terminus of the kinase domain.

Table 3.6 dsRBD and full length PKR binding to 15-15-15 and 0-15-0 measured in AU75.

Protein	RNA	K_{d1} (nM)	K_{d2} (nM)	K_{d3} (nM)	RMSD[a]
Full length	ppp-15-15-15	4 (2, 6)	294 (252, 343)	-	0.00821
Full length	ppp-0-15-0	138 (105, 178)	1662 (1311, 2131)	-	0.00906
dsRBD	ppp-15-15-15	111 (76, 160)	190 (121, 279)	2784 (2102, 3930)	0.00358
dsRBD	ppp-0-15-0	218 (155, 300)	1097 (961, 1249)	-	0.00493

Parameters obtained by global nonlinear least square analysis of sedimentation velocity experiments. The values in parentheses represent the 95% joint confidence intervals obtained using the F-statistic.
[a] Root mean square deviation in absorbance units.

3.11 5′-Triphosphate

It has been reported that a 5′-triphosphate (5′-ppp) is crucial for activation of PKR by canonical ss-dsRNAs as well as ssRNAs containing short duplexes (78, 131). Host RNAs are typically capped at their 5′-end prior to export into the cytoplasm while most viral RNAs contain a 5′-ppp. Thus, the 5′-ppp is an important motif which provides the host cell with a structural

element to discriminate between self and non-self RNA (79). Because of the critical role ascribed to the 5′-ppp in the context of ss-dsRNAs and the function of PKR in the innate immunity pathway (80), we have investigated the contribution of 5′-ppp to PKR binding and activation. The series of experiments which emerged from some preliminary measurements are separated for organizational purposes into three sections: 3.11 5′-Triphosphate, 3.12 Synthetic RNA, and 3.13 Tetraloop. However, each section is inherently linked and briefly summarized here so that the reader can be mindful of the results. Our experiments indicate that dephosphorylation of *in vitro* transcribed (IVT) ss-dsRNAs does not inhibit PKR stimulation. Curiously, synthetic versions of ss-dsRNAs containing either a 5′-ppp or 5′-OH do not activate PKR. This surprising and alarming result was not revealed until an important control experiment was performed while investigating the role of the tetraloop. ss-dsRNAs lacking a tetraloop were created by annealing two synthetic RNAs and do not activate PKR. However, ligation of the loop does not restore activation. The corresponding ∆-tetraloop constructs were created by *in vitro* transcription and exhibit the same phenotype as their synthetic counterparts. The constructs fail to activate and cannot be rescued by ligation. In summary, RNAs which should be chemically identical exhibit different stimulatory effects which are dependent on the method of production. Only ss-dsRNAs produced in their entirety by *in vitro* transcription activate PKR. The experiments described in the following sections seek to establish protocols for complete 5′-dephosphorylation and identify the chemical differences between IVT and synthetic RNA.

RNAs transcribed by T7 RNA polymerase contain a 5′-triphosphate. Constructs were converted to the 5′-OH form by dephosphorylation with calf intestinal alkaline phosphatase (CIP). Dephosphorylation of ppp-15-15-15 and ppp-5-15-10 by treatment CIP has no significant effect on the extent of PKR activation (Fig. 3.8A). Several experiments verify that the 5′-ppp is removed by the phosphatase. ppp-15-15-15 and ppp-5-15-10 cannot be labeled with a 5′-^{32}P by treatment with T4 polynucleotide kinase and [γ-^{32}P]ATP because of the presence of a 5′-ppp, but the corresponding dephosphorylated RNAs are substrates (Fig. 3.8B). Additionally, an ss-

dsRNA labeled during *in vitro* transcription in the presence of [γ-^{32}P]GTP displays complete removal of the 5′-ppp after phosphatase treatment (Fig. 3.8C), indicating that the activity of the 5′-OH RNAs is not due to the presence of residual triphosphate-containing RNA. RNAs used in this study are produced by transcription off a template that encodes the HDV ribozyme at the 3′-end of the transcript. The ribozyme is included to circumvent the problem of 3′-end heterogeneity which can plague RNA production using standard run-off transcription techniques (108). Cleavage results in a 2′-3′-cyclic phosphate (144) and we postulated that it may compensate for the absence of the 5′-triphosphate. RNAs are treated with CIP to dephosphorylate the 5′-end yet the activity of CIP on 2′-3′-cyclic phosphates is unknown. T4 polynucleotide kinase (PNK) possesses a phosphatase domain specifically evolved to liberate 2′-3′-cyclic phosphates (113, 145). The phosphatase activity can be promoted by altering the reaction conditions and dephosphorylation can be monitored by a slight mobility shift in a urea PAGE gel (109). We subjected 15-15-15 to sequential treatments with T4 PNK then CIP to dephosphorylate both 5′- and 3′-termini. PNK treatment results in a slight retardation of migration in a urea PAGE gel (Fig. 3.8D). Consistent with other reports, subsequent dephosphorylation of the 5′ end with CIP results in faster migration in urea PAGE (Fig 3.8D, Fig. 3.10B) (146, 147). The relative migration differences indicate that the enzymatic treatments are resulting in the expected activities and the complete shift of the bands provides evidence that the reactions are complete. Neither treatment results in a loss of PKR stimulation (Fig. 3.8E). Finally, MALDI-ToF mass spectrometry analysis provides further evidence that CIP treatment results in homogenous dephosphorylation of both ppp-15-15-15 (Fig. 3.8G) and ppp-5-15-10 (Fig. 3.8F). CIP treated RNAs exhibit a mass decrease of 300-315 Da consistent with the removal of both 5′-ppp and 2′-3′ cyclic phosphate (predicted change of 300 Da). These control experiments indicate that activation by enzymatically dephosphorylated ss-dsRNAs is not due to a residual population of 5′-ppp.

Removal of the 5′-ppp does affect PKR binding affinity (Table 3.7). K_{d1} increases about 10-fold and K_{d2} increase slightly. However, the maximum %RP_2 does not change substantially and the binding parameters remain in the range of ss-dsRNAs that activate, such as ppp-15-15-5 and ppp-5-15-10.

Table 3.7 PKR binding to *in vitro* transcribed and synthetic HO-15-15-15 measured in AU75.

RNA	K_{d1} (nM)	K_{d2} (nM)	Maximum % RP_2	RMSD[a]
IVT ppp-15-15-15	4 (2, 6)	294 (252, 343)	12.9	0.00821
IVT HO-15-15-15	36 (26, 49)	411 (357, 473)	9.9	0.00861
Synthetic HO-15-15-15	28 (21, 37)	481 (421, 551)	8.7	0.00754

Parameters obtained by global nonlinear least square analysis of sedimentation velocity experiments. The values in parentheses represent the 95% joint confidence intervals obtained using the F-statistic.
[a] Root mean square deviation in absorbance units.

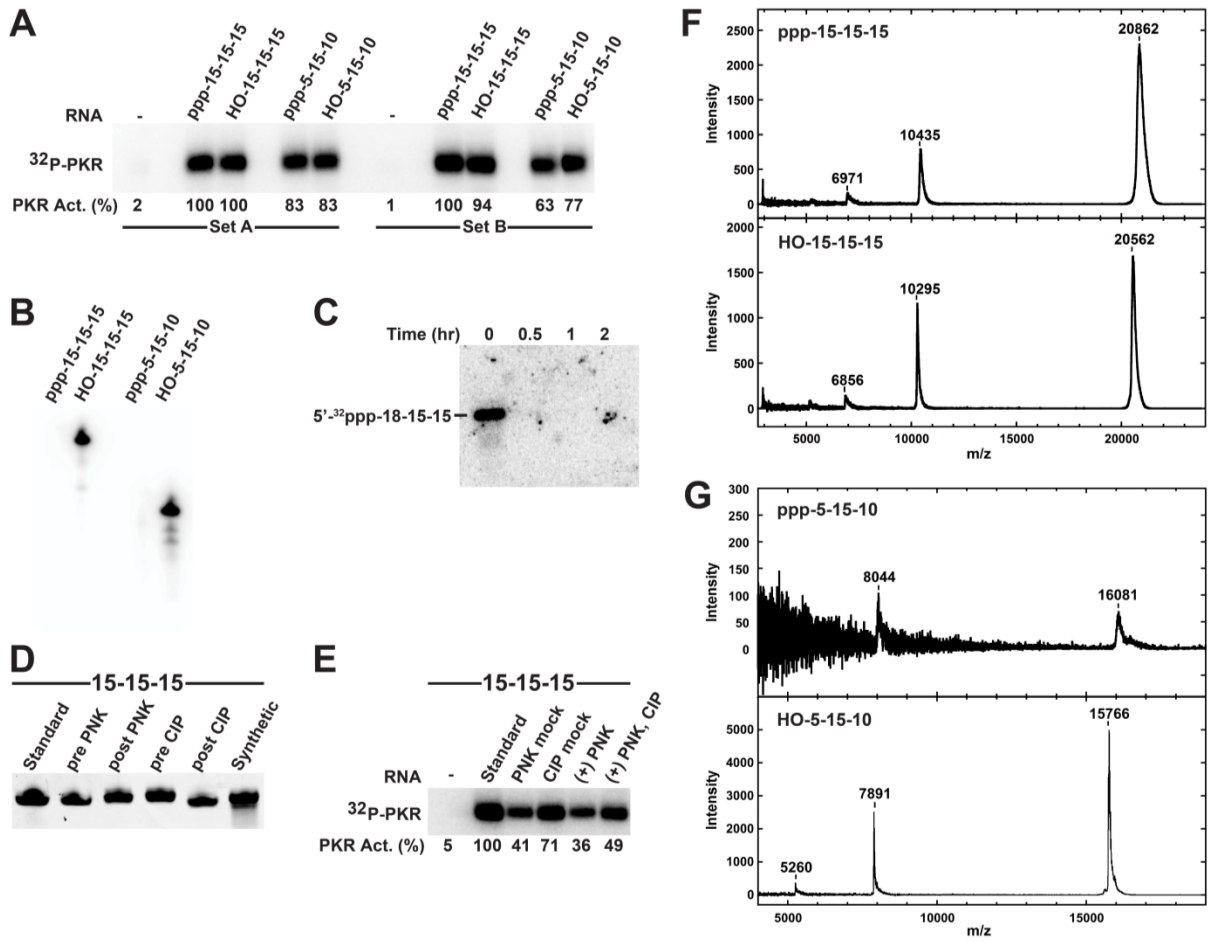

Figure 3.8 Activation by ss-dsRNAs does not require a 5′-triphosphate. (A) Activation by 5′-ppp and 5′-OH ss-dsRNAs. 5′-OH RNAs were prepared by treatment with CIP. Samples contain 300 nM RNA. Autophosphorylation activity is indicated under the gel as a percentage normalized to activation by ppp-15-15-15. **(B)** Assay for dephosphorylation by 5′-^{32}P labeling by T4 PNK. RNAs containing a 5′-OH are substrates for T4 PNK whereas 5′-ppp prevents phosphorylation. **(C)** A ppp-18-15-15 RNA containing a ^{32}P at the 5′-γ-phosphate was incubated with Antarctic phosphatase at 37 °C. Aliquots were removed at time points as indicated in the figure and quenched with denaturing gel loading buffer and resolved by 10% TBE-Urea PAGE. The gel was exposed to a phosphor screen and scanned on a Typhoon phosphoimager. Removal of the 5′-ppp is complete at 30 min. γ^{32}P-labeled 18-15-15 was made by *in vitro* transcription in the presence of γ-^{32}P GTP. RNAs dephosphorylated by Antarctic phosphatase activates PKR. **(D)** Sequential enzymatic treatment of 15-15-15 visualized by a slight mobility change by 12% TBE-Urea PAGE. **(E)** Activation by the enzymatically treated 15-15-15 shown in (D). In the mock reactions, 15-15-15 was submitted to the enzymatic reaction conditions but enzyme was not added. Autophosphorylation activity is indicated under the gel as a percentage normalized to the initial RNA sample labeled as 'Standard'. **(F)** MALDI-ToF analysis of dephosphorylation of ppp-15-15-15. RNAs. **(G)** MALDI-ToF analysis of dephosphorylation of ppp-5-15-10. ppp-15-15-15 exhibits a mass loss of 300 Da and ppp-5-15-10 exhibits a mass loss of 315 Da. The predicted mass loss is 300 Da (removal of the 5′-ppp and the 2′-3′-cylic phosphate resulting from HDV ribozyme cleavage).

3.12 Synthetic RNA

Chemical oligonucleotide synthesis provides a mechanism to produce RNAs of defined sequence devoid of terminal phosphates. We obtained synthetic RNAs to directly test 5′-triphosphate dependence after initial dephosphorylation reactions failed to deactivate ss-dsRNAs produced by IVT. Synthetic versions of two potently activating RNAs, 15-15-15 and 5-15-10, were acquired from two different commercial entities. 15-15-15 was supplied by Dharmacon and 5-15-10 was obtained from Integrated DNA Technologies. Both RNAs contain a 5′-OH. Binding affinity measurements detect a similar reduction in affinity for synthetic HO-15-15-15 as was observed for IVT HO-15-15-15 supporting the idea that PKR recognizes the 5′-ppp (Table 3.7). Despite similar binding behavior, the two forms of 5′-OH RNA differ in their stimulatory properties. As shown in Figure 3.9A the synthetic forms of both 15-15-15 and 5-15-10 fail to activate while the IVT versions potently stimulate PKR in the same assay. Furthermore, synthetic HO-15-15-15 inhibits activation by IVT ppp-15-15-15 (Fig. 3.9B). The inhibition potency provides additional evidence that activation by 5′-OH IVT RNA is not due to residual 5′-ppp. In a mixture containing equal concentrations of synthetic and IVT 15-15-15, the activity is reduced by ~37 % (Fig. 3.9B). Dephosphorylation reactions induce no reduction in activity (Fig. 3.8A) implying the reactions are very inefficient or that synthetic and IVT HO-15-15-15 are not chemically equivalent. Finally, we have used enzymatic ligation to create synthetic 15-15-15 capped by a 5′-ppp yet this RNA also does not activate PKR. This evidence suggests there are unidentified chemical differences between RNA produced by *in vitro* transcription and chemical synthesis.

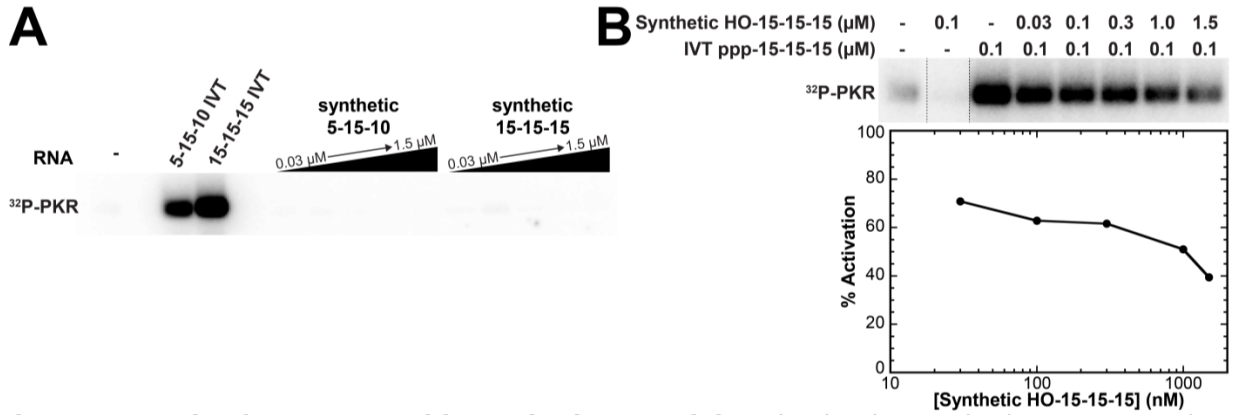

Figure 3.9 Activation assays with synthetic RNA. (A) Activation by synthetic 5-15-10 and 15-15-15. IVT versions are positive controls at 100 nM. **(B)** Inhibition of IVT ppp-15-15-15 by synthetic 15-15-15. Samples contain 100 nM PKR and 100 nM IVT ppp-15-15-15 with a titration of synthetic 15-15-15. Dashed lines indicate where blank lanes were cropped out of the gel. Band intensity is quantified in the plot below the phosphorimage. Activation is expressed as a percentage of the band intensity measured for the sample containing only IVT ppp-15-15-15

Synthetic RNAs are available from a variety of commercial suppliers which typically employ nucleoside phosphoramidite chemistry to build oligonucleotides. Synthesis reactions vary depending on the commercial entity but all utilize a general organic synthesis protocol which relies on selective deprotection to coordinate the appropriate coupling reactions between nucleoside monomers and the oligonucleotide chain. The reaction scheme employed by Dharmacon is summarized below (148, 149). The outline is meant to illustrate the complexity of the procedure to support the hypothesis that chemical impurities can contaminate the synthetic preparation and interfere with PKR activation. Oligonucleotide chains are assembled on a solid phase support in the 3′- to 5′-direction. The building blocks are nucleoside phosphoramidites which contain chemically protected functional groups to prevent undesired reactions. The synthesis cycle involves addition of the desired nucleoside phosphoramidite and an activator which catalyzes the coupling reaction between the newly added nucleoside and free 5′-OH on the anchored oligonucleotide chain. Unreacted 5′-OH termini are chemically protected from subsequent coupling steps via a reaction which yields a 5′-acetyl. Nucleosides successfully coupled to the oligonucleotide contain a 5′-O-silyl ether which is converted to a 5′-OH for subsequent coupling reactions in a reaction catalyzed by fluoride (triethylamine trihydrofluoride).

The cycle is repeated until the desired chain length is achieved. Following synthesis, exocyclic amines present on nucleotide bases are deprotected and the oligonucleotide is released from the solid phase support. Dharmacon provides RNA in a form where the 2′-OH is chemically protected (2′-ACE, 2′-*O*-bis(2-hydroxyethoxy)methyl orthoester) and is deprotected by the customer with a mildly acidic aqueous solution. Production of synthetic RNA free of chemical impurities is dependent on the use of pure ribonucleoside phosphoramidite building blocks and complete deprotection of the appropriate functional groups during every phase of the synthesis cycle. Mild reaction conditions are utilized to prohibit formation of undesired chemical adducts. However, numerous impurities have been identified in chemically synthesized oligonucleotides. These include shorter sequences resulting from incomplete chain elongation (150-152), various protecting groups remaining from synthesis (150-152), depurinated bases (152), the presence of 5-methylcytosine presumably from impure nucleoside phosphoramidite precursors (153), and branched chain oligonucleotides where chain elongation occurs off a deprotected nucleobase exocyclic amine (154, 155). PKR is sensitive to nucleoside modifications although the effects manifest in the RNA stimulatory properties rather than binding affinity (82). This is potentially in agreement with our observations where the synthetic and IVT forms bind with comparable affinities yet exhibit different stimulatory phenotypes.

Analysis of RNA size and shape fails to identify any significant differences between the IVT and synthetic forms. Urea-PAGE analysis of the 2′-ACE-protected form of 15-15-15 provided by Dharmacon indicates that nucleoside modifications can be detected by gel migration differences. RNA containing the 2′-protecting group (2′-ACE) migrates faster through the gel than RNA in the 2′-OH form (Fig. 3.10A). Presumably the increased electronegative charge imparted by the protecting group causes faster migration through the gel. However, the dephosphorylated IVT versions of both 15-15-15 and 5-15-10 run at the same position as their synthetic equivalents in urea-PAGE (Fig. 3.8D and Fig. 3.10B). Hydrodynamic analysis 15-15-15 by sedimentation velocity analytical ultracentrifugation detects slight variation between the

synthetic and IVT forms (Fig. 3.10C). The sedimentation coefficient of synthetic HO-15-15-15 is slightly lower than the IVT forms indicating either the synthetic form has a smaller molecular weight or folds into a slightly more extended structure. Both IVT and synthetic forms of 15-15-15 produce similar digestion patterns from enzymatic structure probing experiments (not shown) indicating cleavage is not affected by chemical impurities which may be present on the RNA.

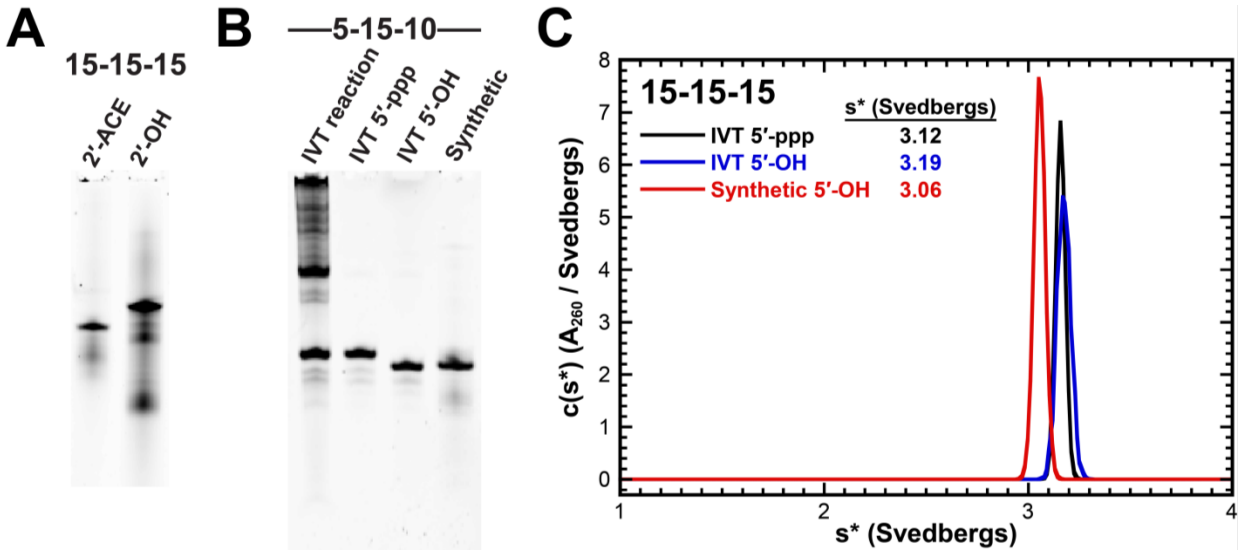

Figure 3.10 Analysis of synthetic RNA. (A) 10% TBE-Urea PAGE analysis of protected (2′-ACE) and deprotected (2′-OH) forms of 15-15-15. Note that the deprotected RNA was analyzed directly after the deprotection reaction. RNAs are purified before use by urea PAGE to eliminate the impurities that are present on the gel. **(B)** 12% TBE-Urea PAGE analysis of 5-15-10. An *in vitro* transcription reaction is shown along with purified ppp-5-15-10 and dephosphorylated IVT HO-5-15-10. The dephosphorylated RNA co-migrates with synthetic HO-5-15-10. **(C)** Sedimentation velocity analysis of 15-15-15. c(s*) distributions for IVT ppp-15-15-15, IVT HO-15-15-15, and synthetic HO-15-15-15 are shown. Best fit sedimentation coefficients obtained by fitting the time difference curves to an ideal species model in SEDANAL are shown in the plot.

Conventional binding assays and analytical ultracentrifugation measurements can determine how many PKRs are bound to an RNA but do not directly assay dimerization via the kinase domain interface. Therefore, we recently developed a sensitive homo-FRET anisotropy assay to directly probe PKR kinase domain dimerization on RNAs (65). Activating duplex RNAs containing ≥30 bp bind two PKRs and induce dimerization detected by depolarization of fluorophore emission using steady-state anisotropy measurements. However, some nonactivating RNAs that also produce a high population of the RP_2 species, as detected by

analytical ultracentrifugation, either fail to induce dimerization or produce an alternative, inactive dimer configuration. This behavior may rationalize the failure of synthetic RNA to induce activation despite populating a similar amount of the RP_2 species as IVT RNA (Table 3.7). Figure 3.11 shows the anisotropy change upon addition of either IVT ppp-15-15-15 or synthetic HO-15-15-15. The amplitude is the same for both RNAs although the IVT form achieves its maxima at slightly lower RNA concentrations. By all measurements synthetic HO-15-15-15 should activate to a similar extent as IVT ppp-15-15-15. Both RNAs populate a similar amount of RP_2 species as measured by analytical ultracentrifugation and both induce kinase domain dimerization to a similar extent. The nature of the chemical differences between IVT and synthetic RNA forms remains elusive.

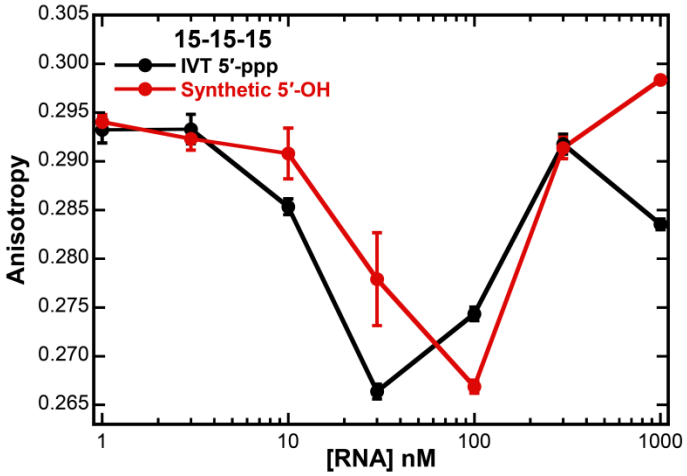

Figure 3.11 Analysis of kinase domain dimerization on 15-15-15 measured by homo-FRET anisotropy. Alexa Fluor 488 is conjugated to *p*-azidophenylalanine which was incorporated at position 261. Dimerization is detected by a change in anisotropy induced by depolarization of homo-FRET emission (65). Samples contain 200 nM PKR and a titration of RNA. The assay was performed in AU75 buffer at 20 °C. Both IVT 5′-ppp and synthetic 5′-OH 15-15-15 induce a similar anisotropy change.

3.13 Tetraloop

There are 256 unique nucleotide combinations for tetraloop sequences yet detailed analysis of 16S ribosomal RNA (156) and bacteriophage T4 mRNA (157) has revealed a biased frequency toward certain nucleotide arrangements which can be categorized as 5′-UNCG-3′ or 5′-GNRA-3′ tetraloops (N = any nucleotide; R = purine). The bias is thermodynamic in origin and

can be attributed to the stability conferred by noncanonical base pair interactions between nucleotides in positions 1 and 4, 2′-OH hydrogen bonds, and base stacking (158). Structural differences between UNCG and GNRA tetraloops arise from variations in sugar puckering and glycosidic bond orientation primarily within nucleotides in positions 2 and 3 (159). These nucleotides pucker out into the solvent to facilitate bending of the RNA backbone and present an additional surface not present within duplex regions to stabilize protein interaction. Five structures are available for dsRBDs bound to stem-loop RNAs and in four of the structures the α1 helix interacts with nucleotides projecting from the loop, thereby orienting dsRBD binding (Fig. 3.11A). In Rnt1p RNaseIII and ADAR2, the positioning of the dsRBD is believed to play a functional role by orientating the catalytic domains for specific modification of the RNA substrate (24, 25). There are some reports indicating that loops modulate PKR binding although the functional relevance is unclear (26-28). Given that the dsRBD binding footprint is ~15 bp (143) it is likely that PKR interacts with tetraloop residues during complex formation with ss-dsRNAs containing shorter duplex regions. To test this interaction the tetraloop within the parental 15-15-15 ss-dsRNA was altered. Figure 3.11B shows schematic representations of the constructs and the nomenclature adopted to describe them. Tetraloop variations include changes to loop sequence (GAAA and UUUU), deletion of the tetraloop (ΔT), and broken loops with the tetraloop sequence projecting from 5′-, 3′-, or both strands (5′-UCCG, 3′-UCCG, 5′/3′-UCCG).

The original 15-15-15 sequence contains a UNCG type tetraloop (5′-UCCG-3′). Versions of 15-15-15 were made which contain the loop sequence 5′-GAAA-3′ or 5′-UUUU-3′ and characterized by PKR binding affinity and activation measurements. The UUUU tetraloop is expected to exhibit a greater degree of conformational flexibility (160, 161) due to the minimal contribution of uridines to base stacking interactions (162). The constructs were created by *in vitro* transcription. Perturbations to the loop sequence have a minimal effect on PKR binding (Table 3.8) and activation (Fig. 3.11C).

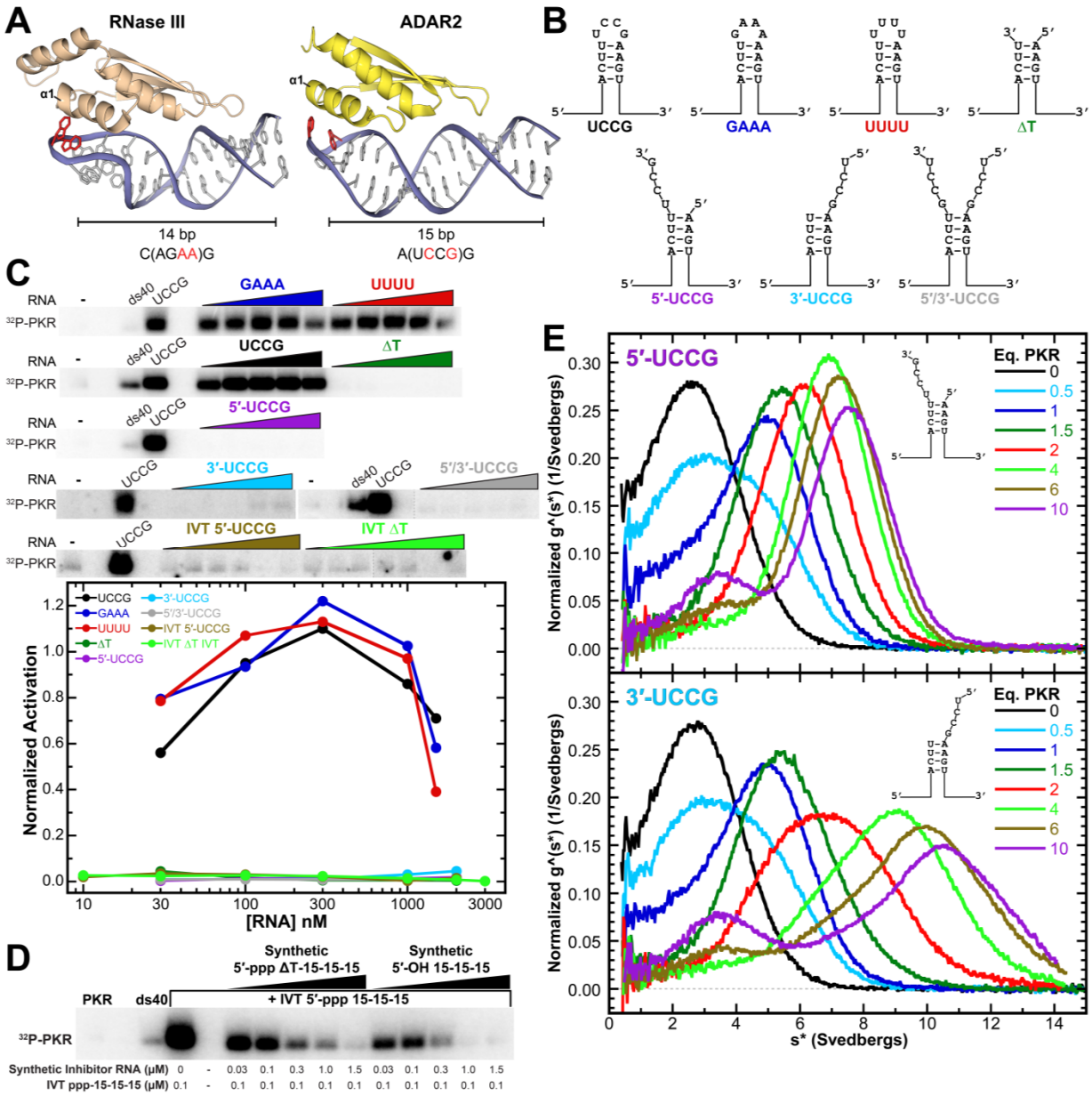

Figure 3.12 Characterization of the tetraloop. (A) dsRBD interactions with tetraloops. Rnt1p RNase III dsRBD1 is shown on the left (1T4L) (47) and ADAR2 dsRBD1 on the right (2L3C) (17). The nucleotide which puckers out of the tetraloop and contacts helix α1 is shown in red. The length of the stem and tetraloop sequence is indicated underneath the structure. **(B)** Schematic representation of constructs designed to probe the tetraloop. Coloring scheme is maintained throughout the figure. **(C)** Activation assays. Constructs containing a broken loop created by *in vitro* transcription (IVT) are assayed in the bottom gel. The data are quantified in the plot beneath the gels. Data are normalized to the wild-type 15-15-15 construct labeled as 'UCCG' in each gel. **(D)** Inhibition of IVT ppp-15-15-15 by synthetic ΔT. **(E)** g^(s*) distributions normalized by area comparing PKR interaction with 5′-UCCG (top) and 3′-UCCG (bottom).

Constructs lacking or containing a broken loop were created by hybridizing two synthetic oligonucleotides to mimic the loop containing 15-15-15. These constructs were analyzed prior to recognition that the full-length synthetic ss-dsRNAs do not activate PKR. Constructs corresponding to 5′-UCCG and ΔT were created by IVT; however, purity and yield from purification were insufficient for detailed analysis. The material was used for activation assays but binding experiments were not performed. Figure 3.11C shows the activity assays performed with all the synthetic and IVT constructs. The synthetic constructs do not mediate activation which is not surprising given the analysis of full-length synthetic constructs presented in the previous section. Note, however, that the synthetic constructs analyzed here contain a 5′-ppp whereas the full-length constructs contain a 5′-OH. Like the full-length synthetic constructs ΔT inhibits activation mediated by IVT ppp-15-15-15 (Fig. 3.12D). The constructs created by IVT also do not activate however a control ligation experiment presented below necessitates cautionary interpretation of this result.

The binding affinity measurements are reported in Table 3.8. Deletion of the tetraloop from 15-15-15 (ΔT) reduces affinity of the first binding event by ~15-fold and decreases the second by ~2-fold indicating that the loop contributes to complex formation. Constructs containing a broken tetraloop exhibit drastically different binding behavior dependent on which strand the loop sequence is placed on. A comparison of the g^(s*) distributions is shown in Figure 3.12E. A construct containing the loop sequence on the 5′-strand (5′-UCCG) exhibits similar binding behavior as the canonical 15-15-15 where two PKR monomers sequentially bind to produce an RP_2 species at ~8 S. The binding affinities are decreased, indicating PKR prefers a folded structure at the top of the stem (Table 3.8). When the loop sequence protrudes from the 3′-strand (3′-UCCG), mixtures containing a molar excess of PKR produce a larger species which sediments at ~11 S. An appropriate model to describe the 3′-UCCG data was not attained. Both the 5′-UCCG and 3′-UCCG constructs have nearly identical distributions for mixtures containing 0.5, 1, and 1.5 equivalents of PKR. A cooperative transition appears to

occur upon addition of 2 equivalents potentially indicating that the second PKR mediates a structural alteration within the RNA which permits formation of higher order complexes. One possibility is that PKR stabilizes an interaction analogous to kissing loop complexes (68) which dimerizes the RNA via the broken tetraloop at the top of the stem. However, it is unclear why a similar complex would not form with the 5′-UCCG construct. Equally puzzling is why a complex of this nature, or any complex which mediates higher-order assembly of multiple PKR molecules, does not stimulate activation. In the PKR mediated RNA dimerization scenario, coaxial stacking of nucleotides at the top of the stem would form a 34 bp duplex interrupted by a two nucleotide bulge in the center. Perfect duplexes 30 bp in length formed by hybridization of synthetic oligonucleotides activate PKR (63).

Table 3.8 Effect of loop on PKR binding affinity measured in AU75 buffer.

Loop sequence	K_{d1} (nM)	K_{d2} (nM)	Maximum % RP_2	RMSD[a]
UCCG	4 (2, 6)	294 (252, 343)	12.9	0.00821
GAAA	17 (12, 22)	345 (324, 366)	11.4	0.00753
UUUU	35 (28, 44)	319 (300, 339)	12.1	0.00798
ΔT[b]	68 (58, 81)	611 (579, 644)	7.1	0.00842
5′-UCCG[b]	112 (96, 131)	583 (548, 619)	7.4	0.00896
3′-UCCG[b]	ND[c]	ND[c]	-	-

Parameters obtained by global nonlinear least square analysis of sedimentation velocity experiments. The values in parentheses represent the 95% joint confidence intervals obtained using the F-statistic. Sedimentation coefficients are fixed to best fit values for UCCG: s (RP) = 4.88 S; s (RP_2) = 8.02.
[a] Root mean square deviation in absorbance units.
[b] Denotes constructs created by hybridization of synthetic oligonucleotides. All RNAs contain a 5′-ppp.
[c] An appropriate model to describe this interaction was not attained. Refer to Fig. 3.12E for g^(s*) distributions.

Constructs corresponding to ΔT and 5′-UCCG that were created by IVT do not activate PKR (Fig. 3.12C) suggesting that the loop is a critical element which mediates activation. However, an essential control experiment disputes the relevance of this finding. Enzymatic ligation of synthetic (3.13A) and IVT constructs (3.13D) does not restore PKR activation. The

full length synthetic constructs previously analyzed contained a 5′-OH. However, the ligated constructs contain a 5′-ppp. Failure to activate provides further evidence for the chemical differences between IVT and synthetic forms. Analysis of the ligated RNA by denaturing gel electrophoresis (3.13A, D) and mass spectrometry (3.13C) indicates that ligation was successful, although the product was typically contaminated with the constituent single-stranded RNAs. Purification of the ligated reaction by size exclusion chromatography or denaturing PAGE did not rescue activation (not shown).

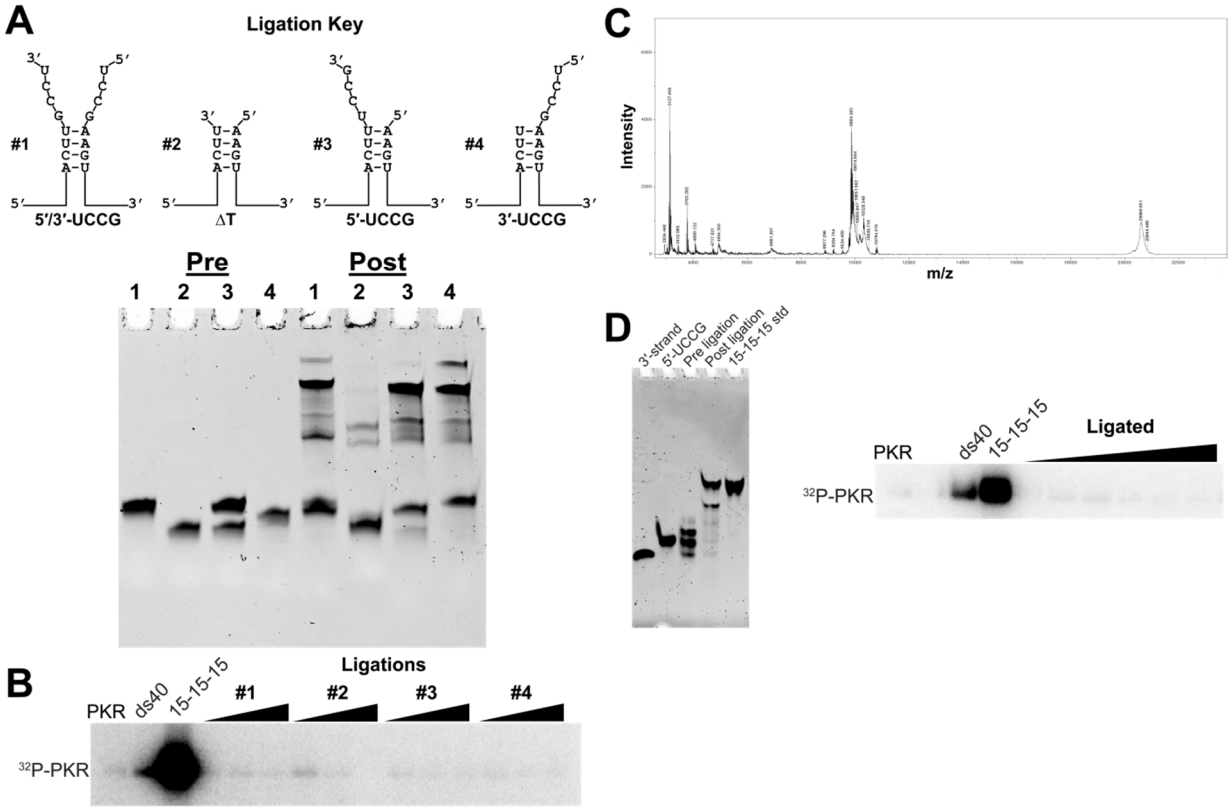

Figure 3.13 Ligation of the tetraloop. (A) Ligation of synthetic constructs. The ligation key indicates the combination of tetraloop sequences which were ligated in the gel below. **(B)** Activation on the ligation reactions shown in (A). **(C)** MALDI-ToF analysis of ligation #3 (5′-UCCG). **(D)** Ligation of IVT RNA. The 5′-UCCG construct produced by IVT reactions was ligated (left) and assayed for PKR activation (right)

3.14 Discussion

We have systematically dissected a model ss-dsRNA activator to determine the contributions of the single-stranded tails, stem-loop, and the 5′-triphosphate to PKR activation

and binding. The model ss-dsRNA activates PKR autophosphorylation strongly and the presence of both flanking 5′- and 3′-ssRNA tails are required for activation. When either tail is truncated, the activation potency drops with tail length and truncation of the 5′-tail is more deleterious to activation than the 3′-tail. However, the effects of tail truncations are not simply additive as the lengths of the tails are reduced. For example, the symmetric construct containing 10 nt 5′ and 3′ tails does not activate PKR yet ppp13-15-10, ppp13-15-5, ppp-10-15-5, and ppp-5-15-10 stimulate autophosphorylation. Activation is also sensitive to stem length: the titration is shifted to higher RNA concentrations for the 10 bp construct and the 5 bp construct is inactive.

The bell shaped curve for activation by ss-dsRNAs supports a model in which lower RNA concentrations activate by inducing PKR dimerization and high RNA concentrations dissociate active, RNA-bound PKR dimers onto separate molecules of dsRNA (61, 67). However, at high salt (200 mM NaCl), our AUC experiments detect the binding of only one PKR monomer to both activating and nonactivating RNAs. Possibly, the observed activation is mediated by very weak binding of a second PKR monomer. At lower salt (75 mM NaCl) ss-dsRNAs bind two PKRs. In cases where the binding affinity is strongly reduced, such that the maximal RP_2 <10%, activation is abolished or greatly attenuated. However, is it not possible to predict activation based on K_{d1}, K_{d2}, or maximal % RP_2 for the ss-dsRNAs with intermediate binding affinities: some (e.g., ppp-5-15-15) are inactive and others (e.g., ppp-5-15-10) are quite active. Thus, a threshold concentration of RP_2 is required, but not sufficient, to elicit PKR autophosphorylation by ss-dsRNA. Potentially, specific sequences in the tail regions may contribute to the relative activation potencies.

Our results implicate the 5′- and the 3′- ssRNA regions in the mechanism of activation of PKR by ss-dsRNAs. The presence of 5′- and 3′-tails in ss-dsRNAs enhance PKR binding affinity suggesting that the tails directly bind to PKR. It has been reported that dsRNA binding domains do not bind to ssRNA (163, 164) and PKR is not activated by ssRNAs (66, 165). However, our

analysis of ssRNA interactions (presented in Chapter 4) reveals two regions on PKR which bind ssRNA with micromolar affinity: the dsRBD and a basic region N-terminal to the kinase domain. Complex formation with ss-dsRNAs is presumably mediated by the nanomolar affinity of the dsRBD for duplex regions (104). Auxiliary interactions with single-stranded regions tethered to the duplex would be promoted by the effect of increased localized concentration (166). An isolated kinase domain construct containing the basic region is weakly stimulated by ssRNA. In the context of full length PKR and ss-dsRNAs direct engagement of the basic region by the single-stranded tails may elicit activation. The lack of correlation between tail length, binding affinity, and activation potency for constructs with intermediate tail lengths may reflect specific conformational requirements of the interaction.

There is evidence that the single-stranded regions may contribute to PKR activation in complex, natural RNAs. In the context of perfect duplex dsRNA, a length of at least 30 bp of dsRNA is required to activate PKR autophosphorylation (62-64). Interestingly, the length of the duplex regions in several natural RNA activators of PKR, including HCV IRES (167, 168), TNFα mRNA (72), interferon-γ mRNA (6), and the 3′-UTR regions of several cytoskeletal muscle mRNAs (3) are below the 30 bp required for PKR activation. Similarly, influenza B ribonucleoprotein is a potent PKR activator that contains only a short 14-16 bp “panhandle" (169). Thus, the single-stranded regions may contribute to PKR activation in these complex natural RNAs.

It has been reported that a 5′-ppp is crucial for activation of PKR by the canonical ss-dsRNAs as well as ssRNAs containing short duplexes (78, 131). In contrast, for RNAs produced by *in vitro* transcription, we find that this moiety does not contribute to PKR activation and only slightly affects binding affinity. RNAs produced by chemical synthesis do not activate in both 5′-ppp and 5′-OH forms. We also obtain similar results using a previously described ss-dsRNA (ss-dsRNA 9,11 see Fig. 1.4A) (77, 78). ss-dsRNA 9,11 activates PKR potently when prepared

by IVT. However, the synthetic counterpart containing a 5′-OH does not activate. Dephosphorylation reactions on the IVT preparation does not eradicate PKR activation (C. Mayo and J.L. Cole, unpublished observations). snoRNAs, which contain short duplexes interspersed with single-stranded regions, were recently reported to activate PKR. In some case activation is dependent on a 5′-ppp whereas others are active in 5′-OH and 5′-p states (7), suggesting that the structural context can modulate the triphosphate dependence. We are currently investigating the chemical differences between synthetic and IVT RNAs.

Chapter 4: Interaction with single-stranded nucleic acids

4.1 Introduction

Although the antiviral kinase PKR was originally characterized as a double-stranded RNA activated enzyme it can be stimulated by RNAs containing limited secondary structure and alternative structural elements are proposed to modulate activity. Single-stranded regions and a 5′-triphosphate appear to be an important determinant for activation yet PKR lacks defined binding sites for both. Stimulatory RNAs typically originate from viral infection but several endogenous RNAs have been identified as PKR activators (3-7). In addition to the canonical activators containing ≥ 30 bp dsRNA regions, PKR is activated by RNAs that contain limited secondary structure and include single-stranded regions or tertiary structure. Examples include a 17 bp stem loop within the 3′-UTR of TNF-α mRNA (72), a pseudoknot within the 5′-UTR of IFN-γ mRNA (4, 6), siRNAs containing short ssRNA overhangs (170, 171), several snoRNAs induced under metabolic stress (7), and certain bacterial RNAs (172, 173). Notably, short stem-loop RNAs with flanking ssRNA tails (ss-dsRNAs) have been identified as a potent PKR activation motif (77, 78). Truncations to the ssRNA regions result in decreased binding affinity and activation potency, and complete deletion of either the 5′- or 3′- flanking tail abolishes activation (119). Surprisingly, a duplex region as short as 10 nt with 15 nt 5′- and 3′- flanking tails binds two PKR monomers and functions as an activator. These observations imply that single-stranded regions can play a role in RNA-mediated activation of PKR.

PKR does not contain a canonical ssRNA binding domain yet there is precedent for ssRNA interactions with both the dsRBD and kinase domain. Complex formation between ssRNAs and dsRBDs from other proteins has been reported (174, 175) although in one case the dsRBD contained a novel C-terminal extension which coordinated a zinc ion as well as an unusually long β1-β2 loop (175). PKR mutations within the dsRBDs that block dsRNA binding do not prevent photocrosslinking to an RNA with minimal secondary structure, suggesting that ssRNA binding may be mediated by other regions of the enzyme (131). Other potential

interaction sites include a basic region adjacent to the N-terminus of the kinase domain (Fig. 4.1) that is important for kinase function (176) as well as a basic cleft lying on the kinase domain which mediates heparin activation (91). The cluster of basic residues N-terminal to the canonical kinase domain boundary was previously implicated in mediated PKR interactions with the ribosome (177). In addition to dsRNA, PKR can be activated by other polyanions (89) the most well characterized of which is heparin (90). The coarse structural similarity between ssRNA and heparin suggests that they could share a similar binding site and activation mechanism. Activation by heparin does not require the dsRBD (178) and the heparin binding site has been mapped to multiple nonoverlapping basic sites within the kinase domain (91, 179). A 5′-triphosphate (5′-ppp) is reported to be critical for PKR activation by RNAs with limited secondary structure, including the ss-dsRNA motif (7, 78, 131, 169, 172) (but see (119)). Duplex RNAs exhibit no triphosphate dependence so it is likely that ssRNA and the 5′-ppp bind to the same site (78).

Here, we seek to provide insight into the role of ssRNA and the 5′-ppp during enzymatic activation by identifying the regions on PKR that interact with free ssRNA and the contribution of the 5′-ppp on binding. We demonstrate that ssRNAs can bind to PKR at both the dsRBD and the basic region with micromolar affinities and can induce activation of the isolated kinase domain. Photocrosslinking measurements demonstrate that that the basic region interacts with RNA in the context of full length PKR. We propose that bivalent interactions with the double stranded RNA binding domain and the basic region underlie the ability of RNAs containing limited structure to activate PKR by enhancing binding affinity and thereby increasing the population of productive complexes containing two PKRs bound to a single RNA. Our data support a model where PKR activation by RNAs is regulated *in vivo* by interaction with both duplex and single-stranded regions.

Results

Based on the critical contribution of single-stranded regions to the binding and activation of PKR by ss-dsRNAs, we have investigated the interactions of PKR with isolated ssRNAs. Domain constructs, depicted in Figure 4.1, are used to localize the ssRNA binding site on the full length protein. The Results section begins with an analysis of the individual components used in the interaction studies. While somewhat tangential to the present study, a previously unappreciated role for the basic region during enzymatic activation is identified.

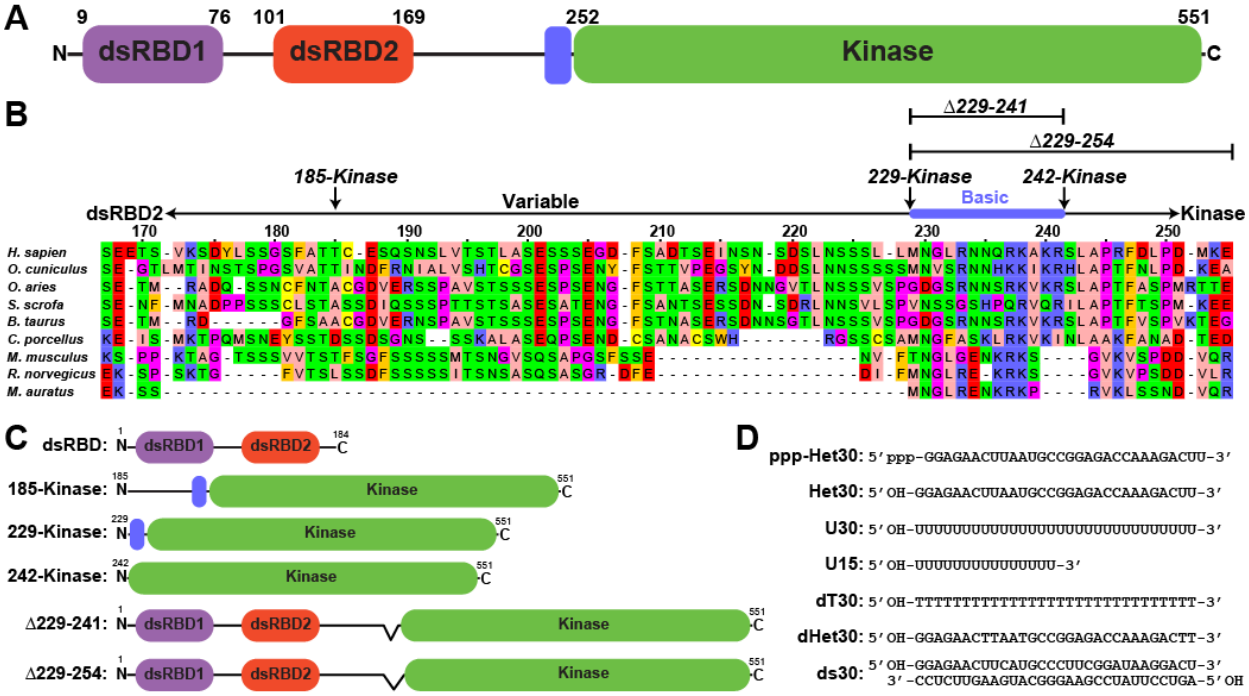

Figure 4.1 PKR domain schematic. (A) PKR domain organization. Canonical domain boundary positions are indicated above each domain. **(B)** Linker sequence alignment. The alignment was generated with ClustalW (180) and prepared in JalView (181). Residues are colored using the Zappo coloring scheme. **(C)** PKR domain constructs used in this study. **(D)** Nucleic acids used in this study.

4.2 Characterization of protein constructs

This study utilizes a number of protein constructs which have never been created in our laboratory. Characterization of both their hydrodynamic and catalytic properties were a necessary prerequisite to analysis of nucleic acid interactions. Notably, active kinase domain constructs were created by insertion of a TEV protease site into full length PKR which is cleaved

during the purification procedure to liberate the kinase domain. This circuitous methodology was required due to low yield of the isolated kinase domain when expressed in *E. coli*. Presumably the autocatalytic activities of the kinase domain are deleterious to expression since constructs containing the inactivating mutation K296R are not problematic (59). Sedimentation velocity analysis indicates each of the constructs is homogeneous and monomeric up to the highest concentration assayed in nucleic acid binding measurements (Fig. 4.2A, Table 4.1). The RNA-independent autophosphorylation activities were measured by the protein concentration dependence on ^{32}P incorporation and reveal a previously unappreciated contribution of the basic region to enzymatic activation. Samples were resolved by SDS-PAGE and imaged by Sypro Orange protein staining and phosphor screen exposure. The protein stain confirms that equivalent amounts of each construct are added to the appropriate lanes. Relative yields of ^{32}P incorporation indicate the basic region contributes to enzymatic activity. The 242-kinase domain construct lacking the basic region requires ~3-fold higher protein concentrations to achieve similar levels of phosphorylation activity as the 229-kinase construct (Fig. 4.2D). In full length constructs deletion of variable lengths of the basic region cause a similar reduction in activity (Fig. 4.2E). The 229-kinase construct requires ~3-fold more protein than full length PKR to achieve similar levels of ^{32}P incorporation (compare D and E). Note however that PKR contains 14 autophosphorylation sites and the full length enzyme contains more phosphorylation sites per mole than the kinase domain constructs (182). It is likely that this difference contributes to increased PKR autophosphorylation. In contrast, 229-kinase and 242-kinase contain the same number of phosphorylation sites so that the differences in the extent of phosphorylation can be attributed to a difference in intrinsic activity. The contribution of the basic region to activation is unclear although it is adjacent to the dimer interface and stabilization of the dimer would presumably lead to enhanced activity.

The full length protein constructs containing TEV cleavage sites provide a method to map PKR phosphorylation sites with very course resolution. The data indicate that the previous

assignment of 14 autophosphorylation sites (182) is underestimated. Full length constructs with a cleavage site located at position 185, 229, or 242 were phosphorylated, cleaved with TEV, and resolved by SDS-PAGE. The gel was stained with Sypro Orange and exposed to a phosphor screen. Both images are shown in Figure 4.2F. The N-terminal portion of cleaved PKR containing the dsRBD stained poorly with Sypro Orange and its position is indicated by a yellow arrow. Protein fragments resulting from cleavage at positions 185 and 229 can be resolved in both images yet the N- and C-terminal fragments which arise from 242 cleavage cannot be resolved in the phosphor image. The relative intensities of the cleavage fragments indicate that a majority of autophosphorylation sites are located in the linker region between residues 185 and 229 (Figure 4.2E). When cleaved at position 185 the C-terminal fragment containing the linker and kinase domain produces ~70% of the measured signal. Cleavage at position 229 inverses the relative intensities so that the N-terminal fragment which now consists of the linker and dsRBD contains ~90% of ^{32}P. Analysis of PKR phosphorylation sites by mass spectrometry identified 14 sites with 71% coverage of the total sequence (182). Yet the missing segment of the analysis corresponds primarily to residues 175-233 which is overrepresented in serine and threonine residues (Fig. 4.1). TEV cleavage of phosphorylated constructs provides only course resolution of the phosphorylation sites yet indicates the linker is the most heavily phosphorylated portion of PKR.

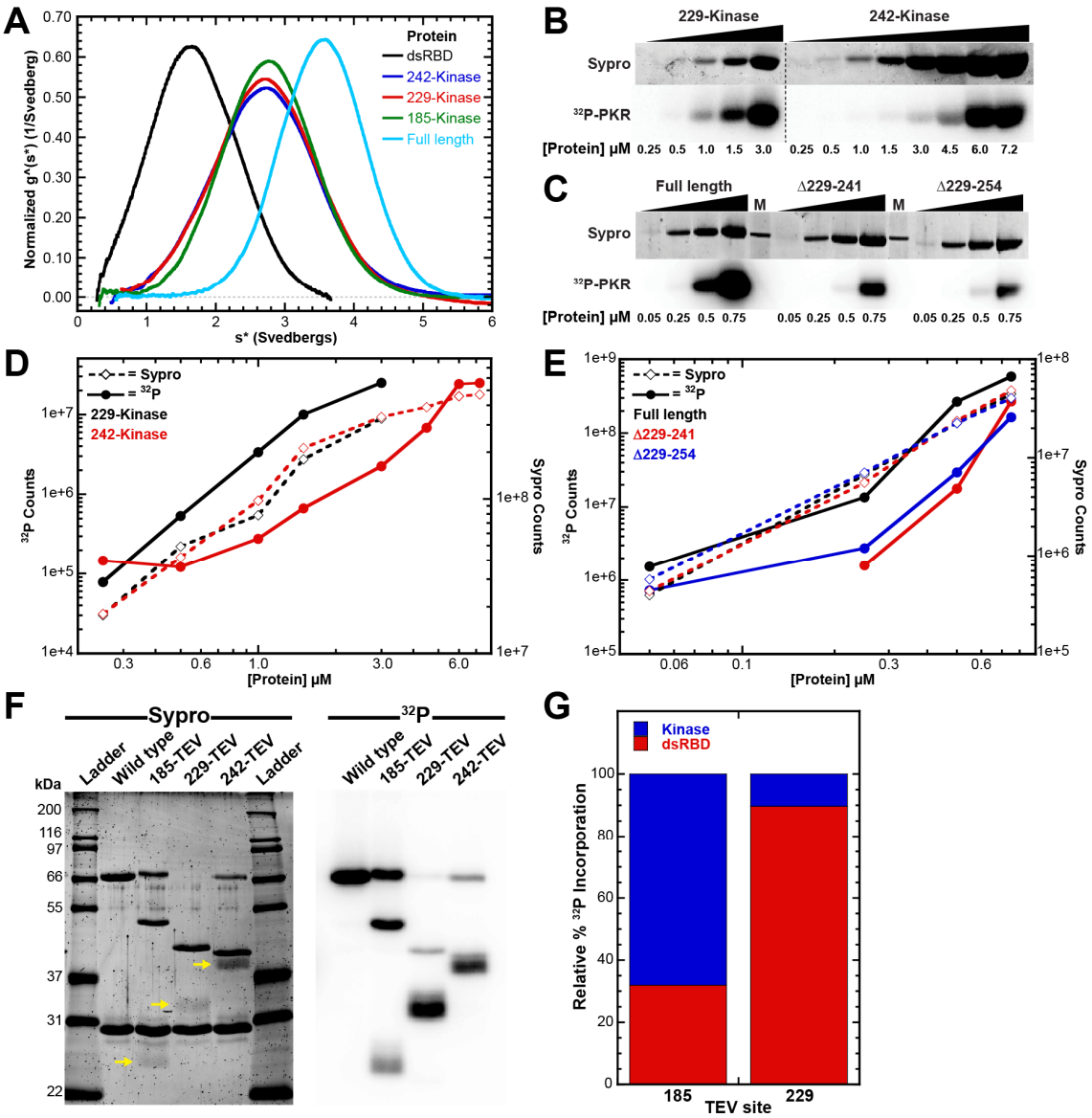

Figure 4.2 Characterization of protein constructs. (A) Sedimentation velocity analysis of PKR domain constructs. g^(s*) distributions are normalized by area. Protein concentrations: PKR, 16 μM; kinase domain constructs, 30 μM; dsRBD, 12 μM. Fits reported in Table 4.1. **(B-E)** RNA-independent autophosphorylation of PKR constructs. Samples were resolved by SDS-PAGE and stained with Sypro Orange to visualize protein and exposed to a phosphor screen to measure autophosphorylation. Kinase domain constructs are shown in **(B)**. Wild-type PKR and constructs containing internal deletions are shown in **(C)**. Protein stain is shown on the top and phosphorimage is shown on the bottom. The marker band, M, in **(C)** corresponds to BSA (66 kDa). **(D, E)** Quantitation of ^{32}P incorporation and Sypro stain as a function of protein concentration. Kinase domain constructs are shown in **(D)** and full length constructs are shown in **(E)**. The data are plotted on a log-log scale. ^{32}P data are shown as a solid line and the Sypro intensities are shown as a dashed line. **(F)** TEV cleavage of phosphorylated PKR. Two images of the same gel are shown with Sypro Orange protein stain on the left and phosphorimage on the right. Molecular weights of the Mark 12 protein ladder are indicated. TEV protease is present in each lane and runs at ~30 kDa. The position of the cleaved fragment containing the dsRBD is indicated by a yellow arrow. **(G)** Quantitation of 185 and 229 cleavage positions. Normalized to the sum of the intensity of the cleaved fragments.

Table 4.1 Sedimentation velocity analysis of PKR domain constructs.

Protein	Predicted Mass[a]	Fitted Mass	$S_{20,w}$ (Svedbergs)[b]	RMSD[c]
dsRBD	20,262	19,797	1.83	0.0061
242-kinase	35,811	32,830	2.89	0.0207
229-kinase	37,436	38,608	2.91	0.0168
185-kinase	41,907	41,626	2.92	0.0221
Full length[d]	62,095	60,774	3.71	0.0211

Parameters obtained by global nonlinear least square analysis of the sedimentation velocity data to a single ideal species model. Protein concentrations used in the global analysis: dsRBD, 12 µM; kinase domains, 5, 15, 30 µM; Full length PKR, 16 µM
[a] Masses predicted based on amino acid sequence.
[b] Sedimentation coefficient corrected to standard conditions (water at 20 °C).
[c] Root mean square deviation in fringes.
[d] Data from (91)

4.3 Characterization of ssRNAs

Experiments were initially performed with the heteropolymeric synthetic oligonucleotide used to create the 5′ side of the 15-15-15-ΔT construct (Chapter 3). The RNA was available in both 5′-ppp and 5′-OH forms and was used to probe the contribution of the triphosphate to binding energetics. At the temperature that binding affinities were measured (20 °C), the heteropolymeric sequence is predicted to fold into two short duplex regions 2 and 3 bp in length (133) (Fig. 4.3A). However, the Gibbs free energy of the structure (-4.01 kcal/mol) indicates the folded form is not stable. Thermal denaturation results in a slight absorbance increase that could be associated with weak secondary structure formation or unstacking but there is no transition which can be assigned to cooperative unfolding (Fig. 4.3B). Transient duplex formation could possibly be further stabilized by PKR binding. To confirm that interactions are specific for single stranded regions we repeated binding analysis with homopolymers of uridylate which should exhibit minimal structure due to lack of stacking interactions between uridines (162). Thermal denaturation of a 30 nt poly-uridylate (U30) verifies the absence of structure (Fig. 4.3B). The small absorbance decrease can be attributed to thermal expansion of the solution.

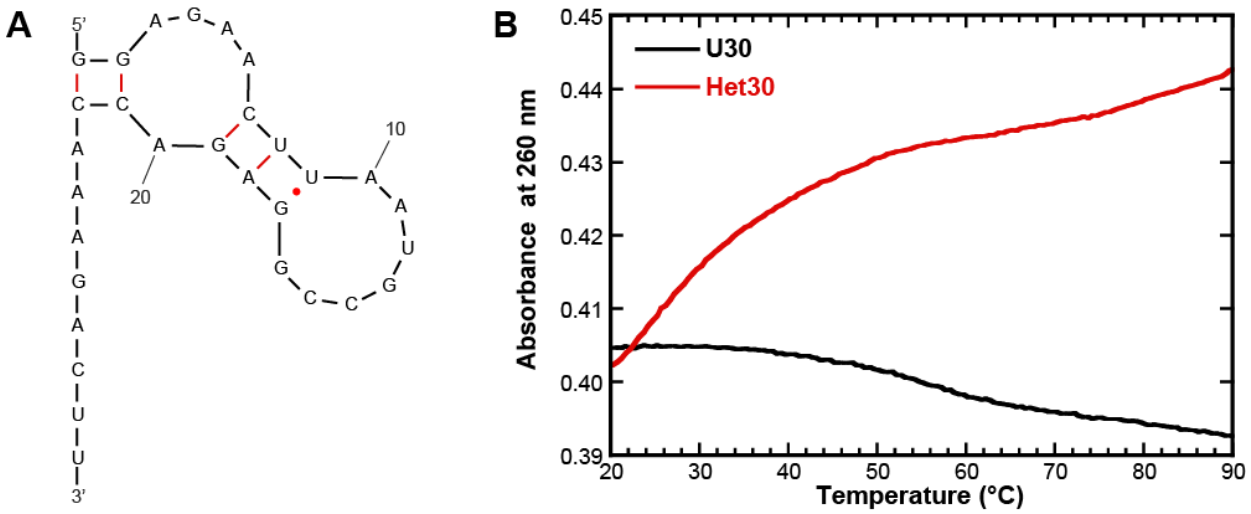

Figure 4.3 Thermal denaturation analysis of ssRNAs. (A) Predicted secondary structure of Het30. Secondary structure was computed at 20 °C using MFOLD (133). The free energy of folding is -4.01 kcal/mol. **(B)** Absorbance melting curves. Thermal denaturation was analyzed by monitoring the absorbance change at 260 nm at a heating rate of 0.5 °C/min. The measurements were conducted in 10 mM $NaPO_4$ (pH 7.0) with 0.1 mM EDTA.

4.4 Analysis of protein:nucleic acid interactions

Protein:nucleic acid interactions were monitored by sedimentation velocity analytical ultracentrifugation in order to detect transient, lower affinity interactions that may not be reliably measured in gel shift (183) or filter binding (184) assays. All of the interactions reported in this chapter are weak and rapidly reversible. Reequilibration of the complexes during sedimentation results in sedimentation profiles which represent reaction boundaries rather than discrete species. The shape of the reaction boundaries are a representation of both the sedimenting particles and association kinetics. In some cases, this behavior led to cross correlation between the dissociation constants and complex sedimentation coefficients during the fitting procedure making assignment of the sedimentation coefficients a critical determinant of affinity and complex stoichiometry. To interpret the data, we chose an approach that would emphasize comparison of binding affinities for different nucleic acids to different regions of PKR. Sedimentation coefficients of complexes were fixed so that their frictional coefficient (f/fo) was 1.5 which is typically what we observe for protein:RNA complexes (138). This was often in good agreement with fitted sedimentation coefficients for systems which exhibited stability during the

fit. The fitted dissociation constants for all the protein:nucleic acid mixtures reported in this Chapter are presented together in Table 4.2 so they may be readily compared. The sedimentation coefficients used in the fits can be found in Appendix 2.

Table 4.2 Sedimentation velocity analysis of PKR constructs binding to RNA.

Protein	Nucleic Acid	K_{d1} (μM)	K_{d2} (μM)	RMSD[a]
Full length	U30	3.51 (3.49, 3.52)	39.9 (39.4, 40.5)	0.00662
	U15	32.51 (30.27, 34.99)	-	0.00611
	ppp-Het30	0.825 (0.761, 0.894)	3.81 (3.49, 4.15)	0.00876
	Het30	1.07 (1.01, 1.12)	10.8 (10.1, 11.6)	0.00667
	dT30[d]	5.28 (4.13, 6.28)	>100	0.00875
	dHet30[d]	10.70 (10.15, 11.26)	>100	0.00911
dsRBD	U30	8.42 (7.98, 8.88)	52.3 (47.6, 57.7)	0.00514
	ppp-Het30[b]	5.36 (4.60, 6.31)	9.66 (8.03, 11.6)	0.00810
	Het30[b]	8.21 (7.38, 9.18)	19.4 (16.3, 23.0)	0.00701
	dT30[d]	40.68 (30.99, 55.50)	46.28 (29.95, 72.07)	0.00476
	dHet30[d]	55.25 (53.42, 59.69)	>100	0.00352
185-kinase	U30	31.9 (29.8, 34.2)	68.9 (51.8, 97.5)	0.00452
229-kinase	U30	1.91 (1.79, 2.05)	7.87 (7.16, 8.64)	0.00706
	ppp-Het30	ND[c]	ND[c]	
	Het30	ND[c]	ND[c]	
	ds30	3.80 (3.37, 4.33)	3.27 (2.82, 3.77)	0.00457
	dT30	2.59 (2.44, 2.76)	16.2 (14.5, 18.2)	0.00630
242-kinase	U30	96.1 (88.1, 106.8)	>100	0.00539
	ds30	24.3 (20.7, 29.1)	>100	0.00452

Parameters obtained by global nonlinear least square analysis of the sedimentation velocity data using a model of sequential binding of two proteins monomers. The values in parentheses represent the 95% joint confidence intervals obtained using the F-statistic.

[a] Root mean square deviation in absorbance units.

[b] Good fits required that the sedimentation coefficients for the protein-RNA complexes be allowed to float to their best-fit values.

[c] Not determined. More than two protein monomers bind to the RNA and the data could not be reliably fit to an association model. Plots of the normalized g^(s*) distributions for these experiments are in Figure 4.9.

[d] These fits were obtained from only one PKR:nucleic acid mixture.

4.5 PKR interaction with ssRNA

Figure 4.4A shows a titration of a model ssRNA, U30, with full length PKR depicted as an overlay of g^(s*) sedimentation coefficient distribution functions. Addition of PKR results in a decrease in the amplitude of the peak at 1.5 S associated with free U30 and formation of a peak at higher sedimentation coefficients due to complex formation. A similar titration against the heteropolymeric RNA, Het30, is shown in Figure 4.9A. The data are plotted as an overlay of g^(s*) distributions for Het30 in 5′-ppp and 5′-OH forms. This representation provides qualitative insight into the contribution of the triphosphate to ssRNA binding energetics which is discussed subsequently. Comparison of g^(s*) distributions for U30 and Het30 reveals significant differences in binding behavior. Complex formation with U30 results in a single broad peak which forms at ~4 S. Addition of 15 equivalents of PKR to Het30 results in a bilobal distribution with a feature at ~3.6 S corresponding to freely sedimenting PKR and a complex which appears at ~6 S. Hydrodynamic constraints restrict the maximal sedimentation coefficient for a 1:1 complex to values less than 6.57 S and it is likely the feature at ~6 S corresponds to a multivalent complex. The time derivative method employed to generate g^(s*) distributions is a model independent analysis and can be used to guide interpretation of the data. In order to define the interaction stoichiometry and obtain dissociation constants the sedimentation velocity profiles were subtracted in pairs to remove systematic noise and the difference curves were fit to alternative association models. A fit of the U30 binding data to a model where two PKR monomers sequentially assembly on a single RNA is shown in Figure 4.4B and the affinities are reported in Table 4.2. Similar to PKR interactions with duplex RNAs, the first PKR binds with the highest affinity, with a K_{d1} = 3.5 μM, and the second binds weaker, K_{d2} = 40 μM. PKR binds about three-fold more strongly to the heteropolymeric ssRNA of the same length with a similar decrease in affinity for the second PKR (Het30, Table 1). Increased affinity toward Het30 may reflect weak secondary structure formation by the heteropolymeric sequence (Fig. 4.3A) or some slight nucleotide identity preferences. PKR gains specificity for dsRNA over other nucleic

acid conformations via its dsRBD which recognizes the register of 2′-OH groups and phosphates presented by the A-form geometry of the RNA helix (23). The requirement for appropriate spatial distribution of 2′-OH is demonstrated by a lack of interaction with dsDNA, RNA/DNA hybrids, or chimeric RNAs partially substituted with either 2′-deoxy or 2′-OCH_3 (15, 65). We asked whether single-stranded nucleic acid interactions exhibit the same specificity by analyzing the DNA versions of U30 and Het30. PKR binds both dT30 and dHet30. Affinity is reduced ~1.5-fold for dT30 and ~10-fold for dHet30 relative to their respective RNA forms indicating the 2′-OH contributes to single-stranded nucleic acid interactions but is not required.

Binding to U30 activates PKR autophosphorylation weakly (Figure 4.4C) to a level about 1.5-fold above the background in the absence of RNA. As in the case of duplex RNAs (67), the bell-shape activation curve implies that ssRNAs induce PKR dimerization. The low extent of activation is likely a consequence of the relatively weak binding affinity. Higher ssRNA concentrations inhibit, consistent with dilution of PKR dimers by the excess nucleic acid.

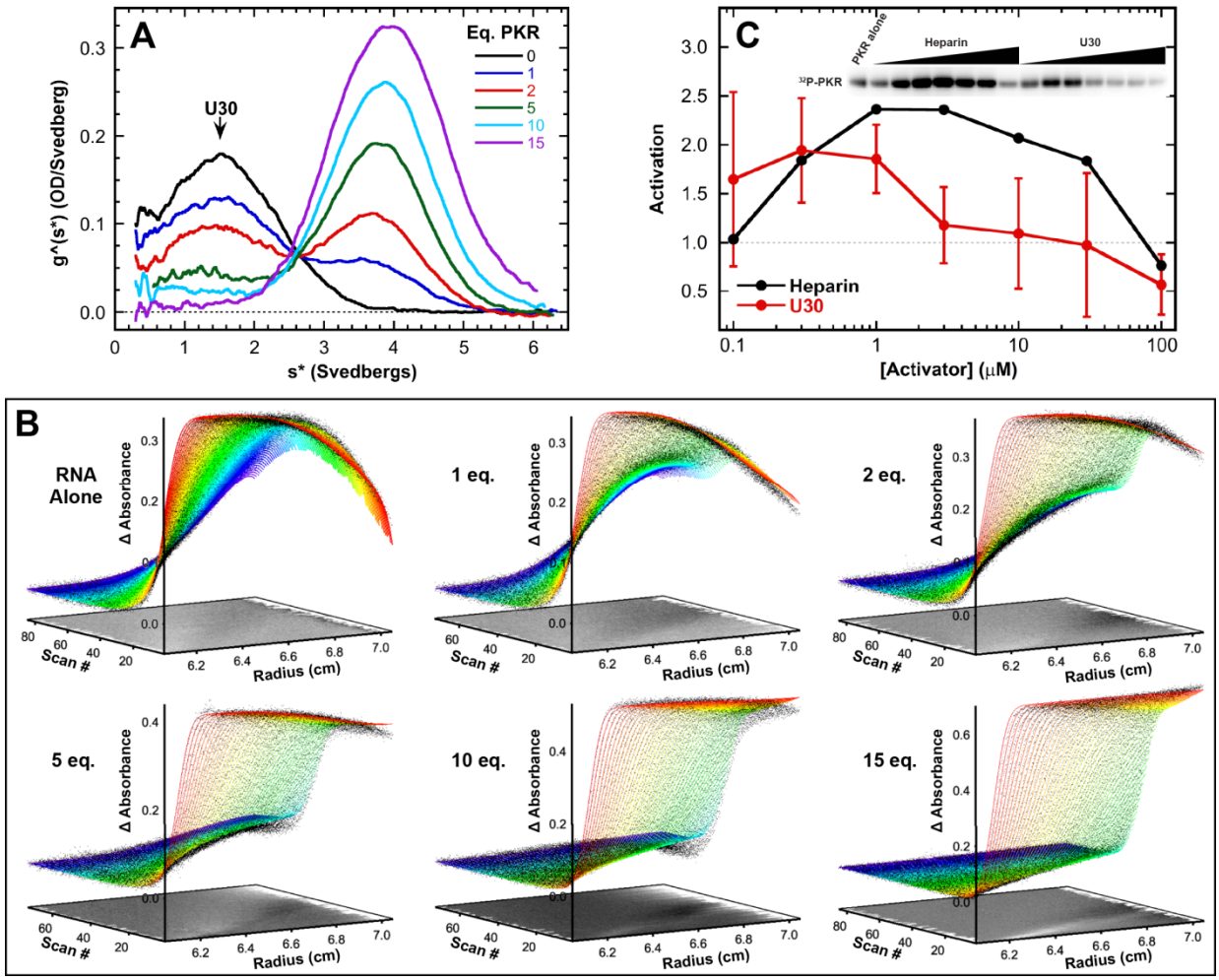

Figure 4.4 Interaction of PKR with U30. PKR binding to U30 ssRNA was assayed by sedimentation velocity analytical ultracentrifugation. Measurements were performed in AU75 buffer at 20 °C and 50,000 rpm using absorbance detection at 260 nm. **(A)** Titration of U30 with PKR represented as an overlay of g^(s*) sedimentation coefficient distribution functions. The samples contained 1 μM U30 (black) and 1 μM U30 plus 0.5 eq. (orange), 1 eq. (blue), 2 eq. (red), 5 eq. (green), 10 eq. (cyan), and 15 eq. PKR (purple). The decrease in the U30 peak and appearance of the peak at higher S are due to complex formation. **(B)** Global analysis of the time difference curves. Scans within each data set were subtracted in pairs to remove time-invariant background noise and fit to a sequential 2:1 binding model using SEDANAL (53). The data are indicated by points and the fit by solid lines. The residuals are plotted as a grayscale image in the x-y plane at z=0. The best-fit parameters are in Table 1. **(C)** Activation of PKR by U30. 500 nM PKR was incubated with variable concentrations of U30 in AU75 buffer with 5 mM $MgCl_2$ for 20 min at 32 °C. Samples were resolved by SDS-PAGE and ^{32}P-PKR was quantified with a phosphorimager. The data are normalized to activation of PKR in the absence of activator.

4.6 PKR interaction with U15

Initial binding measurements with poly-uridylate were performed with a 15 nucleotide RNA to match the single-stranded length of the model 15-15-15 RNA characterized in Chapter

3. Figure 4.5 shows two g^(s*) distributions produced from different time intervals from the experiment. Binding is difficult to assess by g^(s*) analysis because the RNA is small and does not form a discrete peak in the same scan range that a complex would appear (Fig. 4.5A). Analysis of scans collected later during the sedimentation process contain only the freely sedimenting RNA and provide some qualitative insight into binding (Fig. 4.5B). In both plots, addition of PKR causes a decrease in the feature corresponding to free RNA which is indicative of complex formation. Indeed, the data fit better to a model which incorporates formation of a 1:1 complex with a weak binding affinity of 33 μM (Table 4.2) than to a model of freely sedimenting species (not shown). Further characterization of single-stranded interactions in the context of a homopolymer was performed with U30 to avoid ambiguity associated with weak interactions.

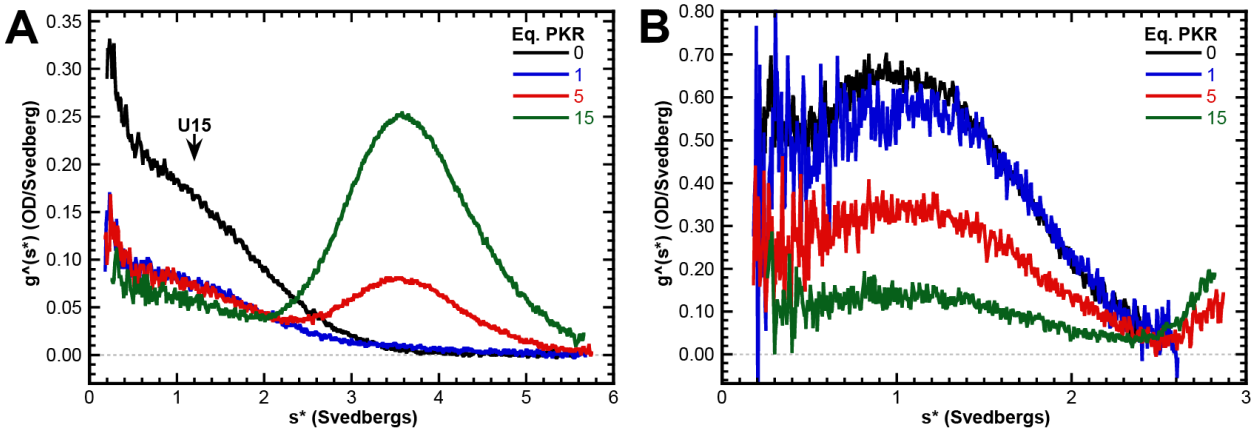

Figure 4.5 Interaction of PKR with U15. Two g^(s*) plots are shown which correspond to scans acquired during different time intervals of sedimentation. The plot in **(A)** was created by analysis of scans taken starting ~124 minutes after rotor acceleration and ending at ~260 minutes. **(B)** Corresponds to scans taken from ~303 to ~440 minutes. The data are plotted on different x-axis scales. Note that the sample of U15 alone contains 2-fold more RNA than the RNA:PKR mixtures. The samples contained 2 μM U15 (black) and 1 μM U15 plus 1 eq. (blue), 5 eq. (red), and 15 eq. PKR (green). The progressive decrease in the U15 peak with addition of PKR is indicative of binding.

4.7 Localization of ssRNA binding: the dsRBD

We characterized U30 and Het30 binding to individual PKR domain constructs to define the region(s) responsible for interaction with ssRNA and the contribution of the 5′-ppp. The dsRBD (residues 1-184) binds U30 (Fig. 4.6A) and Het30 with affinities slightly reduced relative

to the holoenzyme (Table 4.2), indicating that ssRNA can also bind to this canonical dsRNA binding site. Similar to full-length PKR, affinity is greater for the heteropolymer. The dsRBD also exhibits a preferences for the 2′-OH as affinities are slightly reduced toward DNA versions of the nucleic acids.

Binding of the dsRBD to dsRNA distorts the helix causing a slight opening of the major groove and changing the number of bp per helical turn (143). This conformation change can be exploited to monitor binding of the dsRBD to dsRNA by circular dichroism spectroscopy since ellipticity near 260 nm is related to the helix winding angle (110). CD spectroscopy has previously been employed to measure stoichiometries between PKR's dsRBD and RNA duplexes of varying lengths (57). Here, we have used the technique to ask whether the dsRBD induces any structural change detectable by spectroscopy during complex formation with U30. Figure 4.6 shows the CD spectra resulting from titration of the dsRBD against either U30 (B), a 25 bp dsRNA (C), or 0-15-0 (D). The spectra of each nucleic acid agrees with published reports with the duplex absorption maxima at ~260 nm (185) and U30 maxima at ~270 nm (186). As expected, addition of the dsRBD to dsRNA causes an increase of ellipticity at 260 nm. However, the spectra for U30 remains unchanged upon addition of the dsRBD. Although CD spectroscopy only probes some of the possible structural changes associated with binding, these measurements indicate that neither intra or intermolecular base stacking interactions, which typically accompany protein:ssRNA interactions (187), occur between PKR and U30.

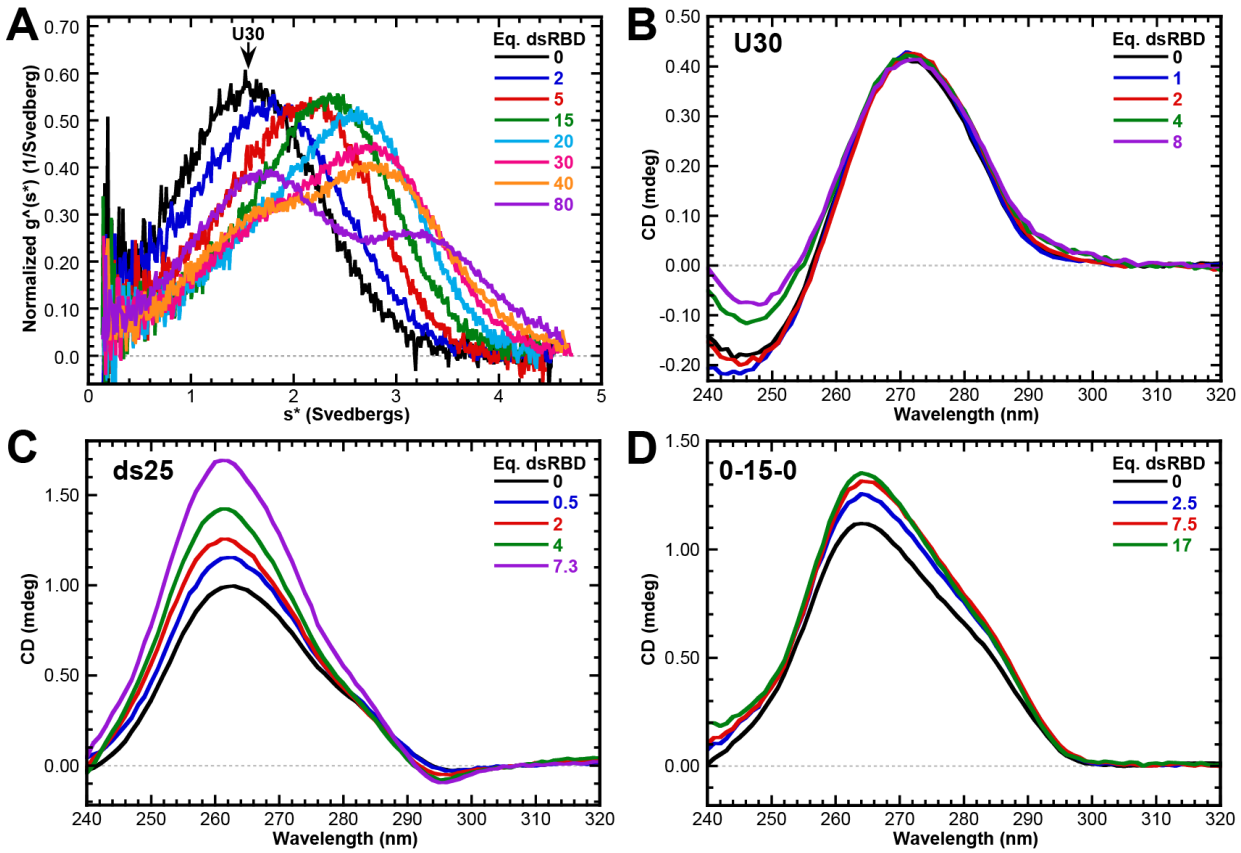

Figure 4.6 Interaction of dsRBD with U30. (A) g^(s*) distributions normalized by area depicting the interaction between U30 and the dsRBD. Samples were prepared as a titration of the dsRBD against 1 µM U30. The dsRBD has a sedimentation coefficient of 1.8 S and begins to appear as it is added in sufficient quantity for detection. **(B-D)** Spectroscopic analysis of dsRBD:RNA interaction by circular dichroism. Samples were prepared as a titration of the dsRBD against 5 µM of U30 **(B)**, ds25 **(C)**, or 0-15-0 **(D)**. Spectra are an average of 5 scans per sample with the contribution of buffer and protein subtract. Data were collected in AU75 buffer

4.8 Localization of ssRNA binding: the kinase domain

Single-stranded nucleic acids bind the dsRBD yet data indicate that this may not be the only binding site. The dsRBD binds single-stranded nucleic acids with affinities that are slightly reduced relative to the holoenzyme. Removal of the single stranded regions from 15-15-15 has a disproportionate effect on the relative binding affinities for full length PKR and the dsRBD (Chapter 3, Table 3.5). Affinities are compared for the first binding event (K_{d1}). Full length PKR binds 0-15-0 with about 35-fold reduced affinity relative to 15-15-15 but removal of the tails reduces dsRBD binding by only about two-fold, indicating that the tails predominantly interact

with regions outside of the dsRBD. In the absence of the tails the two constructs bind about equally well, confirming that binding to duplex regions is mediated primarily by the dsRBD.

In the human enzyme, the dsRBD is separated from the kinase domain by an ~80 residue unstructured linker. The length of the linker is highly variable among PKR orthologs (Fig. 4.1B). This length variability arises within the N-terminal acidic portion of the linker, but a cluster of basic residues within the C-terminal portion is conserved. This portion of the linker is implicated in kinase function (176) and ribosome association (177) and represents a potential RNA interaction site. Alternatively, the heparin binding site is located on the kinase domain (91, 179) and represents another possible ssRNA binding motif. We prepared PKR domain constructs (Fig. 4.1C) to probe the role of the linker, basic region, and isolated kinase domain in ssRNA binding.

Figure 3 shows titrations of U30 and ds30 RNAs with PKR kinase constructs that contain (229-kinase) or lack (242-kinase) the basic region. Addition of stoichiometric 229-kinase to U30 causes a decrease in the RNA peak and a shift of the distribution to higher sedimentation coefficients, indicating that this construct binds to ssRNA. The distribution at the highest protein concentration is bilobal due to the contribution of free 229-kinase at 2.8 S and a protein:RNA complex which sediments at 4.7 S. In contrast, addition of the 242-kinase construct lacking the basic region results in only a minimal decrease in the free RNA peak. The new feature which appears at 2.8 S is primarily due to absorbance of the free protein. The 229-kinase data fit well to the sequential 2:1 binding model with K_{d1} = 1.9 μM and K_{d2} = 7.9 μM. However, the 242-kinase binds very weakly (Table 4.2). Thus, the basic region mediates ssRNA binding to the C-terminal portion of PKR. Affinity is substantially reduced when the remainder of the linker is included in the 185-kinase construct presumably due to the electrostatic effect of the added negatively charged and polar amino acids (Table 4.2). These measurements may be more representative of the affinity of the basic region for ssRNAs in the context of full-length PKR.

Interestingly, 229-kinase also binds a 30 bp dsRNA and the dissociation constants are similar to those observed with U30. Thus, the basic region interaction is not specific for ssRNA. Indeed, 229-kinase also binds to a 30 nt ssDNA, dT30, albeit with reduced affinity indicating a small contribution from the 2′-OH (Table 1). The 242-kinase and ds30 have similar sedimentation coefficients (3.2 and 2.8 S, respectively) so that the two species are not resolved by time derivative analysis. Although the affinity is weak and the 2:1 complex is inadequately populated to obtain a reliable fit the data are best described by models which account for complex formation.

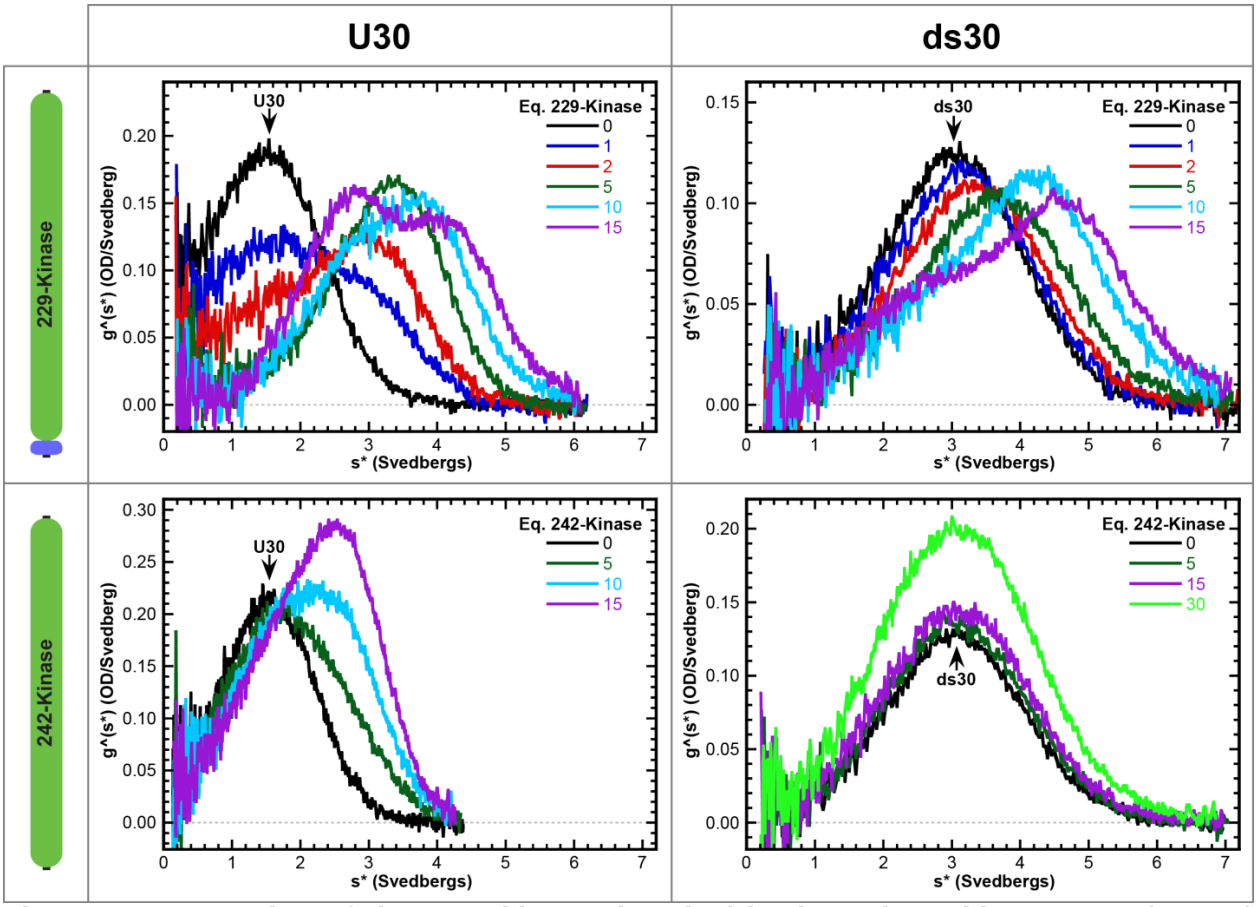

Figure 4.7 Interaction of the PKR kinase domain / basic region with RNA. Each panel shows a titration of RNA with protein depicted as a g^(s*) sedimentation coefficient distribution. Addition of 229-kinase to U30 or ds30 causes a shift in the distributions to the right, indicating complex formation. In contrast, 242-kinase induces only a slight decrease in the peak corresponding to free U30, indicating a very weak interaction. The peak at 2.8 S at higher protein concentrations is due to free 242-kinase. The sedimentation coefficients of 242-kinase and ds30 are similar and the increase in the peak amplitude is primarily due to free protein. The data were fit to a sequential 2:1 binding model to extract the binding parameters displayed in Table 1.

Given the strong binding of ssRNA to 229-kinase we asked whether it could mediate activation. For comparison, we also assayed activation of the 242-kinase construct. The 229-kinase is activated by U30 with a bell-shaped activation curve (Fig. 4A and C). As observed for the full-length enzyme, the maximum extent of activation by ssRNA is fairly weak, corresponding to about 3-fold over the basal level. Consistent with the lower ssRNA binding affinity, 242-kinase is not activated by U30.

The heparin binding site is located on the kinase domain and the 242-kinase construct binds heparin (91). Fig. 4C and D show that both 229- and 242-kinase are activated by heparin, with the maximum shifted to about 100-fold higher heparin concentration for the 242-kinase. Although ssRNA and heparin are both flexible polyanions, the basic region is not required for heparin binding. These data are consistent with a model where ssRNA and heparin bind to different sites on the kinase. Previously, we localized the heparin binding site to a pocket adjacent to helix αC (91) that is distinct from the basic region. The shift in the maximum to higher heparin concentration upon removal of the basic region in 242-kinase may be due to weaker, nonspecific contribution of the basic region. Consistent with this interpretation, heparin binds more weakly to 242-kinase than to the full length enzyme (91).

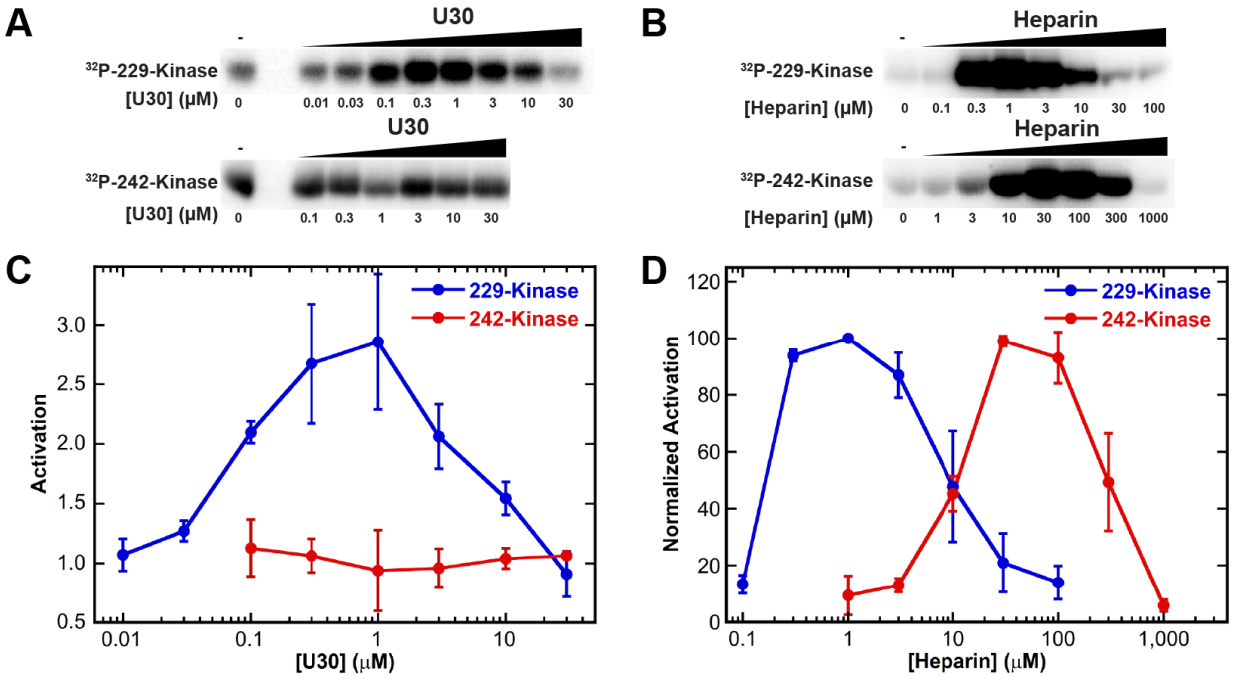

Figure 4.8 Activation of PKR kinase domain by ssRNA. Autophosphorylation reactions were carried out with a fixed concentration of protein and titrated with either U30 **(A, C)** or heparin **(B, D)**. The basal (RNA-independent) activities of 229- and 242-kinase are much lower than the full-length enzyme and are different from each other (Fig. 4.2). Thus, the protein concentrations were adjusted to give approximately equal extents of autophosphorylation in the absence of RNA: 1.5 μM 229-kinase and 5 μM 242-kinase. Phosphorimager scans of SDS-PAGE gels are shown in (A) and (B). The quantitation of ^{32}P-incorporation is shown in **(C)** and **(D)**. The error bars correspond to the standard deviation from three replicates. In **(C)**, the activation by U30 is plotted relative to samples containing no activator. In **(D)**, activation by heparin is normalized to the maximum signal because heparin is a potent activator and quantitation relative to the low signal in the absence of activator is not accurate. The ~100-fold increase in the heparin concentration required for maximal activation of the 242-kinase persists when the protein concentration is reduced to the same concentration used for 229-kinase (1.5 μM).

4.9 Analysis of the 5′-ppp recognition site

Previous reports indicate that a 5′-ppp contributes to PKR activation by certain RNAs with limited secondary structure (7, 78, 169, 172), yet the 5′-ppp recognition site remains undefined (131). We probed the effect of this moiety on binding affinity in the context of the heteropolymer, Het30, and analyzed the domain constructs to localize the 5′-ppp binding pocket. Figure 4.9 shows the measurements for each protein construct as an overlay of g^(s*) distributions for Het30 in 5′-ppp and 5′-OH forms. This representation is meant to provide qualitative insight into the relative contribution of the 5′-ppp to binding affinity toward different

regions of PKR. In each distribution, samples prepared with equal concentrations of Het30 and protein exhibit a shift to higher sedimentation coefficients when the RNA is capped with a 5′-ppp. Qualitatively, the relative shift between 5′-ppp and 5′-OH forms appears similar for each protein construct. Sedimentation coefficients for complexes calculated with frictional ratios of 1.5 are indicated along the x-axis of each g^(s*) distribution. This assumption of macromolecular shape indicates that the dsRBD (Figure 4.9B) and 229-kinase (Figure 4.9C) form complexes larger than RP_2 with Het30. However, fits to models which accommodate a sequential assembly process to form RP_4 produced unreasonable dissociation constants (not shown) indicating the fitting procedure applied to the other interactions reported in this Chapter could not be used here. Reasonable fits to the dsRBD data were obtained by allowing the sedimentation coefficients to float to their best fit values (s_{RP} = 3.55 S, s_{RP2} = 5.02 S, Appendix 2) in a 2:1 sequential binding model. However, after exhaustive attempts, a model to accurately describe the 229-kinase association could not be obtained.

In full length PKR, the presence of a 5′-ppp enhances affinity, reducing K_{d2} by a factor of about 3 relative to the 5′-OH RNA (Table 4.2). A similar magnitude effect of a 5′-ppp is observed for Het30 binding to the dsRBD. Dissociation constants describing 229-kinase affinity are unavailable yet the qualitative comparison provided by Figure 4.9 indicates the 5′-ppp confers a similar increase in affinity as full length PKR and the dsRBD. Thus, the enhancement of ssRNA binding to PKR by the 5′-ppp is not associated with a distinct binding site, as previous suggested (131) but is nonspecific and likely attributable to electrostatic interactions.

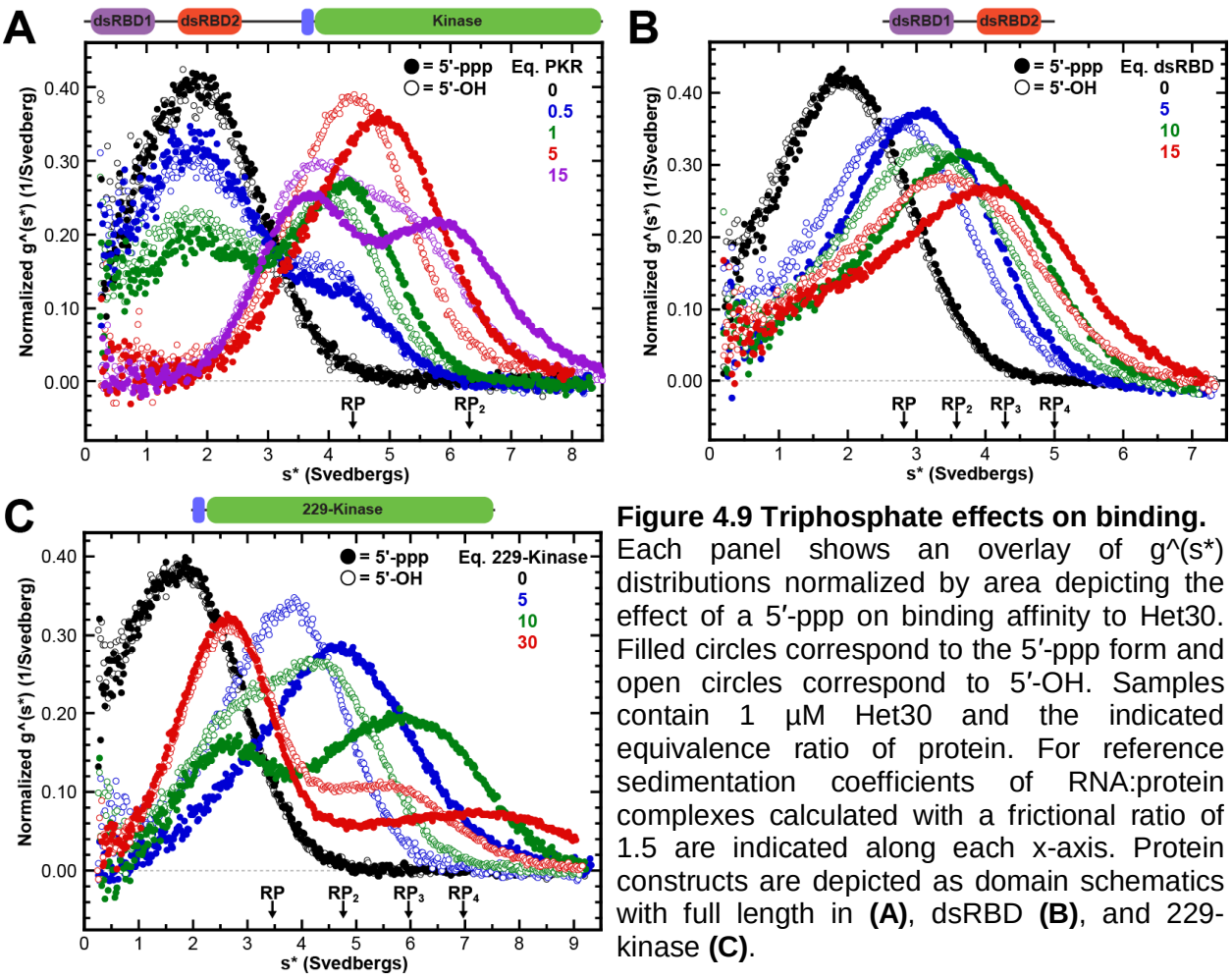

Figure 4.9 Triphosphate effects on binding. Each panel shows an overlay of g^(s*) distributions normalized by area depicting the effect of a 5′-ppp on binding affinity to Het30. Filled circles correspond to the 5′-ppp form and open circles correspond to 5′-OH. Samples contain 1 μM Het30 and the indicated equivalence ratio of protein. For reference sedimentation coefficients of RNA:protein complexes calculated with a frictional ratio of 1.5 are indicated along each x-axis. Protein constructs are depicted as domain schematics with full length in **(A)**, dsRBD **(B)**, and 229-kinase **(C)**.

4.10 Analysis of RNA interaction by crosslinking

Our results indicate that PKR contains two RNA binding loci. The dsRBD and the basic region interact with single-stranded nucleic acids with comparable affinities. Both regions also interact with duplex RNA yet the dsRBD binds with ~100-fold tighter affinity with an intrinsic dissociation constant in the low nanomolar range (104). Complex formation with an RNA containing both duplex and single-stranded regions is presumably driven by the high affinity interaction between the duplex and dsRBD. However, the binding affinities do not indicate where the single-stranded regions interact. The relative binding affinities of full length PKR versus the dsRBD construct for 15-15-15 and 0-15-15 suggests that single-stranded regions engage the protein outside the dsRBD (Section 4.7, Table 3.5). We have designed a

photocrosslinking assay to directly probe the RNA interaction sites on full length PKR. A schematic of the protocol is provided in Figure 4.10A. 15-15-15 and 0-15-0 were transcribed in the presence of 4-thiouridine triphosphate (s4U), resulting in incorporation of the modified nucleotide throughout the RNA, radiolabeled at the 5′-end, and crosslinked to PKR by exposure to 365 nm light. Reactions were performed with wild-type PKR, kinase and dsRBD domain constructs, and full length PKR constructs containing a TEV protease cleavage site located at position 185, 229, or 242. Following crosslinking, samples were cleaved by TEV protease, separated on SDS-PAGE, and visualized by both phosphorimaging and Sypro Orange protein staining. Crosslinking of the ss-dsRNAs to wild type PKR is dependent on s4U and the adduct is not cleaved by TEV protease (Fig. 4.10C lane 3, 4.10D lane 3). The mutants containing TEV sites are efficiently cleaved by the protease giving two predominant products. The relative intensities of the cleavage products provides coarse resolution for the RNA crosslinking site which is further resolved by comparing the fragment intensities produced from the different protease sites. Distributions of the cleavage pattern were generated by measuring pixel intensity vertically across the gel (Fig. 4.10E and F). The cleavage distributions are similar for both 15-15-15 and 0-15-0. When cleaved at positions 185 or 229 that are N-terminal to the basic region, most of the ^{32}P-labeled RNA is associated with the C-terminal kinase domain. Cleavage at position 242 shifts the distribution so most of the label is attached to the N-terminal fragment containing the dsRBD and basic region. This switch in band intensity indicates that the basic region interacts with the ss-dsRNA in the context of full length PKR. The residual crosslinking of the C-terminal fragment may reflect the weak interactions observed between the 242-kinase construct and RNA.

Crosslinking of the ss-dsRNA to the isolated domain constructs mirrors the trends observed with the full-length protein. The kinase domain requires the basic region for crosslinking to both 15-15-15 and 0-15-0. Crosslinking of ss-dsRNAs to the dsRBD is weak and requires addition of 10-fold molar excess of protein relative to the other samples to generate a

similar amount of adduct. An explanation for low crosslinking yields toward the dsRBD is not readily available however several hypothesis are presented. The low amount of product is not due to weak binding. The dsRBD binds duplex RNA strongly (intrinsic K_d ~100 nM (104)) whereas the basic region in the context of the 229-kinase binds a 30 bp duplex with only micromolar affinity (Table 4.2). One possibility is that variations in how the dsRBD and basic region engage the RNA lead to differences in accessibility for s4U. The mechanism for duplex RNA recognition by the dsRBD is well established (13). The dsRBD primarily binds the backbone and makes only a few interactions with the bases all of which occur along the shallow minor groove (23). The basic region loosely resembles arginine rich motifs (ARMs), short peptides enriched in basic residues which bind their cognate RNA by inserting into the deep major groove (188). The reactive sulfur projects into the major groove which may be more accessible to the binding mode of the basic region. However, these proposed differences in binding mechanism only provide rationale for lower crosslinking efficiency toward 0-15-0. The dsRBD also produces less crosslinked product with 15-15-15. Binding affinity may provide the explanation. The dsRBD preferably binds the duplex region which could preclude the ssRNA interaction. In this scenario, crosslinking with single-stranded regions occurs only after duplex binding sites have been saturated.

Sulfur and oxygen have similar electrochemical properties and uridine containing sulfur in the 4′ position rather than oxygen is expected to make canonical base-pairing interactions (189). We had hypothesized that s4U incorporated into duplex regions would only crosslink to its Watson-Crick base pair partner so that crosslinking would specifically map the single-stranded binding site. Yet, we observe crosslinking reactions between 0-15-0 and PKR. Note, however, that the uridine in position one of the tetraloop is more accessible to solvent than duplex residues. A sheared base pair interaction with the guanosine in position four orients the 4′ sulfur toward the solvent (190). This residue could be responsible for crosslinking with 0-15-0 but requires mutagenesis to prove. Crosslinking with 15-15-15 is much more efficient than 0-15-

0, indicating the single-stranded regions substantially contribute to the reaction. Because 15-15-15 and 0-15-0 were labeled to the same specific activity and the gels were exposed simultaneously, the crosslinking efficiency can be directly compared. 0-15-0 yields ~10-fold less complex than 15-15-15 indicating that the single stranded regions enhance crosslinking efficiency (compare y-axis values, Figure 4.10E and F). Thus, while a background of crosslinking toward the duplex region exists, it seems that a majority of the complex is formed from s4U within the single-stranded regions. This assay confirms that the basic region engages both single- and double-stranded regions in the context of the full length protein.

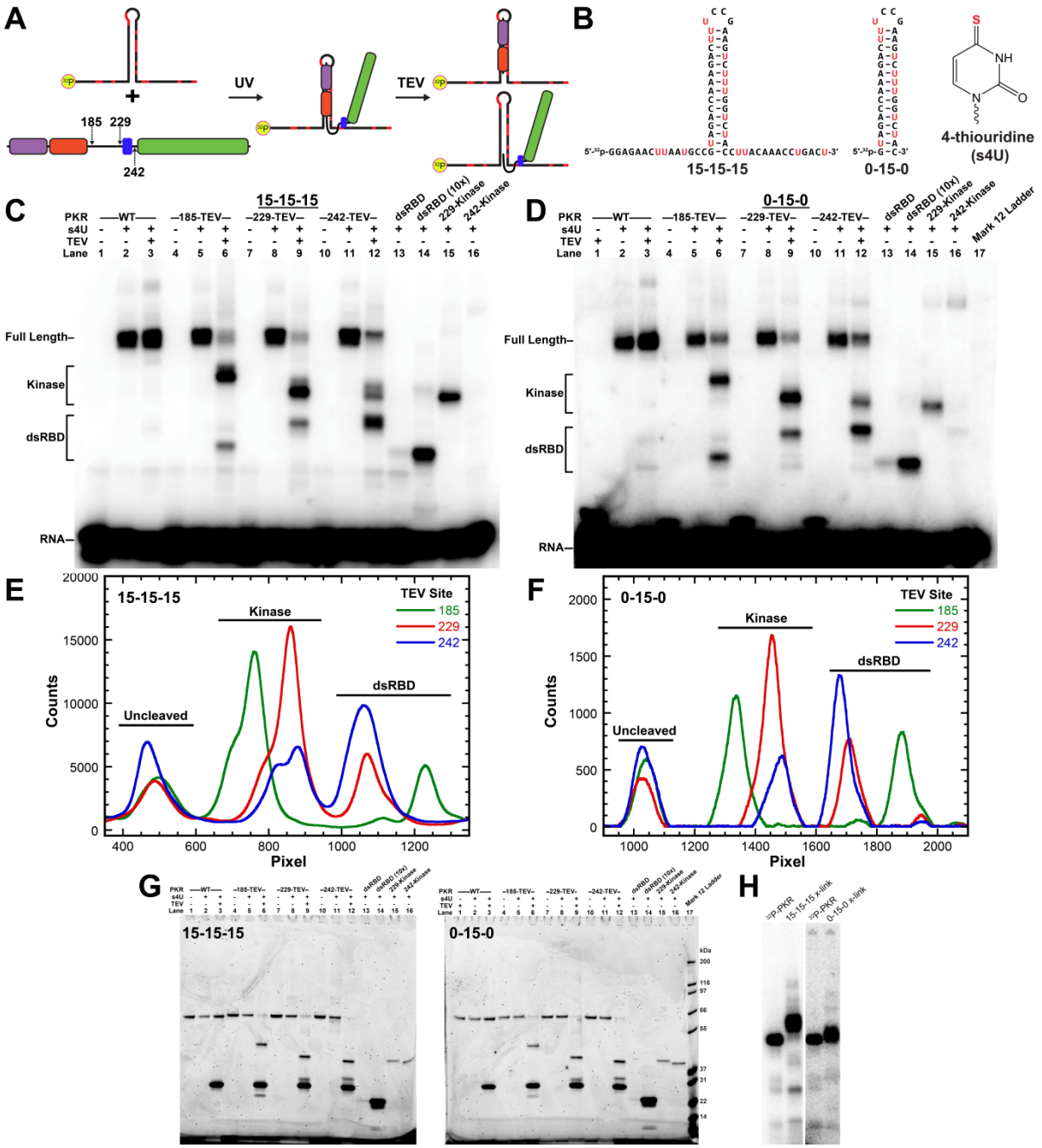

Figure 4.10 Crosslinking analysis of PKR binding to ss-dsRNA. **(A)** Protocol schematic. TEV cleavage positions are indicated. RNAs are labeled at the 5′-end with ^{32}P. **(B)** Secondary structure of the ss-dsRNAs and chemical structure of 4-thiouridine. Modified uridines are highlighted red in the secondary structure and the modified sulfur is highlighted in red in 4-thiouridine. **(C)** Phosphorimage of 15-15-15 crosslinking. **(D)** Phosphorimage of 0-15-0 crosslinking. Samples contained 0.5 µM RNA and 1 µM protein. One sample of dsRBD contained 10 µM protein (labeled 10x). Lanes labeled as (-) s4U contained unmodified ss-dsRNA. **(E)** Quantitation of 15-15-15:protein adducts following TEV cleavage. Distributions created from panel C lanes 7, 10, and 13. **(F)** Quantitation of 0-15-0:protein adducts. Created from lanes 6, 9, and 12 from panel D. **(G)** Sypro stained gels from panels C and D. **(H)** Visualization of crosslink mobility change. WT phosphorylated PKR is run next to the full-length crosslinked species.

4.11 ThioU incorporation abolishes activation

Certain nucleoside modifications are deleterious to RNA-stimulated activation of PKR. Incorporation of 4-thiouridine into a mostly single-stranded RNA reduces PKR activation and abolishes activation by a perfect duplex (82). Curiously, EMSA demonstrates that the affinity of the dsRBD for dsRNA is not significantly perturbed by nucleoside modifications suggesting that kinase domain dimerization may somehow be diminished. Based on these data, we assayed s4U-modified ppp-15-15-15 for activation and find PKR activation is eliminated (Fig. 4.11). The implications of this result with respect to the crosslinking data are unclear since the mechanism of PKR inhibition by nucleoside modification is unknown. Oxygen and sulfur have similar electrochemical properties yet replacement of the 4′-keto oxygen with sulfur may produce slight changes to base pair hydrogen bonding and base stacking interactions. Both stabilizing (191) and destabilizing (192) effects on duplex thermodynamics have been reported and the effects of s4U incorporation into single-stranded regions are unknown. The previously reported disproportionate effect of s4U incorporation on activation mediated by unstructured versus perfect duplex RNA (82) is partially in agreement with our crosslinking analysis. Activating RNAs which contain less than 30 bp of duplex presumably bind PKR with the duplex:dsRBD interaction with auxiliary interactions involving the single-stranded regions serving to elicit stimulatory effects.

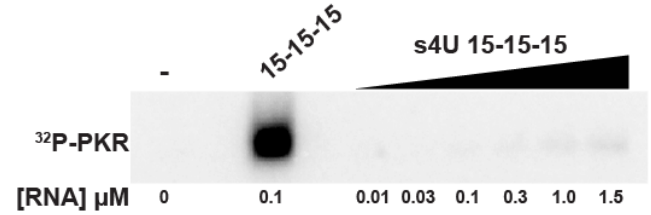

Figure 4.11 Activation by s4U 15-15-15. Titration of PKR by s4U modified 15-15-15. Unmodified 15-15-15 is included as a positive control.

4.12 Deletion of the basic region

PKR constructs with internal deletions to the basic region have been created to directly probe its contribution to activation by ss-dsRNAs. One construct contains a deletion of residues 229-241 (Δ229-241) to complement the kinase domain constructs and the other contains an extended deletion from residue 229 to the canonical kinase domain boundary at position 254 (Δ229-254) (Figure 4.1C). As shown previously, these deletions decrease PKR auto-phosphorylation activity as measured by the protein concentration dependence on ^{32}P incorporation (Figure 4.2E). Activation by U30, 15-15-15, and a 40 bp duplex were measured for each construct (Figure 4.12). In the U30 assay, protein concentrations were adjusted based on the auto-phosphorylation measurements (Figure 4.2E) so that the basal level of phosphorylation activity would be equal. WT PKR was assayed at 400 nM and the two internal deletion constructs were assayed at 800 nM. The level of background activity in the absence of activator is indicated as a dashed line on the graph in Figure 4.12A. Despite the attempt to normalize the basal activity the wild-type protein is ~3 times more active than the deletion constructs. Quantitation of the band intensities indicates that the samples containing U30 are more intense than the corresponding protein alone suggesting U30 activates the internal deletion constructs. These experiments must be repeated to confirm the results. Measuring weak activation is an experimentally challenging task. To reduce basal level activity, samples are prepared at low PKR concentrations. However, within this regime autophosphorylation activity increases considerably. From 250 to 500 nM PKR autophosphorylation activity, as measured by ^{32}P incorporation, increases ~10-fold (Figure 4.2E). Thus, small pipetting errors can produce substantial changes to the sample activity. For strong activators, such as dsRNA, these effects are negligible. However, for weak activators such as U30 this may produce false positive results.

Deletion of the basic region also reduces stimulation by duplex RNAs (Fig. 4.12B) and 15-15-15 (Fig. 4.12C). The reduction in activity indued by duplex RNAs may be related to the

apparent reduction in enzyme activity measured in the absence of activators (Fig. 4.2). Because of the effect on activation by duplex regions we cannot make definitive conclusions regarding the reduced stimulation by 15-15-15 (Fig. 4.12C).

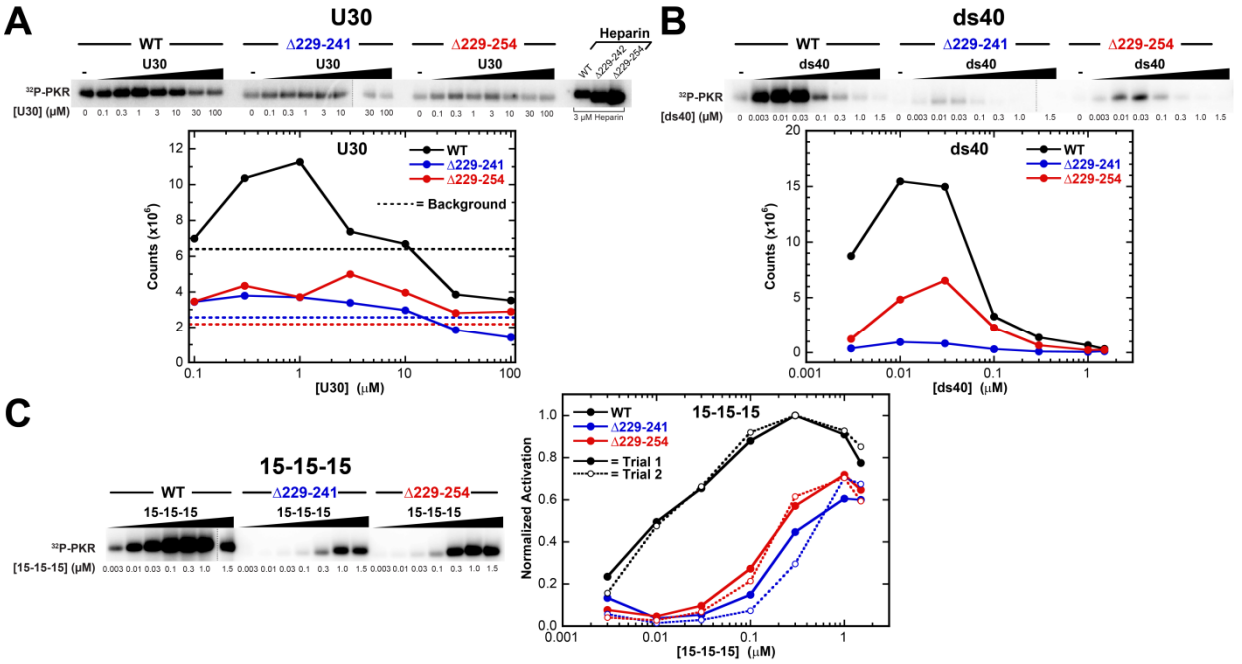

Figure 4.12 Internal deletions of basic region. (A) Activation by U30. Protein concentrations: 400 nM WT, 800 nM Δ229-241, and 800 nM Δ229-254. Heparin (average MW = 5,000 Da) at 3 μM was a positive control. The dashed line on the graph indicates the level of protein phosphorylation in the absence of activator. **(B)** Activation by 40 bp duplex (ds40). **(C)** Activation by 15-15-15. For each trial data are normalized to the activation of the WT protein by 0.3 μM 15-15-15. In both B and C protein concentration of each construct was 200 nM. All of the phosphorimages consist of two merged gels. The site of merger is indicated by a dashed line.

4.13 Discussion

This study provides the first direct evidence that PKR binds to and is activated by single-stranded RNAs and rationalizes previous reports (78, 119, 172) that single-stranded regions present in structured RNAs contribute to PKR interactions. The relatively weak binding of ssRNAs to PKR and the modest activation indicates that isolated single-stranded RNAs are unlikely to form a stable complex with PKR or to promote significant activation *in vivo*. However, these interactions provide a rationale for the contribution of single-stranded regions to PKR binding and activation in the context of structured RNAs. Invariably, potent RNA activators of

PKR possess some secondary and tertiary structure (193). Some of these RNAs lack the minimum 30 bp of duplex required to support PKR activation by simple dsRNAs but can form extended double stranded regions by coaxial stacking of shorter helices (4) or by dimerization of self-complementary stem loops (134, 135). Other RNA activators contain a single duplex as short as 10 - 15 bp (77, 119) or two hairpins of 5 and 4 bp (78), implying a substantial interaction of PKR with the unstructured regions. The crosslinking results demonstrate that both the dsRBD and the basic region-kinase domain interact with RNAs containing structured and unstructured regions. Despite the presence of these two RNA binding sites, sedimentation velocity data for full length PKR binding to ssRNAs and ss-dsRNAs only fit to a model where two monomers sequentially assemble onto a single RNA. The data do not fit well to models which incorporate binding of multiple RNA ligands to a single protein. The ~80 residue region separating the dsRBD and the basic region (Figure 4.1) is intrinsically disordered and PKR adopts multiple conformations in solution (38, 60). NMR data indicate that dsRBD2 can transiently interact with the kinase domain (54, 55) suggesting a model in which PKR exists in an equilibrium between open and closed states (59). In the closed conformation, the dsRBD and basic region/kinase domain would be in close proximity and capable of binding to a single RNA.

The protein:RNA binding behavior is similar to our observations for duplex interactions and follows the expected trend for interaction with a ligand possessing multiple identical binding sites (194). The reported binding affinities are macroscopic measurements influenced by the ensemble of binding conformations. Sequential binding of multiple proteins becomes weaker due to statistical effects (195). Previously, we have applied a binding model which accommodates the statistical effects associated with multiple proteins to an RNA duplex lattice to extract the intrinsic (microscopic) binding affinity for the dsRBD to dsRNA (104). It is unclear whether similar methodology could be applied to determine the intrinsic binding affinity for single-stranded RNA.

The weak dependence of binding affinity on a 5′-ppp is consistent with the absence of a distinct binding site for this moiety in PKR. A 5′-ppp also increases the affinity in the context of a ss-dsRNA containing a 15 bp stem and 15 nt 5′- and 3′-tails (15-15-15) but it is not required to detect kinase activation (Chapter 3, (119)). A 5′-ppp may play a role in PKR activation by RNAs with limited secondary structure (7, 78, 169, 172) by increasing binding affinity and thereby increasing the maximum population of active PKR dimers. However, a 5′-ppp is not absolutely required for activation of PKR, or the 229-kinase, by unstructured RNAs. Proteins with defined 5′-ppp recognition sites, supported by structural analysis, provide the basis for the expected contribution of the triphosphate to binding energetics. The canonical cytosolic sensor for RNAs bearing a 5′-ppp is RIG-I. This protein contains a helicase domain which binds duplex RNA and a regulatory domain which binds the 5′-ppp (196). For RIG-I, the presence of a 5′-ppp increases the binding affinity by >100-fold relative to the 5′-OH form, but the enhancement is only 2.4-fold for the isolated helicase domain (197). The latter is similar in magnitude to PKR and presumably represents the contribution of nonspecific electrostatic interactions. The antiviral proteins IFIT1 and IFIT5 recognize ssRNAs containing a 5′-ppp via a deep, positively-charged cavity (198, 199). IFIT5 binds a 5′-ppp ssRNA with nanomolar affinity yet does not form a detectable complex with ssRNA bearing a 5′-OH (200, 201). The origin of the 5′-ppp effect in RIG-I and IFITs is attributable to well-defined structural information correlated with a large energetic contribution to binding affinity. In the absence of similar information in the context of PKR it is difficult to infer the relevance of the 5′-ppp and the source of experimental differences regarding the dependence of the 5′-ppp for enzymatic activation (Chapter 3, (119)).

We propose that bivalent interactions underlie the ability of RNAs containing limited structure to activate PKR by enhancing binding affinity and thereby increasing the population of productive complexes containing two PKRs bound to a single RNA. In this model, a major contribution driving complex formation is the well-characterized interaction of duplex regions with the dsRBD (62, 104). This interaction is stabilized by adjoining unstructured regions

binding to the basic region. The bivalent interaction gives rise to strong (K_d ~ 100 nM) binding even for ss-dsRNAs containing a stem as short as 5 bp. In addition to enhancing binding, the bivalent interactions may serve to orient the kinase domains to increase the propensity for the formation of active dimers (65).

Chapter 5: Structural analysis of the kinase domain

Authors Note: I would like to acknowledge the contribution of Dr. Heidi Erlandsen to the findings reported in this chapter. Without her expertise in the analysis of X-ray diffraction data and unbridled excitement for science we would not have obtained the atomic resolution models presented here. I crystallized the PKR kinase domain and Heidi solved the structure. Also note that the structural models presented here are still being refined.

5.1 Introduction

The experiments described in Chapter 4 have identified the basic region N-terminal to the canonical kinase domain boundary as an RNA binding site which binds single-stranded and duplex nucleic acids with micromolar affinity. The data indicate that the basic region mediates very weak activation by ssRNA and may also play a role during activation by more complex RNAs. Additional stimulatory properties attributed to the basic region include activation by heparin and activation induced by self-association. The basic region is proximally located in primary sequence to the region which forms the back-to-back dimer interface (29). This dimeric configuration is critical for PKR activation (39) suggesting the basic region may produce its stimulatory effects by facilitating complex formation. SAXS analysis of full length PKR demonstrates that the region lying between the dsRBD and kinase domain is intrinsically disordered (60). This is corroborated by structure prediction of the linker region (residues 170-260) using the Phyre2 web server (202). However, the basic region is predicted to fold into a helix (Fig. 5.1). Models were also built from 30 residue blocks iterated over a 10 residue step size and support the prediction using the full length linker sequence. Note, however, that while the Phyre2 web server relies on homology modeling, homologs for the basic region were not identified. Instead, the models were built primarily by the PSIPRED algorithm (203) which is utilized for secondary structure prediction during the Phyre2 protocol. The length of the linker is variable among PKR orthologs yet the basic region remains relatively conserved supporting a role for PKR function (see Chapter 4, Fig 4.1). These observations have provided the impetus

for structural analysis of the kinase domain construct containing the basic region (229-kinase). Here, we describe the process of protein crystallization and the atomic models we have obtained by X-ray diffraction. Unfortunately, the basic region is unresolved in the current structures yet we observe a unique assembly of PKR molecules which has profound implications for the mechanism of PKR autophosphorylation.

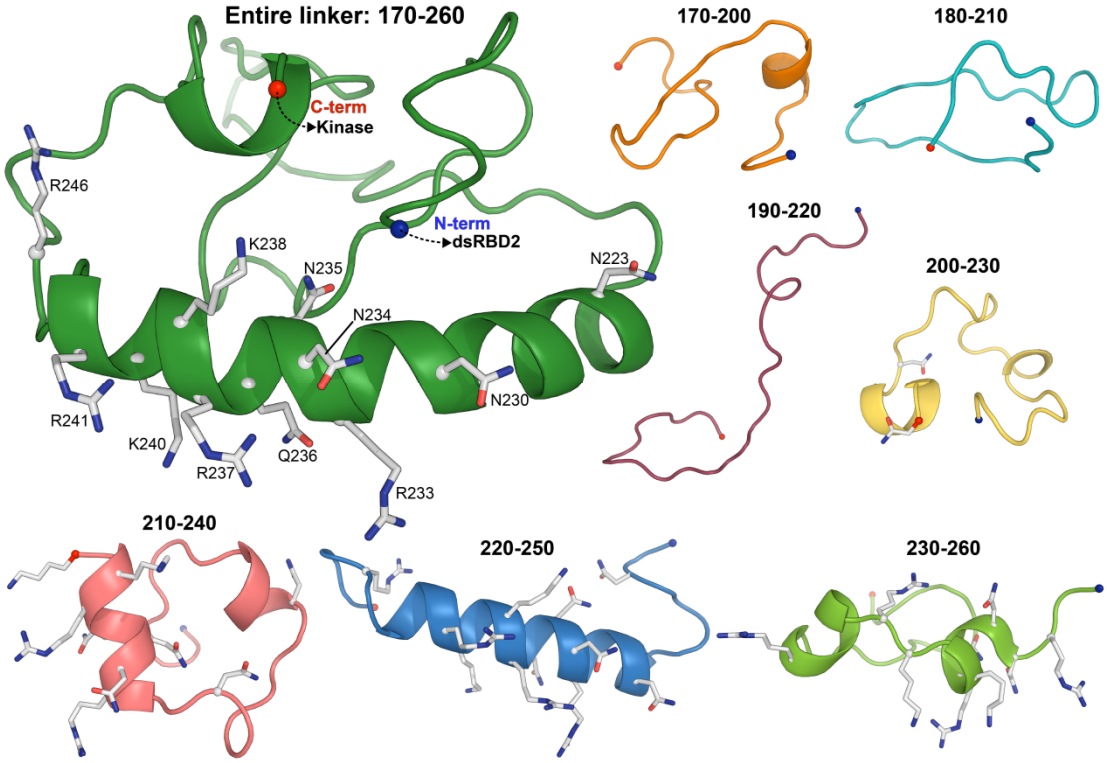

Figure 5.1 Structure prediction of the linker. Structures were predicted using the Phyre2 web server (202). The large model in green was generated using the entire linker sequence (residues 170-260). Residues which may contribute to RNA binding are indicated as sticks with Cα atoms are shown as spheres. The smaller models were generated from 30 residue segments of the linker as indicated. The same residues are shown as sticks but their identity is not annotated. N- and C-termini are indicated as blue and red spheres, respectively.

Structures of the kinase domain have previously been solved by X-ray diffraction yet the constructs used for structure determination lacked the basic region and contained mutations. In two structures, the kinase domain begins at residue 258 and is phosphorylated on threonine 446, representing the active form. The kinase domain was crystallized as a complex with eIF2α in the presence (PDB code: 2A19) and absence (PDB code: 2A1A) of AMP-PNP (29). Mutations

were introduced to facilitate protein expression and crystallization including H412N, C551A, and a 13 residue deletion of residues 338-350. Another study reports the structure of a kinase domain beginning at residue 254 containing the inactivating mutation K296R (PDB code: 3UIU) (30). In all the structures a similar back-to-back dimer is formed mediated by the N-terminal lobe of the kinase. A face-to-face dimer interface is also reported in the 3UIU structure along a 2-fold crystallographic symmetry axis so that alternating back-to-back and face-to-face interfaces contribute to the crystalline lattice.

In many eukaryotic kinases the transition from an inactive to active state is controlled by activation loop phosphorylation and conformational changes in the αC helix. A network of interactions stabilize catalytic residues in the active site, αC helix orientation, and a disordered to ordered transition of the activation loop. PKR belongs to the 'RD' kinase family which contain an invariant arginine neighboring a catalytic aspartate (44). The aspartate plays a critical role in catalysis by accepting a proton from the substrate hydroxyl (31). In the active state, the phosphorylated moiety in the activation loop interacts with the conserved 'RD' arginine to position the aspartate for phosphoryl transfer. The interaction also stabilizes the inherently disordered activation loop, making the active site accessible to substrate. In PKR, the conformational states of the activation loop and αC helix are linked by additional anchoring interactions between the phosphorylated moiety and basic residues emanating from the helix. Correct positioning of the αC helix is critical for catalysis as exemplified by the myriad of conformational arrangements associated with the kinase on/off switching mechanism. In the active orientation, a conserved salt bridge is formed between an αC helix glutamate (E308 in PKR) and lysine (K296 in PKR) residue from the N-lobe which stabilizes ATP phosphates for catalysis. Additionally, a hydrophobic spine is completed in the active orientation which improves catalytic efficiency by reducing conformational dynamics (204). Kinases in an inactive conformation are typically characterized by rotations or translations of the αC helix which disrupt these key interactions. In PKR, the back-to-back interface is partially formed by the αC helix

providing a mechanism coupling dimerization to the catalytic state of the enzyme. It is likely that dimerization controls αC helix orientation rather than activation loop phosphorylation since the helix adopts a similar conformation in both phosphorylated (2A19, 2A1A) and unphosphorylated (3UIU) structures. A structure of the monomeric PKR kinase domain is unavailable but the structural rearrangements which occur upon dimerization may be inferred from structural homologs. Ire1 (205) and the Pkn kinase family (206-209) form a similar back-to-back dimer. In their monomeric structures, distortions to the αC helix break the key interactions addressed above (40). In PKR, the functional importance of the interface is demonstrated by mutagenesis of key interfacial residues which results in both decreased autophosphorylation and phosphorylation of eIF2α (39). Out of the 374 identified 'RD' kinases, 167 require activation loop phosphorylation for full catalytic activity and 94, including PKR, have no upstream kinase (33). These kinases must phosphorylate their own activation loop either through a *cis* or *trans* mechanism. The back-to-back arrangement adopted by the PKR kinase domains disqualifies *trans*-autophosphorylation within the dimer. Instead, dimerization may promote *cis*-phosphorylation or dimers may phosphorylate other dimers or monomers in *trans*. Experiments designed to resolve between these scenarios have relied primarily analyzing whether PKR molecules containing inactivating mutations are phosphorylated by wild-type PKR. Data supporting both *cis* (34) and *trans* (35-38) mechanisms have been reported.

Here, we report a structural model for a putative PKR kinase domain *trans*-autophosphorylation complex solved by X-ray diffraction. We have obtained two structures of the kinase domain from crystals grown under different conditions and into different space groups. Back-to-back and front-to-front interfaces similar to those which have previously been reported (29, 30) are present in the crystals. However, a unique front-to-front configuration is also observed involving activation segments which are exchanged between reciprocal protomers. Functional analyses to investigate the complex have not yet been performed although the significance of the structure is interpreted from structural homologs. Similar kinase

domain complexes have been reported and are interpreted to represent a mechanism for *trans* activation segment phosphorylation (33). Our structure shares many of the conserved features of activation segment exchange. Additionally, proteins which form functionally important back-to-back dimer arrangements analogous to PKR have subsequently been shown to form additional interfaces suggestive of a similar requirement for *trans*-autophosphorylation. The back-to-back Ire1 interface mediates assembly of a larger oligomer which includes an interface in which an activation loops interdigitate into neighboring protomers (210). A face-to-face Ire1 structure has also been reported (211). PknB has been crystallized in both back-to-back (206, 208) and face-to-face (212) orientations and a structural model for activation is proposed which resembles the complex observed in our asymmetric unit (212). Thus, although the functional analyses which typically accompany a crystallographic report are not included, evidence from the literature provides precedent for the structures reported here.

Results and Discussion

5.2 Crystallization and optimization

Both 229-kinase and 242-kinase were initially screened using reagents supplied by Hampton Research. In total, 192 reagents have been tested (Crystal Screen; HR2-110, Index; HR2-144, and PEG/Ion Screen; HR2-126) yielding three excellent hits and two promising leads. Proteins were concentrated, passed through a 0.02 µm syringe filter, and diluted to 10 mg/ml (~285 µM) in a solution consisting of 20 mM HEPES (pH 7.5), 75 mM NaCl, 0.1 mM EDTA, and 0.1 mM TCEP. Samples were mixed in a 1:1 ratio (either 1 µL + 1 µL or 2 µL + 2 µL) with crystallization solution and screened by hanging drop vapor diffusion at 20 °C. The first solution to yield crystals was composed of 0.1 M HEPES (pH 7.5), 2 % v/v polyethylene glycol 400 (PEG-400), and 2.0 M ammonium sulfate. Proteins crystallized into a shower of microcrystals with a plate like appearance over ~ 5 days (Fig. 5.2A). A grid search strategy was employed to optimize the solution pH and reagent concentrations to produce larger crystals suitable for analysis by X-ray diffraction. Changes to pH and ammonium sulfate concentration did not yield

better results than the initial condition yet increasing PEG-400 concentration to 6-7 % v/v produced much larger crystals. Like the initial hit, crystals were numerous throughout the drop indicating that crystal nucleation was occurring too frequently effectively reducing free protein concentration for further growth. Therefore additional elements of optimization included approaches designed to reduce the rate of crystal nucleation by decreasing the speed of equilibration between crystal drop and well solution. These included growth at 4 °C and crystallization by sitting drop vapor diffusion yet neither method improved crystal size. Increasing protein concentration was also ineffective since only the number of protein crystals within the drop was amplified rather than their size. Changes to the mixing ratio between protein and crystallization solution proved most effective to obtaining less crystals of larger size within each drop. This approach has the advantage of sampling both protein concentration and the equilibration path along the crystallographic phase transition in a single experiment. The optimal crystallization condition was identified as a drop prepared by mixing of 3 µL 10 mg/ml protein with 1 µL crystallization solution consisting of 0.1 M HEPES (pH 7.5), 6-7 % v/v PEG-400, and 2.0 M ammonium sulfate and equilibrated over ~5 days by hanging drop or sitting drop vapor diffusion at 20 °C. Crystal production has focused on the 229-kinase although 242-kinase behaves similarly in trials. We have also obtained crystals of the kinase in complex with the ATP analog adenosine-5′-(β,γ-imido)triphosphate (AMP-PNP) and magnesium using the conditions described above. 10 mM of each ligand was added to 10 mg/ml protein solution and allowed to equilibrate for 15 minutes prior to crystallization. A change in crystal morphology provided evidence that ligands were incorporated (Fig. 5.2A) which was subsequently confirmed during structure determination. Curiously, the terminal phosphate from AMP-PNP is hydrolyzed and bound proximal to the active site.

Screening has identified additional conditions including a similar condition to that listed above consisting of 0.05-0.15 M Bis-Tris (pH 5.5) and 2.0 M ammonium sulfate which yielded a crystal used to solve one of the structures reported here. A very promising initial hit has also

been obtained from a solution of 0.1 M HEPES (pH 7.0), 5% v/v Tacsimate, and 10% w/v polyethylene glycol monomethyl ether 5,000 (Fig. 5.2). Optimization trials similar to those reported above are currently underway.

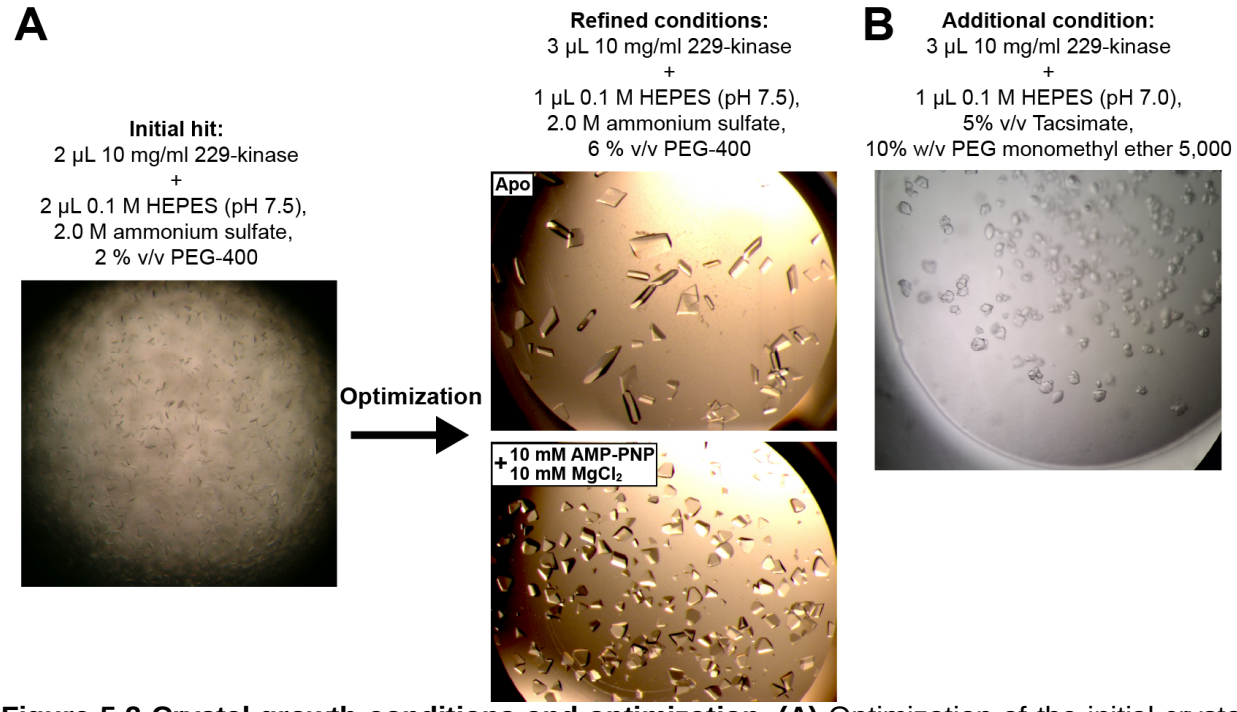

Figure 5.2 Crystal growth conditions and optimization. (A) Optimization of the initial crystal hit. The size of protein crystals grown in the original condition was increased by changing the mixing ratio between protein and precipitant solutions and by increasing the concentration of PEG-400. Crystals grown in the presence of AMP-PNP and $MgCl_2$ have a more cubic appearance than the apo form. Structure two, reported below, was solved from crystals shown in the bottom drop. **(B)** An additional condition has been identified which yields oval shaped crystals but has not yet been optimized.

5.3 Data Collection and analysis

X-ray diffraction data were initially collected on our home source but the crystals diffracted poorly with the highest resolution shell typically occurring at ~6 Å. High quality data were obtained from the more intense X-rays generated by synchrotron radiation sources. To date, we have collected high quality diffraction data from several crystals grown under different conditions and have solved 2 structures. All structures are obtained from crystals of 229-kinase. Data were processed and scaled using iMosflm in the CCP4i2 suite (213). Phases were solved by molecular replacement in CCP4i2 with the PHASER module (214) using the phosphorylated,

AMP-PNP-bound PKR kinase domain as the search model (molecule B, 2A19). Rebuilding was performed in COOT and refinement using Refmac5 in CCP4i2 (215). The first structure was obtained from a crystal grown in a 1:3 molar ratio of heparin (dp8) to protein, 0.1 M Bis-Tris pH 5.5, and 2.0 M AmSO4. The crystal was cryoprotected using a 30 s - 2 min soak in high concentration of Na-malonate (between 1.5 - 1.7 M final concentration) and frozen in liquid nitrogen for transportation to the synchrotron. The crystal diffracted to approximately 3.1 Å and a complete dataset was collected at the NSLS-II FMX beam line at NSLS-II. The structure was solved using one monomer of the 2A19 PKR structure, with one molecule in the asymmetric unit and the following unit cell parameters: a = 92.69 Å, b = 92.69 Å, c = 123.33 Å, α, β = 90°, γ = 120°, and space group P 6_1 2 2. The crystal used to solve the second structure was grown in 0.1 M HEPES (pH 7.5), 2.0 M ammonium sulfate, and 6 % PEG-400 and the protein was complexed with AMP-PNP and Mg^{2+}. Crystals were cryoprotected in 2 M LiSO4 for several weeks, frozen in liquid nitrogen for transportation to the synchrotron, and a dataset was collected at SSRL beamline 14-1. The crystals diffracted to 2.6 Å. Three protein chains comprise the asymmetric unit and the unit cell parameters are: a = 106.48 Å, b = 159.60 Å, c = 172.99 Å, α, β, γ = 90°, and space group C 2 2 2_1. Figures were made in PyMOL (The PyMOL Molecular Graphics System, Schrödinger, LLC).

Table 5.1 Crystallographic data collection and refinement statistics.

	Structure 1	Structure 2
Data Collection		
Beam line	FMX, NSLS-II	14-1, SSRL
Wavelength (Å)	0.9790	0.9795
Space group	P 6_1 2 2	C 2 2 2_1
Unit cell dimensions		
a, b, c (Å)	92.69 92.69 123.33	106.48, 159.60, 172.99
α, β, γ (°)	90, 90, 120	90, 90, 90
Resolution (Å)	123.33-3.10(3.10-3.181)	172.99-2.6 (2.6-2.667)
Molecules/ASU	1	3
R_{meas}	0.268 (0.070)	0.098 (0.034)
I/σI	9.1 (3.2)	9.4 (0.8)
Completeness (%)	100 (100)	97.1 (98.1)
Refinement		
R_{work}/R_{free} (%)	25.9 / 34.7 (38.3 / 38.6)	20.9 / 27.3 (39.9/40.5)
Reflections Unique / Free	5801 / 296 (410 / 16)	42,089 / 2245 (3,154 / 157)
r.m.s deviations from ideal		
Bonds (Å)	0.0108	0.013
Angles (°)	1.560	1.774
B-factor analysis		
Molecule A ($Å^2$)	89.8	78.8
Molecule B ($Å^2$)	-	86.8
Molecule C ($Å^2$)	-	92.6
Model		
Nonhydrogen atoms	2046	6480
Water molecules	-	52
Metals	-	1 Mg^{2+}
Ligands	-	ADP, 1 PO_4, 7 SO_4

Values corresponding to the highest-resolution shell are indicated in parentheses

5.4 Comparison of structures one and two

Both structures of the kinase domain exhibit similar interactions in the crystalline lattice but contain different numbers of protein chains in the asymmetric unit. Figure 5.3 shows the arrangement of molecules in the lattice with the asymmetric units (ASU) labeled. In the first structure, one molecule occupies the asymmetric unit and a filamentous assembly is formed by alternating face-to-face and back-to-back interfaces so that two unique interfaces are formed between each protomer. Each front-to-front interface is stabilized by activation segment

exchange interactions. Structure two has a similar assembly except that three protein chains comprise the asymmetric unit. Each protomer is in complex with AMP-phosphoramidate (AMP-PN), a magnesium ion, and what is presumed to be the hydrolyzed phosphate. The protein chains within the asymmetric unit are assigned a label A, B, and C. Unlike structure one, activation loops do not swap in one face-to-face interface (C:C). Consequently, there are three unique interfaces in the filament: front-to-front with activation segment exchange (IF1, A:B), back-to-back (IF2, B:C and A:A), and front-to-front without exchange (IF3, C:C). Analysis of the interfaces was guided by PDBePISA (216) and calculated parameters are reported in Table 5.3. Note that the back-to-back interface formed by interactions between molecules B and C is nearly identical to the A:A interface which bridges asymmetric units. Additional interactions occur within the crystal between neighboring C-lobes but have a low buried surface area and are presumably an artifact of crystal packing. Structure 2 is the subject of further discussion since the dataset used to generate the structure is generally of better quality than structure 1. In particular, the higher resolution allows for more accurate modeling of the activation segment exchange region. It should be noted, however, that crystals used to generate each dataset were grown in slightly different solutions and structure one was grown in the absence of ligands. The molecules are arranged by different space groups (Table 5.1) each belonging to a different crystal family. Thus, activation segment exchange is likely not an artifact of crystal growth conditions or crystal packing arrangements and is not induced by AMP-PNP or magnesium.

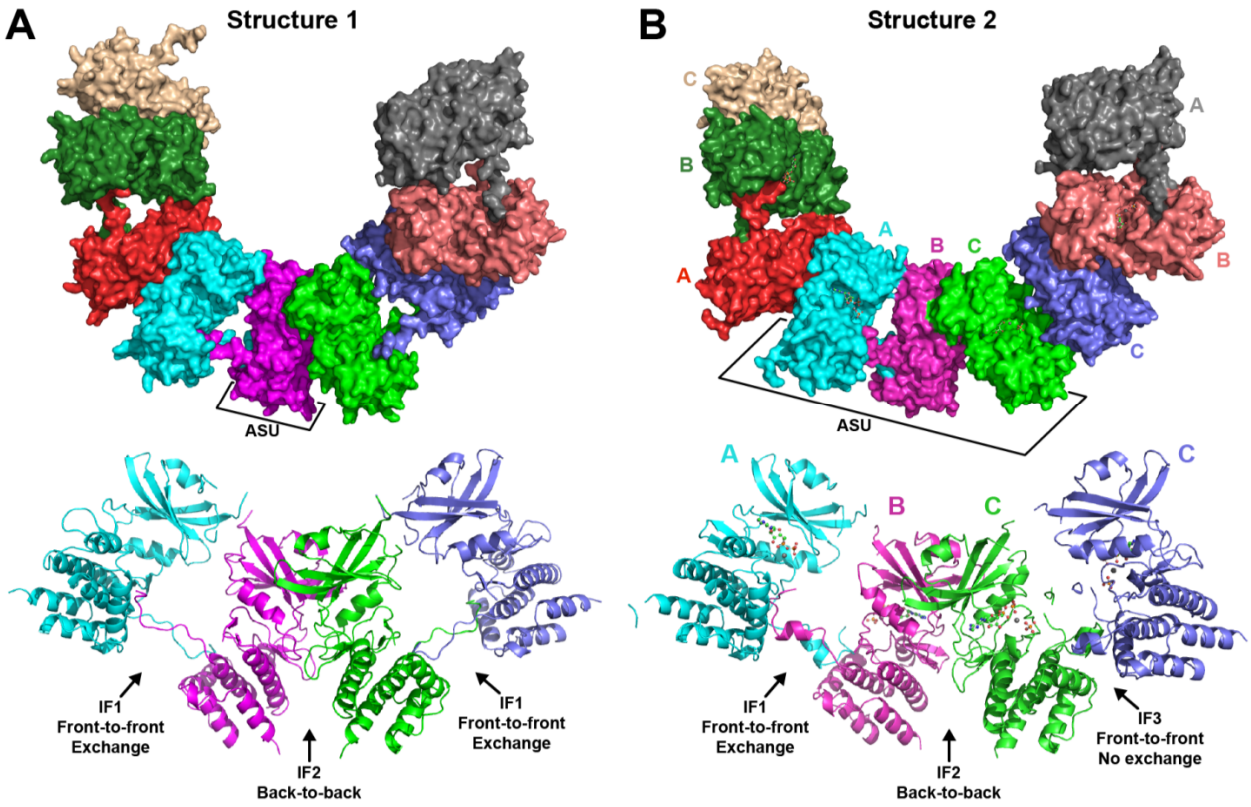

Figure 5.3 Comparison of structures one and two. A surface representation of the filament formed within the crystalline lattice is shown on the top with cartoon representations of four protein chains on the bottom. Structure 1 is shown in **(A)** and structure 2 is shown in **(B)**. One protein chain occupies the asymmetric unit (ASU) in structure 1. Three protein chains comprise the ASU in structure 2 and are labeled A, B, and C. In structure 2, AMP-PN and a phosphate are shown as ball and stick representations and magnesium is shown as a grey sphere. Unique interfaces (IF) are indicated in the cartoon representation of each structure.

5.5 Architecture of the kinase domain

The features of the kinase structure are annotated onto molecule C in Figure 5.4. Note that with the exception of the exchanged region, the structural deviations between monomers are minimal (Table 5.2, Fig. 5.5). Each monomer adopts the typical kinase domain architecture with a smaller N-lobe (olive) and larger C-lobe (cyan) connected by a flexible hinge. The protein is bound by AMP-phosphoramidate, a phosphate, and a magnesium ion in the ATP binding pocket between the two lobes. The N-lobe begins with a short noncanonical α-helix, α0, which contains residues forming a critical salt-bridge in the back-to-back interface, R262 and D266 (Fig. 5.6). The lobe is composed primarily of a five stranded antiparallel β sheet (β1-β5) and the

crucial αC helix. A short hinge connects the N- and C-lobes and forms the back of the ATP binding pocket. The structural elements of the larger C-lobe include eight α helices (αD-αJ), two antiparallel β sheets (β7-β8 and β6-β9), and the activation segment. PKR and other eIF2α kinases contain a slightly elongated αG helix which is also displaced from the canonical position occupied in other kinases (29, 217, 218). The helix forms the docking site for eIF2α (29) thus, it is noteworthy that it occupies that same position in the absence of a binding partner (Fig. 5.4 and 5.5). In eukaryotic kinases, the activation segment is typically defined as the region between two tripeptide motifs DFG and APE (SPE in PKR) and is colored red in Figure 5.4 (32). An important step in the structural analyses presented below is to establish that the catalytic machinery within the active site is appropriately oriented for phosphoryl transfer. One signature of the active kinase conformation is the short β6-β9 β sheet, stabilized by two hydrogen bonds, immediately C-terminal to the DFG motif (32). The absence of this β sheet leads to a destabilizing effect on proximal residues within the active site, D432 and D414 (Fig. 5.4).

Segments missing from the structure are indicated by dashed lines and include a large noncanonical loop between β strands 4 and 5 conserved within the eIF2α kinase family corresponding to residues 334-356 of PKR. A portion of the activation loop is also missing presumably due to disorder in its unphosphorylated state. The residues which are missing vary slightly for each protein chain. Molecule A is missing residues 441-450, B is missing 440-450, and C is missing 440-443 and residue 449.

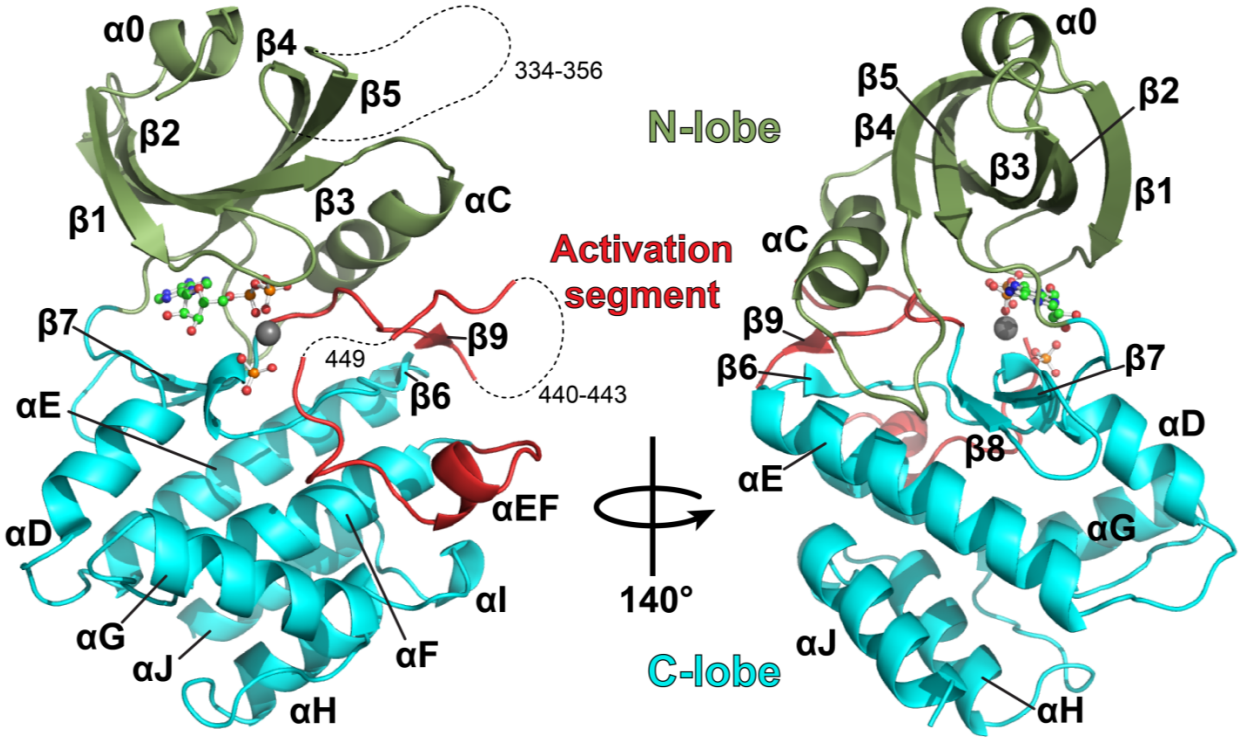

Figure 5.4 Architecture of the kinase domain. A cartoon representation of protomer C is shown in two orientations. The N- and C-lobes are colored olive and cyan, respectively. The activation segment is colored red. Secondary features are annotated. Regions missing from the structure are represented by a dashed line. AMP-PN, a phosphate, and a magnesium ion are bound in the cleft between the two lobes.

5.6 Comparison to the active conformation

Figure 5.4 shows an alignment of each molecule in the asymmetric unit to the phosphorylated kinase domain (2A19). Two sets of RMSD values for the alignment of Cα atoms are reported in Table 5.2. The first set of values is an alignment of the entire protein chain. In the second set, regions which obviously deviate from the 2A19 structure are omitted: the activation segment which swings out in protomers A and B and the segment of the activation loop which has shifted closer to the αC helix in protomer C. When these regions are omitted, the Cα atoms of each protomer align very well to the phosphorylated, active form of the kinase domain. The conformational changes to the region surrounding αEF associated with activation segment exchange are apparent in the alignment. G466 may serve as the flexible hinge

facilitating the domain swap configuration and will be a target of mutational analysis to probe the complex in solution.

Table 5.2 Alignment of Cα atoms to phosphorylated PKR kinase domain (2A19).

Region aligned	Protein Chain	# Atoms aligned	RMSD
Entire	A	252	4.528
	B	252	4.728
	C	257	1.297
With omissions	A	237	0.699
	B	237	0.745
	C	250	0.782

Superposition of active site residues with the phosphorylated 2A19 structure provides evidence that each protomer is in a form that is competent for phosphoryl transfer. An enlarged view of the aligned active site is shown in Figure 5.5B. Note that the active site residues in 2A19 make many of the conserved interactions with AMP-PNP and magnesium which are characteristic of the active kinase conformation (49). Residues critical for catalysis are rendered as sticks. AMP-PNP and the magnesium ions are from the 2A19 structure and bind at the conserved positions. However, the γ-phosphate is not correctly oriented for phosphoryl transfer. Its catalytically appropriate position is between the two magnesium ions directed toward the substrate hydroxyl which binds to the left of D414 (219). The magnesium ion binding positions are designated as I and II. For clarity, only the hydrogen bonding network for 2A19 is shown as the catalytic residues within each of our protomers occupy the same positions and make the same interactions. However, only a single magnesium ion is bound in our structure at MgII (Figure 5.10). The network of hydrogen bond interactions formed by protein residues and magnesium ions not only orient ATP but also provide a mechanism for charge transfer during the reaction (31). The only protein residue which directly engages the phosphates is K296 which stabilizes the α- and β-phosphates. Backbone residues from the G-loop also typically make phosphate interactions (219) but in 2A19 the loop is too far away. Additional charge

neutralization and stability is imparted on the phosphates by the coordinated magnesium ions. MgI is coordinated by D432 and the β-phosphate and is typically also coordinated by the γ-phosphate. MgII interacts with α-, β-, and γ-phosphates, D432, and the carbonyl oxygen from N419. The catalytic residue, D414, is stabilized by hydrogen bond interactions with N419 and K416. K416 interacts with the γ-phosphate and remains bound during all the steps of the reaction pathway (50). In our structure, the γ-phosphate is hydrolyzed but remains proximally bound by interactions partly mediated by K416. D414 acts as a catalytic base during phosphoryl transfer by positioning the substrate hydroxyl for in-line nucleophilic attack on the γ-phosphorous atom and accepting a proton during the reaction (50).

The catalytic apparatus is linked to helix αC and more distantly to the back-to-back interface by three pathways. 1) E308 orients K296 with a crucial salt bridge interaction (Fig. 5.4B). 2) R413 coordinates with pT446 and stabilizes the activation loop. This tethering interaction is a conserved mechanism for activation within the 'RD' family of kinases (44). In PKR, the phosphorylated moiety is further stabilized by K304 and R307 providing a linkage between the activation loop and helix αC (Fig. 5.4B). 3) A conserved hydrophobic spine called the R-spine, shown as a surface representation in Figure 5.4B, has a stabilizing effect on a proximal catalytic residue, D432. The completed spine provides rigidity to the catalytic core and is typically disrupted in inactive kinase structures (42). In PKR, the spine begins with F433 which burrows into the hydrophobic core of the protein. L312 from helix αC interdigitates into the spine and Y323 from β4 completes the spine on the back of the protein. Y323 links the R-spine to the back-to-back interface by engaging in a hydrogen bond triad formed with Y293 and D289 from the interacting partner (Fig. 5.6). In other kinases Y323 is often replaced with a leucine (43) and in PKR mutation to alanine abolishes activity (39). Above Y323, a hydrophobic pocket created by residues from helix αC, β4, and β5 provides a docking site for I288 from the reciprocal protomer (Figure 5.6D). Thus, the active site is intimately linked to both helix αC and the dimer interface by several allosteric pathways. These stabilizing linkage pathways may

provide a mechanism for how back-to-back dimerization induces a catalytically competent conformation within the active site.

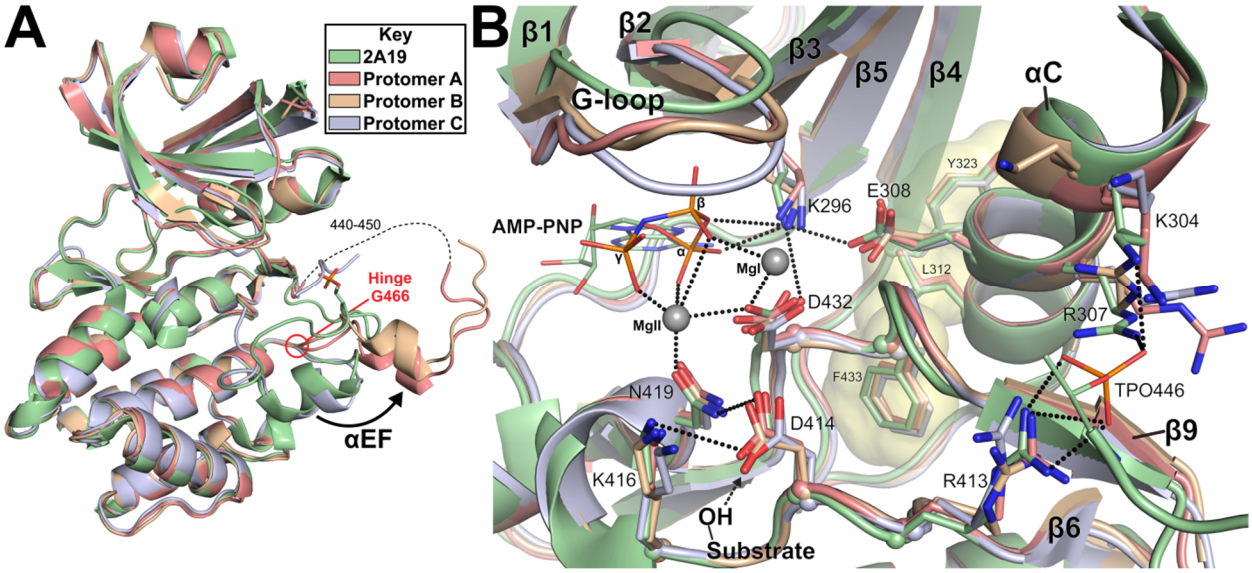

Figure 5.5 Comparison to phosphorylated PKR. (A) Alignment of each unique protomer in our asymmetric unit to the phosphorylated PKR kinase domain (PDB: 2A19). The hinge where the αEF helix flips out is indicated. A hypothetical path for missing residues in protomer A is indicated by a dashed line. The phosphorylated threonine (446) in 2A19 is indicated as sticks. **(B)** View of the active site. Residues important for catalysis are rendered as sticks with the Cα carbon shown as a sphere. AMP-PNP, magnesium (grey spheres), and pThr446 (TPO446) are from 2A19. α-, β-, and γ-phosphates are labeled. Hydrogen bond interactions are denoted as black dashed lines. The R-spine is shown in surface representation. Green and purple arrows represent linkage pathways from helix αC to the active site. Note that the phosphate orientations are slightly distorted. K296 typically does not interact with the α-β bridging oxygen and the γ-phosphate is not correctly oriented for phosphoryl transfer. The correct position of the γ-phosphate is between the two magnesium ions for in-line transfer onto the substrate hydroxyl.

Basic residues involved in coordination of the phosphorylated threonine 446 deviate substantially in the absence of a phosphorylated moiety. These include K304 and R307 emanating from the αC helix and R413 from the canonical HRD motif. However, the absence of phosphocoordinating interactions does not perturb positioning of the αC helix or residues within the active site suggesting dimerization may promote the active state. αC is correctly oriented so that E308 can hydrogen bond to K296, a conserved interaction characteristic of active kinases (31). Interestingly, in protomer A, a sulfate from the crystallization solution is bound in place of a phosphorylated moiety. The sulfate is coordinated by K304 and R413. Similar observations

have been reported for other kinases (220) and it is theorized that anions are coordinated by phosphate binding pockets which are formed prior to phosphorylation (32).

The glycine rich G-loop is a dynamic element of the kinase structure and its conformation changes during the catalytic cycle (221). Thus, it is not surprising that this region is a source of structural deviation between each of our protomers and 2A19. B-factor measurements support that this is a conformationally dynamic region (Figure 5.5). Structures containing transition state analogs have revealed how the loop clamps around the active site during catalysis shielding it from the solvent and helping to position ATP (222-224). In the 2A19 structure, the loop is shifted away from the active site and is not within hydrogen bonding distance of the phosphate. In protomer A, the backbone carbonyl from G279 is close enough to make a weak hydrogen bond (3.6 Å) with the β-phosphate.

The B-factors also highlight the stability imparted to helix αG by complex formation with eIF2α. The 2A19 protomer is bound by eIF2α via this helix and is much less flexible in this region than the unbound protomers present in our structure. This observation correlates with the 2A19 complex structure in which a back-to-back dimer is in complex with a single eIF2α. The molecule lacking an eIF2α binding partner is disordered at the eIF2α binding site and coordinates for αG and αD helices are missing from the structure (29).

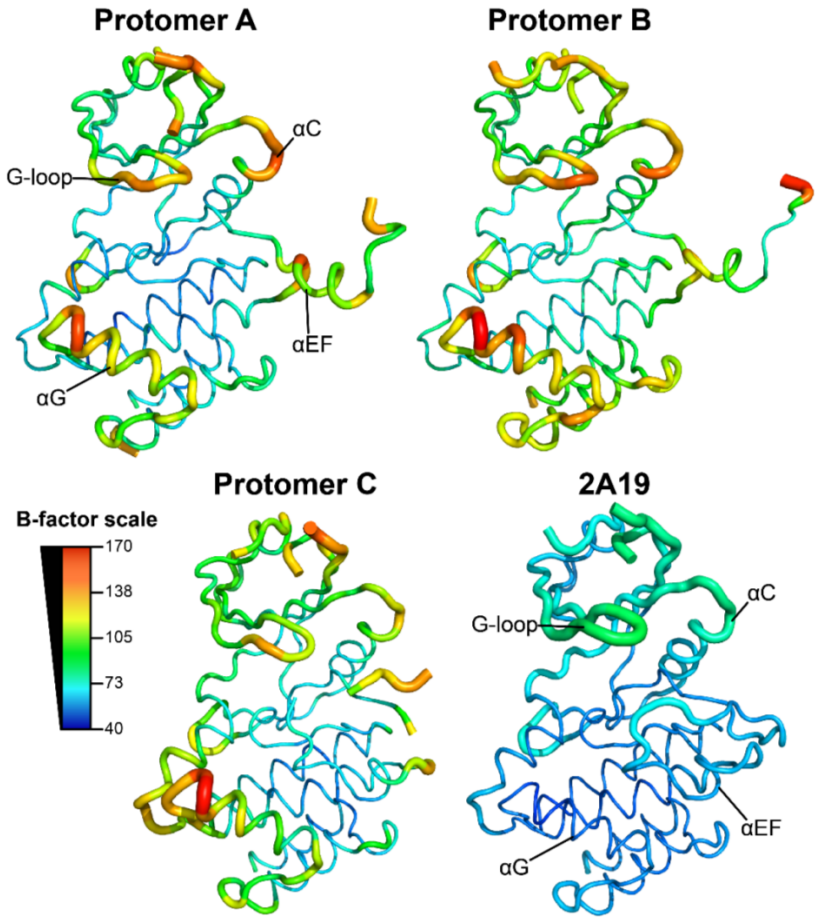

Figure 5.6 B-factor measurements. Cartoon representation of the dynamic features within the crystal environment. Cα B-factors for each protomer and the phosphorylated 2A19 structure are indicated as a blue to red spectrum on an absolute scale. The tubular representation is relative to each protein chain with a wider tube indicating regions with higher B-factors.

5.7 Analysis of interfaces: back-to-back (IF2)

Table 5.3 PISA analysis of interfaces.

Interface	Protein chains	Description	Interface area (Å^2)	ΔG[a] (kcal/mol)	Hydrogen bonds	Salt bridges
IF1	A:B	Front-to-front exchange	1252	-7.0	12	4
IF2	B:C	Back-to-back	863	-5.5	8	6
IF2	A:A	Back-to-back	829	-4.3	8	6
IF3	C:C	Front-to-front no exchange	810	-6.2	6	2

[a]ΔG reflects the thermodynamic gain by buried surface area. Electrostatic contributions are not included.

The back-to-back interfaces formed between protein chains B and C within the asymmetric unit and between asymmetric units by two A protomers are nearly identical as evidenced by alignment and analysis by PDBePISA (IF2, Fig. 5.6A, Table 5.3) (216). The assembly is essentially identical to the previously reported PKR back-to-back interface (30, 39) as well as the interface formed by the PKR homologue PERK (217). Several images of the back-to-back interface formed between protomers B and C are presented in Figure 5.6. Residues from the α0 helix on the top of the N-lobe contribute to the interface via two bifurcated salt bridges from between R262 and D266 (Fig. 5.6B). A hydrogen bond triad is formed between Y323, D289, and Y293 near the αC helix (Fig. 5.6C). Mutagenesis to disrupt these interactions blocks PKR autophosphorylation capability (39) but does not abolish dimerization (65). The C-terminal portion of the αC helix is stabilized by a hydrogen bond interaction between D316 and H322 (bottom of Fig. 5.6D). Additional interactions include two hydrogen bonds in the center of the interface formed between N324 from each protomer involving the side chain amide and main chain carbonyl (Fig. 5.6C). With the exception of H286, the interface is symmetrical. In one half of the interface H286 (protomer B, magenta) hydrogen bonds to the main chain carbonyl of C326 (protomer C, green). In the other half, H286 from protomer C is involved in a water mediated interaction with R262 (Fig. 5.6B).

Without a structure of the monomeric kinase domain, only assumptions can be made about the allosteric linkage between the dimer interface and active site conformation. Structural homologs may provide insight. PknB forms a similar back-to-back dimer and structures are available in both monomeric (225) and dimeric forms (206, 208). The structures demonstrate the conformational changes to helix αC associated with dimerization which, as previously discussed, often regulates the on/off switching mechanism in protein kinases (51). Monomeric structures of PknB were generated by mutating the residue corresponding to I288 in PKR (leucine in PknB) to aspartic acid (225) suggesting that I288 is critical to the interface. In both PKR and PknB, this residue contributes to the dimer by burying into a hydrophobic pocket

formed between αC, β4, and β5. A surface representation of the pocket is shown in in Figure 5.6D. In Section 5.6 an allosteric pathway was presented which linked the dimer interface to the active site via the R-spine (Fig. 5.4). The intimate link between dimerization and the active site can now be fully appreciated with the images of the dimer interface shown in Figure 5.6. The R-spine is completed by Y323 which is right below the hydrophobic pocket and hydrogen bonds to the residue immediately preceding I288 (D289).

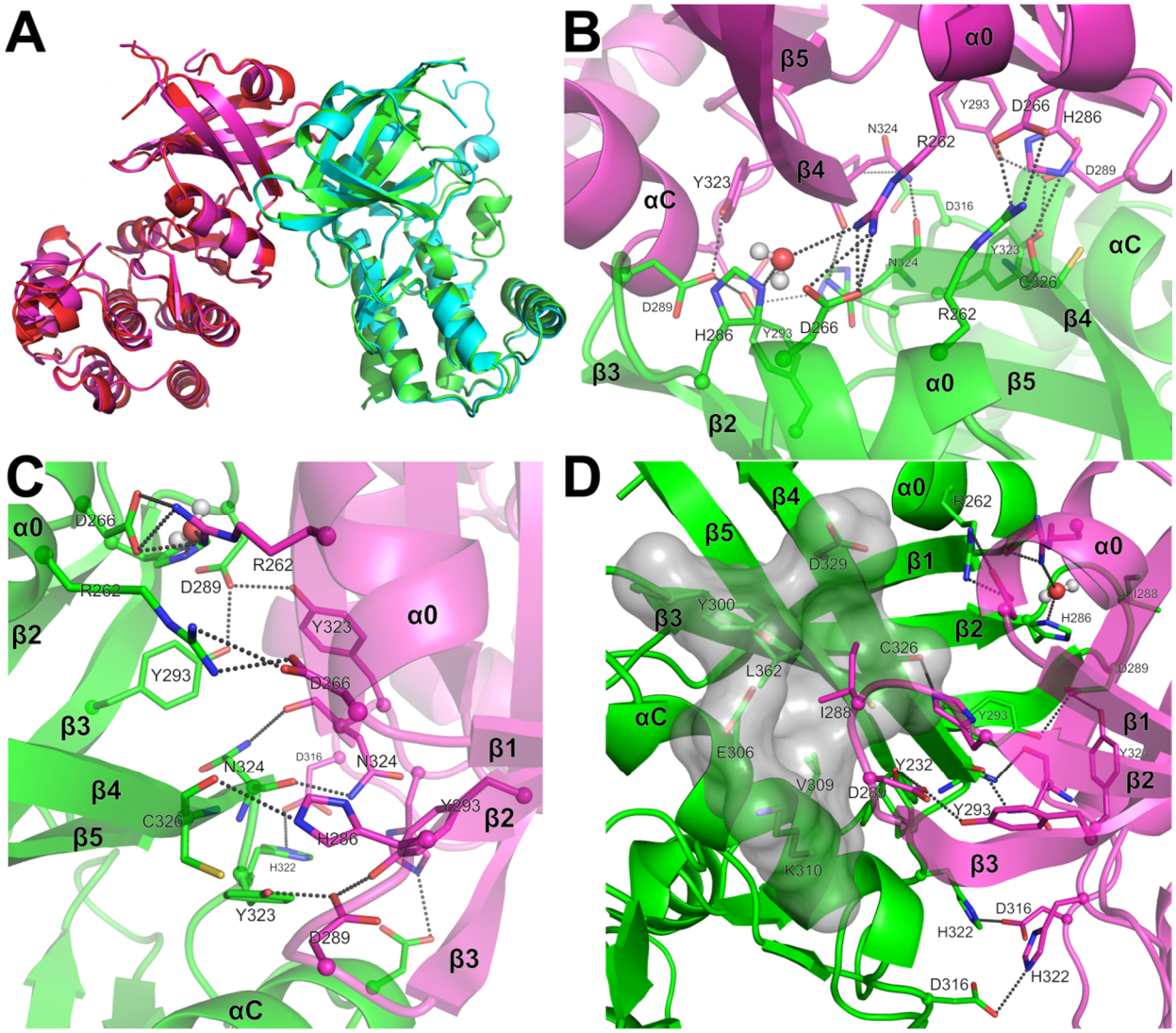

Figure 5.7 Back-to-back interface. (A) Alignment of back-to-back dimers. Both back-to-back dimers (B:C and A:A) are aligned. Color coding in this Figure is as in Figure 5.3. Residues contributing to the interface are shown for B:C in **(B-D)**. A top-down view looking down on the N-lobe is shown in **(B)**. In **(C)** the view is rotated 90° and tilted down slightly. A surface representation is shown in **(D)** to illustrate how I288 packs into a hydrophobic pocket formed between αC, β4, and β5.

5.8 Analysis of interfaces: front-to-front without exchange (IF3)

The front-to-front interface without activation segment exchange (IF3) is formed between C protomers across two asymmetric units. The αEF helix from one protomer docks into the cleft formed between the αEF and αG helices on the reciprocal protomer (Fig. 5.7B). Electrostatic interactions which stabilize the interface include a salt bridge between D500 at the base of αG and K521 from the loop connecting αH and αI and a hydrogen bond triad which is formed between T496 from αG, S461 from αEF, and Q463 immediately following αEF. Perhaps the only significant contribution from hydrophobic residues is I460 which is buried between αEF helices. Few electrostatic interactions and little buried surface area (810 $Å^2$) suggests the interface may be an artifact of crystal packing. However, similar interfaces utilizing the αEF and αG helices have been reported for *trans*-autophosphorylation complexes of PAK1 (226) (see Fig. 5.10) and PknB (212). The interface may also represent a step toward formation of the exchanged conformation.

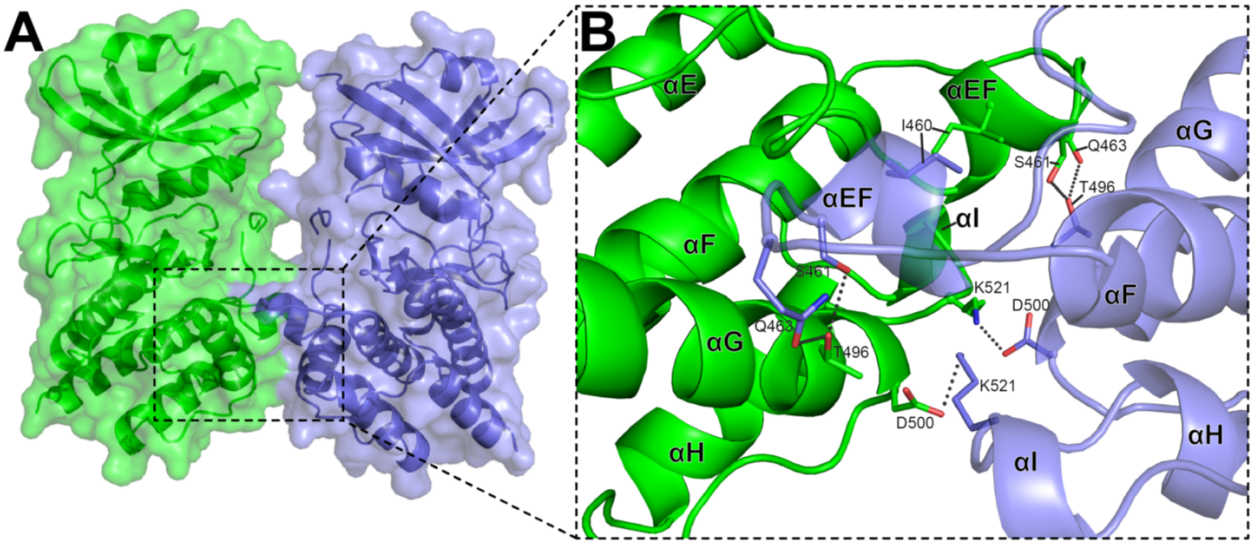

Figure 5.8 Front-to-front interface without exchange. (A) Surface representation of the interface. **(B)** View of the interface. Residues contributing to the interface are rendered as sticks and elements of the secondary structure are labeled.

5.9 Analysis of interfaces: front-to-front with exchange (IF1)

The most provocative interaction within the crystal is the front-to-front interface with exchanged activation segments formed between protein chains A and B (IF1, Fig. 5.9). As is typical in domain swapped oligomers, the exchanged portion of each protomer makes the same interactions in the reciprocal protein chain as in the monomeric form (227). Additional interactions are gained along the interface formed by the exchanging portions. These new interactions, which are absent in the monomer, may provide some of the thermodynamic impetus for formation of the domain swapped structure. Most of the residues participating in the interaction are shown in Figure 5.9B. In 5.9F, a surface representation of protomer A provides a helpful visual which illustrates how exchanged αEF arms dock into the reciprocal protomer. The discussion of the interface will begin by comparing the activation loops in the exchanged conformation to the monomeric configuration of the activation loop in the 2A19 structure. Panels C-D show an alignment of 2A19 onto protomer B. Note that in our structure, a portion of the region presumably involved in exchange, residues 440-450, is unresolved and is indicated by dashed lines in Figure 5.9C. Moving from N- to C-terminus, the region extended from the monomeric conformation begins immediately C-terminal to β9, moves through the αEF helix, and ends at helix αF (Fig. 5.9C). A glycine (G466) N-terminal to helix αF may serve as a flexible hinge facilitating extension of the activation segment. The interface is formed by docking of αEF helices into the cleft formed between helices αF, αG, and αI on the opposite protein chain which is normally occupied by the αEF helix in its monomeric form. Many of the interactions anchoring the αEF helix into the cleft are the same in monomeric and dimeric forms and some are highly conserved in kinases. Panels D and E illustrate the interactions which anchor αEF in both the monomer and dimer. R526 from the loop between αJ and αI anchors the C-terminal portion of the activation loop by engaging in a salt bridge with E458 at the base of αEF (Fig. 5.9D). This is a highly conserved interaction and mutation of the corresponding residues in PKA leads to decreased catalytic efficiency (204). Also, in both monomeric and domain swapped forms, Q459

stabilizes the HRD motif by a hydrogen bond to the main chain carbonyl of R413 (Fig. 5.9B, not shown in 2A19 alignment). Additional interactions anchor αEF to αG (Fig. 5.9E). R499 from αG is positioned proximal to the backbone to make hydrogen bond interactions with main chain carbonyls of R453, L452, and M455. At the tip of the αEF arm a hydrogen bond triad stabilizes the final portion of the activation segment which is resolved in our structure. Residues involved include R453 and Y454 from the activation loop and E460 from αF (Fig. 5.9E). The hydrophobic character of the tyrosine is highly conserved in kinases and this position is invariably occupied by a tyrosine, tryptophan, or phenylalanine. In cases where the tyrosine is replaced by tryptophan or phenylalanine, the glutamate from αF is typically replaced with a hydrophobic residue as well (32).

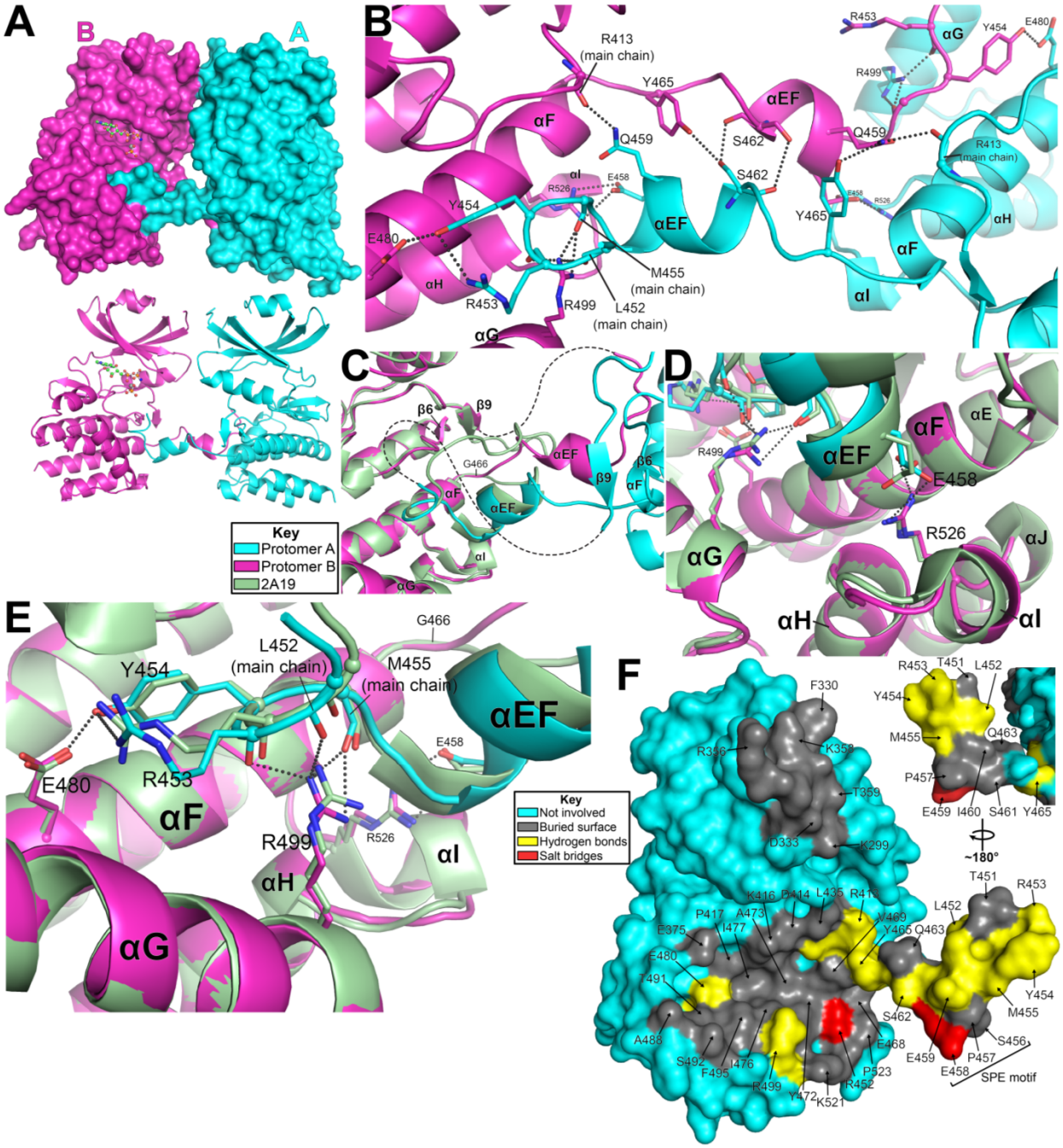

Figure 5.9 Exchanged front-to-front interface. (A) Surface and cartoon representations of the interface. AMP-PN and phosphate are shown as ball and stick. Magnesium is a grey sphere. Protomers are identified A and B as in Figure 5.3. **(B)** Top-down view of the interface. Interacting residues are rendered as sticks and labeled. Cα atoms are shown as spheres. Elements of secondary structure are labeled. **(C-D)** Alignment of the interface with 2A19. A key is provided left of panel **(C)**. In **(C)**, a hypothetical path for the missing segments of the protein chain is indicated by a dashed line. Panels **(D, E)** indicate the interactions that occur in both dimer and monomeric configuration. Note the interaction between Q459 and main chain carbonyl of R413 is not included. **(F)** Surface representation of protomer B with residues participating in the interaction colored according to the key.

Electrostatic interactions are gained as αEF helices pass by one another to dock into the reciprocal protomer. Note that some of these interactions are also associated with a lost interaction in the monomeric form. For example, in the monomeric structure Y465 hydrogen bonds to the R413 side chain, providing further stability to the phosphocoordinating site. In the dimer, Y465 assumes two different conformations dependent on the protein chain. In protomer B, it is oriented toward the side chain of S462 from protomer A (Fig. 5.8B). On the opposite side of the interface, Y465 from protomer A is more favorably orientated to participate in a hydrogen bond interaction with the side chain amine from Q459 in protomer B (right side of Fig. 5.8B). The only residue to gain an interaction in the dimer configuration is S462 which forms a symmetrical hydrogen bond interaction in which each side chain hydroxyl interacts with the reciprocal backbone carbonyl. In the monomer, the S462 side chain interacts with the backbone of D464 but the main chain carbonyl does not have an interacting partner.

Analysis of the interfaces with PISA indicates the face-to-face dimer with activation segment exchange has a larger surface area and predicted dimer stability than any other interface in the crystal (Table 5.3). However, the thermodynamic contribution of this parameter to complex formation should be interpreted with caution due to the structural changes required to form the interface. A majority of residues within the C-lobe and αEF arm buried in the dimer would also be buried in the monomer. Docking of the exchanged portion of the αEF arm (residues 451-465) into the C-lobe in the monomeric configurations yields a buried surface area of 616 $Å^2$ and ΔG = -4.2 kcal/mol. Thus, the change in buried surface area between monomeric and dimeric forms is only 636 $Å^2$. The tip of the N-lobe is also buried in the dimer yet this surface contributes only 119 $Å^2$ and predicted ΔG of -0.2 kcal/mol. Curiously, despite the presence of charged amino acids in this region, none are correctly oriented to contribute electrostatic interactions. The N-lobe interaction surface may be an artifact of crystal packing. Structural homology with other kinase domain *trans*-autophosphorylation complexes is discussed in a subsequent section. Most complexes utilize the general mechanism of

exchanged αEF helices docking into the reciprocal site on the opposite protomer but differ in protomer symmetry. Very few are oriented to utilize the N-lobe in the interaction surface and for those that do, the buried surface area is similarly small. Note that the large loop connecting β4 and β5, comprising residues 334-356, is unresolved in the structure and would be oriented toward the front-to-front interface. This loop contains an abundance of polar and acidic amino acids and could electrostatically contribute to the interface. Mass spectrometry has identified this loop as a region which becomes heavily phosphorylated (182). Although PKR was extracted from yeast and modification could be due to endogenous kinases rather than PKR autophosphorylation.

5.10 Comparisons to similar structures

PKR belongs to a family of kinases which require activation loop phosphorylation as an on/off switching mechanism yet paradoxically have no upstream kinase to activate them *in vivo*. For many members of this family, incubation of purified, unphosphorylated enzyme with ATP and magnesium results in activation loop phosphorylation, demonstrating that a basal level of autophosphorylation activity persists in the 'inactive' state (33). Thus, phosphorylation likely serves to shift a preexisting equilibrium towards a more activate state. A structure elucidating how autophosphorylation of a latent kinase may occur in *trans* by activation loop exchange was first determined for check point kinase 2 (Chk2) (228). Similar complexes have since been reported (229-232). These structures adopt a similar conformation as observed in our interface, utilizing exchange of the αEF helix to bring the activation loop within close proximity of the catalytic apparatus of the opposing protomer. Figure 5.9 presents a structural comparison between PKR and two similar activation segment exchange complexes, Chk2 and SLK. An additional *trans*-autophosphorylation complex for PAK1 is also included and will be discussed subsequently. The distances between the catalytic aspartate and the primary and/or secondary phosphoacceptor sites within the activation loop are indicated in the enhanced view of the active site presented left of the surface representation. For complexes engaged in activation segment

exchange (PKR, Chk2, and SLK) the distances range from 6.3 Å in Chk2 to 18.9 Å in SLK. As shown in the magnified view of the active site, the residues comprising the catalytic machinery are properly oriented for phosphoryl transfer yet the substrate hydroxyl is too remote in the crystallographic configuration. These complexes are generally symmetrical and both protomers could function as either enzyme or substrate. Brownian motion is proposed to transiently orient the complex for phosphorylation (233). Note that only Ser/Thr kinases are discussed here yet similar complexes engaged in activation segment exchange have been described for tyrosine-specific kinases as well. These complexes exchange activation segments but do not exchange the αEF helix. The substrate tyrosine is typically much closer to the catalytic aspartate, however, the active site is disassembled in each protomer (234).

A unique asymmetrical *trans*-autophosphorylation complex has also been described for PAK1 in which only one monomer extends its activation loop into the opposite monomer (226). The structure can be described as an enzyme-substrate complex. The enzyme accepting the activation loop contains a bound AMP-PNP and utilizes its own activation loop as the substrate docking site. N- and C-lobes clamp down on the substrate and the enzyme is poised for catalysis. This geometry is structurally distinct from the substrate molecule, which is in an open conformation and free of ligand. A similar asymmetric complex has been reported for PknB, although the activation loops were less resolved in the structure and both protomers adopted similar conformations (212). Both complexes bury αEF and αG helices within the interfacial area similar to the front-to-front dimer formed without activation segment exchange (IF3) in our crystal. The interfaces reported in both studies are supported by functional analyses correlating mutagenesis of key interfacial residues with decreased catalytic activity. Interestingly, members of the Pkn kinase family also form a back-to-back dimer similar to PKR which is essential for activity (PknB: (206, 208), PknD: (209), PknE: (207)). Thus, PknB forms two essential dimeric configurations mediated by different regions of the protein. Monomeric structures of PknB are also available providing the structural basis for dimerization driven allostery of the active site

(225). In the monomeric state, the N- and C-lobes are shifted relative to each other and the αC helix is rotated orienting the essential glutamate away from the active site. These structural insights have coalesced into a mechanistic model for the PknB activation mechanism in which back-to-back dimerization mediates formation of the active kinase conformation and back-to-back dimers phosphorylate other monomers or dimers in *trans* via the face-to-face interface (212, 225). The model is structurally analogous to the arrangement of protomers within our crystal.

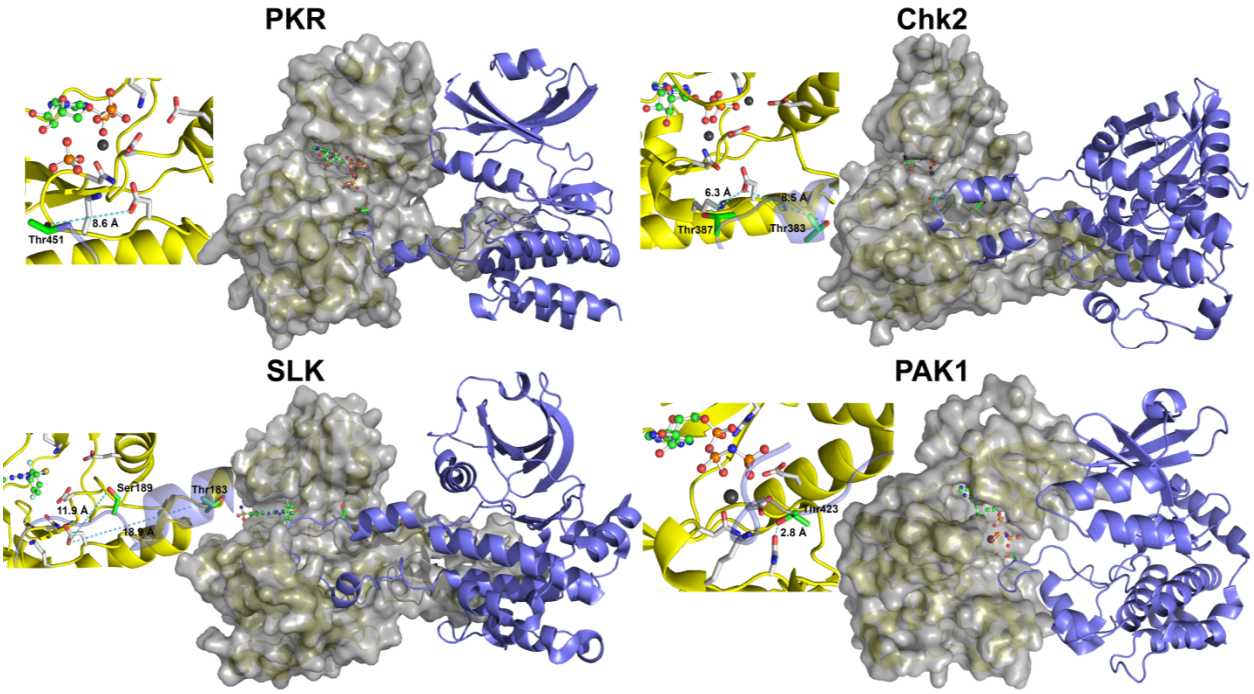

Figure 5.10 Kinase *trans*-autophosphorylation complexes. PDB IDs and literature references: PKR, to be determined; Chk2, 2CN5 (228); SLK, 2J51 (230); PAK1, 3Q4Z (226). Note PAK1 contains inactivating mutations K229R and D389N.

5.11 Analysis of ligands bound in the active site

Structure 2, the primary topic of discussion in this Chapter, was co-crystallized with AMP-PNP yet electron density for the γ-phosphate is missing from the structure. The current structure is modeled with each protomer bound in its active site by AMP-phosphoramidate (AMP-PN), a magnesium ion, and a proximal phosphate. The assignment of the AMP-phosphoramidate and neighboring phosphate are based solely on the appearance of the

electron density map. This model predicts that AMP-PNP was hydrolyzed within the crystal and the terminal phosphate remained proximally bound to the protein. Commercial preparations of AMP-PNP have been shown to be contaminated with decomposition products of AMP-PNP (235). Thus, an alternative possibility is that contaminating ADP from the commercially supplied AMP-PNP preferentially bound to the protein during crystallization. In this scenario, the proximal phosphate is instead a sulfate obtained from the crystallization solution. The atomic scattering factors are similar for phosphorous and sulfur (atomic numbers: Z = 15 and 16, respectively) so that the electron density map alone is insufficient to discern the chemical identity. The analysis proceeds assuming the ligand assignments are correct however methods which probe the chemical identity of the molecules contained within the crystal are required.

Figure 5.10 shows the interactions stabilizing the ligands within the active site. Protomer B is shown with the exchanged portion of protomer A entering on the right. Note that each protomer within the crystal contains the same bound ligands and, with exception to the glycine rich G-loop, adopt similar residue conformations. AMP-PN binds in a hydrophobic pocket in the back of the hinge region between the N- and C-lobes. The pocket is formed primarily by I273, V281, V294, F368, and F421. Of particular note is F421 which emanates from β7 within the C-lobe to stabilize the adenosine ring by pi stacking interactions. Together with V281, V294, and residues within the C-lobe, F421 forms a hydrophobic spine (C-spine) which regulates conformational dynamics. The adenosine ring completes the spine linking protein dynamics and ATP binding (204). The phenyl ring which forms the foundation for ATP binding is unique to PKR as kinases typically contain a leucine in place of F421 (236). At the back of the binding pocket, main chain atoms from E367 and C369 within the hinge region make hydrogen bond interactions with exocyclic and cyclic nitrogens, respectively, of the pyrimidine ring. Interactions are described moving towards the terminal phosphate. The only interaction stabilizing the ribose sugar is a hydrogen bond between the 2′-OH and the backbone carbonyl from S418. The α-phosphate and the bridging α,β-phosphate oxygen are stabilized by the catalytically important

K296. Mutation of this residue, even to arginine, disrupts catalysis in most kinases (31). The β-phosphate is stabilized via the G-loop by G279. The G-loop is a dynamic element within kinases and functions during the catalytic cycle by opening and closing to bind and release ATP and ADP. Structures of eukaryotic Ser/Thr kinases co-crystallized with transition state analogs are limited but demonstrate how the G-loop closes during catalysis to stabilize the phosphates for phosphoryl transfer (222-224). The β-phosphate is also stabilized by D432. In our structure, only a single magnesium ion is bound at the MgII binding site and magnesium site occupancy is discussed further below. A view of magnesium bound at the MgI site is provided in Figure 5.4 for the 2A19 structure. Magnesium ions bind on opposite faces of the ATP phosphates. MgI is coordinated by D432 and the β- and γ-phosphates. In our structure, MgII is bound by N419, D432, the hydrolyzed phosphate, and the α- and β-phosphates. When present, MgII also coordinates with the terminal phosphate to position it for in-line phosphoryl transfer. The free phosphate is bound proximal to AMP-PN and interacts with many of the same moieties that it would in its intact state including MgII and K416. Presumably, water served as a nucleophile to hydrolyze the terminal phosphate and, in the absence of a true substrate, the phosphate retained many of its interactions to remain bound. The phosphate is shifted away from the active site so that it gains an additional coordination from the side chain of S418. In some sense, the presence of the hydrolyzed phosphate recapitulates some of the observations from PKA. Co-crystallization with ATP, Mg^{2+}, and a dummy substrate peptide whose phosphoacceptor serine had been mutated to alanine yielded a structure with partially hydrolyzed ATP. The hydrolyzed phosphate remained bound in a similar position as transition state analogs (237). Relative to the PKA structure, the phosphate in our structure is shifted ~5 Å away from the active site yet still interacts with many of the same moieties. Thus, the dummy substrate peptide retained the hydrolyzed phosphate within the active site.

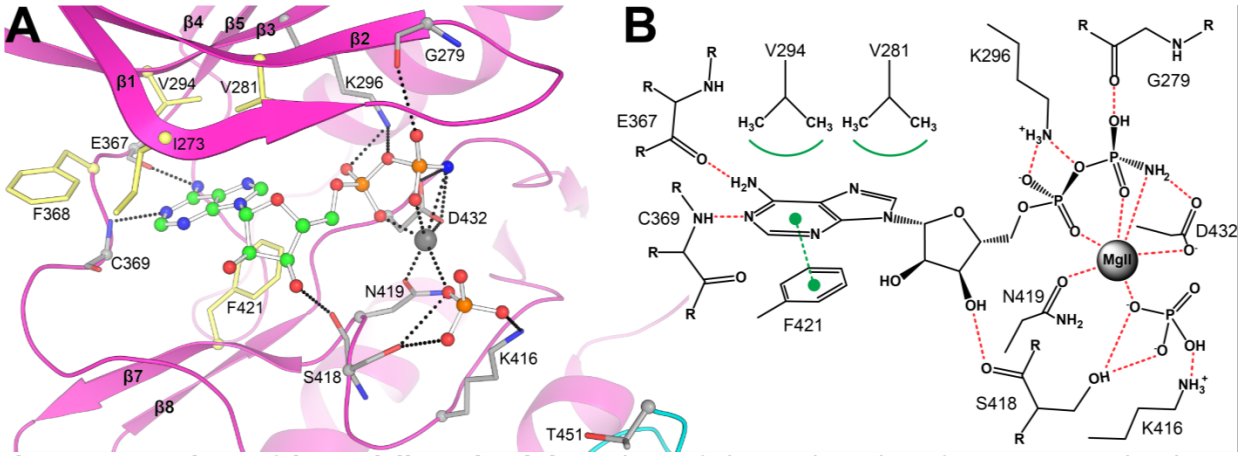

Figure 5.11 View of bound ligands. (A) A view of the active site of protomer B is shown (magenta). The exchanged portion of protomer A is shown in cyan. AMP-PN and the phosphate are shown in ball and stick representation. Magnesium is shown as a grey sphere. Residues contributing to the hydrophobic pocket are shown as yellow sticks. Residues contributing electrostatic interactions are shown as grey sticks with oxygen and nitrogen colored red and blue, respectively. Hydrogen bonds are drawn liberally as black dashed lines with a 3.2 Å cutoff. **(B)** 2-dimensional view of ligand stabilizing interactions. Most of the residues shown in (A) are flattened into a 2-dimensional interaction map for added clarity. Hydrogen bonds are drawn as red dashes. A pi stacking interaction between F421 and the adenine ring is shown as two green circles connected by a dashed line. The hydrophobic surface created by V294 and V281 is shown as a curved green line.

Hydrolysis of AMP-PNP has previously been observed during co-crystallization as reported in several publications (238-243) and several unpublished structures deposited on the PDB (3IED, 4BWP, 4U7O, 5C3Y, 5H9B). Catalysis of the terminal phosphate within free solution has also been reported by many different types of enzymes including alkaline phosphatase (244, 245), ATPases (246, 247), a motor domain (248), a calcium pump (240), but only one kinase, PKA (249). Thus, hydrolysis of the γ-phosphate from AMP-PNP is a relatively common phenomenon. In some crystallographic studies, acidic crystallization solutions, where AMP-PNP is unstable, may induce hydrolysis (241-243). The pH of the solution used to grow our crystals was not acidic (pH = 7.5) and hydrolysis is likely the consequence of enzymatic action.

In a structural analysis of PKA, the slow rate of AMP-PNP hydrolysis was exploited yielding valuable crystallographic snapshots of the phosphoryl transfer mechanism (249). Crystals were obtained in complex with AMP-PNP and a substrate peptide and two sets of diffraction data were obtained ~3 and ~5 months after crystal appearance. In the first data set, the γ-phosphate is partially transferred to the substrate serine and has been fully transferred after ~5 months. While neither structure represents a transition state *per se* (only starting end points of phosphoryl transfer) the structures provide insight into the phosphoryl transfer mechanism, primarily with respect to the role of magnesium ions. Most kinases utilize two magnesium ions to catalyze phosphoryl transfer which were historically assigned as the activating (Mg1) and inhibitory (Mg2) ions. This terminology is misleading and arises from the observation that high concentrations of magnesium decrease catalytic activity. In fact, ADP release from the active site, rather than phosphoryl transfer, is the rate-limiting step and is modulated by magnesium concentration (250). In the 2A19 structure, which is also bound by intact AMP-PNP, the magnesium ions bind the canonical positions and are labeled as MgI and MgII in Figure 5.4. In our structure, only MgII is present but it occupies the same position as MgII from 2A19. This corroborates the observations from the PKA structures where release of MgI occurred coincident with phosphoryl transfer (249). It is also in agreement with structural studies on CDK2 which suggest that ADP is released from the active site in complex with MgII as the rate limiting step during catalysis (251).

5.12 Future directions

The crystal structures reported here suggest that PKR forms a *trans*-autophosphorylation complex during activation. The experiments proposed in this section will probe whether the complex forms in solution and its role during activation. Additional crystallographic approaches and their rationale are also described. For additional clarity, the various experiments are organized in Table 5.4.

Table 5.4 Future directions.

Approach	Remarks
cis vs. *trans*	His-tag catalytically inactive PKR (K296R / D414N) and examine whether it is phosphorylated by WT PKR. Does any phosphorylation occur (^{32}P)? Is the activation loop phosphorylated (anti-TPO446 Western)?
S462A	Destabilize domain swap configuration.
G466L	Impede domain swap by reducing flexibility.
N441G D464G	These substitutions promote domain swap. N441 and D464 H-bond to anchor the N- and C-terminal portions of the activation segment together.
R445G	Similar to N441:D464, R445 anchors N- and C-terminal portions of the activation segment by H-bond interactions to backbone carbonyls.
Y454 → *p*AzF / *p*Bpa	Directly probe domain swap by crosslinking.
T496A / Q463A / S461A D500A / K521A	Mutations designed to disrupt the front-to-front interface without exchange (IF3). May be combined or made individually.
Optimization of other crystallization solutions	0.1 M HEPES (pH 7.0), 5 % v/v Tacsimate, 10 % w/v PEG-MME 5,000 must be optimized.
Co-crystallization with drug candidates	Structural mechanism of activation by small molecules.
Co-crystallization with ssRNA	May induce folding within basic domain.
Co-crystallization with heparin	Confirm heparin binding site (91). May also stabilize basic domain.
Co-crystallization with substrate peptide	Structural information is lacking for how substrate binds in the active site of PKR.
Co-crystallization with transition state analogs	Limited structural information on mechanism of phosphoryl transfer. Could stabilize exchanged complex.
Crystallization of I288D	The homologous mutation in PknB generated a monomeric structure (225).
Crystallization of phospho-PKR	Crystal structure of active PKR is phosphorylated on threonine 446 (29). Yet other phosphorylation sites are present within the kinase domain (182, 252). How do these alternative sites regulate catalytic activity?
Crystallization of full-length PKR alone and with dsRNA	Currently only structures of individual domains are available. Some evidence suggests the dsRBD engages the kinase in an auto-inhibitory interaction (54). Other studies indicate PKR exists in a more open conformation (38, 60). This discrepancy may be resolved by a full length structure. A complex containing dsRNA would be invaluable to understanding activation.

A reexamination of PKR activation by assays which discriminate between *cis* versus *trans*-autophosphorylation mechanisms is required. Both *cis* (34) and *trans* (35-38) mechanisms have been reported. These assays are interpreted by the ability of wild-type PKR to phosphorylate PKR molecules containing inactivating mutations. The two species are separated by a tag(s) inserted onto PKR. A His-tag is sufficient to generate separation from wild-type PKR on an SDS-PAGE gel (36). These experiments will be repeated in our laboratory. Activation will be probed by both ^{32}P incorporation and Western blots using antibodies specific for phosphorylated T446 and T451. Additionally, this assay will be combined with the mutations discussed below in various configurations to provide further insight into the requirements for autophosphorylation. Note, however, that activation of PKR molecules in solution can be conceptualized as a multi-step, self-perpetuating activation cascade (61). The slower initial steps which activate latent kinase molecules may differ from the more efficient subsequent reactions in which activated PKR molecules phosphorylate latent PKR. A model which incorporates both *cis* and *trans* mechanisms at different steps of the activation pathway may be required to reconcile with the functional data.

The hypothesis that the exchanged activation segment complex represents a *trans*-autophosphorylation complex predicts that disruption of interfacial residues will reduce catalytic efficiency. However, the mechanism of domain exchange presents a challenging obstacle in designing mutations to specifically destabilize the strand-exchanged dimer. Inherent to the domain swapped configuration is restoration of the interactions that would stabilize the domain within its folded monomeric form within the reciprocal protomer in the dimer. Mutation to interfacial residues will invariably have an effect on the monomeric conformation, complicating interpretation of functional analysis. Candidate residues for mutational analysis are limited. Indeed, the only residue whose interactions are unique to the dimer configuration is S462 which will be mutated to alanine. Mutagenesis of interfacial residues is a classical approach to confirming the significance of complexes trapped within crystals. To circumvent the issues

previously addressed, investigators of domain swapping interactions typically employ an additional approach that probes the hinge region by mutagenesis (227). In PKR, a flexible glycine, G466 (see Fig. 5.4A), presumably functions as the hinge to facilitate exchange. Conceptually, proline is the residue of choice to reduce flexibility. However, proline residues actually often function as the hinge and facilitate domain swapping by adopting a more favorable conformation in the exchanged configuration (227). Therefore, bulkier residues will be introduced to impede exchange. A similar approach was used to confirm activation segment exchange in SPAK kinase (232). Conversely, mutations will be introduced designed to promote domain swapping by disrupting interactions which anchor the N- and C-terminal portions of the activation segment together (N441, R445, and D464, Table 5.4). Mutants containing S462A, G466L, N441G, D464G, or R445G will test the *trans*-autophosphorylation complex by functional analyses for PKR activity. S462A and G466L are expected to decrease activity while stimulatory effects are anticipated from N441G, R445G, and D464G.

The front-to-front interface without activation segment exchange (IF3) will be probed by the classical mutagenesis approach. Refer to Figure 5.7 for an image of the interface and Table 5.4 of a list of target residues. The electrostatic interactions which stabilize the interface are limited and only include a hydrogen bond triad between T496, Q463, and S461 and a salt bridge between D500 and K521. Similar to other mutations, the effects of mutagenesis will be screened by functional assays for PKR activity. The functional relevance of the back-to-back interface is already well established (39). It may be helpful to include mutations which selectively disrupt the back-to-back interface in the *cis*- vs. *trans*-autophosphorylation assays to provide information on the PKR assembly process. Screening mutational effects by quantification of oligomeric equilibrium constants is an appealing approach but may not be applicable to this system. The presence of multiple interfaces and weak oligomerization in solution complicates the analysis. We have previously measured PKR dimerization by

sedimentation equilibrium analytical ultracentrifugation to obtain a dissociation constant of ~500 μM (35, 91).

Analysis of the oligomeric configuration of PKR molecules within solution will also be probed by crosslinking. Classic methodologies combining bifunctional crosslinking agents with analysis by mass spectrometry are considered. A more elegant approach is afforded by unnatural amino acid mutagenesis of a tyrosine residue, Y454, which interacts with the reciprocal protomer at the tip of the αEF arm. Y454 is positioned similarly in the monomer and the domain swapped configurations and is within hydrogen bonding distance to E480 (see Fig. 5.8E). A method to introduce unnatural amino acids with unique chemistries into proteins is well established (253) and has been utilized by our laboratory to site-specifically label PKR with fluorescent probes (65). The system adds an amino acid to the genetic code by co-expression of an aminoacyl-tRNA synthetase/suppressor tRNA pair which reassign the amber stop codon (TAG) to encode for the amino acid. Y454 will be replaced with a photoreactive crosslinker, either *p*-azido-L-phenylalanine (*p*AzF) or *p*-benzoyl-L-phenylalanine (*p*Bpa). Exposure to UV light activates the amino acids for crosslinking and complexes can be analyzed by SDS-PAGE. Bands corresponding to dimer confirm activation segment exchange and will be further validated by mass spectrometry. *p*AzF is the desirable substitution, generating minimal structural perturbations by replacing the tyrosine hydroxyl with the reactive azide. However, the bulkier *p*Bpa has a longer lived excited state and different reaction chemistry (254) and may produce a crosslinked complex where *p*AzF fails. The probes will be introduced at other sites within the protein to probe the back-to-back and front-to-front interfaces and as negative controls. Note that *p*Bpa has already been introduced at sites to probe the back-to-back interface. Higher-order oligomers appear on an SDS-PAGE gel and are dependent on *p*Bpa and UV light confirming the efficacy of this approach (D. Mouser, S. Hesler, and J. Cole, unpublished results).

The proposed mechanism for PKR activation is phosphorylation of two threonines within its activation loop, T446 and T451 (255). T446 is unresolved in our structure but T451 is located at the tip of the exchanged portion of the αEF helix as the final residue resolved in this region. The hydroxyl is 8.6 Å from the catalytic aspartate in the reciprocal protomer and structural rearrangements may mediate formation of a complex to phosphorylate T451 in *trans*. Similar rearrangements may orient T446 for phosphorylation yet this is even more speculative given that it is absent from our structure. Phosphorylation of the residue corresponding to T446 is conserved in most 'RD' kinases and the structural relevance is well established (256). However, homology does not provide a function for T451 phosphorylation since this residue is not typically phosphorylated in other kinases. Most Ser/Thr kinases contain a threonine or serine at this position yet its function is seldom annotated (32). Although, a catalytically function for this residue has been proposed from structural analyses on PKA (237). Substrate peptide induces a reorientation of the residue so that it engages in a trigonal bonding interaction with the catalytic aspartate (D414 in PKR) and neighboring lysine (K416 in PKR). The interaction is proposed to orient the catalytic aspartate carboxylate for proton abstraction. It is unclear whether phosphorylation of T451 is compatible with this catalytic mechanism. Note, however, that while phosphorylation of T451 is often referenced in the literature, evidence for this modification is not convincing. The prescribed function of T451 as a phosphoacceptor site is deduced from the correlations between T451A mutations and phosphomimetic mutations, enzymatic activity, and Western blots with antibodies against phosphorylated T451. However, a catalytic role for T451 would be perturbed by mutation and antibodies may not be specific for T451. Mass spectrometry has failed to detect phosphorylation of T451 even though T446 is phosphorylated in the analysis (48, 182). Furthermore, in the structure of the phosphorylated PKR kinase, only T446 is phosphorylated (29). A reexamination of T451 phosphorylation is necessary prior to its assignment as a phosphoacceptor site in our putative *trans*-autophosphorylation complex.

Finally, additional crystallographic approaches will be pursued. Additional crystallographic conditions, such as crystallization by Tacsimate / PEG-MME 5,000 (see Fig. 5.2), require optimization. Another structure exhibiting domain swapping in a front to front arrangement generated from an additional crystallographic condition and possibly space group would provide further validity to the structures reported here. The ability to make diffraction quality crystals brings a valuable technology to the laboratory which synergizes with many other projects. An ongoing project to identify small molecule activators of PKR (S. Hesler and J. Cole, unpublished results) would benefit greatly from a facile method to analyze the structural function of any hits. We have previously characterized heparin mediated activation of PKR and used mutagenesis to identify a positively charged pocket partially formed by helix αC as the heparin binding site (91). Although, alternative sites have been proposed (179). A structure of PKR bound to heparin would resolve the discrepancy and provide valuable mechanistic insight into how heparin induces activation. The original motivation behind crystallographic analysis of the 229-kinase construct was to obtain structural information on the basic region. Unfortunately, residues 229-256 are unresolved in our structure. The basic region exhibits cursory resemblance to arginine rich motifs (ARMs), short stretches enriched in basic residues which bind RNA (257). One of the most well characterized ARMs is HIV-1 Rev which has been shown to fold into an alpha helix upon binding its target RNA, RRE (258, 259). Thus, a ligand may be required to induce folding within the basic region and co-crystallization trials with short ssRNAs are currently underway. Under the assumption that our structure represents an enzyme-substrate complex, the front-to-front interfaces recapitulate some of the observations from the PKR-eIF2α complex. In both structures, the substrate for phosphorylation (T446 in PKR and S51 in eIF2α) and neighboring residues are disordered. A structure containing substrate peptide bound at the active site is unavailable, necessitating assumptions for how substrate may interact from homologous kinases where such information is available. Such a complex may also provide information on the role of T451 during activation. Structural information on the

Ser/Thr kinase transition state gleaned from co-crystallization with transition state analogs is limited (222, 223, 260). Dissociative (S_N1) and associative (S_N2) mechanisms for phosphoryl transfer have been proposed which differ primarily in the relative distances and bonding interactions between the β-phosphate, γ-phosphate, and substrate hydroxyl during the transition state (250). Molecular dynamics simulations indicate a dissociative mechanism is more likely (50). A structure of PKR containing a transition state analog would provide much needed information on the nature of phosphoryl transfer but also may stabilize activation loops in the front-to-front interface in active sites of reciprocal protomers. Finally, a structure of monomeric PKR would provide valuable structural information on the conformation changes associated with the assembly of PKR molecules into the activating complex. Structural investigations of the Pkn family of kinases, which are structural homologous to PKR and form similar interfaces, are a useful guide (261). A monomeric structure of PknB was produced by mutating residues contributing to the back-to-back interface. One residue is conserved in PKR, I288, which packs into a hydrophobic pocket on the back of the αC helix (Fig. 5.6).

Chapter 6: Host and viral protein regulators of PKR

6.1 Introduction

The canonical PKR activators are long stretches of duplex RNA. However a protein activator, PACT, has been identified more recently (92). PACT activates PKR in response to a variety of cellular stressors to induce apoptosis in the absence of viral infection (96). Similar observations have been reported for the mouse ortholog, RAX (262). PACT contains two N-terminal dsRBDs homologous to PKR (dsRBD1 and 2) and a dsRBD at the C-terminus that lacks residues that mediate RNA binding (D3). The model describing PACT-mediated PKR activation hinges upon the proposed autoinhibitory intramolecular interaction within PKR between dsRBD2 and the kinase domain (see Section 1.4) as well as the proposed role of the dsRBDs in mediating protein-protein interactions (54, 55). PKR is stimulated in a concerted mechanism whereby dsRBD1 and 2 from PACT relieve autoinhibition by engaging dsRBD1 and 2 in PKR and D3 interacts with the kinase domain to promote activation (94, 95). A MBP-D3 fusion construct binds PKR weakly yet is able to potently activate PKR *in vitro*. However, full length PACT is required for PKR activation *in vivo* (95). Phosphorylation of two sites within D3, S246 and S287, increases PKR affinity and activation potency (97, 263). S246 appears to be constitutively phosphorylated and S287 phosphorylation transduces the stress response signal. The upstream activating kinase is unknown (97). Phosphomimetic (S→D) mutations functionally substitute for phosphorylation (97, 263). Deletion mapping and alanine scanning experiments have identified a region within the N-lobe of the PKR kinase domain corresponding to residues 328-335 which interacts with D3 (98). In NMR experiments, addition of D3 to a labeled peptide consisting of residues 326-337 from PKR produced chemical shifts, indicating binding. The same effect occurred upon addition of PKR-dsRBD2, supporting the hypothesis that D3 and dsRBD2 interact with the same site on the kinase domain (98). Note, however, that an alternative site within the C-lobe has been proposed to maintain the dsRBD2-kinase autoinhibitory interaction (55).

The solution structure of the first dsRBD from PACT has been solved (PDB ID 2DIX; RIKEN Structural Genomics Initiative) (Fig. 6.1D). PACT is the human homologue to Xlrbpa and the two proteins share ~67% sequence identity within dsRBD2 (Fig. 6.1C). The crystal structure of Xlrbpa dsRBD2 in complex with dsRNA is presented in Fig 1.2B. D3 belongs to a class of motifs categorized as type-B dsRBDs which resemble the canonical dsRBD in sequence yet lack the residues necessary for dsRNA binding (Fig. 6.1B) (93, 164). To date, the structure of only a single type-B dsRBD has been solved, dsRBD5 from STAU1 (STAU1-5) (264). The structure reveals how the domain has retained a group of conserved residues which engage in hydrophobic packing interactions in the region between α1 and α2 to stabilize the dsRBD αβββα fold. A sequence alignment between 'true' (type-A) and 'false' (type-B) dsRBDs which is relevant to this study is shown in Fig. 6.1B. Domain 3 from PACT and TRBP both contain the appropriate conserved hydrophobic residues which stabilize the dsRBD fold. Thus, it is likely that, like STAU1-5, they form the canonical αββββα structure. Based on the sequence alignment (Fig. 6.1B) the expected positions for the phosphorylated residues within PACT-D3 are indicated on the structure of PACT-dsRBD1 shown in Figure 6.1D. S246 is expected to replace a RNA-binding residue in region 1 within helix α1. S287 resides in the β2-β3 loop expected to be bigger in both PACT-D3 and TRBP.

PKR activation is intricately controlled *in vivo* by PACT and its functional antipode TRBP (Tar RNA Binding Protein). TRBP is homologous to PACT in sequence and domain organization, with tandem dsRBDs at the N-terminus and a type-B dsRBD at the C-terminus (265). TRBP was originally identified as an endogenous component which enhances HIV replication (266). This activity has been attributed to sequestration of dsRNA by the dsRBDs (267). However, subsequent analyses have indicated that TRBP directly interacts with PKR to inhibit it (268). The proposed interaction mechanism is similar to PACT where the N-terminal dsRBDs interact with the dsRBDs of PKR. In TRBP, the third domain elicits an inhibitory effect (269). As shown in Figure 6.1A and C the third domains of TRBP and PACT are highly

homologous. Thus, the residues which confer the stimulatory phenotype to PACT must be highly specific. PACT and TRBP both homodimerize and can interact with one another allowing for precise control of PKR activity within the cell (265, 270). The PACT-TRBP interaction prevents the stimulatory interaction between PACT and PKR. Phosphorylation of S287 within PACT in response to stress inhibits the TRBP interaction to promote PKR activation (271, 272).

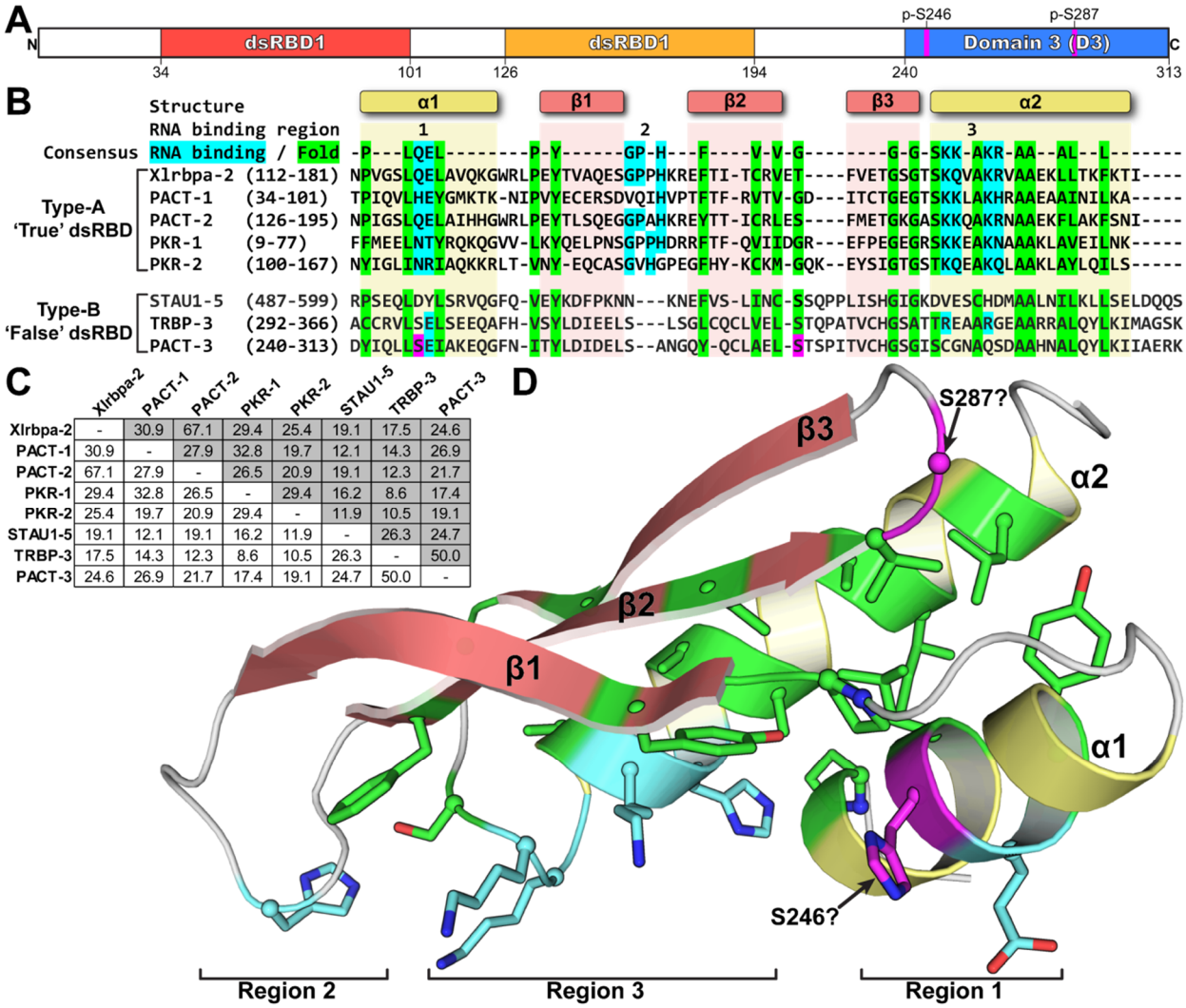

	Xlrbpa-2	PACT-1	PACT-2	PKR-1	PKR-2	STAU1-5	TRBP-3	PACT-3
Xlrbpa-2	-	30.9	67.1	29.4	25.4	19.1	17.5	24.6
PACT-1	30.9	-	27.9	32.8	19.7	12.1	14.3	26.9
PACT-2	67.1	27.9	-	26.5	20.9	19.1	12.3	21.7
PKR-1	29.4	32.8	26.5	-	29.4	16.2	8.6	17.4
PKR-2	25.4	19.7	20.9	29.4	-	11.9	10.5	19.1
STAU1-5	19.1	12.1	19.1	16.2	11.9	-	26.3	24.7
TRBP-3	17.5	14.3	12.3	8.6	10.5	26.3	-	50.0
PACT-3	24.6	26.9	21.7	17.4	19.1	24.7	50.0	-

Figure 6.1 Structure of PACT. (A) Domain organization. **(B)** Structure based sequence alignment of dsRBDs. The protein name is indicated and the number after the hyphen corresponds to the respective dsRBD within each protein. Values in parenthesis represent the amino acids shown in the alignment. A combination of resources was used to generate a sequence alignment. The consensus residues which contribute to RNA binding (cyan) and the dsRBD fold (green) are adapted from (13). Sequences were first aligned in Clustal Omega (180). An additional alignment was performed in Pymol for the sequences with associated structures. The alignment was further manipulated by hand guided by the interpretations of Gleghorn et. al. (93). The phosphorylated residues within domain 3 of PACT are indicated in magenta. **(C)** Pairwise amino acid percent identity matrix for alignment shown in (B). Prepared by Clustal Omega (180). **(D)** Structure of PACT dsRBD1 (PDB ID 2DIX). Amino acids are color coded according to the alignment shown in (B). Cα atoms are shown as spheres. The alignment suggests PACT-D3 adopts a similar fold. Hypothetical locations for the two phosphorylation sites in D3 (S246 and S287) are shown in magenta.

Viruses whose propagation is inhibited by PKR often develop methods to inhibit PKR activation. Examples include RNAs that irreversibly bind PKR, proteins which inhibit PKR dimerization, and proteins that act as decoy phosphorylation substrates (9). Influenza encodes a 26 kDa protein, NS1, which is not part of the virion but is expressed during infection. NS1 is a multifunctional protein which interacts with a variety of host components to promote viral replication (99). The primary role of NS1 appears to be inhibition of the cellular 3′-end processing system which results in retention of host mRNAs in the nucleus (273). By sequestering host mRNA in the nucleus, NS1 increases the amount of viral RNA translated. NS1 has also been associated with inhibition of PKR. Influenza mutants lacking NS1 are attenuated in mice yet replication is rescued in mice containing PKR knockouts (274). The mechanism of PKR inhibition remains controversial. Some studies indicate that NS1 binds and sequesters viral dsRNA from PKR (275, 276) while others show NS1 binds directly to PKR to inhibit activation (100-102). NS1 inhibits PKR activation by both dsRNA and PACT (100, 101). The PKR interaction site has been mapped to residues 123-127 in NS1 (100). The NS1 interaction site on PKR is mapped to the linker region and a mechanism of inhibition has been proposed where NS1 locks PKR in an auto-inhibited state (101).

NS1 contains a unique N-terminal RNA binding domain and a C-terminal effector domain (ED) separated by a short ~15 residue linker (Fig. 6.2A) (277). A disordered C-terminal tail has a strain-specific length up to 33 amino acids and interacts with host components, although its contribution to virulence is unclear (278). The RNA-binding domain dimerizes to form a six-helical bundle (279, 280). The structure of the RNA-binding domain in complex with dsRNA reveals how two long helices lay along the duplex making contacts with the RNA backbone (Fig. 6.2B) (281). The first crystallographic studies of the isolated effector domain (ED) reported multiple dimeric interfaces (282-284). Biochemical and biophysical analysis of isolated effector domain constructs support the helix-helix interface shown in Figure 6.3C in which a highly conserved tryptophan (W187) packs into a hydrophobic pocket on the reciprocal protomer (283,

285, 286). The isolated ED dimerizes weakly in solution (286) yet several studies indicate that this activity contributes to cooperative assembly of NS1 molecules onto dsRNA. Cryo-EM studies have detected tubular filamentous assemblies of NS1 molecules onto long duplex RNAs (287). Mutation of the invariant interfacial tryptophan decreases RNA binding affinity (285). Virulence is severely attenuated in influenza viruses expressing a truncated NS1 lacking the ED yet can be partially rescued by attachment of heterologous dimerization domains (288). The structures of full length NS1 (287, 289) have led to a mechanistic model which reconciles much of the crystallographic and functional data. The model proposes that the relative orientations of the RNA binding domain and the effector domain change to promote different oligomeric configurations of the effector domain. These changes facilitate the myriad of binding interactions and functions attributed to NS1 (289). The proposed assembly of NS1 molecules on a dsRNA is shown in Figure 6.2D.

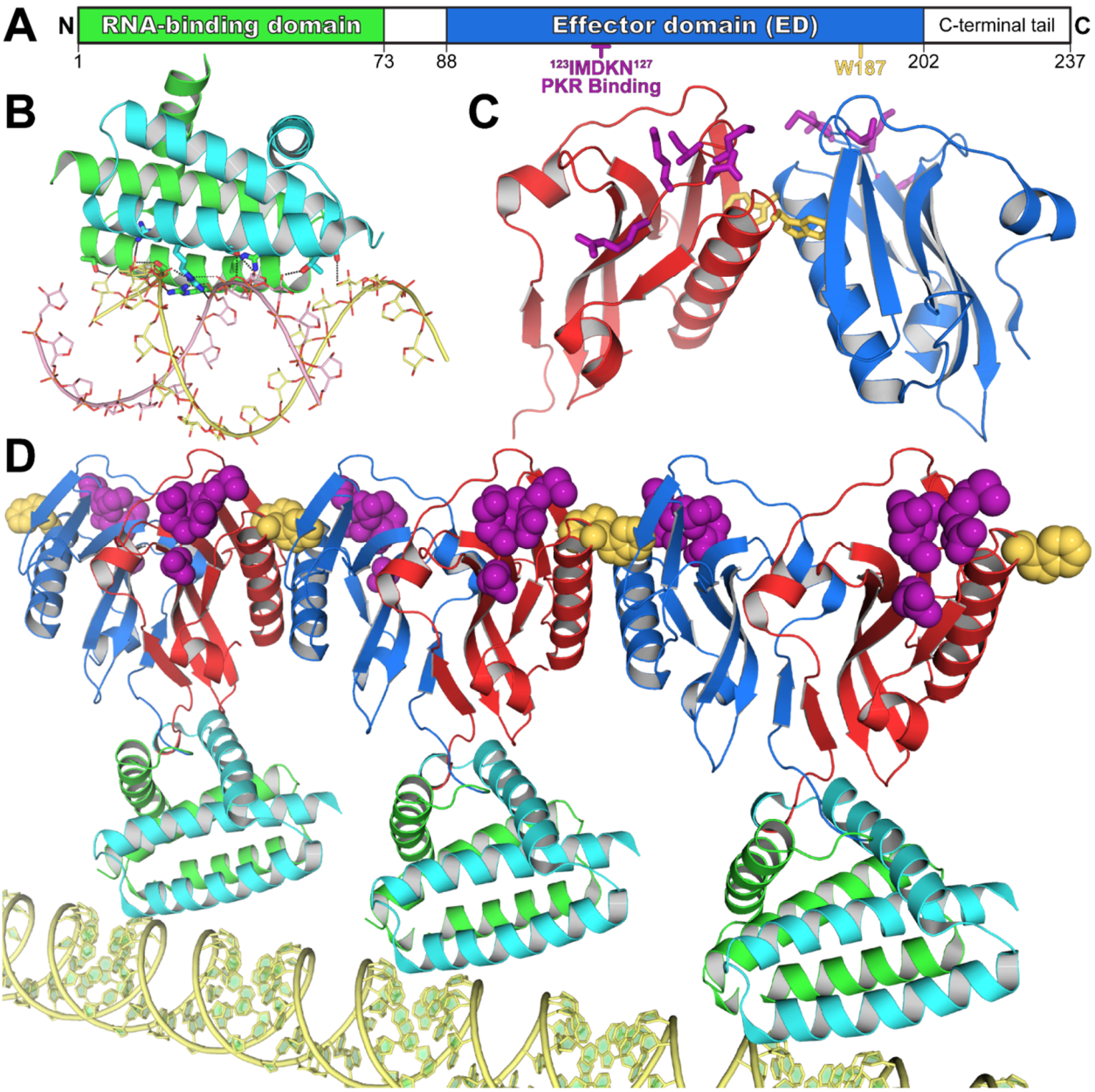

Figure 6.2 NS1 domain organization and structure. (A) NS1 domain organization. The positions of residues implicated in PKR interaction (IMDKN) are indicated in purple. The conserved tryptophan (W187) which mediates dimerization is also shown in yellow. Color coding is maintained throughout the figure. **(B)** Dimer of the RNA-binding domain in complex with dsRNA. Residues which contribute to the interaction are shown as sticks. For clarity nucleotide bases are omitted. (PDB: 2ZKO, (281)). **(C)** Dimeric structure of the effector domain (PDB: 3D6R, (283)). PKR-binding residues and W187 are shown is sticks. Note that in this strain of influenza contains a N127R mutation in the PKR binding site. **(D)** Proposed assembly of NS1 molecules onto dsRNA. Full length NS1 containing a truncation to the linker region (Δ80-84) crystallizes as a dimer (PDB: 4OPA, (289). Effector domains dimerize via the interface shown in (C) across a 2-fold crystallographic symmetry axis. Three asymmetric units are shown in (D). PKR-binding residues and W187 are shown as spheres. Importantly note that duplex RNA has been manually added. This model is adapted from references: (285, 289).

The purpose of this study is to examine the mechanisms by which protein regulators modulate PKR activity. NS1 and PACT elicit opposite effects yet both are proposed to operate by controlling the same conformational switch in PKR. PACT interacts with a region in the kinase domain to break an intramolecular autoinhibitory interaction between PKR-dsRBD2 and the kinase domain (98). NS1 interacts with the linker region (residues 170-230) to lock PKR into the autoinhibited conformation (100, 101). However both these mechanisms are incompatible with evidence which indicates PKR does not adopt the autoinhibited conformation in the latent state (reviewed in Section 1.4). Heparin and dsRNA both activate PKR by facilitating kinase domain dimerization (63, 91). Thus it seems likely that PACT activates PKR by promoting oligomerization or by inducing a similar allosteric effect within the activate site as mediated by the back-to-back PKR dimer interface. The interactions of PACT and NS1 with PKR have been assayed primarily by the use of two-hybrid assays and co-immunoprecipitation assays often in crude or partially purified lysates (92, 95, 96, 100, 101). These assays cannot distinguish the stoichiometry of the interacting complexes or whether additional components are involved. Here we apply sedimentation velocity analytical ultracentrifugation using purified protein preparations to probe these interactions.

Results

6.2 Characterization of NS1 and PKR interaction

We have expressed the effector domain of NS1 encoding residues 74-230 from H1N1 influenza A/Puerto Rico/8/1934 (NS1-ED) containing a N-terminal his-tag. As an initial step toward analyzing the interaction with PKR we characterized the association state of NS1-ED by sedimentation velocity in AU200 buffer. In agreement with earlier reports (285, 286) the effector domain dimerizes in solution (Fig. 6.3A). The time difference curves were fit to a monomer-dimer equilibrium model in SEDANAL (118). The K_d obtained from the fit was 7.1 μM (4.47, 9.73) with a monomer s value of 1.80 S (1.78, 1.82) and dimer s value of 2.50 S (2.50, 2.51) and rmsd of 0.0347. A similar sedimentation velocity protocol was employed to investigate the

interaction of NS1-ED with PKR. NS1-ED was titrated against PKR up to a 2:1 molar equivalence ratio. Our analysis does not detect the interaction with PKR which has been reported in the literature (100, 101). The NS1-ED monomer-dimer equilibrium causes concentration dependent formation of a complex at 2.50 S. However, a species does not form at sedimentation coefficient values above ~3.4 S where PKR freely sediments.

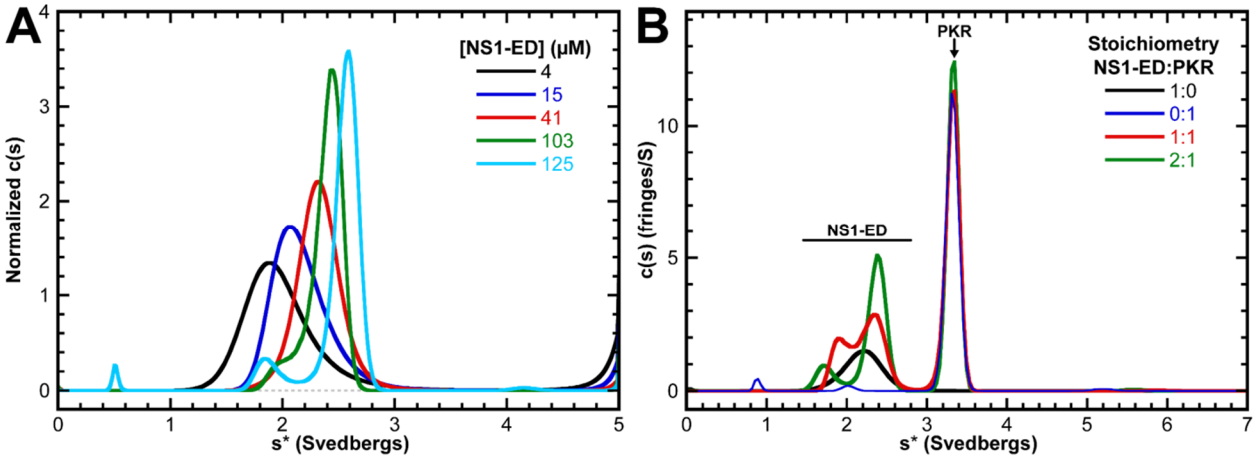

Figure 6.3 Characterization of NS1 and PKR. (A) Dimerization of the NS1 effector domain. Sedimentation velocity was used to monitor the concentration dependence of NS1-ED oligomerization. Measurements were obtained in AU200 buffer at 20 °C and 55,000 rpm using interference optics. The data are represented as c(s) distributions which are normalized by area. Parameters obtained from fitting the data to a monomer-dimer equilibrium model are reported in the text. **(B)** Analysis of NS1-ED:PKR interaction. Sedimentation was monitored at 50,000 rpm in AU200 buffer at 20 °C and 55,000 rpm using interference optics. Samples were prepared at a fixed concentration of PKR with addition of NS1-ED. Sedimenting species are labeled. The trace for PKR alone is drawn thinner to show the distributions underneath.

6.3 Characterization of PACT

In agreement with earlier reports (92, 94) full length PACT resides in the insoluble fraction when expressed in *E. coli*. Attempts to optimize expression and cell lysis protocols failed to yield soluble protein. A His-tagged version of PACT was solubilized with 4 M urea and refolded while bound to Ni^{2+}-NTA resin by running a decreasing gradient of urea. The His-tag was cleaved prior to most of the assays reported here. The initial set of experiments were designed to examine the refolded protein (Fig. 6.4). The protein readily aggregates at 20 °C so most experiments are performed at 4 °C. The circular dichroism spectra indicates the presence of secondary structure with minima at 208 and 222 nm characteristic alpha helical content (290)

(Fig. 6.4A). PACT sediments as a strongly associated dimer with a corrected sedimentation coefficient ($s_{20,w}$) of 3.8 S (Fig. 6.4B). Misfolded protein are expected to aggregate. Sedimentation velocity was used analyze the interaction of a 20 bp dsRNA with PACT at 4 °C in 200 mM NaCl (Fig. 6.4C). The distributions shift to a sedimentation coefficient of ~6 S as PACT is added indicative of complex formation. The data fit well to a model where the PACT homodimer interacts with the RNA to form a 2:1 complex with a K_d = 94 nM and RMSD = 0.00816 OD. For comparison, full length PKR binds to the same 20 bp dsRNA with an affinity of 300 nM in 200 mM NaCl at 20 °C (62). This result demonstrates that PACT is competent to bind dsRNA with high affinity and indicate that the refolding protocol was successful. Finally, resistance to proteolytic digestion by trypsin indicates regions that are protected (Fig. 6.4D). In the protease titration PACT remains largely intact until addition of a 1:2,500 ratio of trypsin/PACT. In contrast, a 1:20,000 ratio induces substantial cleavage of PKR within the unstructured linker region (59). The ~17 kDa intermediate band that forms from proteolysis of PACT presumably corresponds to either of the dsRBDs or D3 which are all approximately equal in size and expected to have molecular weights of ~15 kDa. Taken together, these analyses indicate PACT is refolded and suitable for further characterization.

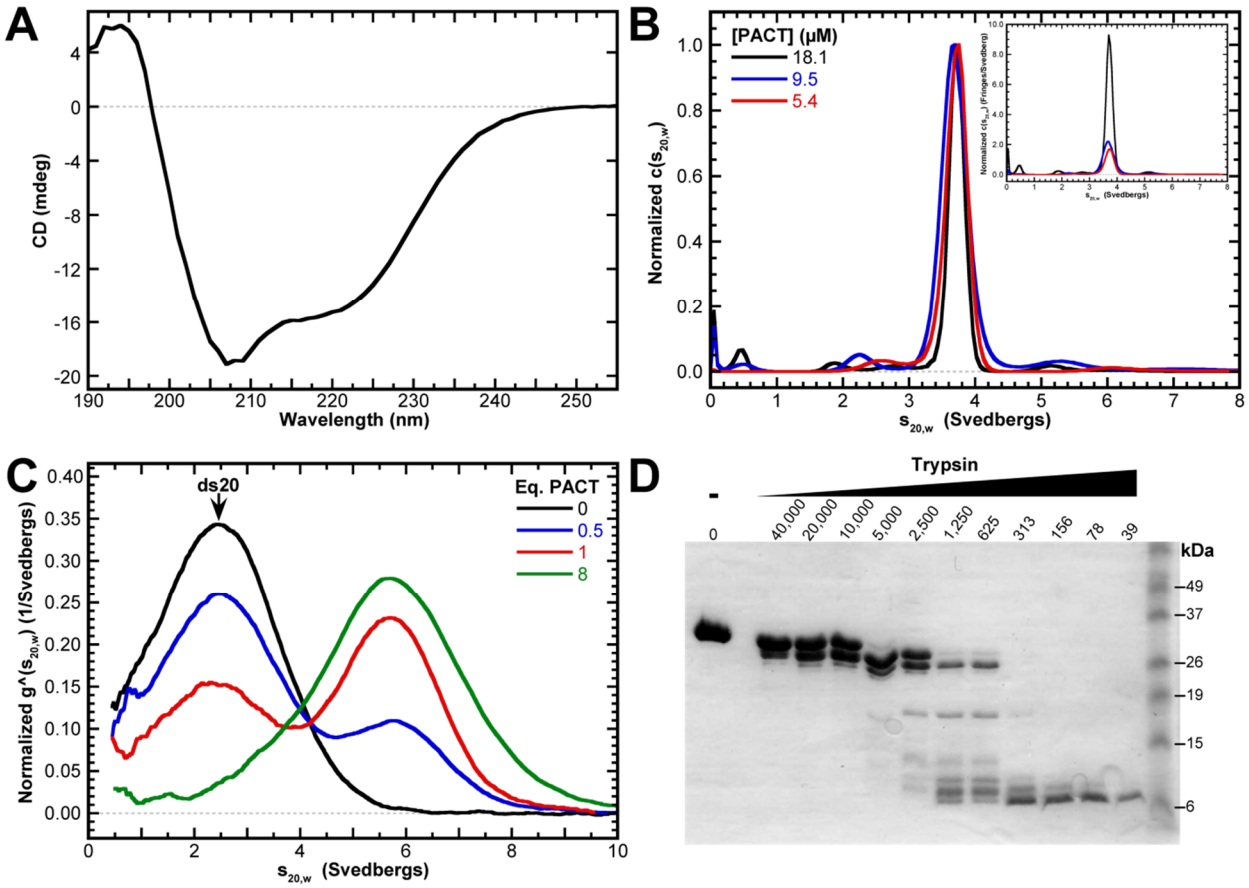

Figure 6.4 Characterization of full length PACT. (A) Circular dichroism analysis of the refolded protein. **(B)** Sedimentation velocity analysis. Sedimentation was monitored at 50,000 rpm by the interference optical system in AU200 buffer at 4 °C. c($s_{20,w}$) distributions normalized by amplitude are shown with the raw data in the inset. PACT sediments as a strongly associated dimer with $s_{20,w}$ = 3.8 S. The data were fit to a discrete species model yielding a molecular weight of 65.3 kDa (predicted monomer = 34.7 kDa). **(C)** Interaction with duplex 20 bp RNA. g^($s_{20,w}$) distributions are normalized by area. Samples contained 1.5 μM 20 bp dsRNA and the indicated equivalence ratio of PACT. The data were fit a model where the PACT dimer binds the RNA to form a 2:1 complex. The fit produced a K_d = 94 nM (76, 114) with an RMSD of 0.00816 OD. The fitted complex sedimentation coefficient was $s_{20,w}$ = 5.98 S (5.90, 6.05). **(D)** Limited proteolysis of PACT. Full length PACT(his) was incubated at 0.67 mg/ml with various ratios of PACT/trypsin for one hour at 4 °C. A 3 hour incubation yielded the same digestion

6.4 Interaction studies with PKR

Sedimentation velocity was used to investigate the interaction between PACT and PKR at 4 °C in 200 mM NaCl (Fig. 6.5A). Under these conditions, PKR exists as a monomer with $s_{20,w}$ = 3.5 S and PACT is a dimer with $s_{20,w}$ = 3.8 S. Mixtures were prepared at multiple PACT:PKR ratios. Formation of a complex would result in the appearance of higher s species. However, the

$c(s_{20,w})$ distributions of the mixtures appear as sums of the individual components, indicating that PACT and PKR do not interact under these conditions. We introduced the phosphomimetic mutations within D3 purported to enhance PKR affinity (263). S246D/S287D PACT has a slightly higher sedimentation coefficient ($s_{20,w}$ = 3.9 S) than the wild-type protein indicating that it may adopt a more compact structure (Fig. 6.5B). Like wild-type PACT, the $c(s_{20,w})$ distributions are the sum of individual components indicating that in our analysis the phosphomimetic mutations do not promote a PACT PKR interaction. Activation of PKR by PACT was assayed by monitoring the stimulation of ^{32}P incorporation from [γ-^{32}P]ATP into PKR (Fig. 6.5C). The data are quantitated in Figure 6.5D and normalized to the autophosphorylation of PKR in the absence of an external activator. Control samples demonstrate that a 40 bp dsRNA activates PKR. However, both wild-type and S246D/S287D PACT fail to activate PKR and actually inhibit the baseline activation. At elevated PACT concentrations an additional band appears lower on the gel which corresponds to phosphorylated PACT. Thus, PKR can phosphorylate PACT indicating the two proteins must at least transiently interact. PACT activation is allegedly RNA-independent (92) yet RNA can contaminate purification of RNA-binding proteins (291). Additional samples were included in the S246D/S287D PACT experiment to ask whether PACT promotes dsRNA-induced activation of PKR. PACT inhibits activation by 40 bp dsRNA at higher concentration (1.8 µM), presumably due to competition for the RNA. At lower concentrations (0.2 µM) PACT facilitates a slight increase in ds40 induced activation. An assay to investigate this result has not been performed.

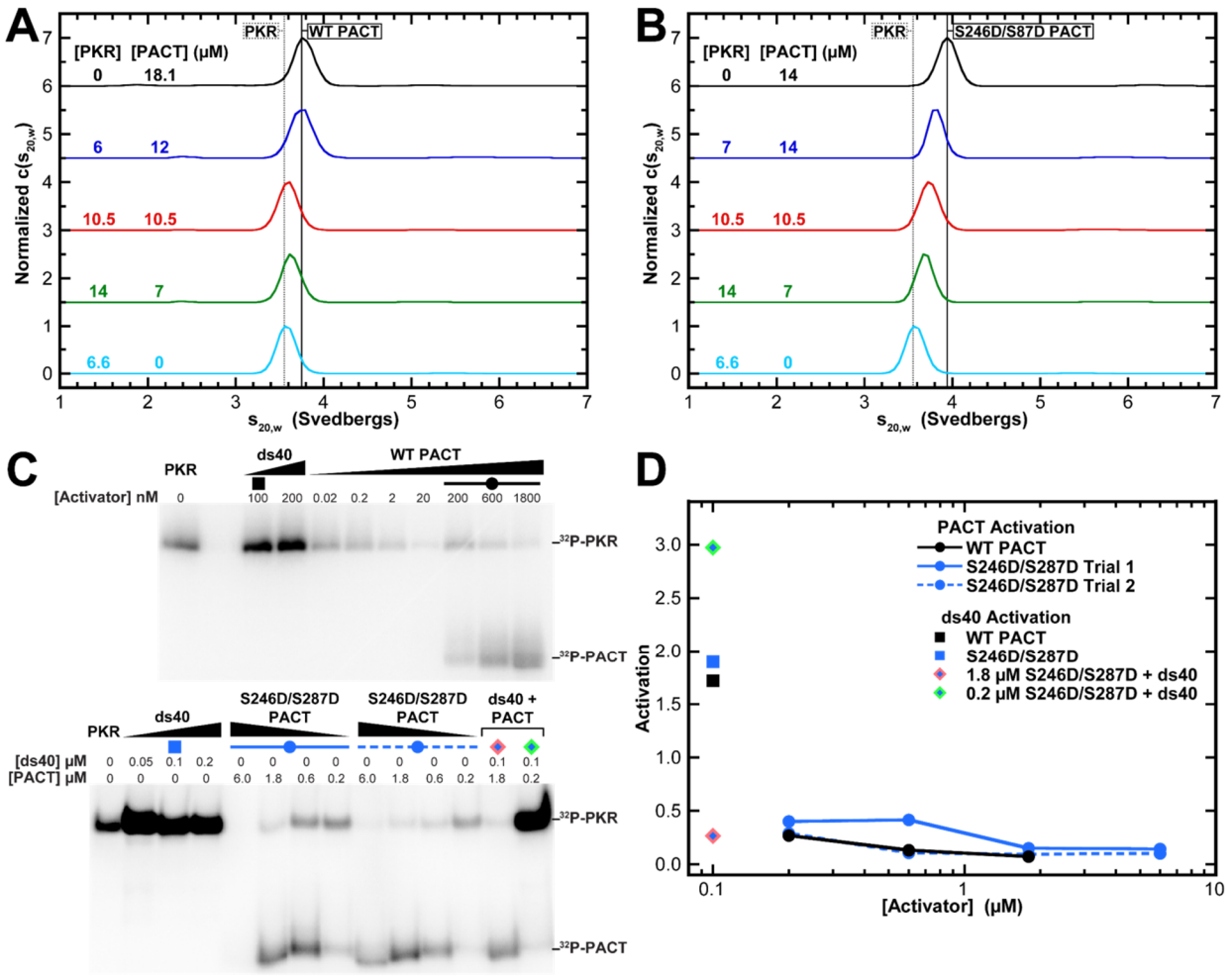

Figure 6.5 Full length PACT and PKR. (A) Sedimentation velocity analysis of WT PACT and PKR. c($s_{20,w}$) distributions are normalized by amplitude and offset. Sedimentation was monitored at 50,000 rpm by the interference optical system in AU200 buffer at 4 °C. Loading concentrations of PACT and PKR are indicated along the traces. A dashed vertical line indicates the sedimentation coefficient of PKR and a solid line is drawn for PACT. **(B)** Sedimentation velocity analysis of S246D/S287D PACT and PKR. Experimental conditions and data representation are as in (A). **(C)** Activation assays with PACT. 200 nM PKR was assayed for activation by both wild-type (top) and S246D/S287D PACT (bottom). The assay was performed in P50 buffer at 32 °C over a 20 min time course. A duplex RNA consisting of 40 bp served as a positive control. PKR phosphorylates PACT and the position of the two proteins are indicated on the gel. The symbols correspond to quantitated values shown in (D). **(D)** Quantitation of

6.5 PACT domain 3

Our functional analysis of refolded PACT confirmed the protein was competent to bind dsRNA indicating at least one of the dsRBDs was properly folded. However the only functional analysis for D3 is PKR activation and our results disagree with published observations (92). Previous studies have had success with purification of a recombinant isolated D3 construct from

the soluble fraction of *E. coli* lysates (94). We created domain constructs to match the previous report (94). A construct encoding dsRBD1 and 2 consists of residues 1-194. The isolated D3 construct contains residues 195-313. The dsRBD1+2 construct is insoluble indicating this is the region responsible for insolubility of the full length protein. However the D3 construct is soluble and was purified to high yield. As a first step toward characterizing the interaction of D3 with PKR we measured the protein concentration dependence of self-association of the newly isolated construct. D3 was much more stable than the full length protein permitting experiments at 20 °C. Like the full length protein, D3 sediments as a strongly associated dimer with an $s_{20,w}$ = 2.41 S (Fig. 6.6A). Others have found that domain 3 induces dimerization of full length PACT and its homologue Xlrbpa (292). In Xlrbpa, the region which mediates dimerization has been mapped to the last five residues at the C-terminus.

Next, we performed binding assays with PKR. The analyses on full length PACT were performed at 4 °C in AU200 buffer (200 mM NaCl). We have probed for a D3-PKR interaction at 20 °C in AU200, AU75 (75 mM NaCl), and P50 (50 mM KCl, 5 mM $MgCl_2$) buffers and the sedimentation profiles are similar. The data generated in P50 buffer is presented in Figure 6.6B since P50 is the buffer used in activation assays. PACT-D3 and PKR have different sedimentation coefficients so the two species are resolved by c(s) analysis. Like full length PACT we do not detect a complex between D3 and PKR. However, domain 3 induces concentration-dependent activation of PKR (Fig. 6.6C). Activation is weak, with a maximum ~1.8-fold over PKR background activity occurring at 6 µM D3, corresponding to a 30-fold molar excess over PKR. Similar to activation by RNA (63) and heparin (91), the activation curve is bell-shaped, implying that PACT induces dimerization similar to other activators. Activation implies, of course, that D3 and PKR interact. The complex may be transient or too weak to detect by sedimentation velocity. To trap the complex we employed chemical crosslinking with the homobifunctional amine-reactive crosslinker disuccinimidyl suberate (DSS) (Fig. 6.6D). Samples were prepared with a fixed concentration of PKR and titration of D3 up to a 10-fold

molar excess. Addition of DSS induces concentration-dependent formation of D3 dimer adducts but a PKR-D3 crosslink is not detected. Additional samples were included to ask whether ATP and magnesium facilitates complex formation. However no PACT-D3 crosslink was detected in these samples either. We have extended the titration to higher D3-PKR stoichiometries (up to 700 μM D3) but still did not detect a complex (data not shown). At elevated concentrations of D3, crosslinking by DSS induces a laddering effect indicating D3 may form even higher oligomeric species than dimer.

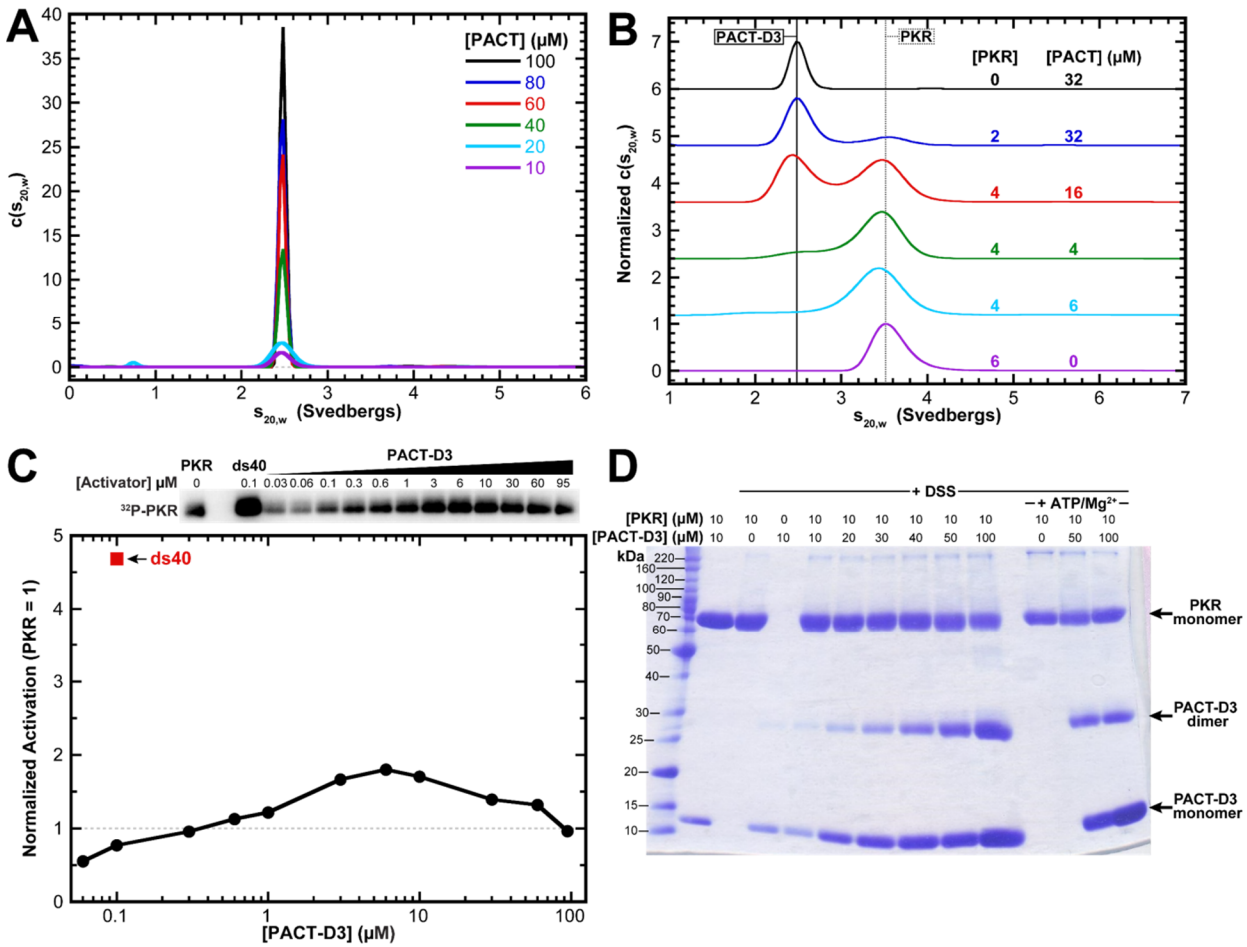

Figure 6.6 PACT domain 3 and PKR. (A) Sedimentation velocity analysis of PACT D3 construct. Sedimentation was monitored at 50,000 rpm by the interference optical system in AU200 buffer at 20 °C. Domain 3 sediments as a strongly associated dimer with $s_{20,w}$ = 2.41 S. The data were fit to a discrete species model to yield a molecular weight of 30,591 Da (expected monomeric weight = 15,173 Da). **(B)** Sedimentation velocity analysis of PACT-D3 and PKR. The experiment was conducted in P50 buffer at 20 °C. Each distribution is normalized to peak amplitude and offset along the y-axis. Loading concentrations of PACT-D3 and PKR are indicated along each distribution. Vertical lines indicate the sedimentation coefficients for PACT-D3 (solid line) and PKR (dashed line). **(C)** Activation assays with PACT-D3. 200 nM PKR was assayed for activation by the domain 3 construct in P50 buffer at 32 °C over a 20 min time course. The 40 bp dsRNA serves as a positive control. The phosphorimage is shown on the top. The data and quantitated in the plot below and normalized to the activation of PKR in the absence of activator. Activation by ds40 is indicated by a red square. **(D)** Chemical crosslinking. PKR was titrated with PACT-D3 in P50 buffer. DSS was added to 10-fold molar excess and the reaction was allowed to proceed for 30 min at RT. Samples were resolved on a 4-12% acrylamide tris-glycine gel run under denaturing conditions and visualized by Coomassie Blue staining. The final three lanes contain 400 μM ATP plus 5 mM $MgCl_2$. The molecular weights of the protein ladder are indicated on the left (kDa) and the species within the gel are indicated on the right. Concentration dependent formation of a PACT-D3 dimer is detected however a PACT-PKR adduct is not formed.

6.6 Discussion

This study reports the analysis of two RNA-binding proteins reported to interact with PKR and elicit opposite effects. However, our analyses do not detect complex formation with either protein. The commonality between all the proteins under investigation is their RNA-binding activity and this behavior may rationalize the experimental differences. Co-immunoprecipitation in cell extracts or two-hybrid experiments are the primary assays which have defined the interactions between PKR and NS1 (100-102) or PACT (92, 94-97). Convincing control experiments are sometimes included to rule out co-precipitation of proteins on a single RNA (92, 101). However, these controls are often not incorporated into the studies which have defined the protein-protein interaction sites. One study has demonstrated that the RNA-binding domains of NS1 are required for PKR interaction (102) and another showed that NS1 interacts with a region encompassing the dsRBDs and linker on PKR (101). The models for PACT and TRBP modulation of PKR activity postulate that high-affinity interactions between the dsRBDs anchor protein-protein interactions and the third domains of PACT or TRBP elicit opposite enzymatic effects (269). Mutations to RNA-binding residues within PKR's dsRBDs (K60A, K64A, K150A, K154E, see Fig. 1.2) diminish interaction with both PACT or TRBP in a two-hybrid assay (269). Based on these effects the residues have been implicated in direct protein-protein interactions. However, it seems more likely that an interaction facilitated by dsRNA produced false positive results in the two-hybrid assays. PACT, TRBP, and NS1 belong to an expanding family of RNA-binding proteins reported to directly engage PKR. ADAR (293), NF90 (294), DUS2 (295), and the herpes simplex virus type 1 protein Us11 (296) have all been identified by pulldown assays and are implicated in PKR inhibition by direct protein-protein interactions.

Additional experimental differences may contribute to the divergent outcomes between our analysis of PACT- and NS1-PKR interactions and earlier reports. In previous PACT and NS1 studies, PKR is typically obtained from cellular extracts of human cell lines and partially

purified using an affinity tag. Cellular components which remain bound to PKR or post-translational modifications which would not be present in our PKR preparations may contribute to the interaction between PACT or NS1. Both the NS1 and PACT protein constructs used in the studies are also different. We have used NS1 from the H1N1 influenza A/Puerto Rico/8/1934 (PR8) virus whereas PKR-NS1 interactions have primarily been characterized in the context of NS1 from H3N2 A/Udorn/1972 (Udorn) (100, 101). PR8 contains the residues at positions 123-127 which have been implicated in PKR interaction (100). However, Udorn NS1 has a 7 residue addition to the C-terminal tail and additional amino acid changes which may be important for binding PKR. We have obtained a plasmid encoding full length Udorn NS1 to test for strain specific PKR interactions.

Our NS1 study supports the PKR inhibition model in which NS1 shields duplex RNA from PKR (275, 276). The alternative model suggests that residues 123-127 within NS1 directly engage the N-terminal region of PKR to lock PKR in an autoinhibited state (100, 101). Residues 123-127 were identified by the effects of mutagenesis on co-immunoprecipitation in cell extracts (100). However, RNase was not added to the assay and residues 123-127 are located proximal to the effector domain dimeric interface (see Fig. 6.2C, D). The dimerization activity of the effector domain is critical for cooperative association of NS1 molecules onto duplex RNA (286, 297). Thus, it is possible that mutagenesis of residues 123-127 affects RNA binding rather than PKR interaction. Filamentous assemblies of NS1 onto RNA has been observed by cryo-EM (287) and a model has been proposed in which NS1 encapsulates the RNA with effector domains forming an oligomeric chain along the outside of the complex (289) (Fig. 6.2D). NS1 has been implicated in the inhibition of other antiviral proteins which respond to viral RNA including 2′-5′-oligo (A) synthetase (298) and RIG-I (299). The encapsulating assembly of NS1 molecules around an RNA would provide a common mechanism to inhibit a variety of intracellular immune receptors.

Similar to our NS1 analysis, we do not detect formation of a PKR-PACT complex in sedimentation velocity experiments. Full length PACT does not activate in PKR autophosphorylation assays, however, the isolated D3 construct weakly activates. We are unable to characterize the activation mechanism since a complex is not formed in sedimentation velocity experiments or captured by chemical crosslinking. The absence of measurable complex formation may be explained by a weak, transient interaction between PKR and D3 below the detection limits of the optical system in the analytical ultracentrifuge. Phosphorylation enhances PKR dimerization affinity by ~ 500-fold and we have previously proposed a branched chain reaction model to explain how strong PKR activation can be induced by dimerization at concentrations well below the K_d for latent enzyme (61). By analogy, weak complex formation between the PACT-D3 and PKR may serve to initiate a cascade of PKR autophosphorylation resulting in activation.

The experimental differences previously addressed in the context of NS1-PKR interaction studies extend to the PACT-PKR investigations. PKR prepared from cellular extracts of human cell lines may contain post-translational modifications or additional components which contribute to the interaction. In support of this, the results from one study indicates the PACT-PKR interaction may be specific to certain cell lines (300). Others have found that PACT actually inhibits PKR activation in some cell types (271). Also analogous to the NS1 interaction study, the PACT constructs used here are different from those previously analyzed. The original PACT expression vector contained a frameshift mutation at the 3′-end which results in a construct encoding the wild-type sequence at residues 1-300 with five random amino acids at the C-terminal end (KLCSI) (92). The mutation is addressed in a subsequent study (95) although it was not corrected and it appears as though this mutated form of PACT is used in all subsequent analyses. Others have had difficulties recapitulating the stimulatory effect of PACT *in vivo* and have analyzed the mutant form of PACT (PACTΔ13) to resolve the discrepancy (271). PACTΔ13 activates PKR more potently than wild-type PACT in certain cell lines but both

forms of PACT have no effect in others. The C-terminal residues in the PACT homologue Xlrbpa mediate protein dimerization (292). We have expressed PACTΔ13 and characterized its association state by sedimentation velocity. The experiment was performed under different conditions than wild-type PACT. However, PACTΔ13 was monomeric up to the highest concentration assayed. It may be worthwhile to extend the analysis to further characterize PACTΔ13 and the effect of PACT oligomerization on PKR activation. A PACT-TRBP interaction is proposed to inhibit the stimulatory interaction between PKR and PACT (271). Likewise, formation of the PACT dimer may prohibit PKR binding and activation by a similar mechanism.

Chapter 7: Conclusions

The canonical activators of PKR are long stretches of duplex RNA regions (>30 bp) present in viral transcripts. However, an expanding family of RNAs characterized by limited regions of extended duplex has been described as PKR activators. These RNAs lack the minimal duplex length requirements for PKR activation and alternative structural elements are proposed to modulate PKR activity. Notably, single-stranded regions and a 5′-triphosphate (5′-ppp) were reported to be important determinants for activation when attached to minimally structured regions. This class of minimally structured RNAs has been defined as ss-dsRNAs although the structural variability of RNAs within this category has become increasingly broad.

We began our analysis of the ss-dsRNA motif by creating a 15 bp duplex stem capped by a tetraloop and flanked by 15 nt single-stranded tails. To gain insight into the contribution of the single-stranded regions to PKR activity we systematically dissected each tail in 5 nt increments and characterized the effects on binding affinity and activation. Activation distributions reveal a bell-shaped activation profile suggesting that, like duplex RNAs, ss-dsRNAs mediate PKR dimerization to induce activation by formation of the RP_2 complex. We have previously characterized the length dependence of perfect duplexes on binding affinity and activation. Activation by dsRNAs requires a 2:1 binding stoichiometry and activation potency increases with the population of the RP_2 species. Under the conditions we analyzed the ss-dsRNAs all bind two PKR, however, not all activate. Thus, ss-dsRNAs do not exhibit the same strict requirement for binding stoichiometry as perfect duplexes. Our measurements detect a weak correlation between tail length, binding affinity, and activation potency. Deletion of the tails drastically reduces binding affinity and abolishes activation. However, some constructs with intermediate tail lengths bind with only moderate affinity yet activate potently. Conversely, other constructs bind tightly but fail to activate. The composition of nucleotides within the tails is not identical and there may be nucleotide identity preferences for activation. Alternatively, the variability may reflect specific conformational requirements which determine how two PKR

molecules interact on the RNA. Our model for PKR activation by duplex regions postulates that dsRNA serves as a scaffold for the assembly of PKR monomers. Single-stranded regions may have a more activate role in coordinating the orientation of interacting PKR molecules. In this scenario longer tail lengths may not promote the appropriate assembly of PKR monomers bound to the RNA.

More broadly, the results imply that single-stranded regions interact with PKR and can induce activation. The isolated dsRBD construct does not exhibit the same magnitude increase in affinity toward an ss-dsRNA containing tails as observed in full length PKR indicating single-stranded region engage a region outside the dsRBD. Based on this analysis we extended our study to examine interactions between isolated ssRNAs and PKR domain constructs. We used analytical ultracentrifugation to determine the affinity of single-stranded RNA and other nucleic acids toward different regions of PKR and the contribution of the 5′-ppp to binding. Our analysis identifies a previously unrecognized RNA binding site N-terminal to the canonical kinase domain boundary (the basic region). The basic region and the dsRBD bind single-stranded nucleic acids with low micromolar affinities. Both regions also engage dsRNA although the affinity of the dsRBD for duplex region is ~100-fold tighter. We developed a crosslinking assay to gain insight into the how an RNA containing duplex and single-stranded regions engages these two distinct regions on PKR. PKR constructs containing a TEV protease cleavage site were crosslinked to ^{32}P-15-15-15 containing 4-thiouridine. The TEV cleavage distributions indicate that RNA contacts the basic region in the context of full length PKR. Isolated ssRNA weakly activates full length PKR and a kinase domain construct containing the basic region. The affinity and activation potency of isolated ssRNA is most likely insufficient to elicit an effect *in vivo*. However, anchoring interactions between the dsRBD and duplex regions may promote an interaction between auxiliary single-stranded RNA and the basic region by induced proximity effects (166). This type of bivalent complex may be responsible for PKR activation by ss-dsRNAs.

Activation by ss-dsRNAs has been reported to be dependent on a 5′-ppp. However, our analysis of the ss-dsRNA motif does not recapitulate these observations. We show that RNAs produced by *in vitro* transcription reactions are efficiently dephosphorylated by enzymatic treatment yet PKR stimulation is not affected. The relative binding affinities support the activity measurements. In the context of 15-15-15 affinity is only moderately enhanced for the 5′-ppp form so that the populations of RP_2 species formed by interaction with 5′-ppp and 5′-OH 15-15-15 are similar. We extended our analysis of single-stranded RNA interactions to localize the 5′-ppp recognition site using the PKR domain constructs. However, we find there is no specific 5′-ppp binding site. Instead, affinity toward both the dsRBD and the basic region is enhanced by the presence of a 5′-ppp. The enhancement is moderate and similar in magnitude as observed in the context of full length PKR binding 15-15-15. The isolated helicase domain of RIG-I also binds 5′-ppp RNAs with slightly enhanced affinities and this activity has been attributed to a nonspecific electrostatic effect (197). However, RIG-I contains a C-terminal domain which imparts 5′-ppp specificity by a cluster of basic residues molded to cradle the triphosphate (196). The isolated CTD binds to an RNA containing a 5′-ppp with 12,000-fold enhanced affinity relative to the 5′-OH form (197).

The basic region binds nucleic acids with moderate affinity, contributes to enzymatic activation, and is conserved among PKR orthologs. These observations provided the impetus for structural analysis of this region. We crystallized a kinase domain construct containing the basic region and obtained an atomic resolution structure by X-ray diffraction. Unfortunately, the basic region is unresolved in the structure and we are currently attempting to stabilize the basic region by co-crystallization with heparin and ssRNA. However, a unique arrangement of PKR molecules within the crystalline lattice challenges the current models for PKR activation. PKR forms an oligomeric chain consisting of alternating back-to-back and front-to-front interfaces. The back-to-back interface is similar to those previously reported (29, 30). Two front-to-front interfaces are formed. One is formed by crystallographic symmetry across two asymmetric units

and involves interactions between αG and αEF helices. The other occurs within the asymmetric unit and is formed by activation segments which are exchanged between reciprocal protomers. Similar arrangements have been reported for other kinases and functional data indicate that they represent *trans*-autophosphorylation complexes (33, 230). Mutational analysis indicates the back-to-back PKR dimer interface is critical for function (39). Experiments to investigate the front-to-front interface have not yet been performed. A structural homolog to PKR, PknB, may provide insight, both into the allosteric coupling between dimer interface and active site residues and the mechanistic relevance of the front-to-front interface. PknB forms a back-to-back interface similar to PKR which is also important for function (206, 208). In the monomeric structure of PknB, the N- and C-lobes are misaligned and the αC helix is rotated, positioning the catalytically important glutamate away from the active site (225). A front-to-front interface has also been reported for PknB and is also essential for enzymatic function (212). Based on these observations, a model has been proposed in which the back-to-back dimer interface activates the enzyme. Subsequently, the active dimer phosphorylates other PknB molecules in *trans* via the front-to-front interface (212, 225). The proposed model is strikingly similar to the arrangement of molecules within the asymmetric unit of structure 2 (Fig. 5.3B) suggesting PKR may achieve activation loop phosphorylation by a similar mechanism. The functional assays proposed in Section 5.12 are required to assess the role of the front-to-front interface during PKR activation. If experiments support the front-to-front interface, models for PKR activation must be revised to account for a trimeric complex. Previously, we have correlated activation potency with the ability of molecules to facilitate PKR dimerization (62, 63, 91, 119). However, a trimeric PKR complex may be the more enzymatically relevant species.

Appendix 1: Nucleic acid sequences and molar extinction coefficients

Table A1.1 Sequences and molar extinction coefficients of nucleic acids.

Nucleic acid	Sequence[a]	ε_{260}[b] ($M^{-1}cm^{-1}$)
15-15-15	GGAGAACUUAAUGCCGGAGACCAAAGACUUUCCGAAGUCUUUGGUCUCCCUUACAAACCUGACU	517184
15-15-15 ΔT (GAAA)	GGAGAACUUAAUGCCGGAGACCAAAGACUUGAAAAAGUCUUUGGUCUCCCUUACAAACCUGACU	531851
15-15-15 ΔT (UUUU)	GGAGAACUUAAUGCCGGAGACCAAAGACUUUUUUAAGUCUUUGGUCUCCCUUACAAACCUGACU	519511
15-15-15 ΔT	5′-GGAGAACUUAAUGCCGGAGACCAAAGACUU-3′ 3′-UCAGUCCAAACAUUCCCUCUGGUUUCUGAA-5′	500938
15-15-10	GGAGACAAUAAUACAGGAGACCAAAGACUUUCCGAAGUCUUUGGUCUCCAAACCUGACU	497376
15-15-5	GGAGAACUUAAUGCCGGAGACCAAAGACUUUCCGAAGUCUUUGGUCUCCAGACU	453418
10-15-15	GGACAUAAUAGGAGACCAAAGACUUUCCGAAGUCUUUGGUCUCCCAAACAAACAUAACU	490269
10-15-10	GGAGAACUUAGGAGACCAAAGACUUUCCGAAGUCUUUGGUCUCCAAACCUGACU	414156
13-15-10	GGACCAUAAUAUAGGAGACCAAAGACUUUCCGAAGUCUUUGGUCUCCAAACCUGACU	485892
13-15-5	GGACCAUAAUAUAGGAGACCAAAGACUUUCCGAAGUCUUUGGUCUCCAGACU	444663
10-15-5	GGACAAUAUAGGAGACCAAAGACUUUCCGAAGUCUUUGGUCUCCAAACU	416785
5-15-15	GGACAGGAGACCAAAGACUUUCCGAAGUCUUUGGUCUCCCAAACAAACAUAACU	447230
5-15-10	GGAUAGGAGACCAAAGACUUUCCGAAGUCUUUGGUCUCCAAACAUAACU	413329
5-15-5	GGAGAGGAGACCAAAGACUUUCCGAAGUCUUUGGUCUCCAGACU	341236
15-15-0	GGAGAACUUAAUGCCGGAGACCAAAGACUUUCCGAAGUCUUUGGUCUCC	404417
0-15-15	GGAGACCAAAGACUUUCCGAAGUCUUUGGUCUCCCUUACAAACCUGACU	380311
0-15-0	GGAGACCAAAGACUUUCCGAAGUCUUUGGUCUCC	340834
15-10-15	GGAGACAAUAAUACAGGAGACCAAAUCCGUUUGGUCUCCCAAACAAACAUAACG	455786

Table A1.1 Continued.

Nucleic acid	Sequence[a]	ε_{260}[b] ($M^{-1}cm^{-1}$)
15-5-15	GGAGAAUAGAAUACAGCGACUCCGGUCGCACAUAAGAUAAGAGG	404000
0-5-0	GCGACUCCGGUCGC	117499
U30	UUUUUUUUUUUUUUUUUUUUUUUUUUUUUU	291200
U15	UUUUUUUUUUUUUUU	145700
ppp-Het30	GGAGAACUUAAUGCCGGAGACCAAAGACUU	309700
Het30	GGAGAACUUAAUGCCGGAGACCAAAGACUU	309700
dT30	dTdTdTdTdTdTdTdTdTdTdTdTdTdTdTdTdTdTdTdTdTdTdTdTdTdTdTdTdTdTdT	243600
dHet30	dGdGdAdGdAdAdCdUdUdAdAdUdGdCdCdGdGdAdGdAdCdCdAdAdAdGdAdCdUdU	298300
ds20	5′-GGAGAACUUCAUGCCCUUCG-3′ 3′-CCUCUUGAAGUACGGGAAGC-5′	321800
ds30	5′-GGAGAACUUCAUGCCCUUCGGAUAAGGACU-3′ 3′-CCUCUUGAAGUACGGGAAGCCUAUUCCUGA-5′	514375
ds40	5'-GGAGGAUGUUAAUUGGCGUGUCUUGUCUGCAACGGUAUUC-3' 3'-CCUCCUACAAUUAACCGCACAGAACAGACGUUGCCAUAAG-5'	661950

[a] Sequences are written 5′ to 3′ with duplex regions underlined.
[b] ss-dsRNA ε_{260} values are determined by the protocol outlined in Materials and Methods. Duplex RNAs are derived from the hypochromic effect upon annealing the single-stranded RNAs. For single-stranded nucleic acids the extinction coefficient provided by the commercial supplier was used.

Appendix 2: Hydrodynamic parameters from sedimentation velocity

Table A2.1 Hydrodynamic properties of nucleic acids.

Nucleic acid	Buffer	Mass[a]	s (Svedbergs)[b]	$s_{20,w}$ (Svedbergs)[c]	f/f_0[d]
IVT ppp-15-15-15	AU75	20,659	3.12	3.21	1.54
IVT HO-15-15-15	AU75	20,359	3.19	3.28	1.49
Synthetic HO-15-15-15	AU75	20,359	3.06	3.17	1.56
ΔT-ppp-15-15-15	AU75	19,398	2.79	2.89	1.38
ΔT-HO-15-15-15	AU75	19,098	2.86	2.96	1.63
ppp-5′UCCG-15-15-15	AU75	20,583	2.98	3.09	1.54
ppp-3′UCCG-15-15-15	AU75	20,583	2.98	3.09	1.63
ppp-15-15-15-GAAA	AU75	20,730	3.15	3.26	1.63
ppp-15-15-15-UUUU	AU75	20,622	3.12	3.23	1.76
ppp-15-15-10	AU75	19,138	2.87	2.95	1.69
ppp-15-15-5	AU75	17,532	2.82	2.90	1.78
ppp-10-15-15	AU75	19,106	2.93	3.01	2.05
ppp-10-15-10	AU75	17,516	2.93	3.01	1.88
ppp-13-15-10	AU75	18,443	2.95	3.05	1.71
ppp-13-15-5	AU75	16,866	2.82	2.92	1.70
ppp-10-15-5	AU75	15,909	2.77	2.85	1.84
ppp-5-15-15	AU75	17,506	2.90	2.97	1.87
ppp-5-15-10	AU75	15,909	2.80	2.88	1.64
ppp-5-15-5	AU75	14,366	2.73	2.80	1.76
ppp-15-15-0	AU75	15,917	2.80	2.88	1.86
ppp-0-15-15	AU75	15,798	2.66	2.73	1.59
ppp-0-15-0	AU75	11,057	2.46	2.52	1.65
ppp-15-10-15	AU75	17,577	2.66	2.74	1.53
ppp-15-5-15	AU75	14,522	2.43	2.50	1.82
ppp-0-5-0	AU75	4,658	1.54	1.60	1.39

Table A2.1 Continued Hydrodynamic properties of nucleic acids.

Nucleic acid	Buffer	Mass[a]	s (Svedbergs)[b]	$s_{20,w}$ (Svedbergs)[c]	f/f_0[d]
ppp-15-15-15	AU200	20,659	3.21	3.36	1.58
ppp-15-15-0	AU200	15,917	2.90	3.03	1.73
ppp-0-15-15	AU200	15,798	2.66	2.78	1.83
ppp-0-15-0	AU200	11,057	2.47	2.58	1.55
ppp-15-15-15	AU75+Mg^{2+}	20,659	3.36	3.45	1.78
ppp-0-15-0	AU75+Mg^{2+}	11,057	2.54	2.61	1.60
ppp-15-15-15	AU60+Mg^{2+}	20,659	3.43	3.53	1.74
ppp-0-15-0	AU60+Mg^{2+}	11,057	2.53	2.60	1.90
U30	AU75	9,123	1.67	1.74	1.66
U15	AU75	4,528	1.21	1.25	1.70
Het30	AU75	9,683	2.05	2.12	1.41
ppp-Het30	AU75	9,923	2.12	2.19	1.39
dT30	AU75	9,064	1.43	1.48	1.93
dHet30	AU75	9,203	1.67	1.73	1.67
ds20	AU200 (4 °C)	12,108	1.64	2.74	1.27
ds30	AU75	19,164	3.16	3.27	1.44

[a] Masses predicted based on composition.
[b] Uncorrected sedimentation coefficient obtained by fitting to a single discrete species model.
[c] Sedimentation coefficient corrected to standard conditions (water at 20 °C).
[d] Frictional ratio.

Table A2.2 Hydrodynamic properties of ss-dsRNA · PKR complexes.

ss-dsRNA·Protein	Buffer	Mass[a]	s (Svedbergs)[b]	$s_{20,w}$ (Svedbergs)[c]	f/f_0[d]
ppp-15-15-15·PKR	AU75	82,754	4.88	5.04	1.60
ppp-15-15-15·PKR_2	AU75	144,848	8.02	8.30	1.33
IVT HO-15-15-15·PKR	AU75	82,454	4.76	4.91	1.64
IVT HO-15-15-15·PKR_2	AU75	144,548	8.39	8.68	1.27
Synthetic HO-15-15-15·PKR	AU75	82,514	4.64	4.79	1.80
Synthetic HO-15-15-15·PKR_2	AU75	144,608	8.23	8.51	1.34
ΔT-ppp-15-15-15·PKR	AU75	81,492	4.46	4.61	1.63
ΔT-ppp-15-15-15·PKR_2	AU75	143,587	7.42	7.68	1.36
ppp-15-15-15-GAAA·PKR	AU75	82,825	4.88	5.04	1.60
ppp-15-15-15-GAAA·PKR_2	AU75	144,919	8.02	8.30	1.33
ppp-15-15-15-UUUU·PKR	AU75	82,717	4.73	4.89	1.73
ppp-15-15-15-UUUU·PKR_2	AU75	144,811	7.97	8.25	1.36
ppp-5′UCCG-15-15-15·PKR	AU75	82,677	4.88	5.04	1.60
ppp-5′UCCG-15-15-15·PKR_2	AU75	144,772	8.02	8.30	1.33
ppp-15-15-10·PKR	AU75	81,233	5.01	5.17	1.61
ppp-15-15-10·PKR_2	AU75	143,327	7.57	7.83	1.44
ppp-15-15-5·PKR	AU75	79,627	4.71	4.86	1.71
ppp-15-15-5·PKR_2	AU75	141,721	7.86	8.13	1.39
ppp-10-15-15·PKR	AU75	81,201	4.84	4.99	1.78
ppp-10-15-15·PKR_2	AU75	143,295	7.80	8.06	1.45
ppp-13-15-10·PKR	AU75	80,538	5.46	5.65	1.77
ppp-13-15-10·PKR_2	AU75	142,632	7.43	7.69	1.69
ppp-13-15-5·PKR	AU75	78960.9	5.05	5.23	1.55
ppp-13-15-5·PKR_2	AU75	141055	7.09	7.34	1.49
ppp-10-15-10·PKR	AU75	79,611	4.88	5.04	1.70
ppp-10-15-10·PKR_2	AU75	141,705	7.36	7.61	1.50

Table A2.2 Continued Hydrodynamic properties of ss-dsRNA · PKR complexes.

ss-dsRNA·Protein	Buffer	Mass[a]	s (Svedbergs)[b]	$s_{20,w}$ (Svedbergs)[c]	f/f_0[d]
ppp-10-15-5·PKR	AU75	78,004	4.80	4.96	1.67
ppp-10-15-5·PKR_2	AU75	140,098	7.40	7.65	1.47
ppp-5-15-15·PKR	AU75	79,601	4.43	4.57	1.86
ppp-5-15-15·PKR_2	AU75	141,695	7.13	7.37	1.55
ppp-5-15-10·PKR	AU75	78,004	4.64	4.79	1.68
ppp-5-15-10·PKR_2	AU75	140,098	6.94	7.18	1.54
ppp-5-15-5·PKR	AU75	76,460	4.67	4.82	1.67
ppp-5-15-5·PKR_2	AU75	138,555	7.12	7.36	1.50
ppp-15-15-0·PKR	AU75	78,012	4.75	4.90	1.70
ppp-15-15-0·PKR_2	AU75	140,106	7.19	7.43	1.52
ppp-0-15-15·PKR	AU75	77,893	4.95	5.11	1.54
ppp-0-15-15·PKR_2	AU75	139,987	6.82	7.05	1.54
ppp-0-15-0·PKR	AU75	73,151	4.58	4.73	1.60
ppp-0-15-0·PKR_2	AU75	135,246	6.19	6.40	1.66
ppp-15-10-15·PKR	AU75	79,671	4.76	4.92	1.60
ppp-15-10-15·PKR_2	AU75	141,766	6.48	6.70	1.62
ppp-15-5-15·PKR	AU75	76,616	4.71	4.87	1.63
ppp-15-5-15·PKR_2	AU75	138,711	6.87	7.10	1.54
ppp-0-15-0·PKR	AU75	66752.5	4.16	4.32	1.46
ppp-15-15-15·PKR	AU200	82,754	5.17	5.46	1.60
ppp-15-15-0·PKR	AU200	78,012	4.96	5.23	1.62
ppp-0-15-15·PKR	AU200	77,893	4.72	4.98	1.68
ppp-0-15-0·PKR	AU200	73,151	4.52	4.78	1.60
ppp-15-15-15·PKR	AU75+Mg^{2+}	82,754	5.48	5.73	1.60
ppp-15-15-15·PKR_2	AU75+Mg^{2+}	144,848	6.98	7.23	1.63
ppp-0-15-0·PKR	AU75+Mg^{2+}	73,151	4.58 (fixed)[e]	4.80	1.62

Table A2.2 Continued Hydrodynamic properties of ss-dsRNA · PKR complexes.

ss-dsRNA·Protein	Buffer	Mass[a]	s (Svedbergs)[b]	$s_{20,w}$ (Svedbergs)[c]	f/f_0[d]
ppp-0-15-0·PKR_2	AU60+Mg^{2+}	135,246	6.19 (fixed)[e]	6.40	1.70
ppp-0-15-0·dsRBD	AU75	31,319	3.07	3.18	1.58
ppp-0-15-0·$dsRBD_2$	AU75	51,581	4.34	4.49	1.37
ppp-15-15-15·dsRBD	AU75	40,922	3.56	3.69	1.78
ppp-15-15-15·$dsRBD_2$	AU75	61,184	4.74	4.91	1.54
ppp-15-15-15·$dsRBD_3$	AU75	84,446	5.90	6.11	1.39

[a] Masses predicted based on composition.
[b] Uncorrected sedimentation coefficient obtained by fitting to a single discrete species model.
[c] Sedimentation coefficient corrected to standard conditions (water at 20 °C).
[d] Frictional ratio.
[e] The value of s(RP) and s(RP_2) could not be measured for these RNAs and were fixed to the values measured in AU75 buffer.

Table A2.3 Hydrodynamic properties of single-stranded nucleic acid · PKR complexes.

Nucleic acid·Protein	Buffer	Mass[a]	s (Svedbergs)[b]	$s_{20,w}$ (Svedbergs)[c]	f/f_0[d]
U30·PKR	AU75	71,218	4.34	4.50	1.50
U30·PKR_2	AU75	133,312	6.31	6.54	1.50
U15·PKR	AU75	66,623	4.04	4.18	1.50
ppp-Het30·PKR	AU75	72,017	4.40	4.56	1.50
ppp-Het30·PKR_2	AU75	134,112	6.36	6.59	1.50
Het30·PKR	AU75	71,778	4.38	4.54	1.50
Het30·PKR_2	AU75	133,872	6.36	6.58	1.50
dT30·PKR	AU75	71,159	4.33	4.49	1.50
dT30·PKR_2	AU75	133,253	6.31	6.53	1.50
dHet30·PKR	AU75	71,298	4.34	4.50	1.50
dHet30·PKR_2	AU75	133,392	6.32	6.54	1.50
U30·dsRBD	AU75	29385	2.71	2.80	1.50
U30·$dsRBD_2$	AU75	49,647	3.53	3.65	1.50
ppp-Het30·dsRBD	AU75	30,185	3.55	3.67	1.18
ppp-Het30·$dsRBD_2$	AU75	50,447	4.85	5.02	1.11

Table A2.3 Continued Hydrodynamic properties of single-stranded nucleic acid · PKR complexes.

Nucleic acid·Protein	Buffer	Mass[a]	s (Svedbergs)[b]	$s_{20,w}$ (Svedbergs)[c]	f/f_0[d]
Het30·dsRBD	AU75	29,945	3.55	3.67	1.18
Het30·$dsRBD_2$	AU75	50,207	4.85	5.02	1.11
dT30·dsRBD	AU75	29,326	2.70	2.80	1.50
dT30·$dsRBD_2$	AU75	49,588	3.52	3.65	1.50
dHet30·dsRBD	AU75	29,465	2.70	2.80	1.50
dHet30·$dsRBD_2$	AU75	49,727	3.52	3.65	1.50
U30·185-kinase	AU75	51,030	3.81	3.95	1.50
U30·185-$kinase_2$	AU75	92,938	5.09	5.27	1.50
U30·229-kinase	AU75	46,559	3.39	3.51	1.50
U30·229-$kinase_2$	AU75	83,995	4.71	4.88	1.50
ppp-Het30·229-kinase	AU75	47,359	3.46	3.58	1.50
ppp-Het30·229-$kinase_2$	AU75	84,795	4.77	4.94	1.50
Het30·229-kinase	AU75	47,119	3.44	3.56	1.50
Het30·229-$kinase_2$	AU75	84,555	4.75	4.92	1.50
ds30·229-kinase	AU75	59,600	4.25	4.40	1.50
ds30·229-$kinase_2$	AU75	94,035	5.44	5.63	1.50
dT30·229-kinase	AU75	46,450	3.38	3.50	1.50
dT30·229-$kinase_2$	AU75	83,936	4.71	4.87	1.50
U30·242-kinase	AU75	44,934	3.31	3.43	1.50
U30·242-$kinase_2$	AU75	80,745	4.59	4.75	1.50
ds30·242-kinase	AU75	54,975	4.19	4.33	1.50
ds30·242-$kinase_2$	AU75	90,786	5.32	5.51	1.50

[a] Masses predicted based on composition.
[b] Uncorrected sedimentation coefficient. In most fits the sedimentation coefficient is calculated from a frictional ratio of 1.50.
[c] Sedimentation coefficient corrected to standard conditions (water at 20 °C).
[d] Frictional ratio.

Table A2.4 Hydrodynamic properties of ds20 · PACT complex.

dsRNA·PACT	Buffer	Mass[a]	s (Svedbergs)[b]	$s_{20,w}$ (Svedbergs)[c]	f/f_0[d]
ds20·$PACT_2$	AU200 (4 °C)	81,480	3.68	5.98	1.26

[a] Masses predicted based on composition.
[b] Uncorrected sedimentation coefficient.
[c] Sedimentation coefficient corrected to standard conditions (water at 20 °C).
[d] Frictional ratio.

References

1. Toth AM, Zhang P, Das S, George CX, Samuel CE (2006) Interferon Action and the Double□Stranded RNA□Dependent Enzymes ADAR1 Adenosine Deaminase and PKR Protein Kinase. *Progress in Nucleic Acid Research and Molecular Biology* 81:369–434.

2. Nallagatla SR, Toroney R, Bevilacqua PC (2011) Regulation of innate immunity through RNA structure and the protein kinase PKR. *Current Opinion in Structural Biology* 21(1):119.

3. Nussbaum JM, Gunnery S, Mathews MB (2002) The 3′-untranslated regions of cytoskeletal muscle mRNAs inhibit translation by activating the double-stranded RNA-dependent protein kinase PKR. *Nucleic Acids Research* 30(5):1205–1212.

4. Cohen-Chalamish S et al. (2009) Dynamic refolding of IFN-γ mRNA enables it to function as PKR activator and translation template. *Nature Chemical Biology* 5(12):896–903.

5. Davis S, Watson JC (1996) In vitro activation of the interferon-induced, double-stranded RNA-dependent protein kinase PKR by RNA from the 3' untranslated regions of human alpha-tropomyosin. *Proceedings of the National Academy of Sciences* 93(1):508–513.

6. Ben-Asouli Y, Banai Y, Pel-Or Y, Shir A, Kaempfer R (2002) Human Interferon-γ mRNA Autoregulates Its Translation through a Pseudoknot that Activates the Interferon-Inducible Protein Kinase PKR. *Cell* 108(2):221.

7. Youssef OA et al. (2015) Potential role for snoRNAs in PKR activation during metabolic stress. *Proceedings of the National Academy of Sciences* 112(16):5023–5028.

8. Pindel A, Sadler A (2011) The Role of Protein Kinase R in the Interferon Response. *Journal of Interferon & Cytokine Research* 31(1):59–70.

9. Langland JO, Cameron JM, Heck MC, Jancovich JK, Jacobs BL (2006) Inhibition of PKR by RNA and DNA viruses. *Virus Research* 119:100–110.

10. Nakamura T et al. (2010) Double-Stranded RNA-Dependent Protein Kinase Links Pathogen Sensing with Stress and Metabolic Homeostasis. *Cell* 140(3):338–348.

11. García MA et al. (2006) Impact of Protein Kinase PKR in Cell Biology: from Antiviral to Antiproliferative Action. 70(4):1032–1060.

12. Lunde BM, Moore C, Varani G (2007) RNA-binding proteins: modular design for efficient function. *Nature Reviews Molecular Cell Biology* 8(6):479–490.

13. Masliah G, Barraud P, Allain FHT (2012) RNA recognition by double-stranded RNA binding domains: a matter of shape and sequence. *Cell Mol Life Sci* 70(11):1875–1895.

14. Nanduri S, Carpick BW, Yang Y (1998) Structure of the double□stranded RNA-binding domain of the protein kinase PKR reveals the molecular basis of its dsRNA-mediated activation. *The EMBO Journal* 70(18):5458–5465.

15. Bevilacqua PC (1996) Minor-Groove Recognition of Double-Stranded RNA by the Double-Stranded RNA-Binding Domain from the RNA-Activated Protein Kinase PKR. *Biochemistry* 35(31):9983–9994.

16. Stefl R, Xu M, Skrisovska L, Emeson RB, Allain FHT (2006) Structure and Specific RNA Binding of ADAR2 Double-Stranded RNA Binding Motifs. *Structure* 14(2):345–355.

17. Stefl R et al. (2010) The Solution Structure of the ADAR2 dsRBM-RNA Complex Reveals a Sequence-Specific Readout of the Minor Groove. *Cell* 143(2):225-237.

18. Leulliot N et al. (2004) A new alpha-helical extension promotes RNA binding by the dsRBD of Rnt1p RNAse III. *The EMBO journal* 23:2468–2477.

19. Bycroft M, Grunert S, Murzin AG, Proctor M, St Johnson D (1995) NMR solution structure of a dsRNA binding domain from Drosophila staufen protein reveals homology to the N-terminal domain of ribosomal protein S5. *The EMBO journal* 14:3563–3571.

20. Ramos A et al. (2000) RNA recognition by a Staufen double-stranded RNA-binding domain. *The EMBO journal* 19:997–1009.

21. Yamashita S et al. (2011) Structures of the first and second double-stranded RNA-binding domains of human TAR RNA-binding protein. *Protein Science* 20:118–130.

22. Jayachandran U, Grey H, Cook A (2016) Nuclear factor 90 uses an ADAR2-like binding mode to recognize specific bases in dsRNA. *Nucleic Acids Research* 44(4):1924-1936.

23. Ryter JM, Schultz SC (1998) Molecular basis of double-stranded RNA-protein interactions: structure of a dsRNA-binding domain complexed with dsRNA. *The EMBO journal* 17(24):7505–7513.

24. Wu H, Henras A, Chanfreau G, Feigon J (2004) Structural basis for recognition of the AGNN tetraloop RNA fold by the double-stranded RNA-binding domain of Rnt1p RNase III. *Proceedings of the National Academy of Sciences* 101(22):8307–8312.

25. Stefl R et al. (2010) The Solution Structure of the ADAR2 dsRBM-RNA Complex Reveals a Sequence-Specific Readout of the Minor Groove. *Cell* 143(2):225-237.

26. Vuyisich M, Spanggord RJ, Beal PA (2002) The binding site of the RNA-dependent protein kinase (PKR) on EBER1 RNA from Epstein-Barr virus. *EMBO Reports* 3(7):622.

27. Kim I, Liu CW, Puglisi JD (2006) Specific Recognition of HIV TAR RNA by the dsRNA Binding Domains (dsRBD1–dsRBD2) of PKR. *Journal of Molecular Biology* 358(2):430–442.

28. Spanggord RJ, Beal PA (2001) Selective Binding by the RNA Binding Domain of PKR Revealed by Affinity Cleavage†. *Biochemistry* 40(14):4272.

29. Dar AC, Dever TE, Sicheri F (2005) Higher-Order Substrate Recognition of eIF2α by the RNA-Dependent Protein Kinase PKR. *Cell* 122(6):887.

30. Li F et al. (2013) Structure of the kinase domain of human RNA-dependent protein kinase with K296R mutation reveals a face-to-face dimer. *Chinese Science Bulletin* 58(9):998–1002.

31. Endicott JA, Noble MEM, Johnson LN (2012) The Structural Basis for Control of Eukaryotic Protein Kinases. *Annual Review of Biochemistry* 81(1):587–613.

32. Nolen B, Taylor S, Ghosh G (2004) Regulation of protein kinases: controlling activity through activation segment conformation. *Molecular Cell* 15:661–675.

33. Beenstock J, Mooshayef N, Engelberg D (2016) How Do Protein Kinases Take a Selfie (Autophosphorylate)? *Trends in biochemical sciences* 41(11):938.

34. Dey M, Mann BR, Anshu A, Mannan MA-U (2013) Activation of Protein Kinase PKR Requires Dimerization-inducedcis-Phosphorylation within the Activation Loop. *Journal of Biological Chemistry* 289(9):5747–5757.

35. Lemaire PA, Lary J, Cole JL (2005) Mechanism of PKR Activation: Dimerization and Kinase Activation in the Absence of Double-stranded RNA. *Journal of Molecular Biology* 345(1):81–90.

36. Thomis DC, Samuel CE (1993) Mechanism of interferon action: evidence for intermolecular autophosphorylation and autoactivation of the interferon-induced, RNA-dependent protein kinase PKR. *Journal of Virology* 67(12):7695–7700.

37. Thomis DC, Samuel CE (1995) Mechanism of interferon action: characterization of the intermolecular autophosphorylation of PKR, the interferon-inducible, RNA-dependent protein kinase. *Journal of Virology* 69(8):5195–5198.

38. McKenna SA et al. (2007) Molecular Framework for the Activation of RNA-dependent Protein Kinase. *Journal of Biological Chemistry* 282(15):11474–11486.

39. Dey M et al. (2005) Mechanistic Link between PKR Dimerization, Autophosphorylation, and eIF2α Substrate Recognition. *Cell* 122(6):901–913.

40. Lavoie H, Li JJ, Thevakumaran N, Therrien M, Sicheri F (2014) Dimerization-induced allostery in protein kinase regulation. *Trends in biochemical sciences* 39(10):475.

41. Johnson DA, Akamine P, Radzio-Andzelm E, Madhusudan, Taylor SS (2001) Dynamics of cAMP-Dependent Protein Kinase. *Chemical Reviews* 101(8):2243–2270.

42. Kornev AP, Taylor SS (2010) Defining the conserved internal architecture of a protein kinase. *Biochimica et Biophysica Acta (BBA) - Proteins and Proteomics* 1804(3):440–444.

43. Taylor SS, Kornev AP (2011) Protein kinases: evolution of dynamic regulatory proteins. *Trends in biochemical sciences* 36(2):65–77.

44. Johnson LN, Noble MEM, Owen DJ (1996) Active and Inactive Protein Kinases: Structural Basis for Regulation. *Cell* 85(2):149.

45. Adams JA, McGlone ML, Gibson R, Taylor SS (1995) Phosphorylation Modulates Catalytic Function and Regulation in the cAMP-Dependent Protein Kinase. *Biochemistry* 34(8):2447–2454.

46. Adams JA (2003) Activation Loop Phosphorylation and Catalysis in Protein Kinases: Is There Functional Evidence for the Autoinhibitor Model?. *Biochemistry* 42(3):601–607.

47. Dey M et al. (2011) Requirement for kinase-induced conformational change in eukaryotic initiation factor 2 (eIF2) restricts phosphorylation of Ser51. *Proceedings of the National Academy of Sciences* 108(11):4316.

48. Zhang X et al. (1998) Autophosphorylation in the Activation Loop Is Required for Full Kinase Activity In Vivo of Human and Yeast Eukaryotic Initiation Factor 2α Kinases PKR and GCN2. *Molecular and Cellular Biology* 18(4):2282–2297.

49. Madhusudan et al. (1994) cAMP-dependent protein kinase: crystallographic insights into substrate recognition and phosphotransfer. *Protein Science* 3(2):176–187.

50. Pérez-Gallegos A, Garcia-Viloca M, González-Lafont À (2015) A QM/MM study of Kemptide phosphorylation catalyzed by protein kinase A. The role of Asp166 as a general acid/base catalyst. *Phys Chem Chem Phys* 17(5):3497–3511.

51. Huse M, Kuriyan J (2002) The conformational plasticity of protein kinases. *Cell* 109(3):275-282.

52. Wu S, Kaufman RJ (1997) A Model for the Double-stranded RNA (dsRNA)-dependent Dimerization and Activation of the dsRNA-activated Protein Kinase PKR. *Journal of Biological Chemistry* 272(2):1291.

53. Galabru J, Hovanessian AG (1987) Autophosphorylation of the protein kinase dependent on double-stranded RNA. *Journal of Biological Chemistry* 262(32):15538–15544.

54. Nanduri S, Rahman F, Williams BRG, Qin J (2000) A dynamically tuned double-stranded RNA binding mechanism for the activation of antiviral kinase PKR. *The EMBO journal* 19(20):5567.

55. Gelev V et al. (2006) Mapping of the Auto-inhibitory Interactions of Protein Kinase R by Nuclear Magnetic Resonance. *Journal of Molecular Biology* 364(3):352.

56. Spanggord RJ, Vuyisich M, Beal PA (2002) Identification of Binding Sites for Both dsRBMs of PKR on Kinase-Activating and Kinase-Inhibiting RNA Ligands. *Biochemistry* 41(14):4511–4520.

57. Ucci JW, Kobayashi Y, Choi G, Alexandrescu AT, Cole JL (2007) Mechanism of Interaction of the Double-Stranded RNA (dsRNA) Binding Domain of Protein Kinase R with Short dsRNA Sequences. *Biochemistry* 46(1):55–65.

58. Robertson HD (1996) The regulation of the protein kinase PKR by RNA. *Biochimie* 78:909–914.

59. Anderson E, Cole JL (2008) Domain Stabilities in Protein Kinase R (PKR): Evidence for Weak Interdomain Interactions. *Biochemistry* 47(17):4887–4897.

60. VanOudenhove J, Anderson E, Krueger S, Cole JL (2009) Analysis of PKR Structure by Small-Angle Scattering. *Journal of Molecular Biology* 387(4):910–920.

61. Cole JL (2007) Activation of PKR: an open and shut case? *Trends in biochemical sciences* 32(2):57–62.

62. Husain B, Mukerji I, Cole JL (2012) Analysis of High-Affinity Binding of Protein Kinase R to Double-Stranded RNA. *Biochemistry* 51(44):8764.

63. Lemaire PA, Anderson E, Lary J, Cole JL (2008) Mechanism of PKR Activation by dsRNA. *Journal of Molecular Biology* 381(2):351.

64. Manche L, Green SR, Schmedt C (1992) Interactions between double-stranded RNA regulators and the protein kinase DAI. *Molecular and Cellular Biology* 12(11):5238–5248.

65. Husain B, Hesler S, Cole JL (2015) Regulation of PKR by RNA: Formation of Active and Inactive Dimers. *Biochemistry* 54(44):6663–6672.

66. Hunter T, Hunt T, Jackson RJ, Robertson HD (1975) The characteristics of inhibition of protein synthesis by double-stranded ribonucleic acid in reticulocyte lysates. *Journal of Biological Chemistry* 250(2):409–417.

67. Kostura M, Mathews MB (1989) Purification and activation of the double-stranded RNA-dependent eIF-2 kinase DAI. *Molecular and Cellular Biology* 9(4):1576–1586.

68. Butcher SE, Pyle A (2011) The Molecular Interactions That Stabilize RNA Tertiary Structure: RNA Motifs, Patterns, and Networks. *Accounts of Chemical Research* 44(12):1302–1311.

69. Zheng X, Bevilacqua PC (2000) Straightening of bulged RNA by the double-stranded RNA-binding domain from the protein kinase PKR. *Proceedings of the National Academy of Sciences* 97(26):14162–14167.

70. Heinicke LA, Nallagatla SR, Hull CM, Bevilacqua PC (2011) RNA helical imperfections regulate activation of the protein kinase PKR: Effects of bulge position, size, and geometry. *RNA* 17(5):957.

71. Kaempfer R (2003) RNA sensors: novel regulators of gene expression. *EMBO Reports* 4(11):1043.

72. Osman F, Jarrous N, Ben-Asouli Y, Kaempfer R (1999) A cis-acting element in the 3′-untranslated region of human TNF-α mRNA renders splicing dependent on the activation of protein kinase PKR. *Genes & Development* 13:3280–3293.

73. Osman F, Jarrous N, Ben-Asouli Y, Kaempfer R (1999) A cis-acting element in the 3'-untranslated region of human TNF-alpha mRNA renders splicing dependent on the activation of protein kinase PKR. *Genes & Development* 13:3280–3293.

74. Dauber B et al. (2009) Influenza B Virus Ribonucleoprotein Is a Potent Activator of the Antiviral Kinase PKR. *PLOS Pathog* 5(6):e1000473.

75. Weber F, Wagner V, Rasmussen SB, Hartmann R, Paludan SR (2006) Double-stranded RNA is produced by positive-strand RNA viruses and DNA viruses but not in detectable amounts by negative-strand RNA viruses. *Journal of Virology* 80:5059–5064.

76. Hsu MT, Parvin JD, Gupta S, Krystal M, Palese P (1987) Genomic RNAs of influenza viruses are held in a circular conformation in virions and in infected cells by a terminal panhandle. *Proceedings of the National Academy of Sciences of the United States of America* 84:8140–445.

77. Zheng X, Bevilacqua PC (2004) Activation of the protein kinase PKR by short double-stranded RNAs with single-stranded tails. *RNA* 10(12):1934–1945.

78. Nallagatla SR et al. (2007) 5'-Triphosphate-Dependent Activation of PKR by RNAs with Short Stem-Loops. *Science* 318(5855):1455–1458.

79. Leung DW, Amarasinghe GK (2016) When your cap matters: structural insights into self vs non-self recognition of 5′ RNA by immunomodulatory host proteins. *Current Opinion in Structural Biology* 36:133–141.

80. Dauber B, Wolff T (2009) Activation of the Antiviral Kinase PKR and Viral Countermeasures. *Viruses* 1(3):523–544.

81. Nallagatla SR et al. (2013) Native Tertiary Structure and Nucleoside Modifications Suppress tRNA's Intrinsic Ability to Activate the Innate Immune Sensor PKR. *PloS one* 8(3):e57905–e57905.

82. Nallagatla SR, Bevilacqua PC (2008) Nucleoside modifications modulate activation of the protein kinase PKR in an RNA structure-specific manner. *RNA* 14(6):1201–1213.

83. Langland JO, Cameron JM, Heck MC, Jancovich JK, Jacobs BL (2006) Inhibition of PKR by RNA and DNA viruses. *Virus Research* 119(1):100–110.

84. Launer-Felty K, Wong CJ, Wahid AM, Conn GL, Cole JL (2010) Magnesium-Dependent Interaction of PKR with Adenovirus VAI. *Journal of Molecular Biology* 402(4):638–644.

85. Launer-Felty K, Cole JL (2014) Domain Interactions in Adenovirus VAI RNA Mediate High-Affinity PKR Binding. *Journal of Molecular Biology* 426(6):1285–1295.

86. Launer-Felty K, Wong CJ, Cole JL (2015) Structural Analysis of Adenovirus VAI RNA Defines the Mechanism of Inhibition of PKR. *Biophysical Journal* 108(3):748–757.

87. Glickman JN, Howe JG, Steitz JA (1988) Structural analyses of EBER1 and EBER2 ribonucleoprotein particles present in Epstein-Barr virus-infected cells. *Journal of Virology* 62(3):902–911.

88. Weber F, Wagner V, Rasmussen SB, Hartmann R, Paludan SR (2006) Double-Stranded RNA Is Produced by Positive-Strand RNA Viruses and DNA Viruses but Not in Detectable Amounts by Negative-Strand RNA Viruses. *Journal of Virology* 80(10):5059–5064.

89. Hovanessian AG, Galabru J (1987) The double-stranded RNA-dependent protein kinase is also activated by heparin. *European Journal of Biochemistry* 167(3):467.

90. George CX, Thomis DC, McCormack SJ, Svahn CM, Samuel CE (1996) Characterization of the Heparin-Mediated Activation of PKR, the Interferon-Inducible RNA-Dependent Protein Kinase. *Virology* 221(1):180.

91. Anderson E, Pierre-Louis W, Wong CJ, Lary JW, Cole J (2011) Heparin Activates PKR by Inducing Dimerization. *Biophysical Journal* 100(3):973–984.

92. Patel RC, Sen GC (1998) PACT, a protein activator of the interferon-induced protein kinase, PKR. *The EMBO journal* 17(15):4379–4390.

93. Gleghorn ML, Maquat LE (2014) 'Black sheep' that don't leave the double-stranded RNA-binding domain fold. *Trends in biochemical sciences* 39(7): 328-340.

94. Huang X, Hutchins B (2002) The C-terminal, third conserved motif of the protein activator PACT plays an essential role in the activation of double-stranded-RNA-dependent protein kinase (PKR). *Biochemical Journal* 366(1):175–186.

95. Peters GA, Hartmann R, Qin J, G. Sen (2001) Modular Structure of PACT: Distinct Domains for Binding and Activating PKR. *Mol. Cell Biol.* 21(6):1908–1920.

96. Patel CV, Handy I, Goldsmith T, Patel RC (2000) PACT, a Stress-modulated Cellular Activator of Interferon-induced Double-stranded RNA-activated Protein Kinase, PKR. *Journal of Biological Chemistry* 275(48):37993–37998.

97. Peters GA, Li S, G. Sen (2006) Phosphorylation of Specific Serine Residues in the PKR Activation Domain of PACT Is Essential for Its Ability to Mediate Apoptosis. *Journal of Biological Chemistry* 281(46):35129–35136.

98. Li S et al. (2006) Molecular basis for PKR activation by PACT or dsRNA. *Proceedings of the National Academy of Sciences* 103(26):10005–10010.

99. Hale BG, Randall RE, Ortin J, Jackson D (2008) The multifunctional NS1 protein of influenza A viruses. *Journal of General Virology* 89(10):2359–2376.

100. Min J, GC Sen, Krug R (2007) A site on the influenza A virus NS1 protein mediates both inhibition of PKR activation and temporal regulation of viral RNA synthesis. *Virology* 363(1):236-243.

101. Li S, Min J-Y, Krug RM, Ganes Sen (2006) Binding of the influenza A virus NS1 protein to PKR mediates the inhibition of its activation by either PACT or double-stranded RNA. *Virology* 349(1):13–21.

102. Tan S-L, Katze MG (1998) Biochemical and Genetic Evidence for Complex Formation Between the Influenza A Virus NS1 Protein and the Interferon-induced PKR Protein Kinase. *Journal of Interferon & Cytokine Research* 18(9):757–766.

103. van den Berg S, Löfdahl P-Å, Härd T, Berglund H (2006) Improved solubility of TEV protease by directed evolution. *Journal of biotechnology* 121(3):291–298.

104. Ucci JW, Cole JL (2004) Global analysis of non-specific protein–nucleic interactions by sedimentation equilibrium. *Biophysical Chemistry* 108(1-3):127–140.

105. Gurevich VV (1996) Use of bacteriophage RNA polymerase in RNA synthesis. *Methods in enzymology* 275:382–397.

106. Walker SC, Avis JM, Conn GL (2003) General plasmids for producing RNA in vitro transcripts with homogeneous ends. *Nucleic Acids Research* 31(15):82e.

107. Uhlenbeck OC (1987) Oligoribonucleotide synthesis using T7 RNA polymerase and synthetic DNA templates. *Nucleic Acids Research* 15(21):8783–8798.

108. Milligan JF, Uhlenbeck OC (1989) Synthesis of small RNAs using T7 RNA polymerase. *Methods in enzymology* 180:51–62.

109. Schurer H, Lang K, Schuster J, Morl M (2002) A universal method to produce in vitro transcripts with homogeneous 3′ ends. *Nucleic Acids Research* 30(12):56e.

110. Bloomfield VA, Crothers DM, Tinoco I (2000) *Nucleic Acids: structures, properties and functions* (University Science Books, Sausalito, CA).

111. Cavaluzzi MJ, Borer PN (2004) Revised UV extinction coefficients for nucleoside-5'-monophosphates and unpaired DNA and RNA. *Nucleic Acids Research* 32(1):13e.

112. Shih I-H, Been MD (1999) Ribozyme cleavage of a 2′,5′-phosphodiester linkage: Mechanism and a restricted divalent metal-ion requirement. *RNA* 5(9):1140–1148.

113. Das U, Shuman S (2012) Mechanism of RNA 2′,3′-cyclic phosphate end healing by T4 polynucleotide kinase-phosphatase. *Nucleic Acids Research* 41(1):355–365.

114. Zhu H, Smith P, Wang LK, Shuman S (2007) Structure–function analysis of the 3′ phosphatase component of T4 polynucleotide kinase/phosphatase. *Virology* 366(1):126–136.

115. Stafford WF (1992) Boundary analysis in sedimentation transport experiments: A procedure for obtaining sedimentation coefficient distributions using the time derivative of the concentration profile. *Analytical Biochemistry* 203(2):295–301.

116. Philo JS (2006) Improved methods for fitting sedimentation coefficient distributions derived by time-derivative techniques. *Analytical Biochemistry* 354(2):238.

117. Schuck P (2000) Size-Distribution Analysis of Macromolecules by Sedimentation Velocity Ultracentrifugation and Lamm Equation Modeling. *Biophysical Journal* 78(3):1606–1619.

118. Stafford WF, Sherwood PJ (2004) Analysis of heterologous interacting systems by sedimentation velocity: curve fitting algorithms for estimation of sedimentation coefficients, equilibrium and kinetic constants. *Biophysical Chemistry* 108:231–243.

119. Mayo CB, Wong CJ, Lopez PE, Lary JW, Cole JL (2016) Activation of PKR by short stem–loop RNAs containing single-stranded arms. *RNA* 22(7):1065–1075.

120. Laue TM, Shah B, Ridgeway TM, Pelletier SL (1992) Computer-aided interpretation of sedimentation data for proteins (Royal Society of Chemistry, Cambridge, England), pp 90–125.

121. Durchschlag H (1986) Specific Volumes of Biological Macromolecules and Some Other Molecules of Biological Interest. *Thermodynamic Data for Biochemistry and Biotechnology*, ed Hinz H-J (Springer-Verlag, Berlin, Berlin), pp 45–128.

122. Petoukhov MV et al. (2012) New developments in theATSASprogram package for small-angle scattering data analysis. *Journal of Applied Crystallography* 45(2):342–350.

123. Semenyuk AV, Svergun DI (1991) GNOM – a program package for small-angle scattering data processing. *Journal of Applied Crystallography* 24(5):537.

124. Svergun DI, Barberato C, Koch MJ (1995) CRYSOL– a Program to Evaluate X-ray Solution Scattering of Biological Macromolecules from Atomic Coordinates. *Journal of Applied Crystallography* 28(6):768.

125. Hornung V et al. (2006) 5'-Triphosphate RNA Is the Ligand for RIG-I. *Science* 314(5801):994.

126. Pichlmair A et al. (2006) RIG-I-Mediated Antiviral Responses to Single-Stranded RNA Bearing 5'-Phosphates. *Science* 314(5801):997–1001.

127. Luo D, Kohlway A, Vela A, Pyle A (2012) Visualizing the Determinants of Viral RNA Recognition by Innate Immune Sensor RIG-I. *Structure* 20(11):1983–1988.

128. Cui S et al. (2008) The C-Terminal Regulatory Domain Is the RNA 5′-Triphosphate Sensor of RIG-I. *Molecular Cell* 29(2):169–179.

129. Ranjith-Kumar CT (2010) Crystal structure of RIG-I C-terminal domain bound to blunt-ended double-strand RNA without 5' triphosphate. *Nucleic Acids Research* 39(4):1565–1575.

130. Takahasi K et al. (2008) Nonself RNA-Sensing Mechanism of RIG-I Helicase and Activation of Antiviral Immune Responses. *Molecular Cell* 29(4):428–440.

131. Toroney R, Hull CM, Sokoloski JE, Bevilacqua PC (2012) Mechanistic characterization of the 5'-triphosphate-dependent activation of PKR: Lack of 5'-end nucleobase specificity, evidence for a distinct triphosphate binding site, and a critical role for the dsRBD. *RNA* 18(10):1862–1874.

132. Dale T, Smith R, Serra MJ (2000) A test of the model to predict unusually stable RNA hairpin loop stability. *RNA* 6(4):608–615.

133. Zuker M (2003) Mfold web server for nucleic acid folding and hybridization prediction. *Nucleic Acids Research* 31(13):3406–3415.

134. Heinicke LA et al. (2009) RNA Dimerization Promotes PKR Dimerization and Activation. *Journal of Molecular Biology* 390(2):319–338.

135. Heinicke LA, Bevilacqua PC (2012) Activation of PKR by RNA misfolding: HDV ribozyme dimers activate PKR. *RNA* 18(12):2157.

136. Svergun DI, Koch M (2003) Small-angle scattering studies of biological macromolecules in solution. *Reports on Progress in Physics* 66(10):1735–1782.

137. Svergun DI (1992) Determination of the regularization parameter in indirect-transform methods using perceptual criteria. *Journal of Applied Crystallography* 25(4):495.

138. Wong CJ, Launer-Felty K, Cole JL (2011) Analysis of PKR–RNA Interactions by Sedimentation Velocity. *Methods in enzymology* 488:59–79.

139. Clarke PA, Pe'eru T, Ma Y, Mathews MB (1994) Structural features of adenovirus 2 virus-associated RNA required for binding to the protein kinase DAI. *Nucleic Acids Research* 22(21):4364–4374.

140. Draper DE (2004) A guide to ions and RNA structure. *RNA* 10(3):335–343.

141. Bizarro CV, Alemany A, Ritort F (2012) Non-specific binding of Na+ and Mg2+ to RNA determined by force spectroscopy methods. *Nucleic Acids Research* 40(14):6922–6935.

142. Chen H, Meisburger S, Pabit S, Sutton J, Webb W, Pollack L (2012) Ionic strength-dependent persistence lengths of single-stranded RNA and DNA. *Proceedings of the National Academy of Sciences* 109(3):799–804.

143. Ryter JM, Schultz SC (1998) Molecular basis of double-stranded RNA-protein interactions: structure of a dsRNA-binding domain complexed with dsRNA. *The EMBO journal* 17:7505–7513.

144. Kuo MY, Sharmeen L, Dinter G (1988) Characterization of self-cleaving RNA sequences on the genome and antigenome of human hepatitis delta virus. *Journal of Virology* 62(12):4439-4444.

145. Cameron V, Uhlenbeck OC (1977) 3'-Phosphatase activity in T4 polynucleotide kinase. *Biochemistry* 16(23):5120.

146. Pak J, Fire A (2007) Distinct populations of primary and secondary effectors during RNAi in C. elegans. *Science* 315(5809):238.

147. Huang F, Yarus M (1997) Versatile 5′ phosphoryl coupling of small and large molecules to an RNA. *Proceedings of the National Academy of Sciences* 94(17):8965–8969.

148. Scaringe SA, Wincott FE, Caruthers MH (1998) Novel RNA Synthesis Method Using 5‘-O-Silyl-2′-O-orthoester Protecting Groups. *Journal of the American Chemical Society* 120(45):11820–11821.

149. Scaringe SA (2001) RNA Oligonucleotide Synthesis via 5′-Silyl-2′-Orthoester Chemistry. *Methods* 23(3):206.

150. Nikcevic I, Wyrzykiewicz TK, Limbach PA (2011) Detecting low-level synthesis impurities in modified phosphorothioate oligonucleotides using liquid chromatography–high resolution mass spectrometry. *International Journal of Mass Spectrometry* 304(2-3):98-104.

151. Hölzl G, Oberacher H, Pitsch S, Stutz A (2005) Analysis of Biological and Synthetic Ribonucleic Acids by Liquid Chromatography−Mass Spectrometry Using Monolithic Capillary Columns. *Analytical Chemistry* 77(2):673.

152. Gilar M (2001) Analysis and Purification of Synthetic Oligonucleotides by Reversed-Phase High-Performance Liquid Chromatography with Photodiode Array and Mass Spectrometry Detection. *Analytical Biochemistry* 298(2):196.

153. Schmid K et al. (2015) Variable presence of 5-methylcytosine in commercial RNA and DNA. *RNA Biology* 12(10):1152.

154. Kurata C et al. (2006) Characterization of high molecular weight impurities in synthetic phosphorothioate oligonucleotides. *Bioorganic & Medicinal Chemistry Letters* 16(3):607.

155. Cazenave C, Bathany K, Rayner B (2006) Formation of N -Branched Oligonucleotides as By-products in Solid-Phase Oligonucleotide Synthesis. *Oligonucleotides* 16(2):181.

156. Woese CR, Winker S, Gutell RR (1990) Architecture of ribosomal RNA: constraints on the sequence of "tetra-loops". *Proceedings of the National Academy of Sciences* 87(21):8467–8471.

157. Tuerk C et al. (1988) CUUCGG hairpins: extraordinarily stable RNA secondary structures associated with various biochemical processes. *Proceedings of the National Academy of Sciences* 85(5):1364–1368.

158. Antao VP, Lai SY, Tinoco I (1991) A thermodynamic study of unusually stable RNA and DNA hairpins. *Nucleic Acids Research* 19(21):5901.

159. Wu L, Chai D, Zimmerly S (2012) Structural Variation and Uniformity among Tetraloop-Receptor Interactions and Other Loop-Helix Interactions in RNA Crystal Structures. *PloS one* 7(11):e49225.

160. Koplin J, Mu Y, Richter C, Schwalbe H, Stock G (2005) Structure and Dynamics of an RNA Tetraloop: A Joint Molecular Dynamics and NMR Study. *Structure* 13(9):1255.

161. Sashital DG, Venditti V, Angers CG, Cornilescu G, Butcher SE (2007) Structure and thermodynamics of a conserved U2 snRNA domain from yeast and human. *RNA* 13(3):328.

162. Norberg J, Nilsson L (1995) Stacking Free Energy Profiles for All 16 Natural Ribodinucleoside Monophosphates in Aqueous Solution. *Journal of the American Chemical Society* 117(44):10832.

163. Bass BL, Hurst SR, Singer JD (1994) Binding properties of newly identified Xenopus proteins containing dsRNA-binding motifs. *Current Biology* 4(4):301–314.

164. Johnston DS, Brown NH, Gall JG, Jantsch M (1992) A conserved double-stranded RNA-binding domain. *Proceedings of the National Academy of Sciences* 89(22):10979–10983.

165. Sen GC, Taira H, Lengyel P (1978) Interferon, double-stranded RNA, and protein phosphorylation. Characteristics of a double-stranded RNA-activated protein kinase system partially purified from interferon treated Ehrlich ascites tumor cells. *Journal of Biological Chemistry* 253(17):5915–5921.

166. Zhou H-X, Gilson MK (2009) Theory of Free Energy and Entropy in Noncovalent Binding. *Chemical Reviews* 109(9):4092–4107.

167. Shimoike T, McKenna SA, Lindhout DA, Puglisi JD (2009) Translational insensitivity to potent activation of PKR by HCV IRES RNA. *Antiviral Research* 83(3):228–237.

168. Toroney R, Nallagatla SR, Boyer JA, Cameron CE, Bevilacqua PC (2010) Regulation of PKR by HCV IRES RNA: Importance of Domain II and NS5A. *Journal of Molecular Biology* 400(3):393–412.

169. Dauber B et al. (2009) Influenza B Virus Ribonucleoprotein Is a Potent Activator of the Antiviral Kinase PKR. *PLoS Pathogens* 5(6):e1000473.

170. Puthenveetil S et al. (2006) Controlling activation of the RNA-dependent protein kinase by siRNAs using site-specific chemical modification. *Nucleic Acids Research* 34(17):4900–4911.

171. Sledz CA, Holko M, de Veer MJ, Silverman RH, Williams BRG (2003) Activation of the interferon system by short-interfering RNAs. *Nature Cell Biology* 5(9):834.

172. Hull CM, Bevilacqua PC (2015) Mechanistic Analysis of Activation of the Innate Immune Sensor PKR by Bacterial RNA. *Journal of Molecular Biology* 427(22):3501–3515.

173. Anmangandla A (2016) Bacterial riboswitches and ribozymes potently activate the human innate immune sensor PKR. *ACS chemical biology* 11(4):1118–1127.

174. Gredell JA, Dittmer MJ, Wu M, Chan C, Walton SP (2010) Recognition of siRNA asymmetry by TAR RNA binding protein (TRBP). *Biochemistry* 49(14):3148–3155.

175. Barraud P et al. (2011) An extended dsRBD with a novel zinc-binding motif mediates nuclear retention of fission yeast Dicer. *The EMBO journal* 30(20):4223–4235.

176. Lee SB, Green SR, Mathews MB, Esteban M (1994) Activation of the double-stranded RNA (dsRNA)-activated human protein kinase in vivo in the absence of its dsRNA binding domain. *Proceedings of the National Academy of Sciences of the United States of America* 91:10551–10555.

177. Wu S, Kumar KU, Kaufman RJ (1998) Identification and Requirement of Three Ribosome Binding Domains in dsRNA-Dependent Protein Kinase (PKR). *Biochemistry* 37(39):13816–13826.

178. Stanton P, Sen GC (1994) Role of the amino-terminal residues of the interferon-induced protein kinase in its activation by double-stranded RNA and heparin. *Journal of Biological Chemistry* 269(28):18593–18598.

179. Fasciano S, Hutchins B, Handy I, Patel RC (2005) Identification of the heparin-binding domains of the interferon-induced protein kinase, PKR. *FEBS Journal* 272(6):1425–1439.

180. McWilliam H et al. (2013) Analysis Tool Web Services from the EMBL-EBI. *Nucleic Acids Research* 41(W1):W597–W600.

181. Waterhouse AM, Procter JB, Martin DMA, Clamp M, Barton GJ (2009) Jalview Version 2--a multiple sequence alignment editor and analysis workbench. *Bioinformatics* 25(9):1189.

182. Zhang X, Szczepanowska J, Brzeska H, Hinnebusch AG, Qin J (1998) Identification of Phosphorylation Sites in Proteins Separated by Polyacrylamide Gel Electrophoresis. *Analytical Chemistry* 70(10):2050–2059.

183. Hellman L, Fried M (2007) Electrophoretic mobility shift assay (EMSA) for detecting protein–nucleic acid interactions. *Nature Protocols, Published online: 18 October 2007;* | *doi:101038/nprot2007380* 2(8):1849–1861.

184. Wong I, Lohman TM (1993) A double-filter method for nitrocellulose-filter binding: application to protein-nucleic acid interactions. *Proceedings of the National Academy of Sciences* 90(12):5428–5432.

185. Liu J-J (1981) Sequence dependence of the circular dichroism of synthetic double-stranded RNAs. *Biopolymers* 20(7):1337–1382.

186. Steely T, Gray D, Ratliff R (1986) CD of homopolymer DNA-RNA hybrid duplexes and triplexes containing A.T or A.U base pairs. *Nucleic Acids Research* 14(24):10071–10090.

187. Auweter SD, Oberstrass FC, Allain FHT (2006) Sequence-specific binding of single-stranded RNA: is there a code for recognition? *Nucleic Acids Research* 34(17):4943–4959.

188. Frankel AD (2000) Fitting peptides into the RNA world. *Current Opinion in Structural Biology* 10(3):332–340.

189. Favre A, Saintomé C, Fourrey J-L, Clivio P, Laugâa P (1998) Thionucleobases as intrinsic photoaffinity probes of nucleic acid structure and nucleic acid-protein interactions. *Journal of Photochemistry and Photobiology B: Biology* 42(2):109.

190. Ennifar E et al. (2000) The crystal structure of UUCG tetraloop. *Journal of Molecular Biology* 304(1):35–42.

191. Turner DH, Kierzek R (1999) Thermodynamics of RNA−RNA Duplexes with 2- or 4-Thiouridines: Implications for Antisense Design and Targeting a Group I Intron. *Biochemistry* 38(50):16655.

192. Kumar R, Davis D (1997) Synthesis and studies on the effect of 2-thiouridine and 4-thiouridine on sugar conformation and RNA duplex stability. *Nucleic Acids Research* 25(6):1272.

193. Hull CM, Bevilacqua PC (2016) Discriminating Self and Non-Self by RNA: Roles for RNA Structure, Misfolding, and Modification in Regulating the Innate Immune Sensor PKR. *Accounts of Chemical Research* 49:1242–1249.

194. McGhee JD, Hippel von PH (1974) Theoretical aspects of DNA-protein interactions: Co-operative and non-co-operative binding of large ligands to a one-dimensional homogeneous lattice. *Journal of Molecular Biology* 86(3):469–489.

195. Cole JL (2004) Analysis of Heterogeneous Interactions. *Methods in enzymology* 384:212–232.

196. Lu C et al. (2010) The Structural Basis of 5′ Triphosphate Double-Stranded RNA Recognition by RIG-I C-Terminal Domain. *Structure* 18(8):1032–1043.

197. Vela V, Fedorova O, Ding SC, Pyle AM (2012) The Thermodynamic Basis for Viral RNA Detection by the RIG-I Innate Immune Sensor. *Journal of Biological Chemistry* 287(51):42564.

198. Pichlmair A et al. (2011) IFIT1 is an antiviral protein that recognizes 5′-triphosphate RNA. *Nature Immunology* 12(7):624–630.

199. Pichlmair A, Superti-Furga G, Nagar B (2013) Structural basis for viral 5′-PPP-RNA recognition by human IFIT proteins. *Nature* 494(7435):60–64.

200. Katibah GE, Qin Y, Sidote DJ, Yao J, Lambowitz AM, Collins K (2014) Broad and adaptable RNA structure recognition by the human interferon-induced tetratricopeptide repeat protein IFIT5. *Proceedings of the National Academy of Sciences* 111(33):12025–12030.

201. Katibah GE et al. (2013) tRNA Binding, Structure, and Localization of the Human Interferon-Induced Protein IFIT5. *Molecular Cell* 49(4):743–750.

202. Kelley LA, Mezulis S, Yates CM, Wass MN, Sternberg MJE (2015) The Phyre2 web portal for protein modeling, prediction and analysis. *Nature Protocols, Published online: 18 October 2007;* | *doi:101038/nprot2007380* 10(6):845–858.

203. Jones DT (1999) Protein secondary structure prediction based on position-specific scoring matrices. *Journal of Molecular Biology* 292(2):195–202.

204. Kornev A, Taylor S (2015) Dynamics-driven allostery in protein kinases. *Trends in biochemical sciences*.

205. Lee KPK et al. (2008) Structure of the Dual Enzyme Ire1 Reveals the Basis for Catalysis and Regulation in Nonconventional RNA Splicing. *Cell* 132(1):89–100.

206. Young TA, Delagoutte B, Endrizzi JA, Falick AM, Alber T (2003) Structure of Mycobacterium tuberculosis PknB supports a universal activation mechanism for Ser/Thr protein kinases. *Nature Structural Biology* 10(3):168–174.

207. Gay LM, Ng H-L, Alber T (2006) A Conserved Dimer and Global Conformational Changes in the Structure of apo-PknE Ser/Thr Protein Kinase from Mycobacterium tuberculosis. *Journal of Molecular Biology* 360(2):409–420.

208. Ortiz-Lombardia M, Pompeo F, Boitel B, Alzari PM (2003) Crystal Structure of the Catalytic Domain of the PknB Serine/Threonine Kinase from Mycobacterium tuberculosis. *Journal of Biological Chemistry* 278(15):13094–13100.

209. Greenstein AE, Echols N, Lombana TN, King DS, Alber T (2007) Allosteric Activation by Dimerization of the PknD Receptor Ser/Thr Protein Kinase from Mycobacterium tuberculosis. *Journal of Biological Chemistry* 282(15):11427–11435.

210. Korennykh AV et al. (2008) The unfolded protein response signals through high-order assembly of Ire1. *Nature* 457(7230):687.

211. Ali MMU et al. (2011) Structure of the Ire1 autophosphorylation complex and implications for the unfolded protein response. *The EMBO journal* 30(5):894–905.

212. Mieczkowski C, Iavarone AT, Alber T (2008) Auto-activation mechanism of the Mycobacterium tuberculosis PknB receptor Ser/Thr kinase. *The EMBO journal* 27(23):3186–3197.

213. Kontogiannis L, Johnson O (2011) iMOSFLM: a new graphical interface for diffraction-image processing withMOSFLM. *Acta Crystallographica Section D Biological Crystallography* 67(4):271–281.

214. Airlie M et al. (2007) Phaser crystallographic software. *Journal of Applied Crystallography* 40(4):658–674.

215. Emsley P et al. (2010) Features and development of Coot. *Acta Crystallographica Section D Biological Crystallography* 66(4):486–501.

216. Krissinel E, Henrick K (2007) Inference of Macromolecular Assemblies from Crystalline State. *Journal of Molecular Biology* 372(3):774–797.

217. Cui W, Li J, Ron D, Sha B (2011) The structure of the PERK kinase domain suggests the mechanism for its activation. *Acta Crystallographica Section D Biological Crystallography* 67(5):423.

218. Padyana AK et al. (2005) Structural Basis for Autoinhibition and Mutational Activation of Eukaryotic Initiation Factor 2 Protein Kinase GCN2. *Journal of Biological Chemistry* 280(32):29289–29299.

219. Akamine P, Madhusudan, Wu J, Xuong N-H, Taylor SS (2003) Dynamic Features of cAMP-dependent Protein Kinase Revealed by Apoenzyme Crystal Structure. *Journal of Molecular Biology* 327(1):159–171.

220. Chen P et al. (2000) Implications for Chk1 Regulation: The 1.7 Å Crystal Structure of Human Cell Cycle Checkpoint Kinase Chk1. *Cell* 100(6):681–692.

221. McClendon CL, Kornev AP, Gilson MK, Taylor SS (2014) Dynamic architecture of a protein kinase. *Proceedings of the National Academy of Sciences* 111(43):4623–4631.

222. Bao ZQ, Jacobsen DM, Young MA (2011) Briefly Bound to Activate: Transient Binding of a Second Catalytic Magnesium Activates the Structure and Dynamics of CDK2 Kinase for Catalysis. *Structure* 19(5):675–690.

223. Cook A et al. (2002) Structural Studies on Phospho-CDK2/Cyclin A Bound to Nitrate, a Transition State Analogue: Implications for the Protein Kinase Mechanism. *Biochemistry* 41(23):7301.

224. Madhusudan, Akamine P, Xuong N-H, Taylor SS (2002) Crystal structure of a transition state mimic of the catalytic subunit of cAMP-dependent protein kinase. *Nature Structural Biology* 9(4):273.

225. Lombana TN et al. (2010) Allosteric Activation Mechanism of the Mycobacterium tuberculosis Receptor Ser/Thr Protein Kinase, PknB. *Structure* 18(12):1667.

226. Wang J, Wu J-W, Wang Z-X (2011) Structural Insights into the Autoactivation Mechanism of p21-Activated Protein Kinase. *Structure* 19(12):1752.

227. Rousseau F, Itzhaki LS (2003) The Unfolding Story of Three-Dimensional Domain Swapping. *Structure* 11(3):243–251.

228. Oliver AW et al. (2006) Trans-activation of the DNA-damage signalling protein kinase Chk2 by T-loop exchange. *The EMBO journal* 25(13):3179.

229. Ma X et al. (2012) Molecular basis of Tank-binding kinase 1 activation by transautophosphorylation. *Proceedings of the National Academy of Sciences* 109(24):9378.

230. Pike ACW et al. (2008) Activation segment dimerization: a mechanism for kinase autophosphorylation of non-consensus sites. *The EMBO journal* 27(4):704–714.

231. Lee SJ et al. (2009) Crystal structure of domain-swapped STE20 OSR1 kinase domain. *Protein Science* 18(2):304.

232. Juang Y-C, Earnest S, Sengupta S (2015) Domain-Swapping Switch Point in Ste20 Protein Kinase SPAK. *Biochemistry* 54(32):5063.

233. Oliver AW, Knapp S, Pearl LH (2007) Activation segment exchange: a common mechanism of kinase autophosphorylation? *Trends in biochemical sciences* 32(8):351.

234. Xu Q et al. (2015) Identifying three-dimensional structures of autophosphorylation complexes in crystals of protein kinases. *Science Signaling* 8(405):rs13.

235. Meyer AS et al. (2003) Closing the Folding Chamber of the Eukaryotic Chaperonin Requires the Transition State of ATP Hydrolysis. *Cell* 113(3):369–381.

236. Kornev AP, Kornev AP (2011) Protein kinases: evolution of dynamic regulatory proteins. *Trends in biochemical sciences* 36(2):65-77.

237. Yang J, Ten Eyck L, Xuong N-H, Taylor SS (2004) Crystal Structure of a cAMP-dependent Protein Kinase Mutant at 1.26Å: New Insights into the Catalytic Mechanism. *Journal of Molecular Biology* 336(2):473–487.

238. Patel O et al. (2016) Biochemical and Structural Insights into Doublecortin-like Kinase Domain 1. *Structure* 24(9):1550–1561.

239. Christie M, Boland A, Huntzinger E, Weichenrieder O, Izaurralde E (2013) Structure of the PAN3 Pseudokinase Reveals the Basis for Interactions with the PAN2 Deadenylase and the GW182 Proteins. *Molecular Cell* 51(3):360–373.

240. Olesen C et al. (2007) The structural basis of calcium transport by the calcium pump. *Nature* 450(7172):1036–1042.

241. Paliwal S, Gray K (2010) Structural basis of CX-4945 binding to human protein kinase CK2. *FEBS Letters* 585(1):104–110.

242. Parthasarathy G, Zuck P (2015) Structure and Function of the Hypertension Variant A486V of G Protein-coupled Receptor Kinase 4. *Journal of Biological Chemistry* 290(33):20360–20373.

243. Subramanian C, Yun M-K, Yao J, Sharma LK, Jackowski S (2016) Allosteric Regulation of Mammalian Pantothenate Kinase. *Journal of Biological Chemistry* 291(42):22302–22314.

244. Yount RG, Babcock D, Ballantyne W, Ojala D (1971) Adenylyl imidiodiphosphate, an adenosine triphosphate analog containing a PNP linkage. *Biochemistry* 10(13):2484-2489.

245. Heppel L, Harkness DR, Hilmoe RJ (1962) A Study of the Substrate Specificity and Other Properties of the Alkaline Phosphatase of Escherichia coli. *Journal of Biological Chemistry* 237(3):841–846.

246. Tomaszek TA Jr, Schuster SM (1986) Hydrolysis of adenyl-5-yl imidodiphosphate by beef heart mitochondrial ATPase. *Journal of Biological Chemistry* 261(5):2264–2269.

247. Taylor JS et al. (1981) Sarcoplasmic reticulum ATPase catalyzes hydrolysis of adenyl-5'-yl imidodiphosphate. *Journal of Biological Chemistry* 256(19):9793–9795.

248. Suzuki Y, Shimizu T, Morii H, Tanokura M (1997) Hydrolysis of AMPPNP by the motor domain of ncd, a kinesin-related protein. *FEBS Letters* 409(1):29–32.

249. Guo Y, Wu J, Taylor SS (2013) Phosphoryl Transfer by Protein Kinase A Is Captured in a Crystal Lattice. *Journal of the American Chemical Society* 135(12):4788–4798.

250. Adams JA (2001) Kinetic and Catalytic Mechanisms of Protein Kinases. *Chemical Reviews* 101(8):2271–2290.

251. O'Brien P et al. (2012) Price To Be Paid for Two-Metal Catalysis: Magnesium Ions That Accelerate Chemistry Unavoidably Limit Product Release from a Protein Kinase. *Journal of the American Chemical Society* 134(37):15357–15370.

252. Taylor DR et al. (2001) Hepatitis C Virus Envelope Protein E2 Does Not Inhibit PKR by Simple Competition with Autophosphorylation Sites in the RNA-Binding Domain. *Journal of Virology* 75(3):1265–1273.

253. Young TS, Ahmad I, Yin JA, Schultz PG (2010) An Enhanced System for Unnatural Amino Acid Mutagenesis in E. coli. *Journal of Molecular Biology* 395(2):361–374.

254. Chin JW, Martin AB, King DS, Wang L, Schultz PG (2002) Addition of a photocrosslinking amino acid to the genetic code of Escherichia coli. *Proceedings of the National Academy of Sciences* 99(17):11020–11024.

255. Zhang F et al. (2001) Binding of Double-stranded RNA to Protein Kinase PKR Is Required for Dimerization and Promotes Critical Autophosphorylation Events in the Activation Loop. *Journal of Biological Chemistry* 276(27):24946–24958.

256. Taylor SS, Haste NM, Ghosh G (2005) PKR and eIF2α: Integration of Kinase Dimerization, Activation, and Substrate Docking. 122(6):823–825.

257. Tan R, Frankel AD (1995) Structural variety of arginine-rich RNA-binding peptides. *Proceedings of the National Academy of Sciences* 92(12):5282–5286.

258. Casu F, Duggan BM, Hennig M (2013) The Arginine-Rich RNA-Binding Motif of HIV-1 Rev Is Intrinsically Disordered and Folds upon RRE Binding. *Biophysical Journal* 105(4):1004–1017.

259. Tan R, Frankel AD (1994) Costabilization of peptide and RNA structure in an HIV Rev peptide-RRE complex. *Biochemistry* 33(48):14579–14585.

260. Madhusudan et al. (2008) cAMP-dependent protein kinase: Crystallographic insights into substrate recognition and phosphotransfer. *Protein Science* 3(2):176–187.

261. Alber T (2009) Signaling mechanisms of the Mycobacterium tuberculosis receptor Ser/Thr protein kinases. *Current Opinion in Structural Biology* 19(6):650–657.

262. Ito T et al. (1999) RAX, a Cellular Activator for Double-stranded RNA-dependent Protein Kinase during Stress Signaling. *Journal of Biological Chemistry* 274(22):15427–15432.

263. Dickerman B, Sen GC (2009) Biochemical analysis of PKR activation by PACT. *Biochemistry* 48(31):7441–7447.

264. Gleghorn ML, Gong C, Kielkopf CL, Maquat LE (2013) Staufen1 dimerizes through a conserved motif and a degenerate dsRNA-binding domain to promote mRNA decay. *Nature Structural & Molecular Biology* 20(4):515–524.

265. Daniels SM, Gatignol A (2012) The Multiple Functions of TRBP, at the Hub of Cell Responses to Viruses, Stress, and Cancer. *Microbiology and Molecular Biology Reviews* 76(3):652–666.

266. Buckler-White A et al. (1991) Characterization of a human TAR RNA-binding protein that activates the HIV-1 LTR. *Science* 251(5001):1597–1600.

267. Park H et al. (1994) TAR RNA-binding protein is an inhibitor of the interferon-induced protein kinase PKR. *Proceedings of the National Academy of Sciences* 91(11):4713–4717.

268. Daher A, Meurs EF, Gatignol A (2001) Two Dimerization Domains in the Trans-activation Response RNA-binding Protein (TRBP) Individually Reverse the Protein Kinase R Inhibition of HIV-1 Long Terminal Repeat Expression. *Journal of Biological Chemistry* 276(36):33899–33905.

269. Gupta V, Huang X, Patel RC (2003) The carboxy-terminal, M3 motifs of PACT and TRBP have opposite effects on PKR activity. *Virology* 315(2):283–291.

270. Laraki G et al. (2008) Interactions between the double-stranded RNA-binding proteins TRBP and PACT define the Medipal domain that mediates protein-protein interactions. *RNA Biology* 5(2):92–103.

271. Daher A, Meurs EF, Patel RC, Gatignol A (2009) TRBP Control of PACT-Induced Phosphorylation of Protein Kinase R Is Reversed by Stress. *Molecular and Cellular Biology* 29(1):254–265.

272. Singh M, Castillo D (2011) Stress-Induced Phosphorylation of PACT Reduces Its Interaction with TRBP and Leads to PKR Activation. *Biochemistry* 50(21):4550–4560.

273. Chen Z, Krug RM (2000) Selective nuclear export of viral mRNAs in influenza-virus-infected cells. *Trends in Microbiology* 8(8):376–383.

274. Bergmann M et al. (2000) Influenza Virus NS1 Protein Counteracts PKR-Mediated Inhibition of Replication. *Journal of Virology* 74(13):6203–6206.

275. Lu Y, Wambach M, Katze MG, Krug RM (1995) Binding of the Influenza Virus NS1 Protein to Double-Stranded RNA Inhibits the Activation of the Protein Kinase That Phosphorylates the eIF-2 Translation Initiation Factor. *Virology* 214(1):222–228.

276. Hatada E, Saito S, Fukuda R (1999) Mutant Influenza Viruses with a Defective NS1 Protein Cannot Block the Activation of PKR in Infected Cells. *Journal of Virology* 73(3):2425–2433.

277. Lin D, Lan J, Zhang Z (2007) Structure and function of the NS1 protein of influenza A virus. *Acta biochimica et biophysica Sin* 39(3):155–162.

278. Hale BG (2014) Conformational plasticity of the influenza A virus NS1 protein. *Journal of General Virology* 95(10):2099–2105.

279. Liu J, Lynch PA, Chien CY, Montelione GT (1997) Crystal structure of the unique RNA-binding domain of the influenza virus NS1 protein. *Nature structural* biology 4(11):896–899.

280. Chien CY et al. (2004) Biophysical Characterization of the Complex between Double-Stranded RNA and the N-Terminal Domain of the NS1 Protein from Influenza A Virus: Evidence for a Novel RNA-Binding Mode. *Biochemistry* 43(7):1950–1962.

281. Cheng A, Wong SM, Yuan YA (2009) Structural basis for dsRNA recognition by NS1 protein of influenza A virus. *Cell Research* 19(2):187.

282. Xia S, Monzingo AF, Robertus JD (2009) Structure of NS1A effector domain from the influenza A/Udorn/72 virus. *Acta Crystallographica Section D Biological Crystallography* 65(1):11–17.

283. Hale BG, Barclay WS, Randall RE, Russell RJ (2008) Structure of an avian influenza A virus NS1 protein effector domain. *Virology* 378(1):1–5.

284. Bornholdt ZA, Prasad BVV (2006) X-ray structure of influenza virus NS1 effector domain. *Nature Structural & Molecular Biology* 13(6):559–560.

285. Ayllon J, Hass C, Lewis A, García-Sastre A (2011) A Transient Homotypic Interaction Model for the Influenza A Virus NS1 Protein Effector Domain. *PloS one* 6(3):e17946.

286. Aramini et al. (2011) Dimer Interface of the Effector Domain of Non-structural Protein 1 from Influenza A Virus: AN INTERFACE WITH MULTIPLE FUNCTIONS. *Journal of Biological Chemistry* 286(29):26050–26060.

287. Bornholdt Z, Prasad BV (2008) X-ray structure of NS1 from a highly pathogenic H5N1 influenza virus. *Nature* 456(7224):985–988.

288. Wang X et al. (2002) Functional replacement of the carboxy-terminal two-thirds of the influenza A virus NS1 protein with short heterologous dimerization domains. *Journal of Virology* 76(24):12951–12962.

289. Carillo B et al. (2014) The Influenza A Virus Protein NS1 Displays Structural Polymorphism. *Journal of Virology* 88(8):4113–4122.

290. Greenfield NJ (2006) Using circular dichroism spectra to estimate protein secondary structure. *Nature Protocols* 1(6):2876–2890.

291. Marenchino M, Armbruster DW, Hennig M (2009) Rapid and efficient purification of RNA-binding proteins: Application to HIV-1 Rev. *Protein Expression and Purification* 63(2):112–119.

292. Hitti EG, Sallacz NB, Schoft VK, Jantsch MF (2004) Oligomerization activity of a double-stranded RNA-binding domain. *FEBS Letters* 574(1-3):25–30.

293. Clerzius G, Daher A, Bonnet M, Meurs EF, Gatignol A (2009) ADAR1 Interacts with PKR during Human Immunodeficiency Virus Infection of Lymphocytes and Contributes to Viral Replication. *Journal of Virology* 83(19):10119–10128.

294. Wen X et al. (2014) NF90 Exerts Antiviral Activity through Regulation of PKR Phosphorylation and Stress Granules in Infected Cells. *The Journal of Immunology* 192(8):3753–3764.

295. Mittelstadt M et al. (2007) Interaction of human tRNA-dihydrouridine synthase-2 with interferon-induced protein kinase PKR. *Nucleic Acids Research* 36(3):998–1008.

296. Peters GA et al. (2002) Inhibition of PACT-Mediated Activation of PKR by the Herpes Simplex Virus Type 1 Us11 Protein. *Journal of Virology* 76(21):11054–11064.

297. Ayllon J et al. (2012) Contribution of NS1 Effector Domain Dimerization to Influenza A Virus Replication and Virulence. *Journal of Virology* 86(23):13095–13098.

298. Min JY, Krug RM (2006) The primary function of RNA binding by the influenza A virus NS1 protein in infected cells: Inhibiting the 2'-5' oligo (A) synthetase/RNase L pathway. *Proceedings of the National Academy of Sciences* 103(18):7100–7105.

299. Leung DW, Basler CF, Amarasinghe GK (2012) Molecular mechanisms of viral inhibitors of RIG-I-like receptors. *Trends in Microbiology* 20(3):139–146.

300. Marques JT, White CL, Peters GA, Williams BRG, Sen GC (2008) The Role of PACT in Mediating Gene Induction, PKR Activation, and Apoptosis in Response to Diverse Stimuli. *Journal of Interferon & Cytokine Research* 28(8):469–476.